Tampere University

MATIAS BERG

# Deadtime Effect and Impedance Coupling in Dynamic Analysis of Grid-Connected Inverters

Tampere University Dissertations 469

Tampere University Dissertations 469

MATIAS BERG

# Deadtime Effect and Impedance Coupling in Dynamic Analysis of Grid-Connected Inverters

ACADEMIC DISSERTATION
To be presented, with the permission of
the Faculty of Information Technology and Communication Sciences
of Tampere University,
for public discussion in the SA207 S4
of Sähkötalo, Korkeakoulunkatu 3, Tampere,
on 24 September 2021, at 12 o'clock.

ACADEMIC DISSERTATION
Tampere University, Faculty of Information Technology and Communication Sciences
Finland

*Responsible supervisor and Custos*
Assistant Professor
Tomi Roinila
Tampere University
Finland

*Pre-examiners*
Assistant Professor
Hiroaki Matsumori
Nagoya Institute of Technology
Japan

Dr. Tech.
Aram Khodamoradi
Hitachi ABB Power Grids
Italy

*Opponent*
Associate Professor
Pasi Peltoniemi
LUT University
Finland



Cover design: Roihu Inc.

ISBN 978-952-03-2092-8 (print)
ISBN 978-952-03-2093-5 (pdf)
ISSN 2489-9860 (print)
ISSN 2490-0028 (pdf)
http://urn.fi/URN:ISBN:978-952-03-2093-5

PunaMusta Oy – Yliopistopaino
Joensuu 2021

# Abstract

Grid-connected power-electronic inverters play a crucial role in the transition from the carbon-based energy production to renewable energy production. Because many power generators that utilize renewable power sources cannot be connected directly to the alternating-current distribution grid for power delivery, an inverter is often required as an interface between the renewable energy source and the distribution grid. However, potential dynamic interactions between feedback-controlled power converters and the power grid can lead to stability issues. Detrimental interactions should be prevented in the inverter controller design phase where the interactions can be modeled with equivalent small-signal impedances of the grid and the grid-connected inverters. However, the impedances are usually unknown.

Previous studies have presented methods to measure the terminal impedances in grid-connected-inverter systems for an improved controller design. Recent developments in the impedance measurement have led to broadband measurement methods that can be implemented in a short amount of time using orthogonal binary sequences and with a low computational effort. However, previous non-parametric measurement methods performed with orthogonal sequences have not dealt in depth with a crucial issue of three-phase impedance measurements: distortion between synchronous reference-frame measurement channels.

Conventionally, an impedance that is measured for the control design is assumed to behave linearly in the system operating point where the measurement is performed. However, under low load conditions, a nonlinearity stemming from the deadtime can be significant. The nonlinear deadtime effect adds significant damping, which can lead to a false interpretation of the system stability margins if not modeled correctly.

This thesis presents a novel synchronous-reference-frame impedance measurement method for three-phase grid-connected power-electronic systems. The method makes it possible to measure an equivalent synchronous-reference-frame system impedance within a single measurement cycle, which provides disturbance rejection capability. In addition, a describing function model for the nonlinear deadtime effect is proposed. The model can be used to compute the sinusoidal steady state of an inverter under low load conditions. These methods and models can be applied to the adaptive control, the real-time stability analysis, and the robust control of grid-connected converters.

# Preface

This research was started at Tampere University of Technology in 2017 and finished at Tampere University in 2021. The research was funded by projects from Business Finland, ABB Oy, and Fimer Oy and in the form of personal grants from Fortum Foundation, the Industrial Research Fund at Tampere University of Technology, and the Finnish Cultural Foundation. All these funds are greatly appreciated.

First of all, I would like to express my deepest appreciation to Assistant Professor Tomi Roinila for supervising my thesis. I would also like to extend my deepest gratitude to Adjunct Professor Tuomas Messo who was my initial supervisor. I am also grateful to Professor Emeritus Teuvo Suntio for encouraging me to enter into the academic world and his helpful advice. My research would not have been possible without the support of Professor Paolo Mattavelli from University of Padua who made my research exchange possible and showed confidence in me. I am extremely grateful to Assistant Professor Hiroaki Matsumori and Dr. Tech. Aram Khodamoradi for pre-examining my thesis.

I would like to extend my sincere thanks to my current and former colleagues Dr. Tech. Aapo Aapro, Dr. Tech. Jyri Kivimäki, Dr. Tech. Jukka Viinamäki, Dr. Tech. Roni Luhtala, Dr. Tech. Jussi Sihvo, M.Sc. Henrik Alenius, M.Sc. Roosa-Maria Sallinen, M.Sc. Tommi Reinikka, and M.Sc. Markku Järvelä who never wavered in their support. I also wish to thank Dr. Tech. Jenni Rekola who played a decisive role in the beginning of my research. I would like to recognize the assistance in control system topics that I received from M.Sc. Veli-Pekka Pyrhönen. Adjunct Professor Kari Lahti and M.Sc. Minna Niittymäki deserve special thanks for the help with laboratory equipment and friendship.

I want to express my gratitude to my parents, Nina and Esa, who gave unparalleled support and had profound belief in my abilities. I also wish to thank Liisa and Timo for encouragement during my research. Finally, many thanks to my friends who provided support and distractions outside of my research.

Tampere, August 2021

*Matias Berg*

# Contents

# Symbols and abbreviations

## Abbreviations

| | |
|---|---|
| AC | Alternating current |
| DC | Direct current |
| DFT | Discrete Fourier transform |
| ESR | Equivalent series resistance |
| IGBT | Insulated-gate bipolar transistor |
| IRS | Inverse-repeat sequence |
| MLBS | Maximum-length binary sequence |
| MOSFET | Metal-oxide-semiconductor field-effect transistor |
| OBS1 | First orthogonal binary sequence |
| OBS2 | Second orthogonal binary sequence |
| PCC | Point of Common Coupling |
| PI | Proportional-integral (controller) |
| PLL | Phase-locked loop |
| PV | Photovoltaic |
| PWM | Pulse-width modulation |
| RMS | Root-mean-squared |
| SPWM | Sinusoidal pulse-width modulation |
| TF | Transfer function |
| TF-intrpl | Transfer-function interpolation |

## Greek characters

| | |
|---|---|
| $\Delta i_{\text{dead}}$ | Maximum current change during the deadtime |
| $\Delta i_{\text{p-p}}$ | Peak-to-peak inductor current ripple |
| $\theta$ | Phase angle |
| $\theta_{\text{C}}$ | Capacitor voltage phase angle |
| $\theta_{\text{L}}$ | Inductor current phase angle |
| $\theta_{\text{o}}$ | Output current phase angle |

| | |
|---|---|
| $\xi$ | Damping factor |
| $\omega$ | Angular frequency |
| $\omega_0$ | Natural frequency |
| $\omega_\mathrm{s}$ | Synchronous frequency |

## Latin characters

| | |
|---|---|
| $a$, $b$, $c$ | Phase leg identifiers (for three phase system) |
| $A$ | Amplitude of the inductor current |
| $C$ | (AC) capacitor |
| $C_\mathrm{dc}$ | DC capacitor |
| $d$ | Direct (channel) |
| $D$ | Diode |
| $D_\mathrm{d}$ | Steady-state d-component of the duty ratio |
| $D_\mathrm{q}$ | Steady-state q-component of the duty ratio |
| $f_\mathrm{gen}$ | Generation frequency |
| $f_k^\mathrm{MLBS}$ | Energetic frequencies of the MLBS |
| $f_k^\mathrm{OBS2}$ | Energetic frequencies of the OBS2 |
| $f_\mathrm{sw}$ | Switching frequency |
| $G_\mathrm{cc}$ | Current controller transfer function |
| $G_\mathrm{ci\text{-}d}$ | Control-to-input transfer function d component |
| $G_\mathrm{ci\text{-}q}$ | Control-to-input transfer function q component |
| $G_\mathrm{cL\text{-}d}$ | Control-to-inductor current transfer function d component |
| $G_\mathrm{cL\text{-}d}^\mathrm{L}$ | Load-affected $G_\mathrm{cL\text{-}d}$ |
| $G_\mathrm{cL\text{-}dq}$ | Control-to-inductor current transfer function d-to-q component |
| $G_\mathrm{cL\text{-}dq}^\mathrm{L}$ | Load-affected $G_\mathrm{cL\text{-}dq}$ |
| $G_\mathrm{cL\text{-}q}$ | Control-to-inductor current transfer function q component |
| $G_\mathrm{cL\text{-}q}^\mathrm{OBS2}$ | $G_\mathrm{cL\text{-}q}$ at OBS2 frequencies |
| $G_\mathrm{cL\text{-}qd}$ | Control-to-inductor current transfer function q-to-d component |
| $G_\mathrm{cL\text{-}qd}^\mathrm{OBS2}$ | $G_\mathrm{cL\text{-}qd}$ at OBS2 frequencies |
| $G_\mathrm{co\text{-}d}$ | Control-to-output current transfer function d component |
| $G_\mathrm{co\text{-}dq}$ | Control-to-output current transfer function d-to-q component |
| $G_\mathrm{co\text{-}q}$ | Control-to-output current transfer function q component |
| $G_\mathrm{co\text{-}qd}$ | Control-to-output current transfer function q-to-d component |
| $G_\mathrm{cv\text{-}q}^\mathrm{OBS2}$ | Control-to-output voltage TF q component at OBS2 frequencies |
| $G_\mathrm{cv\text{-}qd}^\mathrm{OBS2}$ | Control-to-output voltage TF qd component at OBS2 freqs. |
| $G_\mathrm{cv\text{-}q}^\mathrm{TF\text{-}intrpl}$ | Control-to-output voltage TF q obtained by TF-interpolation |
| $G_\mathrm{cv\text{-}qd}^\mathrm{TF\text{-}intrpl}$ | Control-to-output voltage TF qd obtained by TF-interpolation |
| $G_\mathrm{iL\text{-}d}$ | Input-to-inductor current transfer function d component |
| $G_\mathrm{iL\text{-}q}$ | Input-to-inductor current transfer function q component |

| | |
|---|---|
| $G_{\text{io-d}}$ | Input-to-output transfer function d component |
| $G_{\text{io-q}}$ | Input-to-output transfer function q component |
| $G_{\text{oi-d}}$ | Output-to-input transfer function d component |
| $G_{\text{oi-q}}$ | Output-to-input transfer function q component |
| $G_{\text{oL-d}}$ | Output-to-inductor current transfer function d component |
| $G_{\text{oL-dq}}$ | Output-to-inductor current transfer function d-to-q component |
| $G_{\text{oL-q}}$ | Output-to-inductor current transfer function q component |
| $G_{\text{oL-qd}}$ | Output-to-inductor current transfer function q-to-d component |
| $G^{\text{OBS2-}k}$ | Transfer function at $k$:th frequency of OBS2 frequencies |
| $G^{\text{TF-intrpl-}k}$ | General transfer function interpolation result at $k$:th frequency |
| $G_1$ | Voltage reference-to-current transfer function qd component |
| $G_2$ | Voltage reference-to-voltage transfer function qd component |
| $G_3$ | Voltage reference-to-current transfer function q component |
| $G_4$ | Voltage reference-to-voltage transfer function q component |
| $\mathbf{G}_{\text{cc}}$ | Current controller transfer matrix |
| $\mathbf{G}_{\text{ci}}$ | Control-to-input transfer matrix |
| $\mathbf{G}_{\text{cL}}$ | Control-to-inductor current transfer matrix |
| $\mathbf{G}_{\text{cL}}^{\text{L}}$ | Load-affected $\mathbf{G}_{\text{cL}}$ |
| $\mathbf{G}_{\text{co}}$ | Control-to-output transfer matrix |
| $\mathbf{G}_{\text{iL}}$ | Input-to-inductor current transfer matrix |
| $\mathbf{G}_{\text{io}}$ | Input-to-output transfer matrix |
| $\mathbf{G}_{\text{oi}}$ | Output-to-input transfer matrix |
| $\mathbf{G}_{\text{oL}}$ | Output-to-inductor current transfer matrix |
| $i$ | Current |
| $i_{\text{Cd}}$ | Capacitor current d component |
| $i_{\text{Cq}}$ | Capacitor current q component |
| $\bar{i}_{\text{L}}$ | Inductor current phasor |
| $i_{\text{Ld}}$ | Inductor current d component |
| $i_{\text{Lq}}$ | Inductor current q component |
| $\bar{i}_{\text{L}}^{dq}$ | Space vector of inductor current in synchronous reference frame |
| $\bar{i}_{\text{L}}^{\alpha\beta}$ | Space vector of inductor current in stationary reference frame |
| $\bar{i}_{\text{o}}$ | Output current phasor |
| $i_{\text{od}}$ | d-component of the output current |
| $i_{\text{oq}}$ | q-component of the output current |
| $i_{\text{th}}$ | Thévenin equivalent current |
| $i^{\text{inj}}$ | Current injection |
| $I_{\text{d1}}$ | Fourier-transformed d current related to d channel injection |
| $I_{\text{in}}$ | Steady-state input current |
| $I_{\text{Ld}}$ | Steady-state d-component of the inductor current |
| $I_{\text{Ld1}}$ | Fourier-transformed d current related to d channel injection |

| | |
|---|---|
| $I_{\mathrm{Ld2}}$ | Fourier-transformed d current related to q channel injection |
| $I_{\mathrm{Ld2}}^{\mathrm{OBS2}}$ | $I_{\mathrm{Ld2}}$ at OBS2 frequencies |
| $I_{\mathrm{Lq}}$ | Steady-state q-component of the inductor current |
| $I_{\mathrm{Lq1}}$ | Fourier-transformed q current related to d channel injection |
| $I_{\mathrm{Lq2}}$ | Fourier-transformed q current related to 2 channel injection |
| $I_{\mathrm{Lq2}}^{\mathrm{OBS2}}$ | $I_{\mathrm{Lq2}}$ at OBS2 frequencies |
| $I_{\mathrm{Lq2}}^{\mathrm{ref\text{-}OBS2}}$ | $I_{\mathrm{Lq2}}$ reference at OBS2 frequencies |
| $I_{\mathrm{od}}$ | Steady-state d-component of the output current |
| $I_{\mathrm{oq}}$ | Steady-state q-component of the output current |
| $I_{\mathrm{q1}}$ | Fourier-transformed q current related to d channel injection |
| $j$ | Imaginary unit |
| $K_{\mathrm{i\text{-}c}}$ | Current controller integral gain |
| $K_{\mathrm{i\text{-}pll}}$ | PLL controller integral gain |
| $K_{\mathrm{i\text{-}pll}}^{\mathrm{meas.}}$ | Measurement PLL controller integral gain |
| $K_{\mathrm{i\text{-}v}}$ | Direct voltage controller integral gain |
| $K_{\mathrm{i\text{-}c}}$ | Current controller proportional gain |
| $K_{\mathrm{i\text{-}v}}$ | Direct voltage controller proportional gain |
| $K_{\mathrm{p\text{-}pll}}$ | PLL controller proportional gain |
| $K_{\mathrm{p\text{-}pll}}^{\mathrm{meas.}}$ | Measurement PLL controller proportional gain |
| $L$ | Inductor, filter inductance |
| $L_{\mathrm{line}}$ | Line inductance |
| $L_{\mathrm{T}}$ | Transformer inductance |
| $L_2$ | Filter inductance 2 |
| n | Negative inverter DC rail |
| $n$ | Length of a feedback register |
| $N$ | Describing function model; length of a PRBS |
| $N_1$ | Describing function for slope and saturation |
| $N_2$ | Describing function for slope and saturation |
| p | Positive inverter DC rail |
| $q$ | Quadrature (channel) |
| $r_{\mathrm{Cf}}$ | $C_{\mathrm{Cf}}$ ESR and damping resistor |
| $r_{\mathrm{L}}$ | Filter inductance ESR |
| $r_{\mathrm{Lg}}$ | Line inductance ESR |
| $r_{\mathrm{T}}$ | Transformer ESR |
| $R^{\mathrm{dead}}$ | Current limit for the end of the dead zone |
| $R^{\mathrm{sat}}$ | Current limit for the saturation region |
| $S$ | Switch |
| $s$ | Laplace variable |
| $t$ | Time |
| $T_{\mathrm{dead}}$ | Deadtime length |

| | |
|---|---|
| $T_{\text{oi-d}}$ | Reverse transfer function d component |
| $T_{\text{oi-q}}$ | Reverse transfer function q component |
| $\mathbf{T}_{\text{oi}}$ | Reverse transfer matrix |
| $T_{\text{sw}}$ | Period of switching cycle |
| $v$ | Voltage |
| $v_{\text{a}}$, $v_{\text{b}}$, $v_{\text{c}}$ | Three phase voltages with respect to filter capacitor neutral |
| $v_{\text{Cd}}$ | Capacitor voltage d component |
| $v_{\text{Cq}}$ | Capacitor voltage q component |
| $v_{\text{d}}$, $v_{\text{q}}$ | Phase voltages in synchronous reference frame |
| $v_{\text{err}}$ | Instantaneous voltage error due to the deadtime |
| $v_{\text{err}}^{\text{avg}}$ | Average deadtime voltage error over a switching cycle |
| $\bar{v}_{\text{err}}$ | Voltage error phasor |
| $\bar{v}_{\text{L}}^{\text{dq}}$ | Space vector of inductor voltage in synchronous reference frame |
| $\bar{v}_{\text{L}}^{\alpha\beta}$ | Space vector of inductor voltage in stationary reference frame |
| $v_{\text{Ld}}$ | Inductor voltage d component |
| $v_{\text{Lq}}$ | Inductor voltage q component |
| $v_m$ | Voltage over $m$:th impedance element |
| $\bar{v}_{\text{o}}$ | Output voltage phasor |
| $v_{\text{th}}$ | Thévenin equivalent voltage |
| $V_{\text{d1}}$ | Fourier-transformed d voltage related to d channel injection |
| $V_{\text{d1}}$ | Fourier-transformed d voltage related to d channel injection |
| $V_{\text{d2}}$ | Fourier-transformed d voltage related to q channel injection |
| $V_{\text{d2}}^{\text{OBS2}}$ | $V_{\text{d2}}$ at OBS2 frequencies |
| $V_{\text{dc}}$ | DC link voltage |
| $V_{\text{err}}^{\text{avg-max}}$ | Maximum average deadtime voltage error over a switching cycle |
| $V_{\text{err-f1}}$ | Fundamental-frequency voltage error |
| $V_{\text{g-rms}}$ | Grid-voltage RMS value |
| $V_{\text{od}}$ | Steady-state d-component of the output voltage |
| $V_{\text{oq}}$ | Steady-state q-component of the output voltage |
| $V_{\text{q1}}$ | Fourier-transformed q voltage related to d channel injection |
| $V_{\text{q2}}$ | Fourier-transformed q voltage related to q channel injection |
| $V_{\text{q2}}^{\text{OBS2}}$ | $V_{\text{q2}}$ at OBS2 frequencies |
| $x_{\text{d}}$, $x_{\text{q}}$ | Generic variables in synchronous reference frame |
| $x_\alpha$, $x_\beta$ | Generic variables in stationary reference frame |
| $Y_{\text{in}}$ | Input admittance |
| $Y_{\text{o-d}}$ | Output admittance d component |
| $Y_{\text{o-d}}^{\text{TF-intrpl}}$ | $Y_{\text{o-d}}$ obtained by transfer-function interpolation |
| $Y_{\text{o-dq}}$ | Output admittance d-to-q component |
| $Y_{\text{o-dq}}^{\text{TF-intrpl}}$ | $Y_{\text{o-dq}}$ obtained by transfer-function interpolation |
| $Y_{\text{o-q}}$ | Output admittance q component |

| | |
|---|---|
| $Y_{\text{o-q}}^{\text{TF-intrpl}}$ | $Y_{\text{o-q}}$ obtained by transfer-function interpolation |
| $Y_{\text{o-qd}}$ | Output admittance q-to-d component |
| $Y_{\text{o-qd}}^{\text{TF-intrpl}}$ | $Y_{\text{o-qd}}$ obtained by transfer-function interpolation |
| $\mathbf{Y}_{\text{o}}$ | Output admittance matrix |
| z | DC bus midpoint |
| $Z_{\text{C}}$ | Filter capacitor impedance |
| $Z_{\text{C-d}}$ | Filter capacitor impedance d component |
| $Z_{\text{C-dq}}$ | Filter capacitor impedance d-to-q component |
| $Z_{\text{C-q}}$ | Filter capacitor impedance q component |
| $Z_{\text{C-qd}}$ | Filter capacitor impedance q-to-d component |
| $Z_{\text{C-dc}}^{\text{par}}$ | Impedance of parallel connected DC capacitors |
| $Z_{\text{g-d}}$ | Grid impedance d component |
| $Z_{\text{g-d}}^{\text{2MLBS}}$ | $Z_{\text{g-d}}$ obtained by sequential injections |
| $Z_{\text{g-d}}^{\text{TF-intrpl}}$ | $Z_{\text{g-d}}$ obtained by transfer-function interpolation |
| $Z_{\text{g-d}}^{\text{vd/id}}$ | $Z_{\text{g-d}}$ ratio of $v_{\text{d}}$ and $i_{\text{Ld}}$ |
| $Z_{\text{g-dq}}$ | Grid impedance d-to-q component |
| $Z_{\text{g-dq}}^{\text{2MLBS}}$ | $Z_{\text{g-dq}}$ obtained by sequential injections |
| $Z_{\text{g-dq}}^{\text{TF-intrpl}}$ | $Z_{\text{g-dq}}$ obtained by transfer-function interpolation |
| $Z_{\text{g-dq}}^{\text{vq/id}}$ | $Z_{\text{g-dq}}$ ratio of $v_{\text{q}}$ and $i_{\text{Ld}}$ |
| $Z_{\text{g-q}}$ | Grid impedance q component |
| $Z_{\text{g-q}}^{\text{2MLBS}}$ | $Z_{\text{g-q}}$ obtained by sequential injections |
| $Z_{\text{g-q}}^{\text{TF-intrpl}}$ | $Z_{\text{g-q}}$ obtained by transfer-function interpolation |
| $Z_{\text{g-d}}^{\text{vq/iq}}$ | $Z_{\text{g-q}}$ ratio of $v_{\text{q}}$ and $i_{\text{Lq}}$ |
| $Z_{\text{g-qd}}$ | Grid impedance q-to-d component |
| $Z_{\text{g-qd}}^{\text{2MLBS}}$ | $Z_{\text{g-qq}}$ obtained by sequential injections |
| $Z_{\text{g-qd}}^{\text{TF-intrpl}}$ | $Z_{\text{g-qd}}$ obtained by transfer-function interpolation |
| $Z_{\text{g-qd}}^{\text{vqd/iq}}$ | $Z_{\text{g-qd}}$ ratio of $v_{\text{d}}$ and $i_{\text{Lq}}$ |
| $Z_{\text{L}}$ | Inductor branch impedance |
| $Z_{\text{Lg-d}}$ | Inductive grid impedance d component |
| $Z_{\text{Lg-dq}}$ | Inductive grid impedance d-to-q component |
| $Z_{\text{Lg-q}}$ | Inductive grid impedance q component |
| $Z_{\text{Lg-qd}}$ | Inductive grid impedance q-to-d component |
| $Z_m$ | $m$:th impedance element |
| $Z_{\text{o}}$ | Output impedance |
| $Z_{\text{th}}$ | Thévenin equivalent impedance |
| $\mathbf{Z}_{\text{C}}$ | Filter capacitor impedance matrix |
| $\mathbf{Z}_{\text{g}}$ | Grid impedance matrix |
| $\mathbf{Z}_{\text{Lg}}$ | Inductive grid impedance matrix |

## Subscripts

| | |
|---|---|
| a, b, c | Phase leg identifiers (for three phase system) |
| C | Capacitor-related variable |
| ESR | Equivalent series resistance |
| dc | Direct current |
| L | Inductor-related variable |
| pcc | Point of Common Coupling |
| PI | Proportional-integral (controller) |
| PV | Photovoltaic |
| RMS | Root-mean-squared |

# List of publications

This thesis is based on the following original publications, which are referred to in the text as in [P1]–[P5]:

[P1] M. Berg, H. Alenius and T. Roinila, "Rapid Multivariable Identification of Grid Impedance in DQ Domain Considering Impedance Coupling," *IEEE Journal of Emerging and Selected Topics in Power Electronics*, Early Access, 2020.

[P2] M. Berg and T. Roinila, "Nonlinear Effect of Deadtime in Small-Signal Modeling of Power-Electronics System Under Low Load Conditions," *IEEE Journal of Emerging and Selected Topics in Power Electronics*, vol. 8, no. 4, pp. 3204—3213, 2020.

[P3] M. Berg, T. Messo, T. Roinila and P. Mattavelli, "Deadtime Impact on the small-signal output impedance of Single-Phase Power Electronic Converters," in Proc. *IEEE 20th Workshop on Control and Modeling for Power Electronics*, 2019.

[P4] M. Berg, T. Messo, and T. Suntio, "Frequency Response Analysis of Load Effect on Dynamics of Grid-Forming Inverter," in Proc. *International Power Electronics Conference*, pp. 963–970, 2018.

[P5] M. Berg, T. Messo, T. Roinila and H. Alenius, "Impedance Measurement of Megawatt-Level Renewable Energy Inverters using Grid-Forming and Grid-Parallel Converters," in Proc. *International Power Electronics Conference*, pp. 4205–4212, 2018.

# Summary of publications

## [P1]

The paper presents a rapid procedure to measure the synchronous-reference-frame equivalent impedance elements of a three-phase system. The synchronous-reference-frame channels are cross-coupled, which can distort the measurement, and the cross-coupling can be amplified by an interaction of the system under measurement and the measurement device. The presented technique is based on perturbing the system simultaneously with two uncorrelated wideband pseudo-random binary sequences. The responses in the desired voltages and currents are measured, and frequency-domain interpolation is used to obtain two independent sets of data at the same frequencies. With the data obtained from the interpolation, the impedance elements can be computed without the detrimental effect of the cross-coupling.

## [P2]

The paper presents a frequency-domain model for a single-phase inverter affected by the nonlinear deadtime effect under low load conditions. The average voltage error from the deadtime is a function of the inverter current amplitude, and the voltage error forms a nonlinear negative feedback from the inductor current to the bridge voltage. Depending on the operation conditions, the voltage error can be modeled with a dead zone, a linear region, and a saturation. The describing function method is used to model how the voltage error behaves in the frequency domain due to these regions. It is shown that the deadtime causes a significant amplitude-dependent damping under low load conditions. The model can be used to solve the sinusoidal steady state of an inverter system with the deadtime.

## [P3]

The paper presents a heuristic small-signal model for the deadtime effect under a linear operating region. Extensive simulations are used to study the deadtime effect, and it is shown that deadtime behaves nonlinearly. A heuristic linear model is developed for the

deadtime effect. Real-time hardware-in-the-loop simulations are used to show that the deadtime effect can stabilize a system, and experimental measurement are used to verify the damping from the deadtime effect. The presented model can be used to predict the damping from the deadtime effect.

## [P4]

The paper presents the load-affected model for the grid-forming inverter. First, the unterminated model of the grid-forming inverter is developed; the transfer functions related to the converter input and output dynamics are derived when the load is a current sink. Then, the effect of the load dynamics is computed. It is demonstrated that the load-affected model can be used to analyze how different dynamic loads affect the crossover frequency, phase margin, and gain margin of the current controller and voltage controller loop gains. The results can be used to ensure that the controller performance is desired with different loads. Hardware-in-the-loop simulations are used for verification.

## [P5]

The paper presents a method for measuring different frequency regions of a converter output impedance with other converters. The effect of controllers and passive components on different frequency regions of the grid-connected inverter output impedance are discussed, and the importance of the cross-coupling impedance elements is highlighted. In order to get adequate measurement results, it is shown that a voltage-controlled inverter should be used to measure low frequencies, and a current-controlled converter should be used to measure the high frequencies. It is noted that there are complications in the measurements due to the cross-couplings, even though converters with a feedback control were used to perturb the system.

# Author's Contribution

The author was responsible for developing and implementing analytical models, simulations, and experimental measurements in [P1]–[P5]. The supervisors were involved in outlining the research work, as well as helping to write and evaluate the publications. Detailed author contributions are as follows:

- In [P1], the author developed the identification procedure. M.Sc. Henrik Alenius assisted with practical implementation of broadband injections and data processing, and helped with tuning the procedure and the proofreading. The writing process was overseen by Dr. Tomi Roinila.
- In [P2], the author developed the describing-function model, performed the simulations, carried out the experiments, and wrote the manuscript. The writing process was overseen by Dr. Tomi Roinila.
- The study on deadtime effect in [P3] was begun under the supervision of Dr. Paolo Mattavelli at the University of Padua in Italy during a research exchange. The work was finished under the supervision of Dr. Tuomas Messo and Dr. Tomi Roinila at Tampere University. The author was responsible for writing, simulation, and carrying out the experimental measurements.
- In [P4], the author conducted the analysis and simulations on the system. The writing was overseen by Dr. Tuomas Messo, and Dr. Teuvo Suntio helped to refine the publication.
- In [P5], the author performed the simulations and analysis on the system dynamics and wrote the main outline of the publication with Dr. Tuomas Messo. Dr. Tomi Roinila and M.Sc. Henrik Alenius helped with editing.

Chapter 1

# Introduction

This chapter provides the essential background for the topics discussed in this thesis, clarifies the motivation for the conducted research, and revises the existing knowledge related to the topic. It also summarizes the objectives of the thesis.

## 1.1 Background

Emissions from carbon-based electricity generation are a major cause of the climate change that threatens the variety of environment [1]. To retard climate change, a shift to renewable energy generation from the polluting generation is required [2]. The Paris Agreement was established in 2015 to combat climate change and has important goals, including a peaking of emissions as soon as possible, and carbon neutrality [3]. Regarding carbon-based energy production, some countries in Europe have made concrete plans; for example, France and the United Kingdom are closing all of their coal-fired power stations by 2023 and 2025, respectively [4]. To make Europe climate-neutral by 2050 and to promote the development of technologies for clean, reasonably priced, and reliably delivered energy, the Green Deal program was launched in the European Union in 2019 [5]. Between 2008 and 2018, the amount of electrical energy produced from solar power in the European Union increased from 7.4 TWh to 115 TWh [6].

A major technical challenge in increasing the amount of renewable energy involves connecting renewable power plants to the existing distribution grid in order to deliver electricity to customers [2, 7]. In traditional power plants, rotating synchronous machines that are directly connected to the grid are most commonly used to generate electricity. The advantage of a synchronous machine is that the rotating rotor shaft is synchronously coupled to the voltage and currents through a magnetic field. Therefore, the moment of inertia of the rotor shaft contributes to the system inertia, and the stored rotational energy in the rotor shaft can compensate for abrupt changes in the power consumption in the grid.

In the case of many renewable power generation technologies, such as photovoltaic

(PV) solar generators, a direct connection of the generating technology to the grid is typically not possible because the generated electricity is not suitable for the distribution grid. A required interface between distribution grid and the power source is an inverter [8–12]. The inverter transforms the direct current (DC) produced by the photovoltaic panels to suit the 50 Hz or 60 Hz frequency of the alternating-current (AC) distribution grid. Because the inverter-based power sources lack the inertia of the synchronous machines, large numbers of inverter-based power sources can compromise the stability of the distribution grid [13]. Furthermore, the power flow in the distribution grid may change direction due to the increasing number of installed inverter-based power sources because the inverter-based power sources are distributed around the grid, sometimes close to the consumption [14].

The individual inverters can have different control modes depending on the available resources and the grid codes: grid-feeding, grid-forming, current-source-based grid-supporting, and voltage-source-based grid-supporting [15]. The innermost and the most rapidly responding control in all of the modes traditionally consists of current feedback, the purpose of which is to control the harmonic content and the power factor of the current by making the current track the desired reference value. In grid-forming mode, cascaded voltage and current feedbacks are used [15]. The bandwidth of these controllers ranges from a few hundred Hertz to a few kilohertz, depending on the power level and available hardware. An inverter interacts through its feedback control with the grid line impedances [16, 17] or the controllers of parallel inverters [18]. The interaction can be detrimental and distort the power quality, or even destabilize the complete system. Potential adverse interactions between inverter-based power sources should be modeled in the design phase and prevented by the controller design. A proper controller design ensures that the current and voltages fed by the inverter-based power sources track their desired reference values in different operating conditions.

### Modeling and Measurement of Terminal Impedances in Power-Electronic Systems

Conventionally, a linearized state-space model of the grid-connected inverter system is developed for the control design. The advantage of state-space models of complete inverter-based power source systems is that they can accurately represent harmonic modes and indicate how different parameters affect the system [19, 20]. This modeling approach requires precise information about all passive component sizes, voltage and current steady-state values, and the controller structure. However, a practical grid can locally consist of unknown loads, line impedances, and commercial inverter-based power sources from different suppliers whose parameters are unknown. Consequently, only a single inverter-based power source can be commonly modeled in detail due to the lack of information about the system parameters. However, it is not sufficient for an

inverter-based power source to be stand-alone stable because of the possible adverse interaction among the inverter-based power sources [21] or between the inverters and the grid [22] or active loads [23].

An alternative to developing a state-space model of the complete system is to measure the terminal impedance of an unknown converter in the frequency domain in order to gain information about the dynamics at the interface [24]. The measurement requires that the system be perturbed at desired frequencies so that the responses in terminal voltages and currents can be measured. The perturbation can be added to the current reference of another nearby-connected inverter. The system terminal impedance can be then computed by applying Fourier methods to the measured voltage and current responses. The measured impedance can be used with a modeled terminal impedance to perform an impedance-based interaction analysis. The advantage of this approach is that only little information about the system under test is required. The measurement must be done when the system is in operation in order to gain information at the correct operating point because the impedance can vary over time. Therefore, an impedance obtained in real time is most desired.

The measurement of a converter impedance or a grid impedance is typically performed at an interface in the grid. Therefore, the resulting driving-point impedance can consist of combinations of multiple inverter-based power sources, dynamic loads, and line inductances. Consequently, measurement at a wide frequency band is required because the impedance cannot be considered to be a simple resistor-inductor circuit of the line impedance from a medium-voltage distribution grid [25] or a terminal impedance of an inverter with a specific filter and controller. Recent studies have presented wideband techniques based on broadband perturbation and Fourier methods for performing fast and accurate impedance measurements of power-electronics systems [26–29]. The challenge in applying those methods in terminal-impedance measurements is that the current cannot become significantly distorted by the measurement injection, because harmonic emissions into the distribution grid are subject to regulation. Recent literature has addressed the design of broadband injection signals that allow rapid measurement of a three-phase driving-point impedance in the synchronous reference frame [27, 29].

The aforementioned wideband techniques can be adopted to perturb three-phase systems by injecting uncorrelated wideband sequences to the direct (d) and the quadrature (q) channels in the synchronous reference frame (DQ frame) [26–29]. Both channels can be perturbed simultaneously for the measurement because the uncorrelated sequences do not have energy at same frequencies, and data about voltages and currents from both the channels can be obtained rapidly for the impedance calculation. In general, however, no accurate information can be directly computed from such measurements because an equivalent synchronous-reference frame impedance consists of cross-coupling in the form of current-dependent voltage sources in addition to impedance elements. Therefore, an impedance element cannot be measured similarly to Ohm's law. While there are methods

for tackling this problem, they are either parametric [30] or require multiple measurements [31]. A rapid and accurate measurement can be developed from the existing wideband measurement techniques. The development requires that the characteristics of the injected sequence and the synchronous reference impedance be considered in detail.

### Nonlinearities in Dynamic Modeling of Power Electronics Systems

Power electronic converters are based on switching semiconductor switches between the conduction mode and the blocking mode, which is very nonlinear. The traditional dynamic modeling of power-electronic systems is based on averaging the system over a switching cycle and assuming that a frequency-domain model can be developed from a linearized time-domain model [32]. However, the traditional models may not be accurate in the presence of significant nonlinearities that can be potentially caused by many different phenomena. Some of these nonlinearities appear at high-frequency range due to the switching actions of semiconductor switches [33]. Some other nonlinearities can occur due to the phase-locked loop [34], saturation of inductors [35], or the controller behavior; for example, the perturb and observe algorithm that is used in the maximum power point tracking in PV panel generators [36, 37].

One source of nonlinearity in all inverter systems is caused by the deadtime that is required to prevent shoot-through faults [38–40]. The deadtime causes a voltage error that depends on the deadtime length, the direct voltage level, and the instantaneous direction of the current [38]. In inverters, the current direction changes every half cycle of the synchronous-frequency component, and the deadtime creates a voltage error that is in phase with the current [38]. The average of the voltage error over a switching cycle is a nonlinear function of the converter current, and various approaches have been suggested to compensate the voltage error [38, 41–43].

The deadtime effect is visible in the frequency domain as damping because the deadtime effect is a current dependent voltage error [44, 45]. Under low-load conditions, the nonlinearity with respect to the current amplitude is significant, and the deadtime effect cannot be linearized. The accuracy of the traditional linearized model can become compromised and unexpected measurement results can be obtained if the nonlinear behavior is not considered properly. Consequently, it is essential to analyze the conditions under which the voltage error from the deadtime can be linearized and what is a proper way to model the nonlinear effect.

## 1.2 Aim and Scope of the Thesis

The goal of the thesis is to provide techniques to facilitate the design of a resilient power-electronic system. A desirable control system tracks the reference values under disturbances and maintains the stability of the power-electronic system under varying

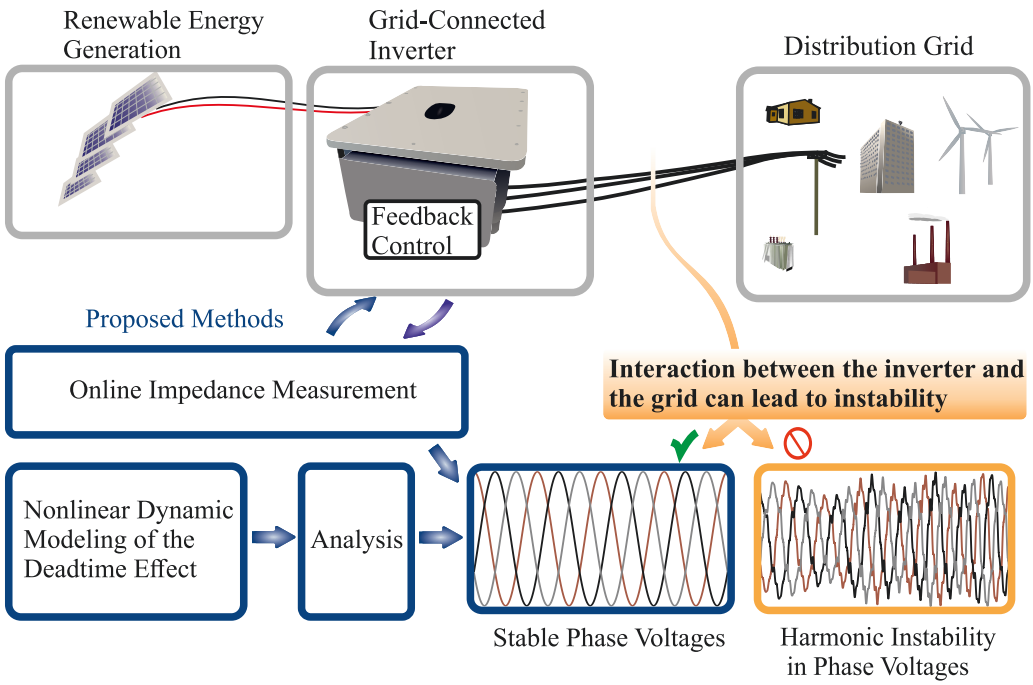


Figure 1.1: Graphical abstract of the thesis.

operating conditions. To achieve the goal, all couplings between the DQ-frame channels and the significant nonlinearity from the deadtime are considered in detail in modeling and measurements of the converters.

This thesis shows that the deadtime effect can significantly affect the damping of an inverter system and the effect is highly nonlinear under low load conditions. A describing function method is proposed to model the amplitude-dependent deadtime effect under low load conditions. The proposed model enhances the dynamic modeling of power-electronic inverters by setting a limit on the linear modeling region.

The present work also investigates how a measurement injection can leak between DQ-frame channels in the presence of a finite-bandwidth closed-loop control. For the analysis, the dynamics of the converter that perturbs the system for the measurement are considered in the impedance interaction. A measurement procedure that avoids the detrimental behavior of the perturbations is proposed.

Fig. 1.1 shows a graphical abstract of the thesis. The converter transforms the direct current produced by the PV panels to alternating current that is fed to the distributing grid. The distribution grid consists of power lines, loads, and local power plants. At the connection point of the inverter, a detrimental interaction between the grid and the converter can occur and destabilize the system. The proposed techniques can be used to prevent the detrimental interaction.

The main advantages of the presented methods can be summarized as follows.

- The nonlinear deadtime effect in frequency response measurements is characterized.
- The developed describing-function-method model for the nonlinear deadtime effect makes it possible to solve the sinusoidal steady state of an inverter with a deadtime.
- The impedance coupling is characterized to occur with a grid-connected converter-performed grid-impedance measurements.
- Disturbance rejection is provided by the novel measurement procedure that is implemented with orthogonal binary sequences.

### Research Questions

The main research questions in this thesis can be given as follows.

- What are the characteristics of the inverter-side inductor current that limit the linear small-signal modeling of the deadtime effect?
- How is the nonlinear injection-amplitude-dependent voltage error modeled under low load conditions in the frequency domain?
- What is the dynamic effect of the interaction between the measurement device dynamics and the measured impedance in measurement of linear impedance systems in the DQ frame?
- How can the impedance coupling be avoided in a non-parametric measurement procedure that is based on simultaneous broadband perturbation of both d and q channels in the DQ frame?

## 1.3 Review of Previous Studies

This section reviews the past literature on the topics of this thesis. It first reviews the synchronous-reference-frame impedance measurement, and then the existing modeling of the deadtime effect.

### Measurement of Driving-Point Impedance in the DQ Frame

Early investigations into DQ-frame impedance measurements found that the DQ-frame equivalent impedance of a balanced three-phase system that consists of four impedance elements cannot be computed as the direct ratio of the voltage and the current related to each impedance element in practical systems. Instead, multiple independent measurement injections must be performed at the same frequencies, and a system of linear equations must be solved for the impedance elements [46, 47]. The solution based on two independent injections was presented in matrix form in [31]. The method relies on the assumption that

the system operating conditions do not vary between the two independent measurements [31]. Nevertheless, the method based on multiple independent injections has been a reliable way of measuring the DQ-frame impedance [31, 48–52]. The work in [31, 48–52] focused primarily on measuring the impedances in a grid-connected converter system by using an additional device to perturb the system.

Another approach to perturbing a converter system for the measurement is to use a grid-connected converter to perturb the system [27, 28]. In the method, the measurement algorithm is implemented in the converter controller system, and the injection signal is summed to the alternating current references. In [26–28], uncorrelated pseudorandom binary broadband sequences that were generated by using the Hadamard modulation [53, 54] were used as the injection signals. Because the uncorrelated sequences have energy on a wide band, but not on same frequencies with each other, both the d and the q channels in the synchronous reference frame were injected simultaneously under same operating conditions. One disadvantage regarding the methodology in [26–28] is that the impedance elements were not solved from a group of linearly independent equations according to the earlier studies of DQ-frame impedance measurement presented in [31, 46, 47], and the impedance elements were computed as direct ratios of the measured voltages and currents, as noted in [30, 55]. Hence, the measured resistor-inductor circuits have resonances that they should not have in [27, 28].

Parametric methods have been used for measuring a three-phase impedance in the frequency domain [55–58] and the time domain [30]. However, parametric methods are not suitable for measuring a driving point impedance of a system whose internal structure is not known, such as a microgrid that can consist of virtually unknown meshed terminal impedances of inverters, loads, and line impedances. Regarding the measurement of a grid impedance, many parametric methods rely on the assumption that a grid-feeding inverter is connected to a stiff grid with a line inductance, whose equivalent network is a resistor-inductor circuit [56–58]. However, results from practical grid-impedance measurements [25, 59] show that a resistor-inductor circuit is not suitable to model a network impedance. There are also passive measurement methods that do not require a perturbation injection into the system. However, these methods may not be available at all times because they rely on existing background distortions in the voltages and currents [60].

### Dynamic Modeling of the Deadtime Effect

In the dynamic modeling and controller design of power electronic converters, the deadtime effect is commonly neglected [19, 23, 61–63]. However, few studies have been published on the small-signal effect of the deadtime on inverters [44, 45, 64, 65] and on DC–DC converters [66, 67]. In [44, 45, 65–67], a resistor-like element was used to model the deadtime effect. The resistor-like element appears in series with the filter inductor that is

connected to the switch leg and adds damping to the system. In the models presented in [44, 45, 65–67], the resistance of the resistor-like element increases as the fundamental current amplitude decreases. This indicates that, under a low-load condition, the deadtime effect causes a stronger damping than under the nominal condition. In the synchronous reference frame, the cross-coupling elements were used in addition to the resistor-like elements in the modeling of deadtime effect in grid-connected three-phase inverters [44, 68]. A similar method was used to model the deadtime effect with three-phase induction motor drives in [69, 70].

The deadtime effect on the open-loop output impedance of a full-bridge inverter was studied in [45]; a clear improvement was made in the dynamic modeling of the deadtime effect by including the current ripple effect on the voltage error in the model. The current ripple affects the voltage error when the current fundamental component crosses zero [45, 71], which is especially visible under low-load conditions. In [45], the describing function method was used to solve a linear resistor-like element as a function of the current ripple and the current fundamental component amplitude. The main weakness in the study was that a single-phase inverter with an inductor (L) filter and resistive load was analyzed, and a current injection between the filter and the load with a small amplitude was used to perturb the current. With this approach, the inverter current that causes the voltage error has a known maximum amplitude at the perturbation frequency. Therefore, the voltage error can be relatively easily modeled at the perturbed frequency because it is known that the current amplitude will be small at the perturbed frequency. However, the situation changes substantially if filtering is accomplished by an inductor-capacitor (LC) circuit. The filter can amplify the current perturbation and the voltage error can significantly affect the inverter current that affects the voltage error, which creates a non-linear feedback into the converter system. In the existing literature [44, 45, 64, 65], the inductor current amplitude is assumed to be small at the frequency of interest, and the nonlinear voltage error is presented by a linear element in the small-signal modeling.

## 1.4 Summary of Scientific Contributions

The main scientific contributions of this thesis are as follows.

- A method to characterize a dead zone, a slope, and a saturation region in the deadtime effect under sinusoidal perturbations.
- A technique based on the describing-function method for modeling the nonlinear deadtime effect in a sinusoidal steady state under low-load conditions.
- A method for modeling the impedance coupling in three-phase system measurements considering the dynamics of the injection device.

- A technique for a rapid DQ-frame impedance measurement in a grid-connected three-phase converter system in the presence of impedance coupling.

## 1.5 Structure of the Thesis

This thesis consists of five chapters and publications [P1]–[P5]. The following chapters can be briefly summarized as follows.

### Chapter 2: Frequency-Domain Analysis of Power-Electronic Converters

Chapter 2 looks at the single-phase and three-phase converter topologies and the frequency-domain models of the converters that are essential for this thesis. First, half-bridge inverters are investigated and their dynamic modeling and the voltage error from the deadtime are reviewed. Then, the dynamic modeling of three-phase inverters is revised, and the load-affected model is examined.

### Chapter 3: Methods

Chapter 3 presents the methods applied in the work. The methods related to the modeling of the deadtime effect and the measurement in the synchronous reference frame are presented in separate parts.

### Chapter 4: Implementation and Verification

Chapter 4 presents the used experimental setups and the experimental verification of the proposed models and techniques.

### Chapter 5: Conclusions

Chapter 5 summarizes the thesis and provides the main conclusions. The benefits and limitations of the proposed methods are discussed.

Chapter 2

# Frequency-Domain Analysis of Power-Electronic Converters

This section presents background information about the inverters applied in the thesis. The deadtime effect on the half-bridge inverter is investigated and the principles of the linear dynamic modeling and issues in the dynamic analysis of power-electronic systems are revised.

## 2.1 Half-Bridge Inverter

An inverter phase leg that consists of two semiconductor switches is the building block of many converters. Fig. 2.1 shows three different models of an inverter phase leg. The positive and the negative rails of the DC bus are denoted by p and n, respectively. The AC phase is denoted by a. In Fig. 2.1a, metal-oxide-semiconductor field-effect transistors (MOSFETs) are used as the switches with diodes connected anti-parallel. Fig. 2.2 shows the gate signal of switches $S_1$ and $S_2$, where $T_{\mathrm{sw}}$ and $T_{\mathrm{dead}}$ denote the switching cycle length and the deadtime length, respectively. Ideally, a switch would be turned on

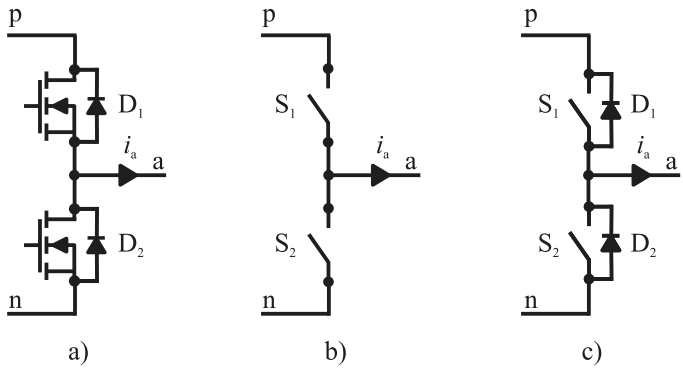


Figure 2.1: An inverter phase leg with (a) MOSFETs , (b) ideal switches, and (c) ideal switches with anti-parallel diodes.

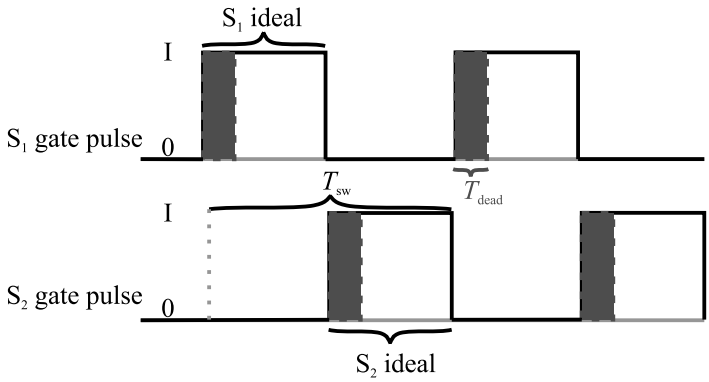


Figure 2.2: Gate signals of switches $S_1$ and $S_2$. The length of $T_{\text{dead}}$ is exaggerated compared to the length of $T_{\text{sw}}$ for illustrative purposes.

immediately after the gate signal of the complementary switch is pulled to zero. However, this cannot be done because practical semiconductor switches, such as MOSFETs and insulated-gate bipolar transistors (IGBTs) have finite turn-on and turn-off times. For example, when the gate signal for $S_1$ is pulled to zero, the gate signal of $S_2$ cannot be pulled up because $S_1$ does not turn off instantaneously. Otherwise, a shoot-through fault, where the direct voltage bus is short-circuited, could occur and the direct voltage sources and the semi-conductor switches could be damaged or destroyed. Therefore, a deadtime is required. The deadtime ensures, with a time margin, that a switch has turned-off before the complementary switch is turned on. The anti-parallel diodes ($D_1$ and $D_2$) are required because the phase current ($i_{\text{a}}$) must have a path at all times. During the deadtime, the current commutates to either of the anti-parallel diodes depending on the instantaneous current direction.

Fig. 2.1b shows an inverter phase leg with ideal switches, but without the anti-parallel diodes. This model is usually sufficient for developing state-space average models of the inverters and simulations related to linear controller system verification. However, the deadtime effect cannot be modeled because there is no path for the current during the deadtime. Fig. 2.1c shows an inverter phase leg with ideal switches and ideal anti-parallel diodes. This model is sufficient to model the voltage error that arises from the deadtime because the anti-parallel diodes provide a path for the phase current during the deadtime.

A half-bridge inverter consists of one inverter phase leg [72]. In order to use a phase leg as an inverter, a connection to the DC bus midpoint must be available. Fig. 2.3 shows the circuit diagram of a single-phase half-bridge inverter, where z denotes the DC bus midpoint. Hence, $+V_{\text{dc}}/2$ ($S_1$ conducts) or $-V_{\text{dc}}/2$ ($S_2$ conducts) can be connected between the phase leg (a) and the DC bus midpoint (z) in order to produce an alternating phase voltage ($v_{\text{az}}$).

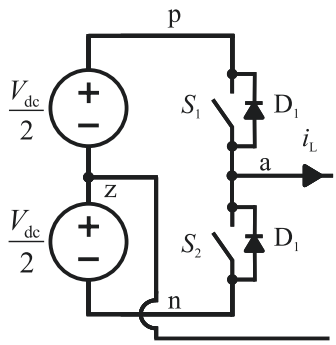


Figure 2.3: Single-phase half-bridge inverter.

### Dynamic Model of Half-Bridge Inverter

Typically, the output voltage and the output current of the inverter must be filtered due to harmonics caused by switching [73]. An inductor (L) filter can be used to filter the current; however, in order to achieve efficient attenuating with an L filter, a high inductance value is required that makes the filters bulky [74]. Therefore, inductor-capacitor (LC) [75] or inductor-capacitor-inductor (LCL) [76, 77] filters are most often used because they provide more efficient attenuation compared to L filters.

Fig. 2.4 shows a voltage-output half-bridge inverter with an LC filter. A half-bridge inverter has no direct steady values on the AC side; the alternating currents and voltages are sinusoidal whose averages are zero. Therefore, the dynamics of a linearly operating half bridge converter can be modeled by the dynamics of the passive-filter components. The half-bridge with ideal switches shown in Fig. 2.1b is used here in order to develop a sinusoidal steady-state model without considering any nonlinearities of the switches.

Fig. 2.5 shows an equivalent sinusoidal steady-state circuit of the converter. It is assumed that the bridge voltage follows the reference voltage ($v^{\mathrm{ref}}$) within the frequency band of interest. The impedances of the filter inductor ($L$) and the filter capacitor ($C$) as the function of the angular frequency ($\omega$) are given as

$$Z_{\mathrm{L}}(\omega) = r_{\mathrm{L}} + j\omega L. \tag{2.1}$$

$$Z_{\mathrm{C}}(\omega) = r_{\mathrm{C}} + \frac{1}{j\omega C} \tag{2.2}$$

where $j$ is the imaginary unit, and $r_{\mathrm{L}}$ and $r_{\mathrm{C}}$ denote equivalent series resistances of the inductor and the capacitor, respectively. The control-to-output voltage dynamics are dictated by the LC filter. The transfer function $G_{\mathrm{co}}$from the duty cycle ($d$) to the output voltage is given as

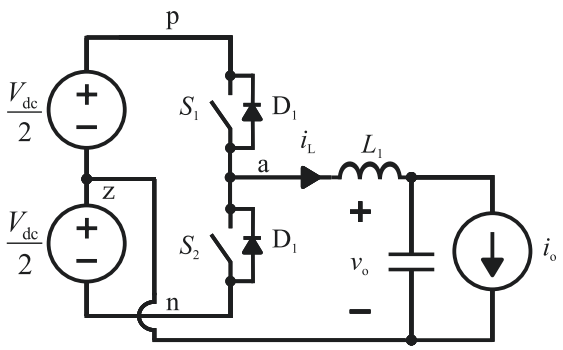


Figure 2.4: Voltage-output half-bridge inverter with an LC filter.

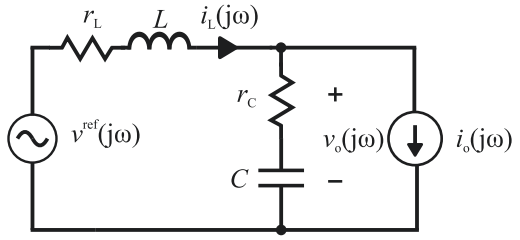


Figure 2.5: Equivalent circuit in a sinusoidal steady state.

$$G_{co} = \frac{v_o}{d} = \frac{Z_C}{Z_L + Z_C} = \frac{j\omega\frac{r_C}{L} + \frac{1}{LC}}{(j\omega)^2 + j\omega\frac{r_L + r_C}{L} + \frac{1}{LC}} \tag{2.3}$$

The control-to-inductor current transfer function is

$$G_{cL} = \frac{i_L}{\hat{d}} = \frac{1}{Z_L + Z_C} = \frac{j\omega/L}{(j\omega)^2 + \frac{r_L j\omega + r_C}{L} + \frac{1}{LC}} \tag{2.4}$$

The second-order polynomial factor in the transfer function can be given in the traditional form of a second-order systems as

$$G_{cL} = \frac{j\omega\omega_0^2}{L\left((j\omega)^2 + 2\xi\omega_0 j\omega + \omega_0^2\right)} \tag{2.5}$$

where $\omega_0$ and $\xi$ denote the natural frequency and the damping factor, respectively. The damping factor and the natural frequency are given as

$$\xi = \frac{R}{2}\sqrt{\frac{C}{L}} \tag{2.6}$$

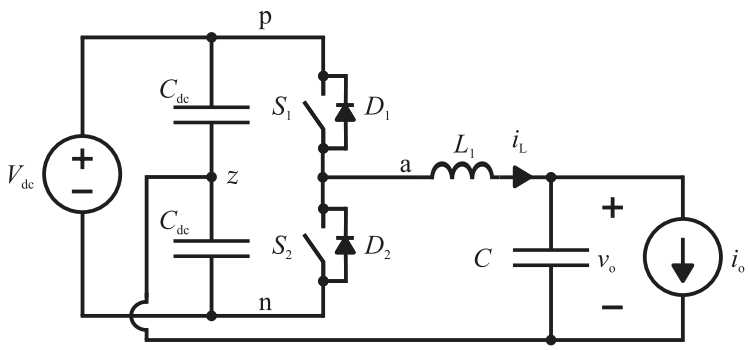


Figure 2.6: Voltage-output half-bridge inverter with an LC filter at the output, and the DC bus voltage is split by the capacitors.

$$\omega_0 = \frac{1}{\sqrt{LC}} \tag{2.7}$$

The output impedance is given as the ratio of the output voltage ($v_\mathrm{o}$) and the output current ($i_\mathrm{o}$) as

$$Z_\mathrm{o}(j\omega) = \frac{Z_\mathrm{L} Z_\mathrm{C}}{Z_\mathrm{L} + Z_\mathrm{C}} = \frac{r_\mathrm{C}(j\omega)^2 + \left(\frac{r_\mathrm{L} r_\mathrm{C}}{L} + \frac{1}{C}\right) j\omega + \frac{r_\mathrm{L} r_\mathrm{C}}{LC}}{(j\omega)^2 + \frac{r_\mathrm{L} + r_\mathrm{C}}{L} j\omega + \frac{1}{LC}} \tag{2.8}$$

Commonly, two identical voltage sources are not used to implement the DC bus in practical half-bridge inverters. Instead, DC capacitors are used to split the direct voltage and provide access to the midpoint (z), as shown in Fig. 2.6. It is assumed that the upper and the lower DC capacitors ($C_\mathrm{dc}$) are identical and, therefore, the DC voltage ($V_\mathrm{dc}$) is evenly divided over the capacitors. The parallel connection of the DC capacitors is visible in the AC output impedance of practical half-bridge inverters. The impedance of the parallel-connected DC capacitors can be given as

$$Z_\mathrm{C\text{-}dc}^\mathrm{par} = \frac{r_\mathrm{C\text{-}dc} + \frac{1}{j\omega C_\mathrm{dc}}}{2} \tag{2.9}$$

where $C_\mathrm{dc}$ and $r_\mathrm{C\text{-}dc}$ are the DC capacitance and its ESR. In the output impedance, the parallel connection appears in series with the inductor impedance, and the output impedance can be given as

$$Z_\mathrm{o} = \frac{\left(Z_\mathrm{L} + Z_\mathrm{C\text{-}dc}^\mathrm{par}\right) Z_\mathrm{C}}{\left(Z_\mathrm{L} + Z_\mathrm{C\text{-}dc}^\mathrm{par}\right) + Z_\mathrm{C}} \tag{2.10}$$

The system in Fig. 2.4 is simulated with Matlab Simulink. A sinusoidal pulse-width modulation (SPWM) with a triangular carrier waveform is used to turn on and turn off the switches. The parameters of the half-bridge inverter Simulink simulation are given in Table 2.1.

The output impedance of the half-bridge inverter is measured with the stepped-sine method. A sinusoidal perturbation is added to the output current in addition to the synchronous-frequency component. The measurement is not performed at the integer multiples of the fundamental (50 Hz) component because of the energy content on those frequencies, which could distort the measurement. The variables are recorded for 10 synchronous-frequency cycles at a sinusoidal steady state. The recorded data is discrete Fourier-transformed (DFT), and the output impedance is calculated as the ratio of the frequency bins at the injected frequencies. Fig. 2.7 shows the result of a Simulink simulation of an output impedance measurement.

The simulations are performed under nominal load conditions (Fig. 2.7a), where the inductor current synchronous-frequency amplitude is 10 A, and under no-load conditions (Fig. 2.7b). The measurements are performed with perturbation amplitudes of 0.5 A and 3 A. As expected according to the linear circuit theory, the results are the same and they follow the linear model in Figs. 2.7a and 2.7b. The dynamic models of power electronics systems are typically based on the assumption of linearity. However, introduction of the deadtime that is essentially required in all converter systems introduces a nonlinearity to the system.

The half-bridge with the ideal switches in Fig. 2.8 is now replaced by the half-bridge shown in Fig. 2.1c, where the anti-parallel diodes are included. A deadtime of 4 $\mu$s that delays the turn-off of both switches is introduced. The output-impedance measurement simulations are repeated with the new half-bridge with perturbation amplitudes of 0.5 A, 1 A, and 3 A, and the results are shown in Fig. 2.8. In Fig. 2.8a, the inductor current is nominal (10 A), and in Fig. 2.8b, the converter is in the no-load condition. A damping can be seen around the resonance under both operating conditions. However, the damping is amplitude dependent. In the case of the no-load condition in Fig. 2.8b, the amplitude

Table 2.1: Simulation parameters of the half bridge inverter.

| **Parameter** | **Symbol** | **Value** | **Parameter** | **Symbol** | **Value** |
|---|---|---|---|---|---|
| Input voltage | $V_{\mathrm{DC}}$ | 700 V | Grid voltage rms | $V_{\mathrm{g}}$ | 120 V |
| Synchronous frequency | $\omega_{\mathrm{s}}$ | $2\pi 50$ rad/s | Switching frequency | $f_{\mathrm{sw}}$ | 10 kHz |
| Filter capacitor capacitance | $C$ | 10 $\mu$F | Filter inductance | $L$ | 4 mH |
| $C$ ESR and damping resistor | $r_{\mathrm{C}}$ | 0.1 $\Omega$ | $L$ ESR | $r_{\mathrm{L}}$ | 0.001 $\Omega$ |
| Output current | $I_{\mathrm{o}}(\omega_{\mathrm{s}})$ | 0—20 A | Deadtime | $T_{\mathrm{dead}}$ | 0—4 $\mu$s |

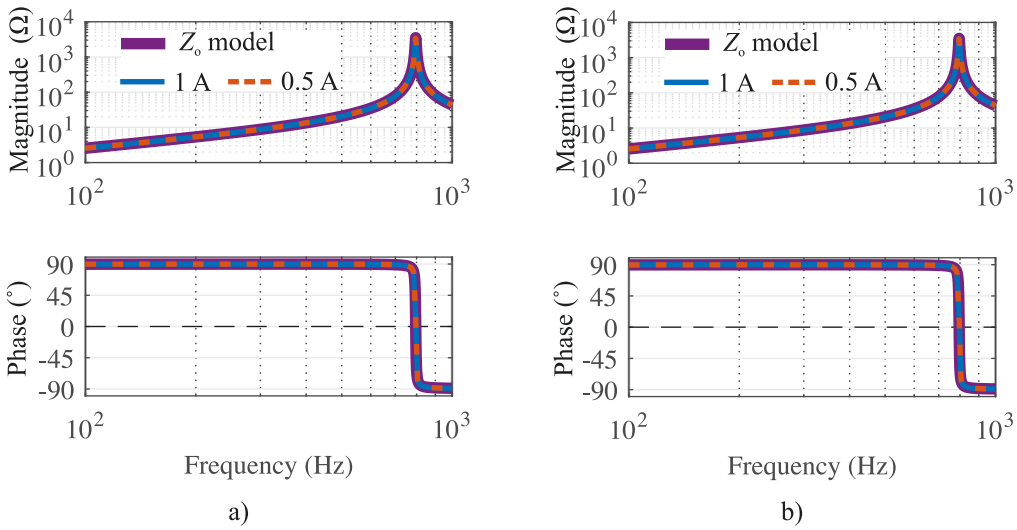


Figure 2.7: Simulation of the output impedance measurement without the deadtime and with different perturbation amplitudes (0.5 A and 3 A) (a) under the nominal load condition and (b) under the no-load condition.

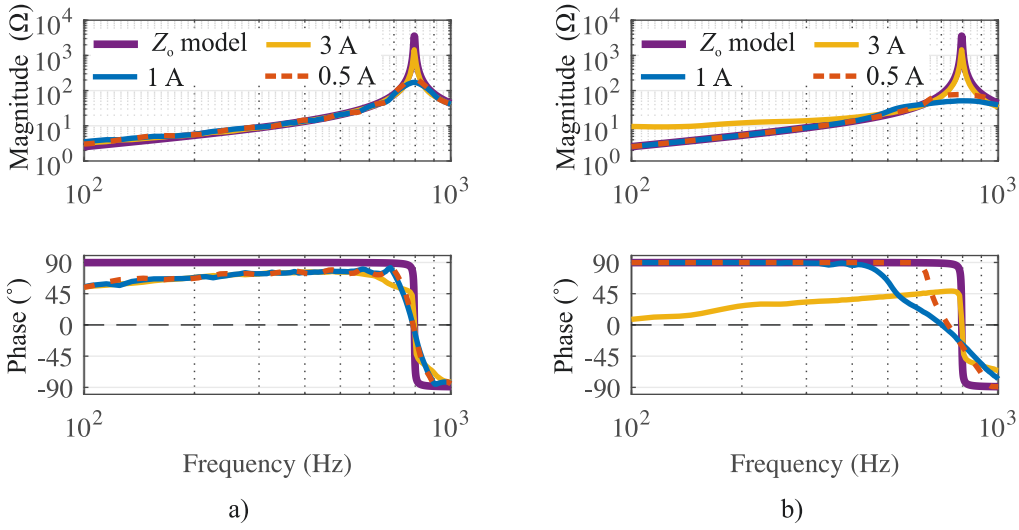


Figure 2.8: Simulation of the output impedance measurement with the deadtime of 4 $\mu$s and with different perturbation amplitudes (0.5 A, 1 A, and 3 A) (a) under the nominal load condition and (b) under the no-load condition.

dependency is higher than under the nominal conditions. With the perturbation amplitude of 0.5 A, only the resonance is damped. With the perturbation amplitude of 3 A, the resonance peak is only slightly damped, but at low frequencies there is more damping, which is more clearly visible in the phase than in the magnitude. Furthermore, the damping is not visible at all frequencies at the same time, which indicates that the

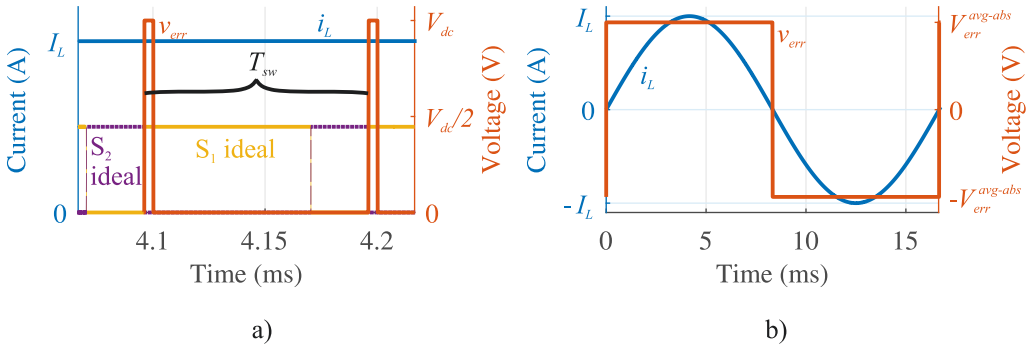


Figure 2.9: (a) Illustration of the voltage error due to the deadtime under positive values of the phase current, and (b) the average error over every switching cycle during a synchronous-frequency cycle.

deadtime effect cannot be modeled by a linear model. Simulation results of the deadtime effect on the output current-to-inductor current dynamics are provided in [P2].

### Deadtime Effect

Fig. 2.9a illustrates the instantaneous voltage error ($v_{\mathrm{err}}$) from the deadtime under positive values of the inductor current ($i_{\mathrm{L}}$). The error is defined as:

$$v_{\mathrm{err}}(t) = v_{\mathrm{ideal}}(t) - v_{\mathrm{az}}(t) \tag{2.11}$$

where $v_{\mathrm{ideal}}$ is the phase voltage without the deadtime. The voltage error occurs when the turn on of $S_1$ is delayed by the deadtime. During the deadtime, the current commutates from $S_2$ to $D_2$, and the phase voltage is $-V_{\mathrm{dc}}/2$. In the ideal case, $S_1$ would conduct and the phase voltage would be $V_{\mathrm{dc}}/2$. Therefore, the error defined in (2.11) can be given as:

$$v_{\mathrm{err}} = V_{\mathrm{dc}}/2 - (-V_{\mathrm{dc}}/2) = V_{\mathrm{dc}} \tag{2.12}$$

A similar phenomenon takes place during the negative values of the phase current when $S_2$ is turned on, and the current commutates to $D_1$ during the deadtime. Thus, the error defined in (2.11) can be given as:

$$v_{\mathrm{err}} = -V_{\mathrm{dc}}/2 - V_{dc}/2 = -V_{\mathrm{dc}} \tag{2.13}$$

Therefore, during the deadtime, the instantaneous voltage error is a function of the phase current sign:

$$v_{\mathrm{err}}(t) = \mathrm{sign}(i_{\mathrm{L}}(t))V_{\mathrm{dc}} \tag{2.14}$$

During a half fundamental frequency cycle, the voltages error relates to turn-on of either of the switches and the sign of the voltage error does not change. The voltage error can be averaged over a switching cycle ($T_{\text{sw}}$) as:

$$v_{\text{err}}^{\text{avg}} = \frac{1}{T_{sw}} \int_{\tau}^{\tau+T_{\text{sw}}} v_{\text{err}}\,(t)dt = \text{sign}(i_{\text{L}})\frac{T_{\text{dead}}}{T_{sw}}V_{\text{dc}} \tag{2.15}$$

where it is assumed that the inductor does not cross zero during the switching cycle. The maximum value of the average voltage error is

$$V_{\text{err}}^{\text{avg-max}} = \left|v_{\text{err}}^{\text{avg-Ts}}\right| = \left|\text{sign}(i_{\text{L}})\frac{T_{\text{dead}}}{T_{\text{sw}}}V_{\text{dc}}\right| \tag{2.16}$$

The synchronous frequency component of the voltage error is given by [38]

$$v_{\text{err - f1}} = \frac{4}{\pi}\frac{T_{\text{dead}}}{T_{\text{sw}}}V_{\text{dc}} \tag{2.17}$$

which is the first harmonic of the Fourier series of the square-wave voltage error.

Fig. 2.9b illustrates one fundamental cycle of the phase current, and the error that is averaged over every switching cycle. The average error clearly follows the sign of the current; therefore, the square-wave voltage error has the main frequency component at the fundamental frequency of the current. It was pointed out in [72] that the deadtime effect corresponds to adding a resistance in series with the load. The main limitation of the resistor model is that the square-wave voltage error stems from a saturation. If the current in Fig. 2.9b was perturbed, the square-wave error (2.15) would not have a response in amplitude, but only in phase. A resistive element could be used to model the voltage error in a steady state; however, this may have limitations in dynamic modeling of the deadtime effect.

In the ideal case, where only the fundamental component of the current is considered, the deadtime effect can be divided into the positive and the negative half cycles of the inductor current. However, multiple zero crossings of the inductor current due to the current ripple changes the behavior of the voltage error [45, 71]. During the zero crossings, the current sign has such a value that during the turn-on of both switches $S_1$ and $S_2$ the deadtime effect causes no error. For example, $S_1$ is turned on always at lowest peak value of the ripple; a voltage error is caused if the current valued is positive. However, if the ripple peak has a negative value, no voltage error occurs. During the zero crossing, a similar phenomenon takes place in the turn-on of $S_2$. Due to the ripple, no voltage error occurs as longs the current has both positive and negative values within a switching cycle, as illustrated in Fig. 2.10a. The zero current crossing period ends when the average (fundamental current amplitude in Fig. 2.10a) is higher than half the peak-to-peak current ripple. The peak-to-peak current ripple ($\Delta i_{\text{p-p}}$) that is approximated as

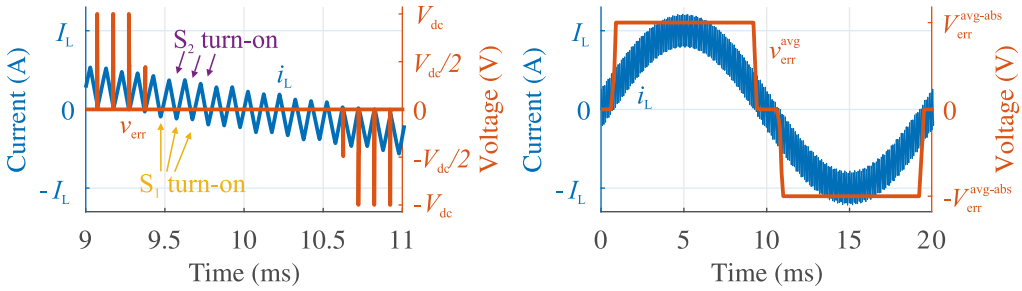


Figure 2.10: (a) Illustration of the instantaneous voltage error during the zero crossings with the ripple in the inductor current. (b) The average error over every switching cycle including the ripple in the inductor current.

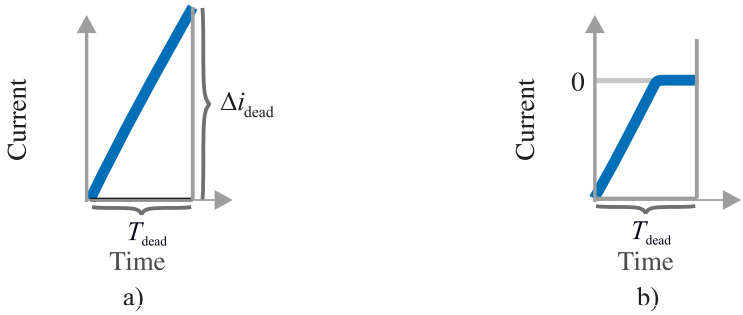


Figure 2.11: a) The current slope during the deadtime. b) If the current value reaches zero during the deadtime, the current remains zero for the rest of the deadtime.

$$\Delta i_{\text{p-p}} = \frac{V_{\text{dc}} T_{\text{sw}}}{4L} \tag{2.18}$$

The effect of the deadtime on the ripple is neglected.

Fig. 2.10a shows that the voltage error is $V_{\text{dc}}/2$ at $t = 9.4$ ms, which indicates that the phase voltage is 0 V. This happens due to a zero-current clamping. The current drops to zero during the deadtime; therefore, the diode stops conducting and none of the semiconductor devices ($S_1$, $S_2$, $D_1$, and $D_2$) conduct for the rest of the deadtime [78]. Hence, the phase voltage is zero. Close to no-load conditions, the current change during the deadtime ($\Delta i_{\text{dead}}$) is approximated here by [P2]

$$\Delta i_{\text{dead}} = \frac{V_{\text{dc}} T_{\text{dead}}}{2L} \tag{2.19}$$

which is calculated at the current zero crossing, assuming a unity power factor.

Fig. 2.11a illustrates the current slope during the deadtime ($\Delta i_{\text{dead}}$). Fig. 2.11b shows that if the current value reaches zero during the deadtime, the current remains zero for

the rest of the deadtime, which takes place in Fig. 2.10a at $t = 9.4$ ms (and for a negative slope at $t = 10.6$ ms).

The following observations can be put together from Fig. 2.8 and the analysis of the voltage error from the deadtime effect:

- The deadtime causes an average voltage error that is in phase with the (inductor) current, and the error depends on the current amplitude at the frequency that is analyzed.

- The voltage error can saturate; therefore, a resistive element may not model properly the dynamics of the error.

- The saturation depends on the operating conditions and the measurement perturbation amplitude.

- A measurement perturbation cannot be commonly made directly to the converter-side inductor current; for example, due to an LC filter. Therefore, the amplitude of the inductor current during the deadtime is not known based on linear models because the voltage error can reduce the inductor current.

The voltage error must be studied in detail under different operating conditions in order to determine whether a linearized model can be used. A describing-function model that can be used solve the sinusoidal steady state is developed in Chapter 3.1.

### Measurement of Linear Systems

The output-terminal dynamics of the half-bridge inverter in Fig. 3.1b can be modeled with a Thévenin equivalent circuit according to the classical circuit theory [79]. In Fig. 2.12a, the Thévenin impedance ($Z_{\mathrm{th}}$) corresponds to the output impedance ($Z_{\mathrm{o}}$) of the half-bridge inverter. The Thévenin equivalent voltage ($v_{\mathrm{th}}$) represents sinusoidal perturbations caused by the controller of the converter ($c$) and the direct input voltage of the converter ($v_{\mathrm{in}}$). In Fig. 2.6, the current sink, which is the load and also used to perturb the output current for the measurement, is directly connected to the output of the converter. Obviously, the converter can be part of a larger system and the perturbation for the measurement source may not be directly connected to the output of the converter.

Fig. 2.12b shows a circuit consisting of $M$ linear impedance elements $Z_M$, including the Thévenin equivalent circuit of the half-bridge inverter. $i^{\mathrm{inj}}$ is a current source that is used to perturb the system, and the responses in the voltage ($v_{\mathrm{m}}$) and the current ($v_{\mathrm{m}}$) over an arbitrary impedance element can be measured in order to calculate the impedance of the element similarly to the Ohm's law:

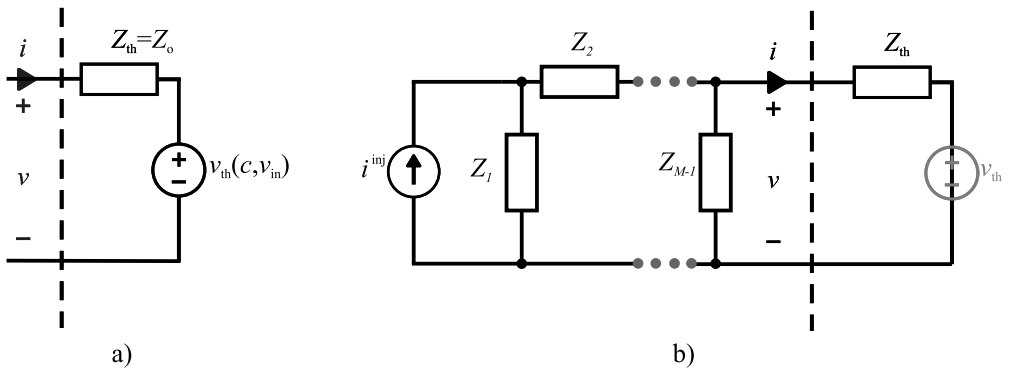


Figure 2.12: (a) Thévenin equivalent of the output dynamics of the single-phase half-bridge inverter. (b) The equivalent circuit of the output dynamics as a part of a larger circuit.

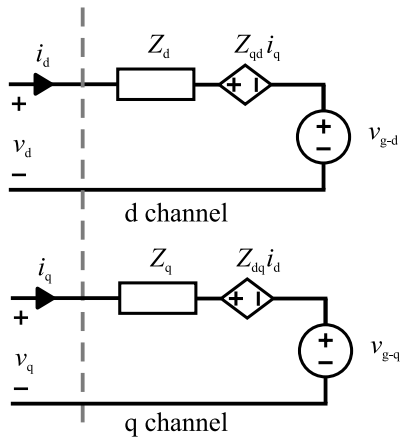


Figure 2.13: An equivalent impedance consisting of two channels that are cross-coupled.

$$Z_{\mathrm{m}} = \frac{v_{\mathrm{m}}}{i_{\mathrm{m}}} \tag{2.20}$$

The Thévenin voltage is assumed to be zero at the frequencies of interest at which the system is perturbed; therefore, the voltage source corresponds dynamically to a short circuit. Hence, the ratio of the terminal voltage ($v$) and current($i$) equals the Thévenin equivalent impedance ($Z_{\mathrm{th}}$) although the system is originally perturbed at a different location in the circuit. This is intuitive to electrical engineers and, in a practical system, this feature can be used provided that perturbation amplitude is not considerably dampened and measurement does not become distorted by noise.

The measurement would be more complicated if the system consists of two (equivalent) circuits that are cross-coupled. Fig. 2.13 shows a circuit that consists of d and q channels. The d channel consists of the impedance element $Z_{\mathrm{d}}$, the coupling from q channel current

by the current-dependent voltage source $Z_{\mathrm{qd}}$ and the equivalent voltage source $v_{\mathrm{g\text{-}d}}$. The q channel consists of $Z_{\mathrm{q}}$, $Z_{\mathrm{dq}}$ and $v_{\mathrm{g\text{-}q}}$. The measurable variables are $i_{\mathrm{d}}$ and $v_{\mathrm{d}}$ in the d channel and $i_{\mathrm{q}}$ and $v_{\mathrm{q}}$ in the q channel.

The goal is to measure the circuit elements $Z_{\mathrm{d}}$, $Z_{\mathrm{qd}}$, $Z_{\mathrm{dq}}$, and $Z_{\mathrm{q}}$. The identification can be done, for example, by perturbing $i_{\mathrm{d}}$ at first, and computing the ratios of $v_{\mathrm{d}}$ and $i_{\mathrm{d}}$ and the ratios of $v_{\mathrm{q}}$ and $i_{\mathrm{d}}$ in order to identify $Z_{\mathrm{d}}$ and $Z_{\mathrm{dq}}$, respectively. In order to identify $Z_{\mathrm{qd}}$ and $Z_{\mathrm{q}}$, $i_{\mathrm{q}}$ can be perturbed, and the ratios $v_{\mathrm{q}}$ to $i_{\mathrm{q}}$ and $v_{\mathrm{d}}$ and $i_{\mathrm{q}}$ can be computed for the identification. The measurement is based on the assumption that when one of the channels is perturbed, the other can be kept at zero.

In practical systems, the measurement of the circuit elements of the system in Fig. 2.13 may not be as straightforward because the circuit is practically part of a larger system and no ideal perturbations exist. Therefore, it cannot be assumed that the current in the channel that is not perturbed is zero. This problem is encountered when the synchronous-reference frame equivalent impedance of a three-phase system is measured.

## 2.2 Three-Phase Inverter

Fig. 2.14 shows a circuit diagram of a three-phase grid-connected inverter that consists of three half-bridge phase legs. The output of the inverter is filtered by a LCL filter. $L_{\mathrm{a,b,c}}$, $C_{\mathrm{a,b,c}}$, and $L_{\mathrm{2\text{-}a,b,c}}$ denote the converter-side filter inductors, the filter capacitors, and the grid-side inductors, respectively. The grid is modeled by stiff grid voltages ($v_{\mathrm{g\text{-}a,b,c}}$) that are behind grid inductances $L_{\mathrm{g\text{-}a,b,c}}$. The grid currents are denoted by $i_{\mathrm{g\text{-}a,b,c}}$. The inverter is connected to the grid at the point of common coupling (PCC) where other parallel-connected loads and sources can be connected. Although the output voltages ($v_{\mathrm{o\text{-}a,b,c}}$) are at the physical output of the inverter, the controller frame is commonly synchronized to the voltages over the filter capacitors.

### Synchronous Reference Frame

The sum of balanced sinusoidal three-phase system voltages or currents can be presented as a phase vector rotating at the frequency of the sinusoidal phase quantities, and a reference frame can be synchronized at the rotating frequency of the phase vector. In the synchronous reference frame (DQ frame), a balanced three-phase system is presented by the direct (d) and quadrature (q) channels that are direct quantities. The fundamental advantage of using the DQ frame is that traditional proportional-integral (PI) controllers can be used because the synchronous frequency (50 Hz or 60 Hz) component is presented by the DC component where the integral term of the controller has an infinite gain, which leads to zero steady-state error [80].

Commonly, the Clarke transformation is first used to transform the balance three-phase system variables ($x_{\mathrm{a}}$, $x_{\mathrm{b}}$, and $x_{\mathrm{c}}$) to the stationary reference frame [81]

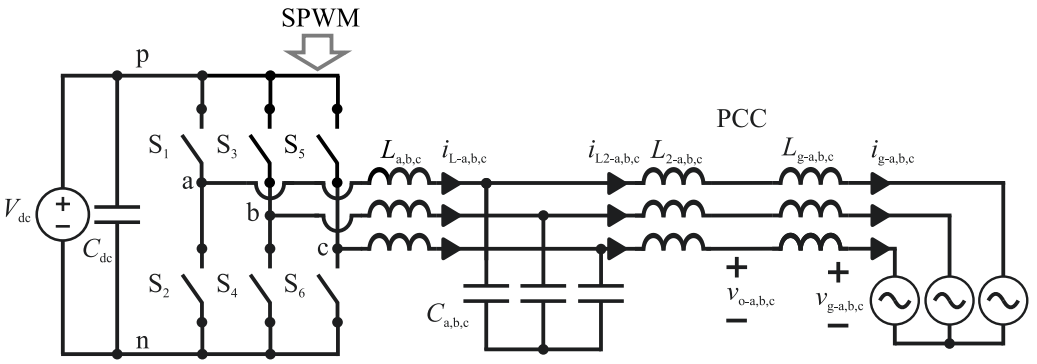


Figure 2.14: Three-phase grid-connected inverter.

$$\begin{bmatrix} x_\alpha \\ x_\beta \end{bmatrix} = \sqrt{\frac{2}{3}} \begin{bmatrix} 1 & \frac{-1}{2} & \frac{-1}{2} \\ 0 & \frac{\sqrt{3}}{2} & \frac{-\sqrt{3}}{2} \end{bmatrix} \begin{bmatrix} x_a \\ x_b \\ x_c \end{bmatrix} \tag{2.21}$$

where $x_\alpha$ and $x_\alpha$ are the variables in the stationary reference frame. Then, the modified Park transformation is used to obtain the direct ($x_\mathrm{d}$) and the quadrature ($x_\mathrm{q}$) components in the synchronous reference frame:

$$\overbrace{\begin{bmatrix} x_\mathrm{d} \\ x_\mathrm{q} \end{bmatrix}}^{\mathbf{x}} = \begin{bmatrix} \cos(\theta) & \sin(\theta) \\ -\sin(\theta) & \cos(\theta) \end{bmatrix} \begin{bmatrix} x_\alpha \\ x_\beta \end{bmatrix} \tag{2.22}$$

where $\theta$ denotes the phase angle that equals the time integral of the synchronous angular frequency, $\omega_\mathrm{s}$. In a grid-connected converter, the phase angle is obtained by a synchronization, where the controller reference frame is synchronized to the phase voltages [15]. In the grid-forming mode, the phase angle is created by the controller [15].

The transformation in (2.22) can be given by presenting $x_\mathrm{q}$ and $x_\beta$ at the imaginary axis and $x_\mathrm{d}$ and $x_\alpha$ at the real axis:

$$x_\mathrm{d} + \mathrm{j}x_\mathrm{q} = (\cos(\omega_s t) - \mathrm{j}\sin(\omega_s t))(x_\alpha + \mathrm{j}x_\beta) \tag{2.23}$$

By using Euler's identity, the equation can be given as

$$\bar{x} = \mathrm{e}^{-\mathrm{j}\omega_s t}\bar{x}^{\alpha\beta} \tag{2.24}$$

where $\bar{x}^{\alpha\beta}$ and $\bar{x}$ denote the stationary-reference frame phasor and the complex-valued synchronous-reference frame variable, respectively. Eq. (2.24) can be solved for $\bar{x}^{\alpha\beta}$:

$$\bar{x}^{\alpha\beta} = \mathrm{e}^{\mathrm{j}\omega_s t}\bar{x} \tag{2.25}$$

The inductor current derivative as a function of the voltage over the inductor in the stationary reference frame can be given as

$$\frac{\delta \bar{i}_{\mathrm{L}}^{\alpha\beta}}{\delta t} = \frac{\bar{v}_{\mathrm{L}}^{\alpha\beta}}{L} \tag{2.26}$$

where $\bar{i}_{\mathrm{L}}^{\alpha\beta}$ and $\bar{v}_{\mathrm{L}}^{\alpha\beta}$ are the inductor current phasor and the voltage over the inductor phasor in the stationary reference frame, respectively. The equation can be expressed in the synchronous reference frame by using (2.25):

$$\frac{\delta e^{\mathrm{j}\omega_{\mathrm{s}}t}\bar{i}_{\mathrm{L}}}{\delta t} = \frac{e^{\mathrm{j}\omega_{\mathrm{s}}t}\bar{v}_{\mathrm{L}}}{L} \tag{2.27}$$

where $\bar{i}_{\mathrm{L}}$ and $\bar{v}_{\mathrm{L}}$ are the complex inductor current and the voltage over the inductor in the synchronous reference frame. The derivative term is computed as follows:

$$\frac{\delta e^{\mathrm{j}\omega_{\mathrm{s}}t}\bar{i}_{\mathrm{L}}}{\delta t} = \frac{\delta e^{\mathrm{j}\omega_{\mathrm{s}}t}}{\delta t}\bar{i}_{\mathrm{L}} + e^{\mathrm{j}\omega_{\mathrm{s}}t}\frac{\delta \bar{i}_{\mathrm{L}}}{\delta t} = \mathrm{j}\omega_{\mathrm{s}}e^{\mathrm{j}\omega_{\mathrm{s}}t}\bar{i}_{\mathrm{L}} + e^{\mathrm{j}\omega_{\mathrm{s}}t}\frac{\delta \bar{i}_{\mathrm{L}}}{\delta t} \tag{2.28}$$

The final form for (2.26) in the synchronous reference frame can be given as

$$\frac{\delta \bar{i}_{\mathrm{L}}}{\delta t} = -\mathrm{j}\omega_{\mathrm{s}}\bar{i}_{\mathrm{L}} + \frac{\bar{v}_{\mathrm{L}}}{L} \tag{2.29}$$

The derivative cross-couples the d and q channels. The cross-coupling is clearly visible when the channels are presented by separate equations:

$$\begin{aligned} \frac{\delta i_{\mathrm{Ld}}}{\delta t} &= \omega_{\mathrm{s}} i_{\mathrm{Lq}} + \frac{v_{\mathrm{Ld}}}{L} \\ \frac{\delta i_{\mathrm{Lq}}}{\delta t} &= -\omega_{\mathrm{s}} i_{\mathrm{Ld}} + \frac{v_{\mathrm{Lq}}}{L} \end{aligned} \tag{2.30}$$

In the synchronous reference frame, the derivatives of the capacitor voltage components are also cross-coupled:

$$\begin{aligned} \frac{\delta v_{\mathrm{Cd}}}{\delta t} &= \omega_{\mathrm{s}} v_{\mathrm{Cq}} + \frac{i_{\mathrm{Cd}}}{C} \\ \frac{\delta v_{\mathrm{Cq}}}{\delta t} &= -\omega_{\mathrm{s}} v_{\mathrm{Cd}} + \frac{i_{\mathrm{Cq}}}{C} \end{aligned} \tag{2.31}$$

where $v_{\mathrm{Cd}}$ and $v_{\mathrm{Cq}}$ denote the capacitor voltage d and q components, respectively, and $i_{\mathrm{Cd}}$ and $i_{\mathrm{Cq}}$ denote the capacitor current d and q components, respectively.

### Dynamic Model in Synchronous Reference Frame

Fig. 2.15 shows the synchronous-reference-frame equivalent circuit of the grid-following inverter in Fig. 2.14. The converter is fed from a direct voltage source ($v_{\mathrm{in}}$), and the input current is denoted by $i_{\mathrm{in}}$. The equivalent series resistance of the DC capacitor is denoted by $r_{\text{C-dc}}$, and the voltage over the DC capacitor is denoted by $v_{\text{C-dc}}$. At the output, the converter is connected to stiff grid voltages presented by the voltage sources

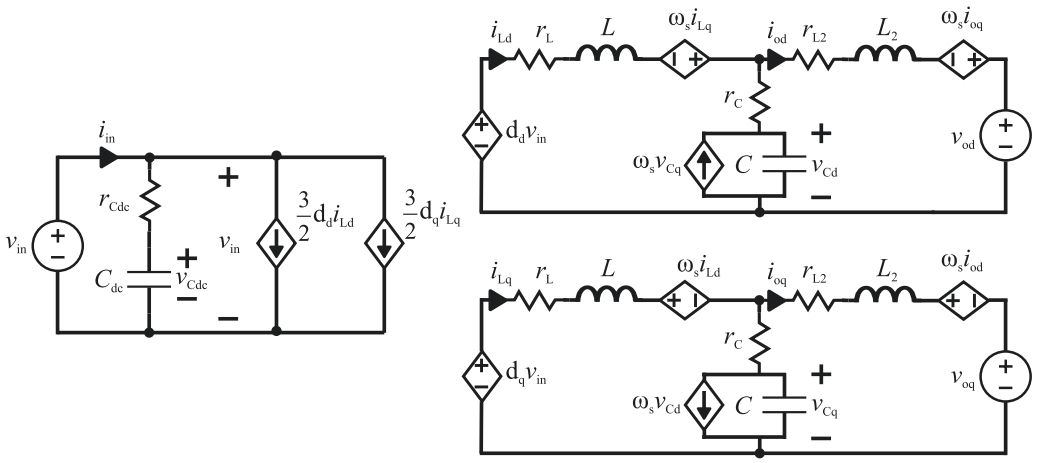


Figure 2.15: Synchronous frame equivalent average circuit of the grid-following inverter.

$v_{od}$ and $v_{oq}$ in the d and q channels, respectively. If the converter was fed from a PV panel string, the input voltage source should be replaced by an equivalent current source that more accurately models the dynamics of a PV panel [62, 82, 83].

The duty ratio d and q components are denoted by $d_d$ and $d_q$, respectively. It is assumed that the passive components are identical in all three phases. Therefore, the passive components can be presented with identical values in both the d channel and the q channel. The equivalent series resistances of the filter inductor and the filter capacitor are denoted by $r_L$ and $r_C$, respectively. At the output terminal of the converter, the d-channel components and the q-channel components of the output current are denoted by $i_{od}$ and $i_{oq}$, respectively. The grid-side filter inductor is denoted by $L_2$ and its ESR by $r_{L2}$.

The inductor current cross-coupling (2.30) and the capacitor voltage cross-coupling (2.31) are visible as current-dependent voltage sources and voltage-dependent current sources, respectively. The switching action is not modeled in the synchronous reference frame equivalent circuit. Instead, the bridge voltage is modeled as the average by the products of the duty ratio of the channel and the input voltage. The two-thirds gain is required in the two current sinks modeling the DC-side dynamics because the power leaving the DC side and entering the AC side must be equal.

The derivation of the synchronous-reference frame small-signal model for the three-phase grid-forming inverter is examined in [P4]. The main steps of deriving the small-signal model for a following inverter are put together here. At first, state-space equations are formulated from the circuit in Fig. 2.15. The capacitor voltage derivatives and the inductor current derivatives are set to zero and the steady state operating point of the converter is solved. Then, the coefficients of the small-signal variables, which are obtained after a linearization at the steady state, are collected to state-space matrices.

The state-space presentation can be solved for the transfer functions from the system input variables ($\hat{v}_{\mathrm{in}}$, $\hat{v}_{\mathrm{od}}$, $\hat{v}_{\mathrm{oq}}$, $\hat{d}_{\mathrm{d}}$, $\hat{d}_{\mathrm{q}}$) to the system output variables ($\hat{i}_{\mathrm{in}}$, $\hat{i}_{\mathrm{Ld}}$, $\hat{i}_{\mathrm{Lq}}$, $\hat{i}_{\mathrm{od}}$, $\hat{i}_{\mathrm{oq}}$). The hat denotes small-signal variables. With the $G$ transfer functions [62], the relation from the inputs to the output can be given as:

$$\begin{bmatrix} \hat{i}_{\mathrm{in}} \\ \hat{i}_{\mathrm{Ld}} \\ \hat{i}_{\mathrm{Lq}} \\ \hat{i}_{\mathrm{od}} \\ \hat{i}_{\mathrm{oq}} \end{bmatrix} = \left[\begin{array}{c|cc|cc} Y_{\mathrm{in}} & T_{\mathrm{oi\text{-}d}} & T_{\mathrm{oi\text{-}q}} & G_{\mathrm{ci\text{-}d}} & G_{\mathrm{ci\text{-}q}} \\ \hline G_{\mathrm{iL\text{-}d}} & G_{\mathrm{oL\text{-}d}} & G_{\mathrm{oL\text{-}qd}} & G_{\mathrm{cL\text{-}d}} & G_{\mathrm{cL\text{-}qd}} \\ G_{\mathrm{iL\text{-}q}} & G_{\mathrm{oL\text{-}dq}} & G_{\mathrm{oL\text{-}q}} & G_{\mathrm{cL\text{-}dq}} & G_{\mathrm{cL\text{-}q}} \\ \hline G_{\mathrm{io\text{-}d}} & -Y_{\mathrm{o\text{-}d}} & -Y_{\mathrm{o\text{-}qd}} & G_{\mathrm{co\text{-}d}} & G_{\mathrm{co\text{-}qd}} \\ G_{\mathrm{io\text{-}q}} & -Y_{\mathrm{o\text{-}dq}} & -Y_{\mathrm{o\text{-}q}} & G_{\mathrm{co\text{-}dq}} & G_{\mathrm{co\text{-}q}} \end{array}\right] \begin{bmatrix} \hat{v}_{\mathrm{in}} \\ \hat{v}_{\mathrm{od}} \\ \hat{v}_{\mathrm{oq}} \\ \hat{d}_{\mathrm{d}} \\ \hat{d}_{\mathrm{q}} \end{bmatrix} \tag{2.32}$$

where $Y_{\mathrm{in}}$ denotes the input admittance, $T_{\mathrm{oi}}$ denotes the reverse transfer function, $G_{\mathrm{ci}}$ denotes the control-to-input transfer function, $G_{\mathrm{iL}}$ denotes the input-to-inductor current transfer function, $G_{\mathrm{oL}}$ denotes the output-to-inductor current transfer function, $G_{\mathrm{cL}}$ denotes the control-to-inductor current transfer function, $G_{\mathrm{io}}$ denotes the input-to-output transfer function, $Y_{\mathrm{o}}$ denotes the output admittance transfer function, and $G_{\mathrm{co}}$ denotes the control-to-output transfer function. The subscripts d and q indicate that the transfer functions are related to the d or q channels, respectively. If the transfer function is from a d-channel input to a q-channel output, the input channel is denoted first. For example, $G_{\mathrm{cL\text{-}qd}}$ is the transfer function from the q-channel duty ratio ($\hat{d}_{\mathrm{q}}$) to the inverter-side current d component ($\hat{i}_{\mathrm{Ld}}$). The transfer functions are responses to the Laplace variable ($s$), which is omitted for brevity.

The transfer functions in (2.32) that are related to same variables, but with different channels, can be presented with matrices, and the input and output variables can be collected to vectors. The compact notation can be given as:

$$\begin{bmatrix} \hat{i}_{\mathrm{in}} \\ \hat{\mathbf{i}}_{\mathrm{L}} \\ \hat{\mathbf{i}}_{\mathrm{o}} \end{bmatrix} = \begin{bmatrix} Y_{\mathrm{in}} & \mathbf{T}_{\mathrm{oi}} & \mathbf{G}_{\mathrm{ci}} \\ \mathbf{G}_{\mathrm{iL}} & \mathbf{G}_{\mathrm{oL}} & \mathbf{G}_{\mathrm{cL}} \\ \mathbf{G}_{\mathrm{io}} & -\mathbf{Y}_{\mathrm{o}} & \mathbf{G}_{\mathrm{co}} \end{bmatrix} \begin{bmatrix} \hat{v}_{\mathrm{in}} \\ \hat{\mathbf{v}}_{\mathrm{o}} \\ \hat{\mathbf{d}} \end{bmatrix} \tag{2.33}$$

where the bold font means 2×1 vector in the case of the input and the output variables, and in the case of the transfer functions the bold font denotes a transfer matrix. In (2.32), the transfer functions are grouped by the lines to show which transfer function are presented by a single matrix in (2.33). The effect of the phase synchronization by means of a phase-locked loop (PLL) on the system can be computed by linearizing the PLL and computing the PLL effect on the open-loop dynamics [62].

Fig. 2.16 shows the transfer-matrix block diagram of the grid-following inverter with a converter-side inductor-current feedback, which is commonly applied to grid-connected inverters. In addition to the transfer matrices in (2.33), the current-controller transfer matrix is used

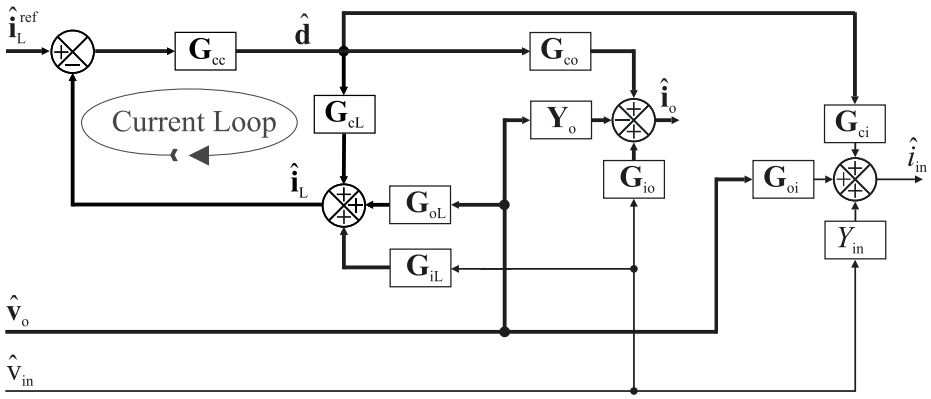


Figure 2.16: Block diagram of the dynamics of the grid-following inverter with the inductor-current feedback.

$$\mathbf{G}_{cc} = \begin{bmatrix} G_{cc} & 0 \\ 0 & G_{cc} \end{bmatrix} = \begin{bmatrix} K_{p\text{-}c} + \dfrac{K_{i\text{-}c}}{s} & 0 \\ 0 & K_{p\text{-}c} + \dfrac{K_{i\text{-}c}}{s} \end{bmatrix} \tag{2.34}$$

where $K_{p\text{-}c}$ and $K_{i\text{-}c}$ are the P gain and the I gain of the proportional-integral (PI) controller, respectively. The delay from the digital control and the pulse width modulation ($e^{-s1.5T_{sw}}$) can be approximated by Padé approximation [P4], and the delay can be modeled as a part of the current-controller transfer function ($G_{cc}$). The closed-loop current-reference-to-current transfer matrix can be calculated as follows:

$$\mathbf{G}_{cL}^{c} = (\mathbf{I} + \mathbf{L}_c)\,\mathbf{L}_c \tag{2.35}$$

where $\mathbf{L}_c = \mathbf{G}_{cL}\mathbf{G}_{cc}$ is the multi-variable current loop gain, and the superscript 'c' denotes that the current-control loop is closed. However, the superscripts are omitted for the rest of this thesis when dq-frame systems are analyzed. The closed-loop presentation of the other transfer matrices can be computed by similar principles as in the case of the grid-forming mode [P4].

Fig. 2.14 shows a simplified diagram of the grid-connected three-phase inverter. If the grid impedance is unknown, the output current of the inverter can be perturbed and the grid-impedance can be measured. Here, the grid impedance is a series RL circuit whose impedance matrix is given as

$$\mathbf{Z}_{Lg} = \begin{bmatrix} Z_{Lg\text{-}d} & Z_{Lg\text{-}qd} \\ Z_{Lg\text{-}dq} & Z_{Lg\text{-}q} \end{bmatrix} = \begin{bmatrix} r_g + sL_g & -L_g\omega_s \\ L_g\omega_s & r_g + sL_g \end{bmatrix} \tag{2.36}$$

where $L_g$ and $r_g$ denote the grid inductance and the grid-inductance equivalent series resistance. Because the inverter current measurement and feedback are from the converter-side inductor current, the filter capacitor is considered part of the grid impedance. The impedance of the filter capacitor is given as:

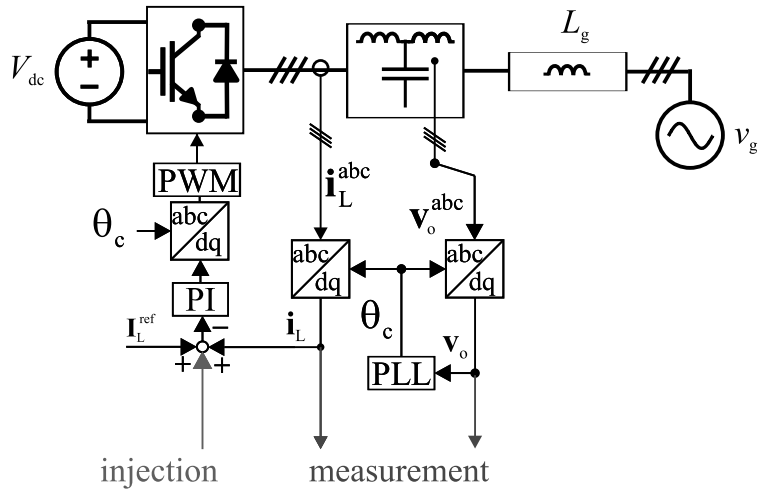


Figure 2.17: A block diagram of the grid impedance measurement performed with a grid-connected inverter.

$$\mathbf{Z}_{\mathrm{C}} = \begin{bmatrix} Z_{\text{C-d}} & Z_{\text{C-qd}} \\ Z_{\text{C-dq}} & Z_{\text{C-q}} \end{bmatrix} = \begin{bmatrix} \dfrac{s}{Cs^2 + C{\omega_{\mathrm{s}}}^2} + r_{\mathrm{C}} & \dfrac{\omega_{\mathrm{s}}}{Cs^2 + C{\omega_{\mathrm{s}}}^2} \\ \dfrac{\omega_{\mathrm{s}}}{Cs^2 + C{\omega_{\mathrm{s}}}^2} & \dfrac{s}{Cs^2 + C{\omega_{\mathrm{s}}}^2} + r_{\mathrm{C}} \end{bmatrix} \tag{2.37}$$

The parallel connection of the grid inductance and the filter capacitor forms the grid impedance ($\mathbf{Z}_{\mathrm{g}}$) that is measured:

$$\mathbf{Z}_{\mathrm{g}} = \left(\mathbf{I} + \mathbf{Z}_{\mathrm{Lg}}\mathbf{Z}_{\mathrm{C}}^{-1}\right)^{-1}\mathbf{Z}_{\mathrm{Lg}} \tag{2.38}$$

The small-signal output voltages can be presented as a function of the small-signal inductor current and the impedance elements:

$$\begin{bmatrix} \hat{v}_{\text{o-d}} \\ \hat{v}_{\text{o-q}} \end{bmatrix} = \overbrace{\begin{bmatrix} Z_{\text{g-d}} & Z_{\text{g-qd}} \\ Z_{\text{g-dq}} & Z_{\text{g-q}} \end{bmatrix}}^{\mathbf{Z}_{\mathrm{g}}} \begin{bmatrix} \hat{i}_{\text{L-d}} \\ \hat{i}_{\text{L-q}} \end{bmatrix} \tag{2.39}$$

Assuming that only either $\hat{i}_{\text{L-d}}$ or $\hat{i}_{\text{L-q}}$ is perturbed at a time, the impedance elements can be computed as

$$\begin{bmatrix} Z_{\text{g-d}} & Z_{\text{g-qd}} \\ Z_{\text{g-dq}} & Z_{\text{g-q}} \end{bmatrix} = \begin{bmatrix} \dfrac{\hat{v}_{\text{o-d}}}{\hat{i}_{\text{L-d}}} & \dfrac{\hat{v}_{\text{o-d}}}{\hat{i}_{\text{L-q}}} \\ \dfrac{\hat{v}_{\text{o-q}}}{\hat{i}_{\text{L-d}}} & \dfrac{\hat{v}_{\text{o-q}}}{\hat{i}_{\text{L-q}}} \end{bmatrix}. \tag{2.40}$$

### Impedance coupling

Fig. 2.17 shows a block diagram of a voltage-fed grid-connected inverter that is feedback-controlled from the converter-side inductor current. A grid-impedance measurement is performed with the inverter by using the inverter and applying a broadband perturbation (maximum-length binary sequence) [26]. The perturbation is injected on top of the current reference d and q components, and the resulting responses in the inductor current and the output voltage are measured and Fourier transform is applied to extract the spectral information of the grid impedance. The system is simulated with Matlab Simulink Simscape toolbox, and the system parameters are given in Table 2.2. The grid inductance value $L_{\mathrm{g}}$ in the simulation is the sum of $L_{\mathrm{line}}$ and $L_{\mathrm{T}}$.

The synchronous-reference-frame impedance elements are computed from the responses in the output voltage and the inductor current d and q components according to (2.40). Fig. 2.18 compares the modeled grid impedance d and dq components to the results from a simulated measurement performed with Simulink. The superscripts vd/id and vq/id denote that the impedance elements are calculated as the ratios of the corresponding voltages and currents according to (2.40). There are clear differences between the modeled and the measured impedance elements. In the d component in the simulation result, there is additional resonance at around 120 Hz and the resonance peaks at around 500 Hz are merged [P1]. In the dq-component simulation result, only the low-frequency part below 40 Hz matches the model. The simulation result shows that, regardless of the feedback-controlled converter used in perturbing the system, some errors occur in the

Table 2.2: Grid-connected inverter parameters and operating point values.

| Parameter | Symbol | Value | Parameter | Symbol | Value |
|---|---|---|---|---|---|
| Input voltage | $V_{\mathrm{dc}}$ | 413 V | Grid voltage rms | $V_{\mathrm{g\text{-}rms}}$ | 120 V |
| Output current d component | $I_{\mathrm{od}}$ | 10.6 A | Output current q component | $I_{\mathrm{oq}}$ | 0.71 A |
| Synchronous frequency | $\omega_{\mathrm{s}}$ | $2\pi 50$ rad/s | Switching frequency | $f_{\mathrm{s}}$ | 8 kHz |
| Filter capacitor capacitance | $C_{\mathrm{f}}$ | 10 $\mu$F | Filter inductance | $L$ | 2.5 mH |
| $C_{\mathrm{f}}$ ESR and damping resistor | $r_{\mathrm{Cf}}$ | 1.81 Ω | $L$ ESR | $r_{\mathrm{L}}$ | 0.065 Ω |
| Filter inductance 2 | $L_2$ | 0.1 mH | $L_2$ ESR | $r_{\mathrm{L2}}$ | 0.022 Ω |
| Line inductance | $L_{\mathrm{line}}$ | 8.83 mH | Line inductance ESR | $r_{\mathrm{Lg}}$ | 0.262 Ω |
| Transformer inductance | $L_{\mathrm{T}}$ | 0.507 mH | Transformer inductance ESR | $r_{\mathrm{T}}$ | 0.417 Ω |
| Current controller P gain | $K_{\mathrm{p\text{-}c}}$ | 0.0149 | Current controller I gain | $K_{\mathrm{i\text{-}c}}$ | 23.4 |
| PLL P gain | $K_{\mathrm{p\text{-}pll}}$ | 0.0120 | PLL I gain | $K_{\mathrm{i\text{-}pll}}$ | 0.0144 |

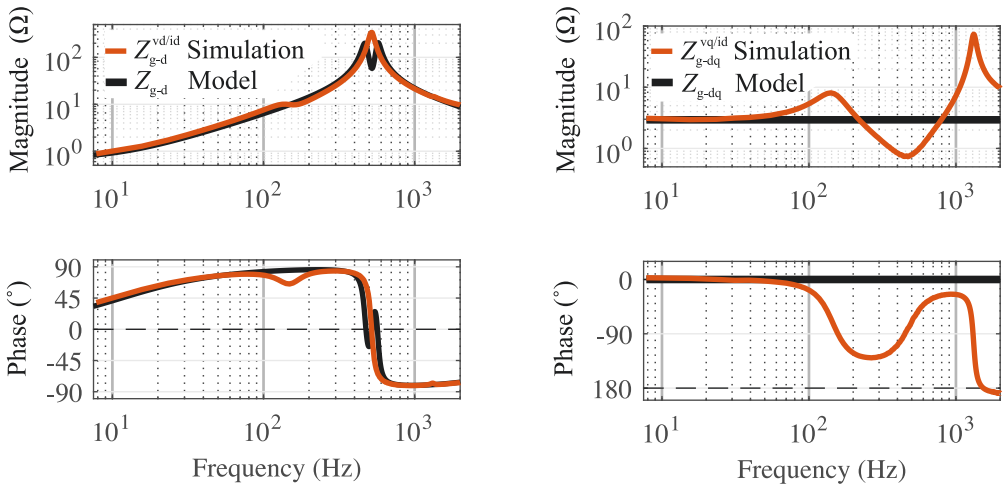


Figure 2.18: Modeled and simulated measurement results of the grid impedance (a) d component and (b) dq component.

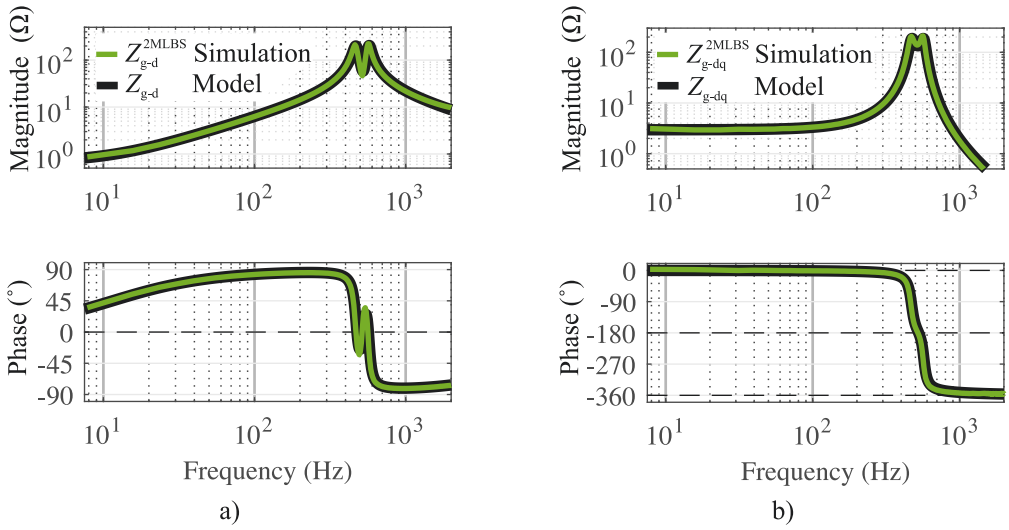


Figure 2.19: Modeled and simulated measurement results based on two independent injections of the grid impedance (a) d component and (b) dq component.

measurement. The distorting effect is also visible in the voltage-perturbed simulated measurements in [P5].

In the traditional approach to tackle the impedance coupling, multiple independent measurements are performed at the same frequencies [31, 48–52]. Two measurement cycles are performed. First, the injection is summed on top of the d-channel current reference. Secondly, the injection is summed on top of the q-channel current reference. The results from the two sets of measurements can be used to form a group of equations based on (2.39) and solved for the impedance elements [31]:

$$\begin{bmatrix} Z_{\mathrm{d}} & Z_{\mathrm{qd}} \\ Z_{\mathrm{dq}} & Z_{\mathrm{q}} \end{bmatrix} = \begin{bmatrix} V_{\mathrm{d1}} & V_{\mathrm{d2}} \\ V_{\mathrm{q1}} & V_{\mathrm{q2}} \end{bmatrix} \begin{bmatrix} I_{\mathrm{Ld1}} & I_{\mathrm{Ld2}} \\ I_{\mathrm{Lq1}} & I_{\mathrm{Lq2}} \end{bmatrix}^{-1} \tag{2.41}$$

where subscripts 1 and 2 denote the results from the first and the second independent measurements, respectively. The capital letters in the currents and the voltages denote discrete Fourier transformation (DFT) of the variables. Fig. 2.19 shows the impedance elements identified with the method based two independent injections and based on (2.41). Evidently, the simulated measurements match the models. Figs. 2.18 and 2.19 only show the d and dq impedance elements; nevertheless, similar behavior is visible in q and qd components as it is shown in [P1].

The main disadvantage of the described method is the requirement for at least two sequentially performed measurements during which the system is prone to disturbances. In order to improve the measurement, a procedure that is based on one measurement cycle is developed in Chapter 3.

## 2.3 Discussion

This chapter has presented background information on the nonlinear deadtime effect and the measurement of equivalent synchronous-reference frame impedance of a three-phase system. The nonlinear deadtime effect in the time domain was revised, which is the basis for the development of the nonlinear frequency-domain model in the following sections. The unterminated model for a three-phase inverter in the synchronous-reference frame was revised, and the cause of the cross-coupling between the direct and the quadrature channels in the synchronous-reference frame was derived. The measurement of the equivalent impedance of a three-phase system in the synchronous-reference frame was investigated, revealing that the cross-coupling can distort the measurement even though a feedback-controlled inverter was used to perform measurement. The background information presented in this chapter acts as prerequisites for the following chapters where a novel nonlinear frequency-domain model for the deadtime effect, and a novel real-time synchronous-reference-frame impedance-measurement procedure is proposed.

Chapter 3

# Methods

This chapter is divided into two sections. The first section looks in detail into the deadtime effect in a sinusoidal steady state of the inverter, and a describing function model is derived for the nonlinear deadtime effect. The second section starts by examining the impedance coupling in impedance measurements with a load-affected model in the synchronous reference frame. Then, the generation and the characteristics of orthogonal pseudo-random binary sequences are revised. Finally, a measurement method is proposed that utilizes the orthogonal sequences to tackle the impedance coupling is proposed.

## 3.1 Dynamic Modeling of Nonlinear Deadtime Effect

The average voltage error caused by the deadtime depends on the deadtime length, the switching frequency, the direct voltage value, and the converter-side inductor current sign. In the presence of a synchronous frequency (50 Hz) current component, the current sign changes every half cycle, and the voltage error sign changes with the current sign at the synchronous frequency, provided that the current amplitude is higher than half the peak-to-peak ripple. When an additional frequency component to synchronous-frequency component is added to the current, the current may cross zero at the perturbation frequency; therefore, a voltage error can occur at the perturbation frequency (Fig. 3.2a). In following, the behavior of the voltage is analyzed in the presence of an additional current perturbation.

A voltage error appears at the perturbation frequency if the sum of the perturbation-frequency current amplitude, the synchronous current amplitude, and the zero-current-clamping-occurrence current is higher than half the peak-to-peak current ripple. Therefore, in the occurrence of the voltage error as a function of the current, there is a dead zone if the synchronous-frequency current amplitude ($A_{\mathrm{sync}}$) subtracted by the zero-current clamping value is less than half the peak-to-peak ripple ($\Delta i/2$). This current value is the limit where the dead zone ends, and the error begins to appear [P2]:

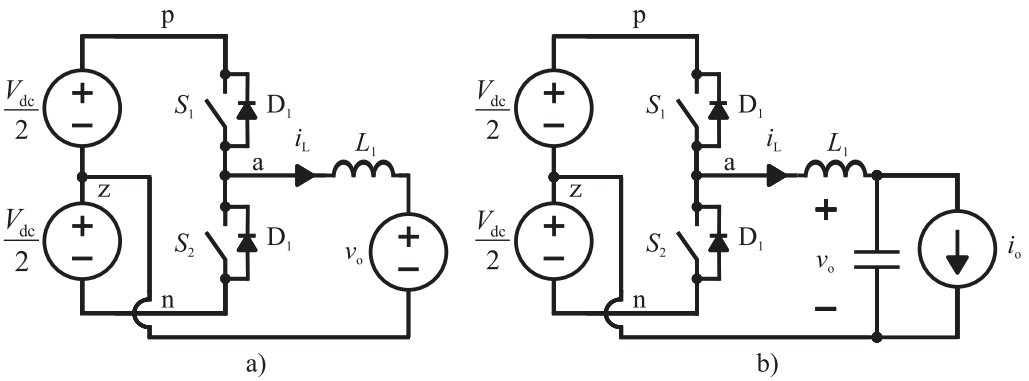


Figure 3.1: Half-bridge inverter with (a) an L filter connected to an alternating voltage source, and (b) an LC filter connected to a current sink.

$$R^{\text{dead}} = \frac{\Delta i}{2} - A_{\text{sync}} - \Delta i_{\text{dead}} \tag{3.1}$$

The minimum value of $R^{\text{dead}}$ is zero. When the perturbation amplitude equals the sum of the synchronous-frequency current amplitude and half the peak-to-peak ripple, the current error saturates for the first time at one point in the synchronous-frequency cycle, which is visible as the end of the linear in region in the voltage error that is averaged over a switching cycle [P2]. At higher perturbation amplitudes, the error approaches the maximum voltage error. The limit for the beginning of saturation region can be given as [P2][1]:

$$R^{\text{sat}} = \frac{\Delta i}{2} + A_{\text{sync}} \tag{3.2}$$

The voltage-output inverter in Fig. 3.1b is preferred over the current-output inverter in Fig. 3.1a in the detailed study of the deadtime effect. If the filter inductor of the half-bridge inverter is connected directly to an alternating voltage source and perturbations are summed to the alternating voltage source in Fig. 3.1a, the perturbations become visible in the inductor current and the voltage error at the injection frequency. However, the voltage error may also significantly affect the current fundamental component, and hence change the operating conditions. If the synchronous-frequency current is created by a current sink (Fig. 3.1b), the voltage error from the deadtime has a small effect on the fundamental current that flows through the inductor. Therefore, the operating conditions remain mostly unchanged for the study of the deadtime effect.

The voltage error under current perturbations from the output current is studied with an LC filter that is critically damped with the capacitor series resistance:

[1] In [P2], $A_{\text{sync}}$ is multiplied by $\cos\theta$, where $\theta$ is the phase angle. This is not relevant because the ripple ($\Delta i_{\text{p-p}}$) is based on the approximation (2.18).

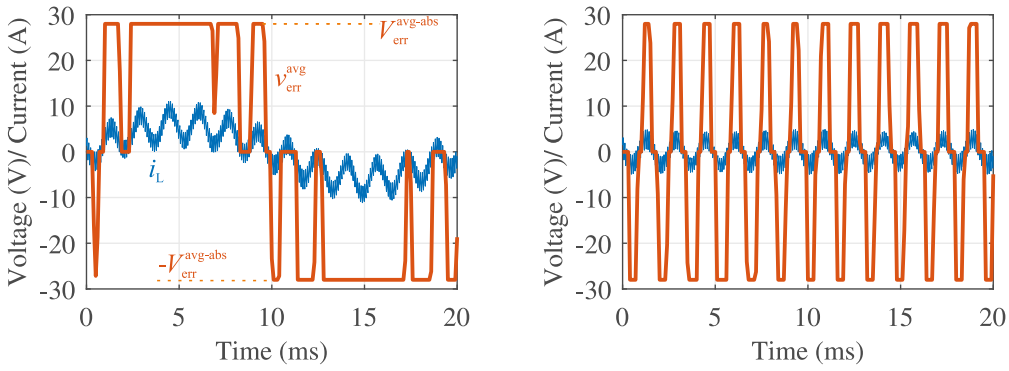


Figure 3.2: Fundamental cycle of the inductor current and the average voltage error (a) with a synchronous current of 6 A and inductor current perturbation of 3.2 A, and (b) with a synchronous current of 0 A and inductor current perturbation of 2.8 A.

$$r_C = 2\sqrt{\frac{L}{C}} \tag{3.3}$$

Matlab Simulink simulations are used to verify the behavior of the voltage error. Parameters given in Table 2.1 are used. Fig. 3.2a shows a simulated synchronous-frequency cycle of the inductor current and the average voltage error with a synchronous-frequency current amplitude of 6 A and inductor current perturbation of 3.2 A at 625 Hz. The perturbation is visible in the inductor current ($i_L$) that has the ripple. The average voltage error is clearly affected by the current sign changes, and the voltage error has visible components at the perturbation frequency [P2]. The errors at the perturbation frequency are around the original zero crossing of the synchronous-frequency current component because the perturbation is more likely to change the current direction at the lowest synchronous-frequency current values [P3].

Fig. 3.2b shows a simulated synchronous-frequency cycle of the inductor current and the average voltage error with a fundamental current of 0 A and an inductor current perturbation of 2.8 A at 625 Hz. Because there is no current at the synchronous frequency, there is also no voltage error at the synchronous frequency. The error at the perturbation frequency resembles a square wave [P2]. It can be observed from Figs. 3.2a and 3.2b that the voltage error at the perturbation frequency is periodic over a synchronous-frequency cycle.

The simulations are repeated with different combinations of the synchronous-frequency current amplitude and the perturbation current amplitude. Fig. 3.3 shows the resulting voltage error and the inductor current at the perturbation frequency in frequency domain. The synchronous-frequency current values are taken from the conditions when no perturbations are added to the inductor current. When the perturbation amplitude

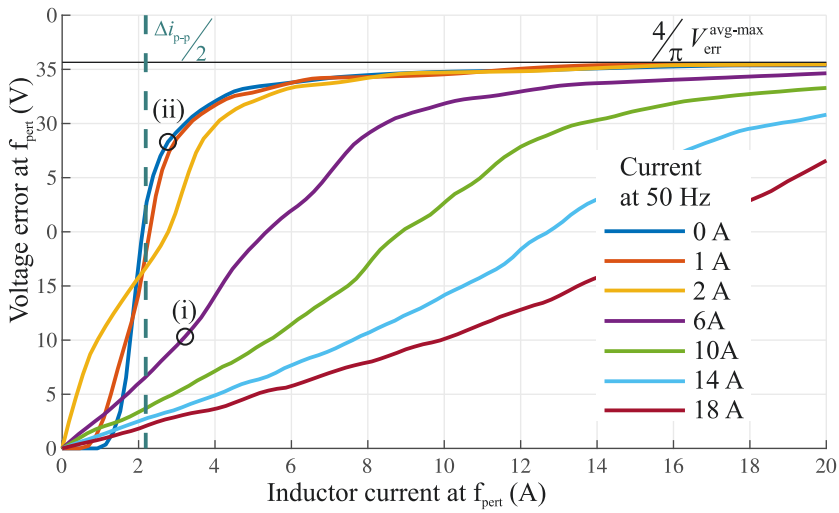


a) b)

Figure 3.3: Voltage error at the perturbation frequency ($f_{\text{pert}} = 625$ Hz) as a function of the inductor current perturbation amplitude at different synchronous-frequency current amplitudes.

and the synchronous-frequency current amplitude are high enough ($R^{\text{dead}}$ is zero), the error begins to increase from zero as a linear function of the current [P3]. Furthermore, when the synchronous-frequency current is high, the saturation is less likely to occur because required perturbation current for the saturation is relatively high, which implies that a resistive-element model can be used under such operating conditions. A heuristic model for the linear-region voltage error is developed in [P3]. Another linear model was published simultaneously with [P3]; it was suggested in [45] that the ripple effect must be considered in detail in the model and this seems to be a reliable approach.

The frequency-domain results that correspond to the time-domain waveforms in Figs. 3.2a and 3.2b are denoted by (i) and (ii) in Fig. 3.3, respectively. Clearly, in case (ii), where there is no synchronous-frequency current component, the error is closer to the square wave and the saturation in the frequency domain, although the perturbation amplitude is around the same range as in case (i). It can be observed from Fig. 3.3 that the higher the fundamental current, the lower the voltage error is for a given perturbation amplitude when the synchronous-frequency current amplitude is higher than half the peak-to-peak ripple ($\Delta i_{\text{p-p}}/2$).

The limits $R^{\text{dead}}$ and $R^{\text{sat}}$ are presented in Fig. 3.4a and 3.4b for synchronous-frequency amplitudes of 1 A and 6 A, respectively. In Fig. 3.4a, $R^{\text{dead}}$ accurately models the end of the dead zone. Between $R^{\text{dead}}$ and $R^{\text{sat}}$, the error increases relatively linearly when the perturbation amplitude is increased. When the perturbation amplitude equals $R^{\text{sat}}$, the error begins to saturate.

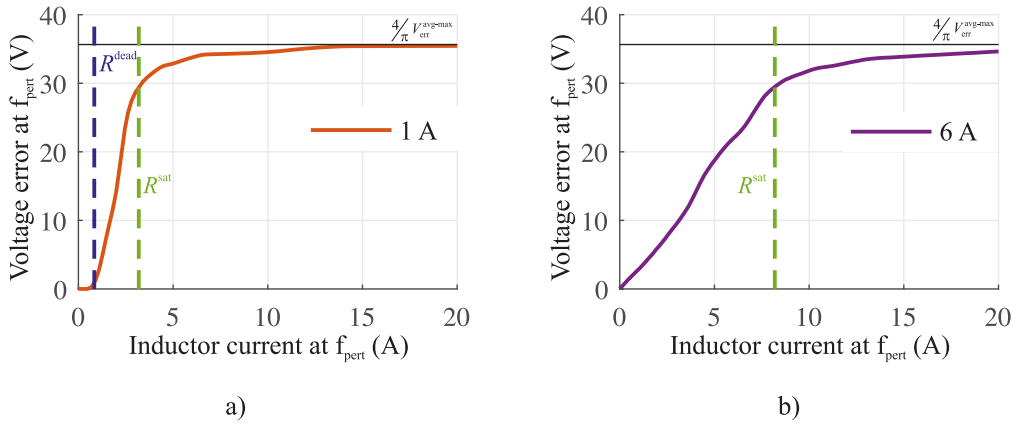


Figure 3.4: The voltage error with different synchronous-frequency current amplitudes of (a) 1 A and (b) 6 A at ($f_{\text{pert}} = 625$ Hz).

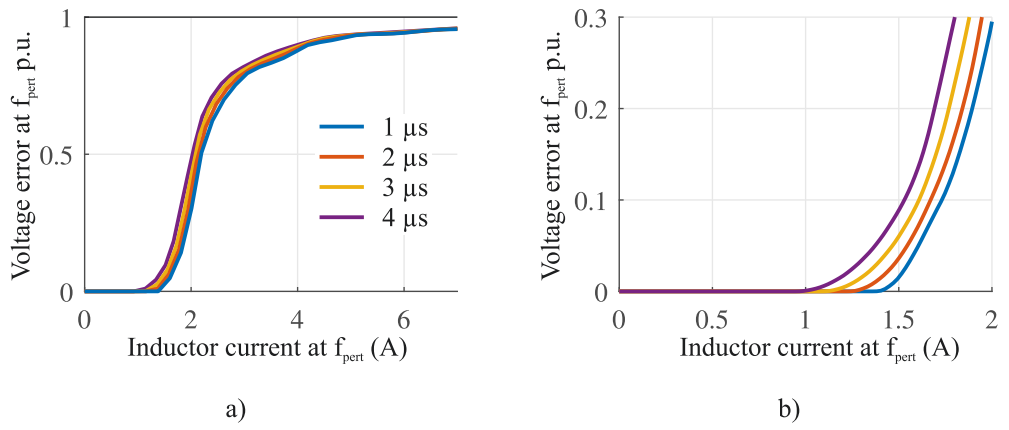


Figure 3.5: The voltage error with different deadtime lengths under no-load conditions at ($f_{\text{pert}} = 625$ Hz.

When the synchronous-frequency current amplitude is 6 A, there is no dead zone in Fig. 3.4b. $R^{\text{sat}}$ accurately models the perturbation current value when the error begins to saturate. From 0 A to $R^{\text{sat}}$, the approximation of the linear increase in the error with the perturbation current amplitude seems to be valid.

The voltage error as a function of the perturbation current is analyzed with different deadtime lengths. The voltage errors are normalized by dividing the voltage errors by $\pi/4V_{\text{err}}^{\text{avg-max}}$ so that the maximum magnitude of the voltage errors is 1. Fig. 3.5a shows that the error behaves similarly with different deadtime lengths in operating conditions that are otherwise the same. The error saturates at high current perturbation amplitudes. However, at low perturbation amplitudes, there are differences in the error behavior. Fig. 3.5b shows in detail the region where the voltage error begins to appear. With longer deadtime lengths, the error appears with smaller perturbation amplitudes. This

is considered in $R^{\text{dead}}$ in (3.1) where the zero-current clamping effect ($\Delta i_{\text{dead}}$) reduces the value of $R^{\text{dead}}$ and makes the dead zone shorter. Table 3.1 shows the most important values related to the deadtime in the simulations. The values are calculated with the parameters given in Table 2.1. Parameters $V_{\text{err}}^{\text{avg-max}}$ and $\Delta i_{\text{dead}}$ are linearly dependent on the deadtime length.

The detailed analysis of the deadtime effect under sinusoidal perturbations shows that the deadtime effect behaves nonlinearly depending on the inductor current amplitude at the perturbation frequency and the synchronous frequency. Effectively, the deadtime effect is a nonlinear negative feedback. The inductor current is not only dependent on the system filter dynamics; the voltage error reduces the inductor current that causes the voltage error. Therefore, the inductor current and perturbation-frequency component of the voltage error are in a sinusoidal steady state.

### Describing-Function Model

The average voltage error from the deadtime is time periodic. When the average error is inspected over a synchronous frequency cycle, the effect of the error can be represented with the dead zone, the slope, and the saturation regions as a function of the current amplitude at the analyzed frequency. The describing-function method is suitable for signals with such shapes as the output of a system with sinusoidal inputs [84]. Regarding power-electronic systems, the describing function method has been applied in dynamic modeling of maximum power point tracking in PV generators [36, 37], current-mode control of buck converters [85], and developing a linear model for the deadtime effect [45].

The describing function is, by definition, the ratio of the fundamental component of the system output and the sinusoidal input [86]. In other words, the describing function approximates a periodic waveform with its first (fundamental frequency) Fourier series term [87, 88]. However, a nonlinear element produces higher harmonics than the fundamental that are present in the system; therefore, the system must be assumed to have low-pass characteristics [84, 86, 87]. However, this assumption may not be valid in power-electronic systems that have undamped resonances.

Under low load conditions, the average deadtime effect as a function of the inductor

Table 3.1: Current and voltage parameters related to the deadtime effect.

| Variable | Deadtime length ($T_{\text{dead}}$) | | | |
|---|---|---|---|---|
| | 1 $\mu$s | 2 $\mu$s | 3 $\mu$s | 4 $\mu$s |
| $V_{\text{err}}^{\text{avg-max}}$ (2.16) | 7 V | 14 V | 21 V | 28 V |
| $\frac{4}{\pi}V_{\text{err}}^{\text{avg-max}}$ | 8.91 V | 17.83 V | 26.74 V | 35.65 V |
| $\Delta i_{\text{dead}}$ (2.19) | 0.0875 A | 0.175 A | 0.263 A | 0.350 A |
| $\Delta i_{\text{p-p}}/2$ (2.18) | 2.19 A | 2.19 A | 2.19 A | 2.19 A |

current amplitude can be approximated over an integer amount of the synchronous-frequency cycles by a dead zone, a linear zone, and a saturation. A describing function model ($N(A)\bar{i}_{\mathrm{L}}$) can be derived for such conditions, where $A$ is the amplitude of the inductor current phasor ($\bar{i}_{\mathrm{L}}$). The expression for the voltage error phasor with the describing function is defined as

$$\bar{v}_{\mathrm{err}} = N\left(\left|\bar{i}_{\mathrm{L}}\right|\right)\bar{i}_{\mathrm{L}} \tag{3.4}$$

With this definition, the voltage error phasor is in phase with the inductor current phasor. The describing function model ($N(A)\bar{i}_{\mathrm{L}}$) can be created by summing two describing function models ($N_1(A)\bar{i}_{\mathrm{L}}$ and $N_2(A)\bar{i}_{\mathrm{L}}$), both of which model a slope and a saturation [84]. The describing function model for the saturation is well known [84, 86], and $N_1(A)$ and $N_2(A)$ can be given as

$$N_1(A) = \frac{-2k}{\pi}\left[\sin^{-1}\left(\frac{R^{\mathrm{dead}}}{A}\right) + \frac{R^{\mathrm{dead}}}{A}\sqrt{1-\left(\frac{R^{\mathrm{dead}}}{A}\right)^2}\right] \tag{3.5}$$

$$N_2(A) = \frac{2k}{\pi}\left[\sin^{-1}\left(\frac{R^{\mathrm{sat}}}{A}\right) + \frac{R^{\mathrm{sat}}}{A}\sqrt{1-\left(\frac{R^{\mathrm{sat}}}{A}\right)^2}\right] \tag{3.6}$$

where $k$ is the slope that is given by

$$k = \frac{V_{\mathrm{err}}^{\mathrm{max}}}{R^{\mathrm{sat}} - R^{\mathrm{dead}}} \tag{3.7}$$

where it is assumed that the error linearly rises from 0 to $V_{\mathrm{err}}^{\mathrm{max}}$ when the current amplitude is increased from $R^{\mathrm{dead}}$ to $R^{\mathrm{sat}}$ [P2]. The sum of $N(A)_1$ and $N(A)_2$ is the final model

$$N(A) = \Re\left[N_1(A) + N_2(A)\right]. \tag{3.8}$$

where only the real parts of $N_1(A)$ and $N_2(A)$ are considered because the square-root factors result in imaginary values at lower amplitudes than $R^{\mathrm{dead}}$ and $R^{\mathrm{sat}}$, respectively. It is known that the voltage error is in phase with the current, and therefore the final expression for the voltage error is defined as $N(A)\bar{i}_{\mathrm{L}}$. On amplitudes below $R^{\mathrm{dead}}$, $N_1(A)$ and $N_2(A)$ cancel out each other because they have the same slope $k$ but with different signs. $N_1(A)$ saturates at $R^{\mathrm{dead}}$ and no longer cancels the positive slope; therefore, the positive slope becomes visible in $N(A)$. At $R^{\mathrm{sat}}$, $N_2(A)$ saturates and the saturation becomes visible in $N(A)$. The summation is illustrated in [P2]. Figs. 3.6a and 3.6b show the simulated and modeled ($N(A)\bar{i}_{\mathrm{L}}$) voltage error as a function of the perturbation current

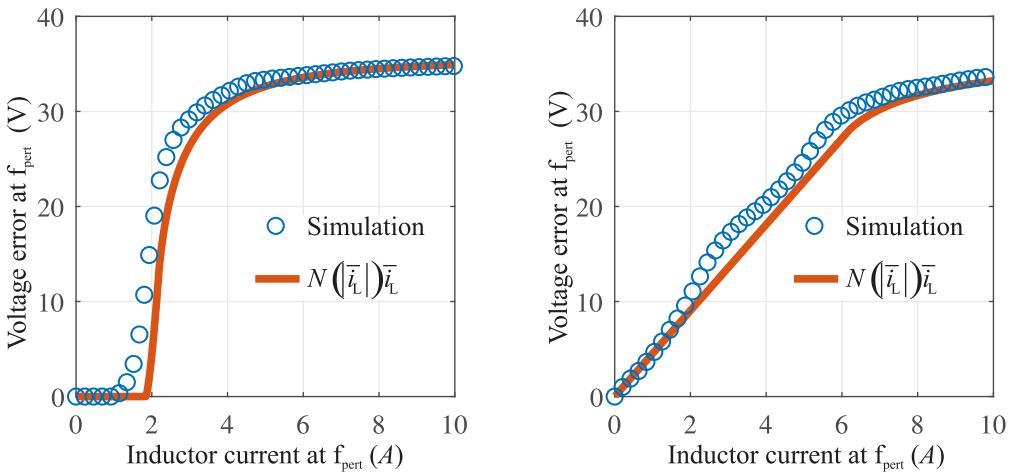


Figure 3.6: The voltage error with different synchronous-frequency current amplitudes of (a) 0 A (no-load condition) and (b) 4 A at ($f_{\mathrm{pert}} = 625$ Hz).

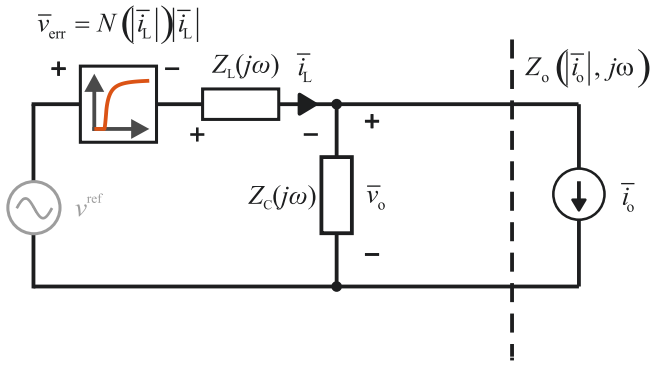


Figure 3.7: An equivalent circuit of the half-bridge inverter including the deadtime effect in a sinusoidal steady state.

amplitude under the no-load condition and with the load current of 4 A, respectively. The model clearly catches the main nonlinear behavior of the voltage error as a function of the perturbation current amplitude.

Fig. 3.7 shows a circuit diagram of the half-bridge inverter in a sinusoidal steady state. The inductor current ($i_{\mathrm{L}}$), output voltage ($v_{\mathrm{o}}$), and the output current ($i_{\mathrm{o}}$) at frequency $\omega$ are expressed with phasors $\bar{i}_{\mathrm{L}}$, $\bar{v}_{\mathrm{o}}$, and $\bar{i}_{\mathrm{o}}$, respectively. The bridge voltage is assumed to provide only the 50 Hz component; therefore, $v^{\mathrm{ref}}$ is grayed out. At first, only the output current is known at the perturbation frequency. The voltage amplitude over the capacitor branch and the inductor branch is equal:

$$\begin{aligned}&\left|N\left(\left|i_{\mathrm{L}}\left(\bar{i}_{\mathrm{L}},\omega\right)\right|\right)+Z_{\mathrm{L}}\left(j\omega\right)+Z_{\mathrm{C}}\left(j\omega\right)\right| i_{\mathrm{L}}\left(\bar{i}_{\mathrm{L}},\omega\right)\\&-\left|Z_{\mathrm{C}}\left(j\omega\right) i_{\mathrm{o}}\left(\bar{i}_{\mathrm{o}},\omega\right)\right|=0\end{aligned} \tag{3.9}$$

Due to the nonlinear term, $N\left(\left|i_{\mathrm{L}}\left(\bar{i}_{\mathrm{L}},\omega\right)\right|\right)$, the equation cannot be solved analytically for the inductor current; nevertheless, the equation can be solved numerically. The solved inductor current is real-valued; therefore, the output current must be resolved in order to obtain the correct phasor for the output impedance expression:

$$i_{\mathrm{o}}\left(\bar{i}_{\mathrm{o}},\omega\right)=\frac{\left[N\left(\left|i_{\mathrm{L}}\left(\bar{i}_{\mathrm{L}},\omega\right)\right|\right)+Z_{\mathrm{L}}\left(j\omega\right)+Z_{\mathrm{C}}\left(j\omega\right)\right] i_{\mathrm{L}}\left(\bar{i}_{\mathrm{L}},\omega\right)}{Z_{\mathrm{C}}\left(j\omega\right)} \tag{3.10}$$

The output voltage is the product of the capacitor impedance and the capacitor current:

$$v_{\mathrm{o}}\left(\bar{v}_{\mathrm{o}},\omega\right)=Z_{\mathrm{C}}\left(j\omega\right)\left[i_{\mathrm{o}}\left(\bar{i}_{\mathrm{o}},\omega\right)-i_{\mathrm{L}}\left(\bar{i}_{\mathrm{L}},\omega\right)\right] \tag{3.11}$$

The solved output current (3.10) and the output voltage (3.11) can be used to express the output impedance:

$$Z_{\mathrm{o}}\left(\left|\bar{i}_{\mathrm{o}}\right|,j\omega\right)=-\frac{v_{\mathrm{o}}\left(\bar{v}_{\mathrm{o}},\omega\right)}{i_{\mathrm{o}}\left(\bar{i}_{\mathrm{o}},\omega\right)} \tag{3.12}$$

The model is compared to simulation results of the output impedance measurement under no-load conditions where the synchronous-frequency inductor current consists of only 0.54 A reactive current charging the capacitor. Under these conditions, $R^{\mathrm{dead}}$ and $R^{\mathrm{sat}}$ are 1.30 A and 2.73 A, respectively. The used perturbation amplitudes are 0.5 A, 1 A and 3 A. The simulated and modeled inductor current and the voltage error are shown in Figs. 3.8a and 3.8b, respectively. The model matches the simulation adequately at a wide frequency range. With the perturbation amplitudes of 0.5 A and 1 A, the region where the dead zone changes to the slope is not modeled especially accurately, which is also visible in Fig. 3.6a. In the case of 3 A perturbation amplitude, the model satisfactorily approximates the voltage error. The simulation results deviate the most from the model between 200 Hz and 300 Hz. However, this is probably because the third harmonic of the square-wave-like voltage error is not negligible, and the third harmonic is amplified by the resonance peaking at 795 Hz. The describing function model is based on the assumption that higher harmonics than the fundamental are filtered out in the system [84, 86, 87].

Fig. 3.9 shows the simulated and modeled output impedance with different perturbation amplitudes. The model clearly catches the nonlinear amplitude dependent damping that can be explained with $R^{\mathrm{dead}}$ and $R^{\mathrm{sat}}$. With the perturbation amplitudes of 0.5 A and 1 A, the voltage error is zero at low frequencies because the current amplitude is below $R^{\mathrm{dead}}$, as shown in Fig. 3.8a. At $R^{\mathrm{dead}}$, the error begins to appear. The current amplitude

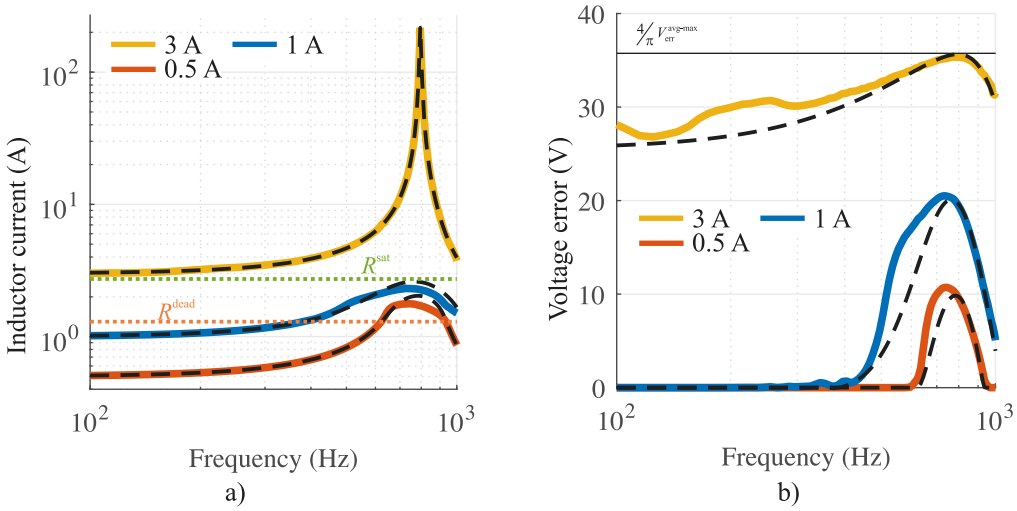


Figure 3.8: Simulated (solid line) and modeled (dashed line) (a) inductor current amplitude and (b) voltage error amplitude with different perturbation amplitudes at ($f_{\text{pert}} = 625$ Hz).

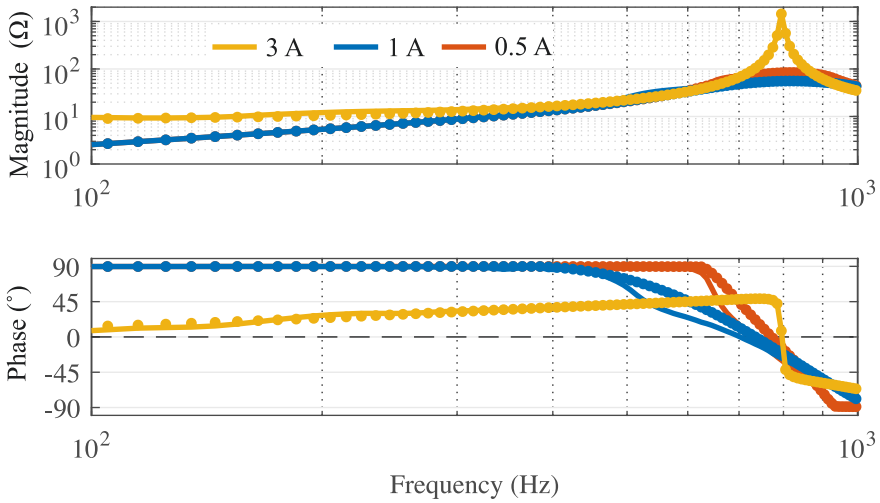


Figure 3.9: Simulated (lines) and modeled (dots) output impedance in the no-load condition (0.54 A capacities current) with perturbation amplitudes of 3 A, 1 A, and 0.5 A.

never reaches the beginning of saturation region $R^{\text{sat}}$. Therefore, with the perturbation amplitudes of 0.5 A and 1 A there is visible damping in the output impedance in Fig. 3.9.

With the perturbation amplitude of 3 A the error appears immediately when the perturbation is injected, as shown in 3.8b; the injection amplitude is higher than $R^{\text{dead}}$ even without amplification from the system dynamics. This is visible as damping at low frequencies in Fig. 3.9. The injection amplitude is also even higher than $R^{\text{sat}}$, which means that error is in the saturation region. Fig. 3.8b shows that the error saturates

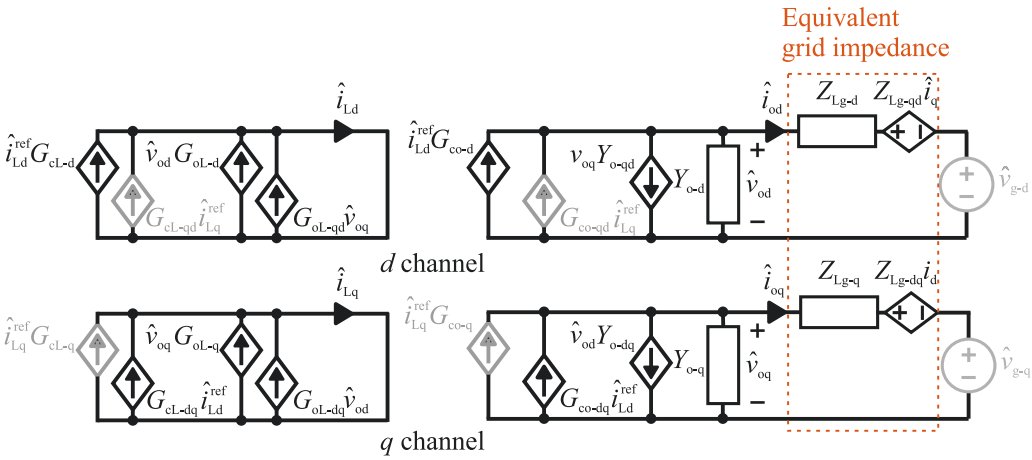


Figure 3.10: Inductor-current dynamics and output dynamics of the grid-connected inverter.

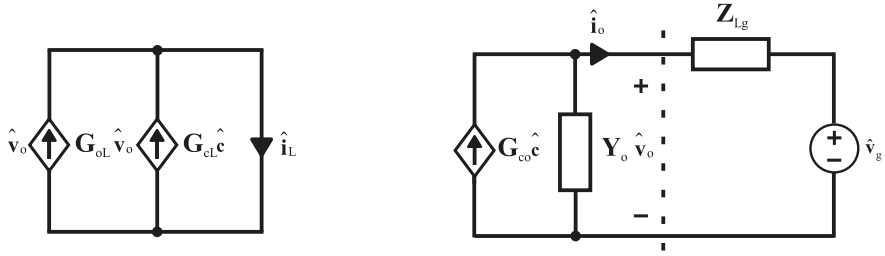

Figure 3.11: Inductor-current dynamics and output dynamics of the grid-connected inverter with equivalent matrix elements.

around the resonance, therefore, the error does not hinder the current from increasing. Hence, the resonance is not visibly damped in Fig. 3.9.

## 3.2 DQ-Frame Impedance Measurement in Presence of Impedance Coupling

This section begins by analyzing the impedance coupling in the DQ frame with a load-affected model. Characteristics of uncorrelated pseudorandom-binary sequences are then looked into. Finally, a measurement procedure that utilizes uncorrelated pseudo-random binary sequences in tackling the impedance coupling is proposed.

### Load Effect on the Injection Path

It was shown in Chapter 2.2 that erroneous impedance measurement results were obtained on a wide frequency range even though the three-phase inverter used in the measurement

was feedback-controlled. Fig. 3.10 shows the equivalent-circuit model of the control-to-inductor current and the control-to-output current dynamics of the grid-connected converter. Due to the complex interaction of the output-admittance elements and the grid-impedance elements ($Z_{\mathrm{Lg}}$), a significant cross-coupling between the d and q channels can occur regardless of the feedback control. A load-affected model can be used to analyze the cause for this behavior [P1]. Therefore, the load effect is revised for the grid-feeding inverter in order to analyze the load effect on the cross-coupling in the synchronous reference frame. The load-affected model of the grid-feeding inverter has been analyzed in [62, 83, 89, 90].

Load-affected models have been widely used to analyze the effect of different dynamic loads on converter dynamics [62, 83, 91]. Typically, the converter model is first developed for a voltage-output converter with a current sink load and for a current-output converter with a stiff voltage-source at the output [62, 83, 91]. Then the effect of the load dynamics is computed using the model for the impedance-based interaction. The capabilities of the load-affect model for modeling the loop gain of a grid-forming inverter under different dynamic loads is demonstrated in [P4].

Fig. 3.11 shows the equivalent inductor-current dynamics and the output dynamics of the grid-feeding inverter with transfers matrices. The grid dynamics are modeled by $\mathbf{Z}_{\mathrm{Lg}}$, and $\hat{\mathbf{v}}_{\mathrm{g}}$ denotes the small-signal stiff grid voltages. The equivalent grid impedance ($\mathbf{Z}_{\mathrm{Lg}}$) can consist, for example, of an RL-circuit that models a resistive-inductive medium-voltage distribution grid or a more complex meshed circuit of active and passive impedances. The duty ratio ($\hat{\mathbf{d}}$) is replaced by a general control variable ($\hat{\mathbf{c}}$) that can be the inductor current reference or the input voltage reference when analyzing the system with feedback loops closed.

The load-affect control-to-inductor current dynamics are derived as follows. When the controller variable ($\hat{\mathbf{c}}$) is perturbed, a response is caused to the converter-side inductor current ($\hat{\mathbf{i}}_{\mathrm{L}}$) according to $\mathbf{G}_{\mathrm{cL}}$. Additionally, a response is visible in the output current ($\hat{\mathbf{i}}_{\mathrm{o}}$) that is modeled by $\mathbf{G}_{\mathrm{co}}$ in the unterminated case. However, in the presence of non-zero grid impedance, the output voltage ($\hat{\mathbf{v}}_{\mathrm{o}}$) is not stiff. The output current affects the output voltage through the impedance interaction $\mathbf{Z}_{\mathrm{Lg}}(\mathbf{I}+\mathbf{Y}_{\mathrm{o}}\mathbf{Z}_{\mathrm{g}})^{-1}$. The inductor current is affected by the output voltage through $\mathbf{G}_{\mathrm{oL}}$. The load-affected inductor current dynamics can be given as

$$\mathbf{G}_{\mathrm{cL}}^{\mathrm{L}} = \mathbf{G}_{\mathrm{cL}} + \mathbf{G}_{\mathrm{oL}}\mathbf{Z}_{\mathrm{Lg}}(\mathbf{I}+\mathbf{Y}_{\mathrm{o}}\mathbf{Z}_{\mathrm{Lg}})^{-1}\mathbf{G}_{\mathrm{co}} \tag{3.13}$$

where superscript ´L' denotes that the transfer matrix is load-affected.

The grid-connected inverter is analyzed with the parameters given in Table 2.2. Fig. 3.12a shows the unterminated closed-loop control-to-inductor current d and dq transfer functions. It can be seen that the inductor current d component reference causes only a weak response in the current q component. However, when the grid inductance of

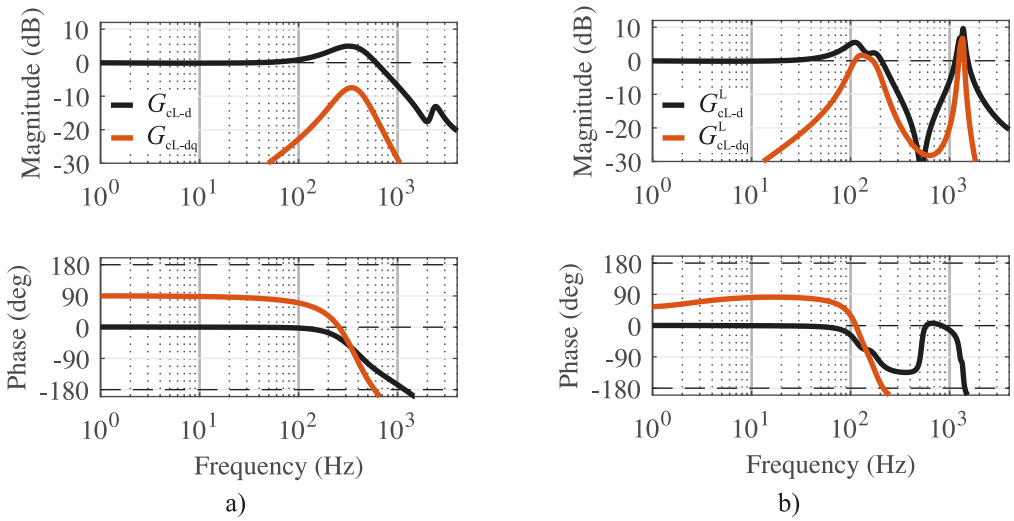


Figure 3.12: Bode plot of the current reference-to-inductor current transfer function d and dq components in the (a) unterminated and (b) the load-affected case.

8.83 mH ($\mathbf{Z}_{\mathrm{Lg}}$) is introduced, the dynamics change substantially, as shown in Fig. 3.12b. The magnitude of the dq component transfer function is significantly amplified. Both d and dq components have a drop in the gain at around 500 Hz, and the transfer functions have approximately the same gain at a wide frequency range. Clearly, the response in $\hat{i}_{\mathrm{Lq}}$ caused by $\hat{i}^{\mathrm{ref}}_{\mathrm{Ld}}$ can no longer assumed to be small, either absolutely or in comparison to the response in $\hat{i}_{\mathrm{Ld}}$. With aid of a scalar equivalent dynamic circuit, further analysis of the system is provided in [P1]. The present analysis shows that the impedance coupling affects the measurement regardless of the current-feedback-controlled inverter that is connected in series with the measured impedance. The impedance coupling in a similar system was analyzed in [30, 55]; however, the perturbations were injected by an external device, the dynamics of which were not modeled, that was connected parallel to the grid-connected inverter. In the following, a measurement procedure that is rapid and tackles the impedance coupling is developed.

### Orthogonal Pseudo-Random Binary Sequences

Pseudorandom-binary sequences (PRBSs) are two-level broadband signals that are periodic and predetermined [53]. The PRBS has the lowest possible peak factor, which makes it suitable for systems whose operation may not be disturbed excessively [92]. The PRBS has been widely used in rapid wide-band frequency-domain analysis of power electronic systems [92, 93].

One class of the PRBS is the maximum-length binary sequence (MLBS). The MLBS has become very popular because the signal can be easily generated using simple shift-register circuit [53, P1]. An $n$-stage feedback register can be used to generate a binary

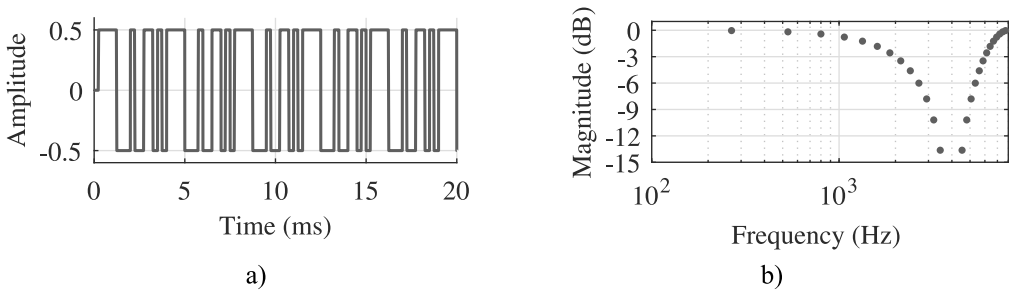


Figure 3.13: (a) 20 ms sample of the repeating MLBS ($n = 4$) in the time domain and (b) the MLBS magnitude in the frequency domain.

sequence whose length is N, given as

$$N = 2^n - 1 \tag{3.14}$$

With a generation frequency of $f_{\text{gen}}$, the lowest frequency that has energy is $f_{\text{gen}}/N$, and the frequencies that have energy are:

$$f_k^{\text{MLBS}} = k\frac{f_{\text{gen}}}{N}, k = 1, 2, 3...N \tag{3.15}$$

where $k$ denotes the sequence number of the spectral line and $f_{\text{gen}}$ is the highest frequency considered.

Fig. 3.13a shows a sample of the MLBS in the time domain. The length of the feedback register is 4 and the sequence generation frequency is 4 kHz. Fig. 3.13b shows the amplitude spectrum. The energy of the MLBS drops to zero at the signal generation frequency.

In DC–DC and single-phase converter systems, the output impedance is modeled as the ratio of a single output (voltage) and a single input (current). However, in three-phase systems modeled in the synchronous reference frame, there are impedance elements related to both d and q channels and the cross-couplings between the channels. Hence, in the DQ frame, the impedance is defined as a combination of multiple inputs and multiple outputs; there are up to four transfer functions to be measured. The traditional technique to measure the DQ-frame impedance element requires sequential injection into both d and q channels [31], which can be implemented with the maximum-length binary sequence. However, the sequential measurements can compromise the measurement accuracy because the system is prone to disturbances during the injections. Therefore, the capability to measure multiple transfer functions simultaneously is desired.

A system with multiple coupled inputs and multiple outputs can be measured in a short time by applying orthogonal binary sequences [27, 54, 92]. Because the orthogonal sequences have energy at different frequencies, they can be injected simultaneously to

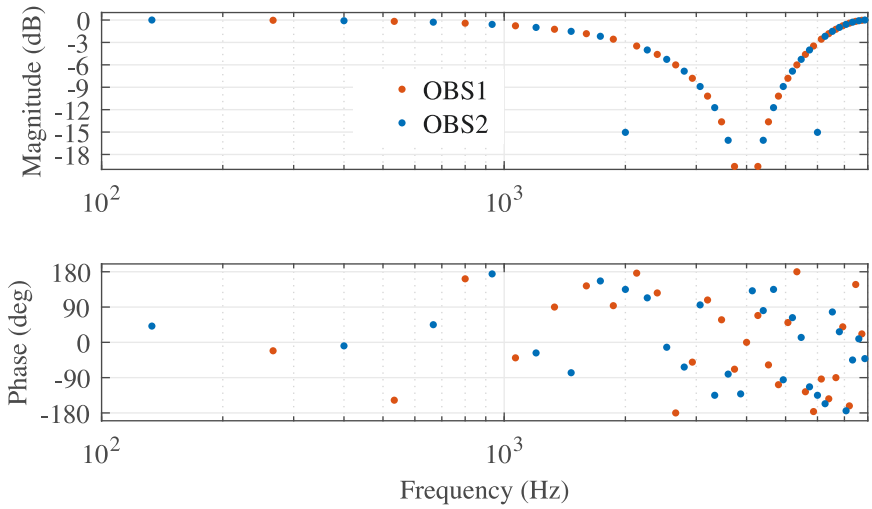


Figure 3.14: OBS1 ($n = 4$) and OBS2 in frequency domain.

different inputs of the system, and several frequency responses can be measured at the same time within one measurement cycle. This approach is a viable alternative to applying sequential perturbations because the frequency responses are measured under the same system operating conditions, which may not be the case if sequential perturbations are applied.

Uncorrelated pseudo-random binary sequences can be generated with the Hadamard-matrix modulation [54]. When two orthogonal sequences are created, the MLBS can be considered as the first orthogonal sequence (OBS1), and the second orthogonal sequence (OBS2) can be generated by modulating OBS1 by the second Hadamard matrix. This corresponds to combining the maximum-length binary sequence (OBS1) twice, one after the other, and inverting every second bit [94]. The length of the resulting OBS2 is $2N$ if the length of the original sequence is $N$. The frequencies where OBS2 has energy are:

$$f_k^{\mathrm{OBS2}} = (2k-1)\frac{f_{\mathrm{gen}}}{2N}, k = 1, 2, 3...N \tag{3.16}$$

Fig. 3.14 shows the amplitude spectrum and the phase of two orthogonal binary sequences (OBS1 and OBS2). The first sequence is obtained by using a four-bit-length shift register and the second sequence by the Hadamard modulation. Both sequences have been generated at 4 kHz. According to (3.15) and (3.16), the energy of OBS1 falls exactly in between the frequencies of OBS2; therefore, OBS2 and OBS1 are uncorrelated. Thus, OBS1 and OBS2 can be simultaneously injected into different inputs of a linear multiple-input system. Therefore, multiple transfer functions can be measured simultaneously from a multiple-input and multiple-output system under the same operating conditions [27, 93].

### Transfer-Function Interpolation

OBS1 and OBS2 have energy at different frequencies and can be injected independently of each other into a linear system. Therefore, the orthogonal sequences can be used to simultaneously measure the four synchronous-reference frame impedance elements. However, the measurements related to both sequences are affected by the impedance coupling similarly to the single-injection measurement [30, 55, P1]. Nevertheless, due to the deterministic nature of the sequences, frequency domain data can be easily interpolated from the frequencies of OBS2 to the frequencies of OBS1 or vice versa, and two independent sets of measurements can be obtained at the same frequencies [P1]. The traditional method [31] to overcome the impedance coupling can be used with the obtained data.

As shown in Fig. 3.14, the magnitudes of OBS1 and OBS2 are approximately constant over a wide frequency range. However, the phases have a pseudo-random behavior. The jumps in the phase are not suitable for interpolation, which is discussed in [P1]. Therefore, the responses in the voltages and currents ($I_{\mathrm{Ld2}}^{\mathrm{OBS2}}$, $V_{\mathrm{d2}}^{\mathrm{OBS2}}$, $I_{\mathrm{Lq2}}^{\mathrm{OBS2}}$, and $V_{\mathrm{q2}}^{\mathrm{OBS2}}$) are first divided by the injected spectrum:

$$\begin{bmatrix} G_{\mathrm{cL\text{-}qd}}^{\mathrm{OBS2}} \\ G_{\mathrm{cv\text{-}qd}}^{\mathrm{OBS2}} \\ G_{\mathrm{cL\text{-}q}}^{\mathrm{OBS2}} \\ G_{\mathrm{cv\text{-}q}}^{\mathrm{OBS2}} \end{bmatrix} = \begin{bmatrix} I_{\mathrm{Ld2}}^{\mathrm{OBS2}} \\ V_{\mathrm{d2}}^{\mathrm{OBS2}} \\ I_{\mathrm{Lq2}}^{\mathrm{OBS2}} \\ V_{\mathrm{q2}}^{\mathrm{OBS2}} \end{bmatrix} \frac{1}{I_{\mathrm{Lq2}}^{\mathrm{ref\text{-}OBS2}}} \tag{3.17}$$

The results are the control-to-inductor current ($G_{\mathrm{cL\text{-}qd}}^{\mathrm{OBS2}}$ and $G_{\mathrm{cL\text{-}q}}^{\mathrm{OBS2}}$) and control-to-output voltage-related transfer function components ($G_{\mathrm{cv\text{-}qd}}^{\mathrm{OBS2}}$ and $G_{\mathrm{cv\text{-}q}}^{\mathrm{OBS2}}$) at the OBS2 frequencies. The transfer functions no longer have the pseudorandom behavior in the phase and they can be interpolated to the OBS1 frequencies [P1]. The deterministic nature of the sequences is advantageous in the interpolation because the energy of OBS1 is exactly between the frequencies of OBS2. Therefore, the interpolation is a straightforward arithmetic mean [P1]:

$$G^{\text{TF-intrpl-}k} = \frac{G^{\text{f-OBS2-}k} + G^{\text{f-OBS2-}k+1}}{2}, \tag{3.18}$$

where $G^{\text{TF-intrpl-}k}$ and $G^{\text{f-OBS2-}k}$ denote the $k$:th frequency of OBS1 (resulting from the interpolation) and OBS2, respectively. The interpolation results can be used to replace $V_{\mathrm{d2}}$, $V_{\mathrm{q2}}$, $I_{\mathrm{Ld2}}$, and $I_{\mathrm{Lq2}}$ in (2.41), resulting in

$$\begin{aligned} &\begin{bmatrix} Z_{\mathrm{d}}^{\mathrm{TF\text{-}intrpl}} & Z_{\mathrm{qd}}^{\mathrm{TF\text{-}intrpl}} \\ Z_{\mathrm{dq}}^{\mathrm{TF\text{-}intrpl}} & Z_{\mathrm{q}}^{\mathrm{TF\text{-}intrpl}} \end{bmatrix} \\ &= \begin{bmatrix} V_{\mathrm{d1}} & G_{\mathrm{cv\text{-}qd}}^{\mathrm{TF\text{-}intrpl}} \\ V_{\mathrm{q1}} & G_{\mathrm{cv\text{-}q}}^{\mathrm{TF\text{-}intrpl}} \end{bmatrix} \begin{bmatrix} I_{\mathrm{Ld1}} & G_{\mathrm{co\text{-}qd}}^{\mathrm{TF\text{-}intrpl}} \\ I_{\mathrm{Lq1}} & G_{\mathrm{co\text{-}q}}^{\mathrm{TF\text{-}intrpl}} \end{bmatrix}^{-1} \end{aligned} \tag{3.19}$$

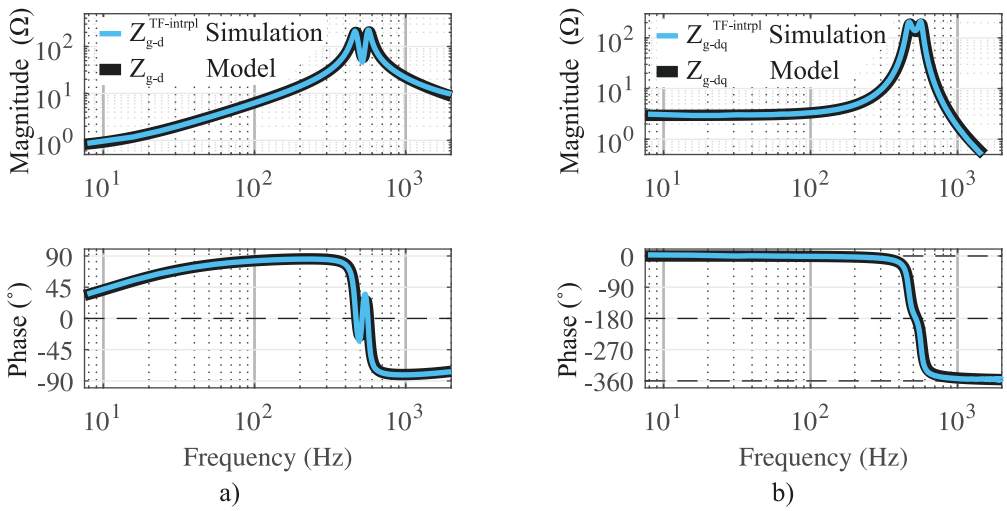


Figure 3.15: Models and simulation results with the proposed transfer function interpolation method of the grid impedance (a) d component and (b) dq component.

where the superscript 'TF-intrpl' denotes that the elements are resulting from the proposed method [P1].

A Matlab Simulink Simscape simulation is used to test the proposed technique. The used system parameters are given in Table 2.2. The lengths of the applied OBS1 and OBS2 were 511 and 1022 bits, respectively, and OBS1 and OBS2 were injected for 160 cycles and 80 cycles, respectively. Fig. 3.15 compares the d and dq components of the grid-impedance elements obtained with the proposed method to the grid-impedance model. The impedance coupling is clearly tackled. Furthermore, the proposed method utilizes the advantageous averaging capabilities of the simultaneously-injected orthogonal pseudo-random binary sequences that are demonstrated in [P1].

Chapter 4

# Implementation and Verification

This chapter presents the experimental verification of the proposed models and methods. The chapter is divided into three sections. The first section introduces the used experimental setups. In the second section, the describing-function model for the nonlinear deadtime effect is verified. The third section presents the experimental implementation of the novel synchronous-reference-frame impedance measurement technique. The experiments can be summarized as follows:

**Experiment set 1:**

The first experiment set verifies the proposed describing function model for the deadtime effect under low load conditions. In the experiment set, the output impedance of a single-phase grid-connected inverter is measured by perturbing the output voltage with a grid emulator.

**Experiment set 2:**

The second experiment set verifies the proposed synchronous-reference impedance measurement method. First, the method is implemented with a three-phase inverter and the grid-impedance is measured. Then, the output admittance of a grid-connected PV inverter is measured by perturbing the PCC voltages with a grid emulator.

## 4.1 Experimental Setups

Two different experimental setups are applied. Experimental Setup 1 consists of a single-phase inverter that is connected to a grid-emulator and is used to study the deadtime effect. The single-phase inverter is implemented with both MOSFETs and IGBTs. In Experimental Setup 2, both a DC voltage source and a PV panel emulator are used to feed a three-phase inverter that is connected to a grid emulator. The setup is used to implement the proposed synchronous-reference frame impedance measurement technique.

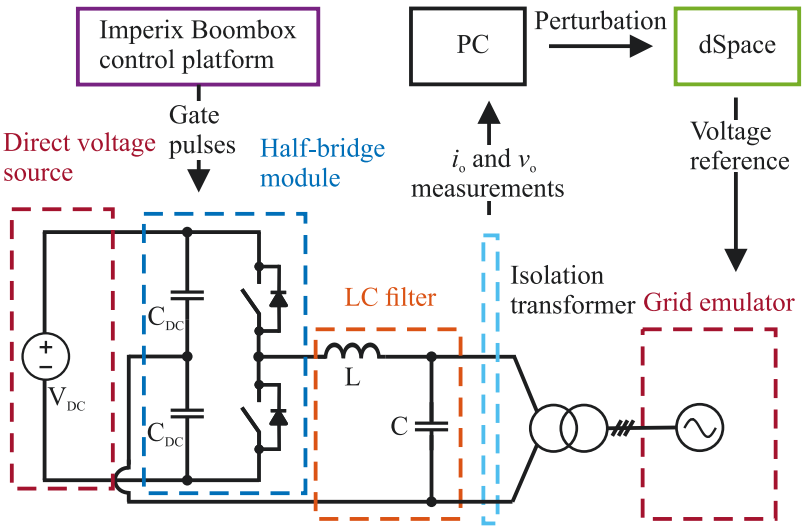


Figure 4.1: Diagram of the laboratory setup for the half-bridge inverter.

### Experimental Setup 1

Fig. 4.1 shows a diagram of the experimental setup that includes a single-phase inverter, a DC voltage source, an isolation transformer, and a grid-emulator. The converter topology is the half-bridge inverter that is implemented with Imperix half-bridge power module PEB 8024 (MOSFET) and alternatively with PEB 8032 (IGBT). The switches are controlled with an Imperix Boombox rapid control prototyping system.

The direct and alternating voltage sources used are a Spitzenberger & Spies PV Simulator PVS 7000 and a Spitzenberger & Spies Three-Phase Mains Simulation System DM 15000/PAS, respectively. A 380V/380V transformer is used for isolation. The synchronous-frequency voltage reference for the grid-emulator is created by a dSpace

Table 4.1: System parameter values of the single-phase inverter.

| Parameter | Symbol | Value | Parameter | Symbol | Value |
|---|---|---|---|---|---|
| Input voltage | $V_{\mathrm{DC}}$ | 700 V | Grid voltage rms | $V_{\mathrm{g}}$ | 120 V |
| Synchronous frequency | $\omega_{\mathrm{s}}$ | $2\pi 60$ rad/s | Switching frequency | $f_{\mathrm{sw}}$ | 10 kHz |
| Filter capacitor capacitance | $C$ | 10 $\mu$F | Filter inductance | $L$ | 1.2 mH |
| $C$ ESR and damping resistor | $r_{\mathrm{C}}$ | 0.1 $\Omega$ | $L$ ESR | $r_{\mathrm{L}}$ | 0.13 $\Omega$ |
| DC capacitor capacitance | $C_{\mathrm{DC}}$ | 470 $\mu$F | $C_{\mathrm{DC}}$ ESR | $r_{\mathrm{C\text{-}DC}}$ | 0.246 $\Omega$ |
| PLL P gain | $K_{\mathrm{p\text{-}pll}}$ | 0.03 | PLL I gain | $K_{\mathrm{i\text{-}pll}}$ | 10.5 |
| Deadtime | $T_{\mathrm{dead}}$ | 4 $\mu$s | | | |

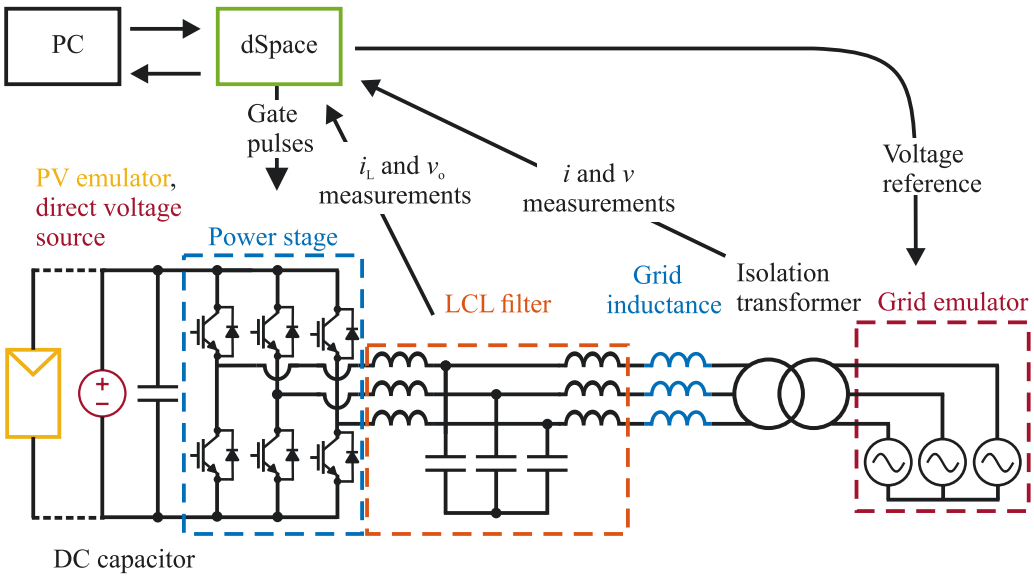


Figure 4.2: Diagram of the laboratory setup for the grid-connected three-phase inverter.

real-time simulator. A PC is used to generate a sinusoidal perturbation that is summed to the emulator voltage reference. The output voltage and the inductor current are recorded with a measurement card (NI USB-3636) that is used with the PC. The system parameters are given in Table 4.1, and a picture of the setup is shown in [P2].

### Experimental Setup 2

Fig. 4.2 shows a diagram of the three-phase grid-connected inverter. The power stage is a Myway PlusMWINV-9R144 that has six IGBTs. The filtering is accomplished by an LCL filter. The output of the inverter is connected to the Spitzenberger & Spies Three-Phase Mains Simulation System DM 15000/PAS over the additional inductance that emulates a grid inductance and a 380V/380V isolation transformer. A dSpace real-time simulator controls the inverter and produces the references for the grid emulator. The Spitzenberger & Spies PV Simulator PVS 7000 is used as the DC voltage source. A measurement card (NI USB-3636) is used with the PC to record data.

The setup is also used to measure the converter output admittance by injecting perturbations with the grid emulator. When the converter output admittance is measured with the grid emulator, a PV emulator, Spitzenberger & Spies Photovoltaic Simulator PVS 7000/BS, is used as the DC source, and the grid inductance and the isolation transformer switch places with each other due to the phase shift over the isolation transformer, which could add unnecessary complication to measurements. The system parameters are given in Table 2.2, and the controller parameters used with the PV inverter are given in Table 4.2. When the output admittance of the PV inverter is measured, an additional measurement

Table 4.2: Controller parameters of the experimental PV inverter.

| Parameter | Symbol | Value | Parameter | Symbol | Value |
|---|---|---|---|---|---|
| Current controller P gain | $K_{\text{p-c}}$ | 0.0149 | PLL P gain | $K_{\text{p-pll}}$ | 0.7760 |
| Current controller I gain | $K_{\text{i-c}}$ | 23.4 | PLL I gain | $K_{\text{i-pll}}$ | 39.52 |
| DC-voltage controller P gain | $K_{\text{p-v}}$ | -0.0962 | Measurement PLL P gain | $K_{\text{p-pll}}^{\text{meas.}}$ | 0.0120 |
| DC-voltage controller I gain | $K_{\text{i-v}}$ | -1.209 | Measurement PLL I gain | $K_{\text{i-pll}}^{\text{meas.}}$ | 0.0144 |

PLL is used to synchronize the measurement to the voltages at the grid emulator-side of the isolation transformer.

## 4.2 Experiment Set 1: Deadtime Effect

The deadtime causes a voltage error as a function of the inductor current, and the voltage error is visible as damping in frequency-domain measurements [P2, P3]. The error behaves nonlinearly, especially under low load conditions, and the deadtime effect on an undamped resonance was studied with simulations in Section 3.1. However, in the simulations, the measurement perturbation was injected by an ideal current sink that is not practically available. In Experimental Setup 1, a voltage injection is used, and the measured frequency range focuses on the anti-resonance that is caused by the parallel connection of the DC capacitors where the impedance is low. The parallel resonance of the output LC filter is at 1.45 kHz.

The half-bridge inverter shown in Fig. 4.1 is run under low load conditions in the open loop. The converter is connected to the grid emulator that provides the grid voltage at the synchronous frequency ($\omega_{\text{s}}$). A low-bandwidth phase-locked-loop is used to synchronize the controller to the voltage over the filter capacitor ($C$). To perform an impedance measurement requires perturbing the output voltage at a desired frequency, in addition to the fundamental frequency; a sinusoidal perturbation is summed to the emulator voltage reference.

For the sake of simplicity, the capacitor branch is not considered part of the converter output impedance. The output voltage and the inductor current are measured and Fourier-transformed, and the output impedance ($Z_{\text{o}}$) is computed at the perturbation frequency as the ratio of the output voltage and the inductor current as:

$$Z_{\text{o}} = -\frac{V_{\text{o}}(\omega)}{I_{\text{L}}(\omega)} \tag{4.1}$$

In the experimental validation of the describing function model, it must be taken into

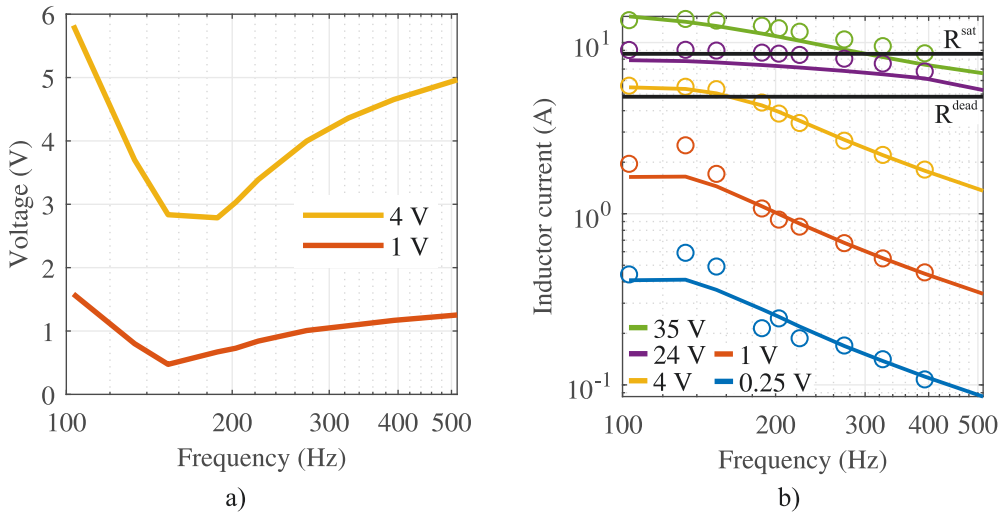


Figure 4.3: (a) Output voltage with the nominal voltage injection amplitudes of 1 V and 4 V. (b) Experimental (lines) and modeled (dots) inductor current amplitude with different perturbation amplitudes.

account that the voltage perturbation is injected by the grid emulator behind the isolation transformer as shown in Fig. 4.1, not directly at the converter output. Fig. 4.3a shows the output voltage amplitude at the perturbation frequency with nominal perturbation amplitudes of 4 V and 1 V when the converter is built with MOSFETs, and the inductor current amplitude at the synchronous frequency is 1.3 A when no perturbations are injected. The converter output voltage is clearly not the ideal injection at the grid emulator. In order to verify the proposed model properly, the measured output voltage that varies slightly over the frequencies is used as the input to the model, not a constant voltage amplitude. Nevertheless, the injections are referred to by their nominal amplitudes.

With the voltage injection $(v_\mathrm{o}\left(\bar{v}_\mathrm{o},\omega\right))$ as the input and the output impedance definition without the capacitor branch, the nonlinear equation for the sinusoidal steady state reduces to

$$\left|N\left(\left|i_\mathrm{L}\left(\bar{i}_\mathrm{L},\omega\right)\right|\right)+Z_\mathrm{L}\left(j\omega\right)\right| i_\mathrm{L}\left(\bar{i}_\mathrm{L},\omega\right)+\left|v_\mathrm{o}\left(\bar{v}_\mathrm{o},\omega\right)\right|=0 \tag{4.2}$$

which is solved numerically for the inductor current amplitude $(i_\mathrm{L}\left(\bar{i}_\mathrm{L},\omega\right))$. The parameters of the describing function model are given in Table 4.3. Fig. 4.3b compares the measured and the modeled inductor current amplitudes. The model accurately represents the inductor current amplitude. With perturbation amplitudes of 0.25 V and 1 V, the current amplitudes are below $R^\mathrm{dead}$, which indicates that there is no error from the deadtime effect. However, the modeled current is higher than the measured current at around 130 Hz. A reasonable explanation for this may be that voltage drop over the MOSFETs

and the anti-parallel diodes, which is not taken into account in the model, adds damping to the system.

The solved inductor current satisfies (4.2) only for the amplitude. The output voltage must be resolved for the correct phase difference between the current and the voltage. The solution for the output impedance reduces to

$$Z_{\mathrm{o}}\left(\left|\bar{v}_{\mathrm{o}}\right|, j\omega\right) = N\left(\left|i_{\mathrm{L}}\left(\bar{i}_{\mathrm{L}}, \omega\right)\right|\right) + Z_{\mathrm{L}}\left(j\omega\right) \tag{4.3}$$

Fig. 4.4 shows the modeled output impedance and the result of the experimental output impedance measurements from the half-bridge inverter that is built with the MOSFETs. The proposed model clearly catches the nonlinear deadtime effect. With the lowest perturbation amplitudes, the anti-resonance is visible. The damping becomes visible with the perturbation amplitude of 4 V because the current is higher than $R^{\mathrm{dead}}$ in the sinusoidal steady state, as shown in Fig. 4.3b. With the perturbation amplitude of 24 V, there is a considerable amount of damping. At the low frequencies, there is less damping with the perturbation amplitude of 35 V than with 24 V. This indicates that the error is in the saturation region with the highest perturbation amplitude. This is also visible in Fig. 4.3b, where the current amplitude is clearly above $R^{\mathrm{sat}}$ with a perturbation amplitude of 35 V.

Fig. 4.5 shows the modeled output impedance and the result of the output impedance measurements with the inverter implemented with the IGBTs. The inductor current amplitude at the synchronous frequency is 1.4 A when no perturbations are injected. $R^{\mathrm{dead}}$ and $R^{\mathrm{sat}}$ are 4.7 A and 8.7 A, respectively. The other parameters are the same as given for the MOSFET-inverter experiment in Table 4.3. The measured output voltage is used as the input to the describing function model. The similar behavior as a function of the perturbation amplitude as with the MOSFETs can be seen. However, with the lowest perturbation amplitudes, the model does not match the measurement. This is expected given that IGBTs have a constant voltage drop term in the collector-emitter voltage drop, which causes a voltage error even with low current amplitudes. In [P2],

Table 4.3: Parameters of the describing function model for the MOSFET-inverter experiment.

| **Parameter** | **Symbol** | **Value** | **Parameter** | **Symbol** | **Value** |
|---|---|---|---|---|---|
| Half the peak-to-peak inductor current ripple | $\Delta i_{\mathrm{p\text{-}p}}/2$ | 7.3 A | Maximum current change during the deadtime | $\Delta i_{\mathrm{dead}}$ | 1.2 A |
| End of dead zone current limit | $R^{\mathrm{dead}}$ | 4.8 A | Saturation region current limit | $R^{\mathrm{sat}}$ | 8.6 A |
| Maximum average voltage error | $V_{\mathrm{err}}^{\mathrm{max}}$ | 28 V | | | |

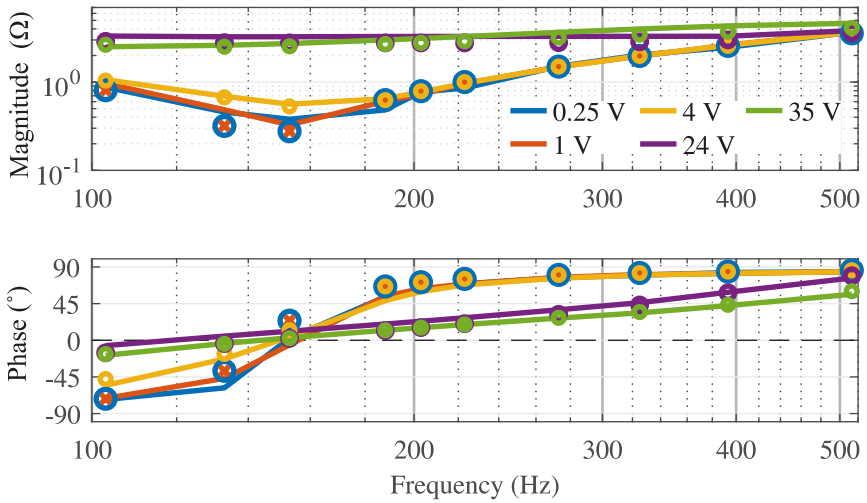


Figure 4.4: Experimental output impedance with MOSFETs (lines) and modeled output impedance (dots and crosses) under low load condition (1.3 A synchronous-frequency current) with different voltage perturbation amplitudes.

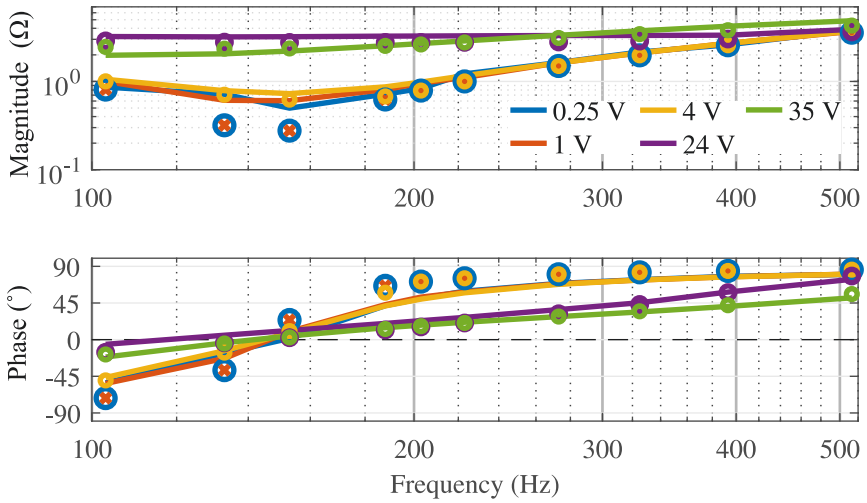


Figure 4.5: Experimental output impedance with IGBTs (lines) and modeled output impedance (dots and crosses) under low load condition (1.4 A synchronous-frequency current) with different voltage perturbation amplitudes.

the experimental results with the MOSFETS and the IGBTs are compared to hardware-in-the-loop real-time simulations where ideal switch models are used. The findings are similar; the ideal-switch simulation results correspond accurately to the experimental measurements with the MOSFETs and are less accurate with the IGBT experimental results [P2].

The evidence from this experiment set implies that the deadtime effect under low load

conditions can be modeled with the describing function of the dead zone, the linear region, and the saturation. For a more detailed analysis, the voltage drops over the semiconductor switches have to be modeled. Nevertheless, the purpose of these experiments was to verify the describing function model and the behavior of the deadtime effect in a practical system. The highest perturbation amplitudes of 24 V and 35 V, which were used to demonstrate the saturation region, are unlikely to be used to in a practical measurement. However, the saturation can occur with more moderate injection amplitudes in current-injection-based measurements, which were only simulated in Section 3.1 due to limitations in the experiment setup.

## 4.3 Experiment Set 2: Synchronous-Reference-Frame Impedance Measurements

The synchronous-reference-frame equivalent impedance of a balanced three-phase system consists of four elements related to the d and the q channels and the cross-couplings between the channels. When the equivalent impedance is measured by injecting a perturbation into the d or the q channel currents or voltages, the perturbation can also appear in the other channel due to the impedance coupling between the measurement device and the measured impedance [P1]. Experimental measurements are used to show how the interaction can cause erroneous results, and the proposed technique is shown to tackle the impedance coupling similarly to the traditional technique. First, a grid-impedance is measured with a grid-connected inverter, then, the output admittance of a PV inverter is measured by injecting the perturbations with a grid emulator.

### Grid-Impedance Measurement

Experimental Setup 2, shown in Fig. 4.2, is used to study a grid connected inverter that is connected to a stiff grid over an inductive grid impedance ($\mathbf{Z}_{\mathrm{Lg}}$). The converter is fed from a DC voltage source, and the feedback control is from the converter-side inductor current. A grid impedance measurement is performed by perturbing the converter side inductor current by injecting PRBSs into the current references, and the impedance components are computed from the measured converter-side inductor current and the output voltage over the filter capacitor [P1]. Hence, the filter capacitor impedance is included to the measured grid impedance ($\mathbf{Z}_{\mathrm{g}}$).

Orthogonal binary sequences OBS1 and OBS2 are injected into the d current reference and the q current reference of the inverter, respectively. The OBS1 is a maximum-length binary sequence whose length is 511 bits, and the length of the OBS2, which is generated by the Hadamard modulation, is 1022 bits. The amplitude of the injections is 0.5 A. In order to avoid spectral leakage of the 50 Hz component DFT, the OBS1 and OBS2 are injected for 160 cycles and 80 cycles, respectively [95].

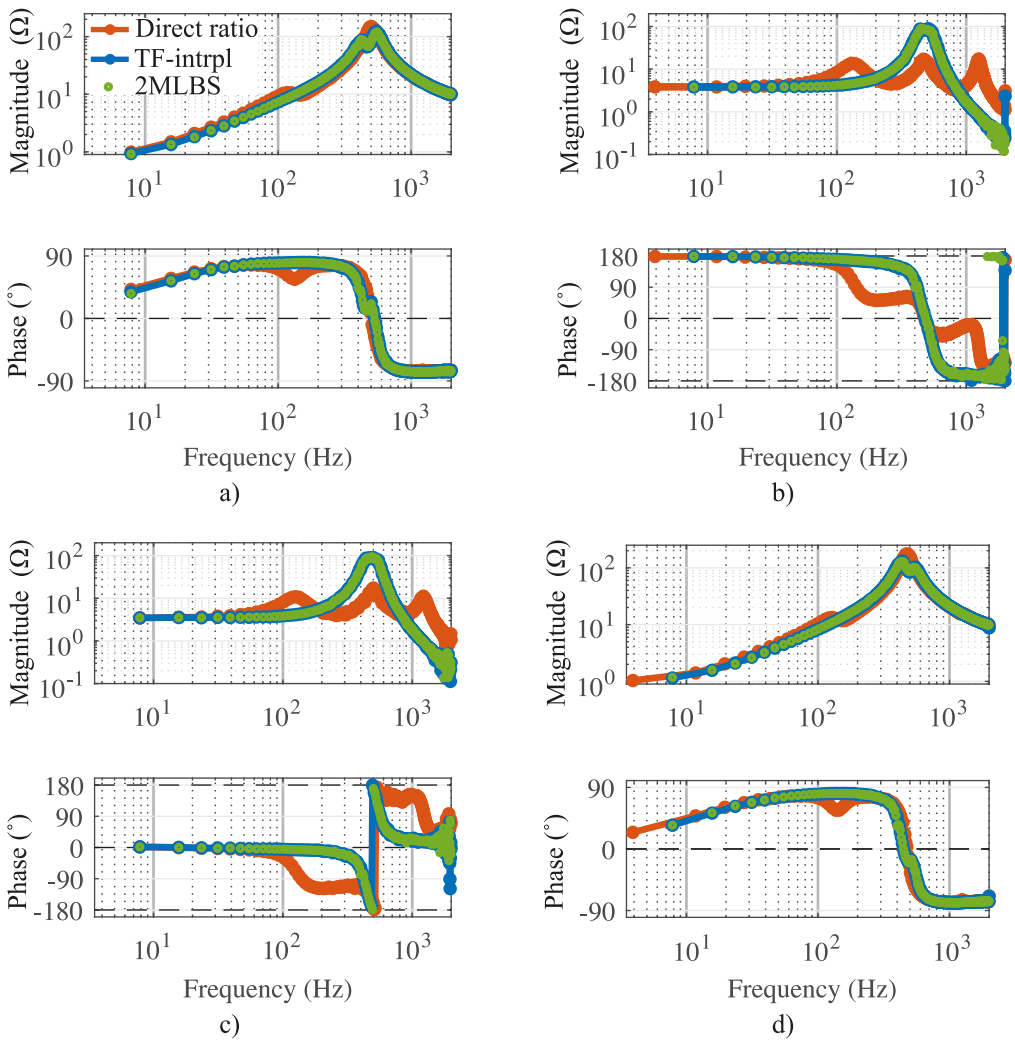


Figure 4.6: Experimental grid impedance (a) d component, (b) qd component, (c) dq component, and (d) q component with different measurement methods.

First, the impedance elements are calculated based on the direct ratios of the voltage and the current corresponding to each element:

$$Z_{\text{g-d}}^{\text{vd/id}} = \frac{V_{\text{od}}(j\omega)}{I_{\text{Ld}}(j\omega)},\ Z_{\text{g-dq}}^{\text{vq/id}} = \frac{V_{\text{oq}}(j\omega)}{I_{\text{Ld}}(j\omega)},\ Z_{\text{g-qd}}^{\text{vd/iq}} = \frac{V_{\text{od}}(j\omega)}{I_{\text{Lq}}(j\omega)},\ Z_{\text{g-q}}^{\text{vq/iq}} = \frac{V_{\text{oq}}(j\omega)}{I_{\text{Lq}}(j\omega)} \tag{4.4}$$

The results $Z_{\text{g-d}}^{\text{vd/id}}$ and $Z_{\text{g-dq}}^{\text{vq/id}}$ are measured at the OBS1 frequencies and the results $Z_{\text{g-qd}}^{\text{vd/iq}}$ and $Z_{\text{g-q}}^{\text{vq/iq}}$ are measured at the OBS2 frequencies. It is convenient to perform the measurement this way, and the *direct ratio* results are shown in Fig. 4.6. However, it is known that impedance coupling can occur in this type of measurement [P1].

The impedance measurement is performed with the technique based on two sequential

independent injections. First, the OBS1 is injected into the d channel current reference. Then, after the first injection, the OBS1 is injected into the q channel current reference. The voltage and the current data obtained from the injections is Fourier-transformed and the impedance elements are computed as

$$\begin{bmatrix} Z_{\text{g-d}}^{\text{2MLBS}} & Z_{\text{g-qd}}^{\text{2MLBS}} \\ Z_{\text{g-dq}}^{\text{2MLBS}} & Z_{\text{g-q}}^{\text{2MLBS}} \end{bmatrix} = \begin{bmatrix} V_{\text{d1}} & V_{\text{od2}} \\ V_{\text{q1}} & V_{\text{oq2}} \end{bmatrix} \begin{bmatrix} I_{\text{Ld1}} & I_{\text{Ld2}} \\ I_{\text{Lq1}} & I_{\text{Lq2}} \end{bmatrix}^{-1} \tag{4.5}$$

where the superscript ´2MLBS' denotes that the results are based on the two sequential injections. The technique gives a clearly different result than the direct-ratio method, as shown in Fig. 4.6. The result corresponds to the dq-frame equivalent of a parallel LC circuit; the resonance has two peaks in the d and the q components, and there are no other additional resonances [P1].

The proposed measurement technique based on the simultaneous injection of the OBS1 and OBS2 is implemented next. After the injection of the sequences, the measured inductor currents and the output voltages are Fourier-transformed. The responses at the OBS2 frequencies ($I_{\text{d2}}^{\text{OBS2}}$, $V_{\text{d2}}^{\text{OBS2}}$, $I_{\text{q2}}^{\text{OBS2}}$, and $V_{\text{q2}}^{\text{OBS2}}$) are divided by the injected spectrum (OBS2) and interpolated to the frequencies of the OBS1 in order to apply (4.5). Fig. 4.6 shows that the impedance coupling is avoided similarly to the existing method (2MLBS), but without the requirement of sequential injections [P1].

### PV Inverter Output Admittance Measurement

The output admittance of the grid-connected PV inverter of Experimental Setup 2 is measured by perturbing the output voltages with the grid emulator. The PV inverter has a DC voltage control cascaded with the d channel current control and a low-bandwidth phase-locked loop, both of which are visible in the output admittance at low frequencies.

The OBS1 and the OBS2 are summed to the d and the q voltage references of the grid emulator, respectively. The transfer functions for the interpolation are calculated with respect to the q-voltage reference ($V_{\text{q2}}^{\text{ref}}$). The amplitudes of the injected OBS1 and OBS2 are 10 V. The OBS1 is obtained by a 10-bit-length shift register, yielding a frequency resolution of 3.9 Hz.

The transfer functions from $V_{\text{q2}}^{\text{ref}}$ to $I_{\text{d2}}$, $V_{\text{d2}}$, $I_{\text{q2}}$, and $V_{\text{q2}}$,which are the interpolated intermediate results of the proposed method, are denoted by $G_1$, $G_2$, $G_3$, and $G_4$, respectively. The transfer functions and the measurements at the OBS1 frequencies ($I_{\text{d1}}$, $V_{\text{d1}}$, $I_{\text{q1}}$, and $V_{\text{q1}}$) are used to solve the output admittance elements [P1]:

$$\begin{bmatrix} Y_{\text{o-d}}^{\text{TF-intrpl}} & Y_{\text{o-qd}}^{\text{TF-intrpl}} \\ Y_{\text{o-dq}}^{\text{TF-intrpl}} & Y_{\text{o-q}}^{\text{TF-intrpl}} \end{bmatrix} = \begin{bmatrix} I_{\text{d1}} & G_1 \\ I_{\text{q1}} & G_3 \end{bmatrix} \begin{bmatrix} V_{\text{d1}} & G_2 \\ V_{\text{q1}} & G_4 \end{bmatrix}^{-1} \tag{4.6}$$

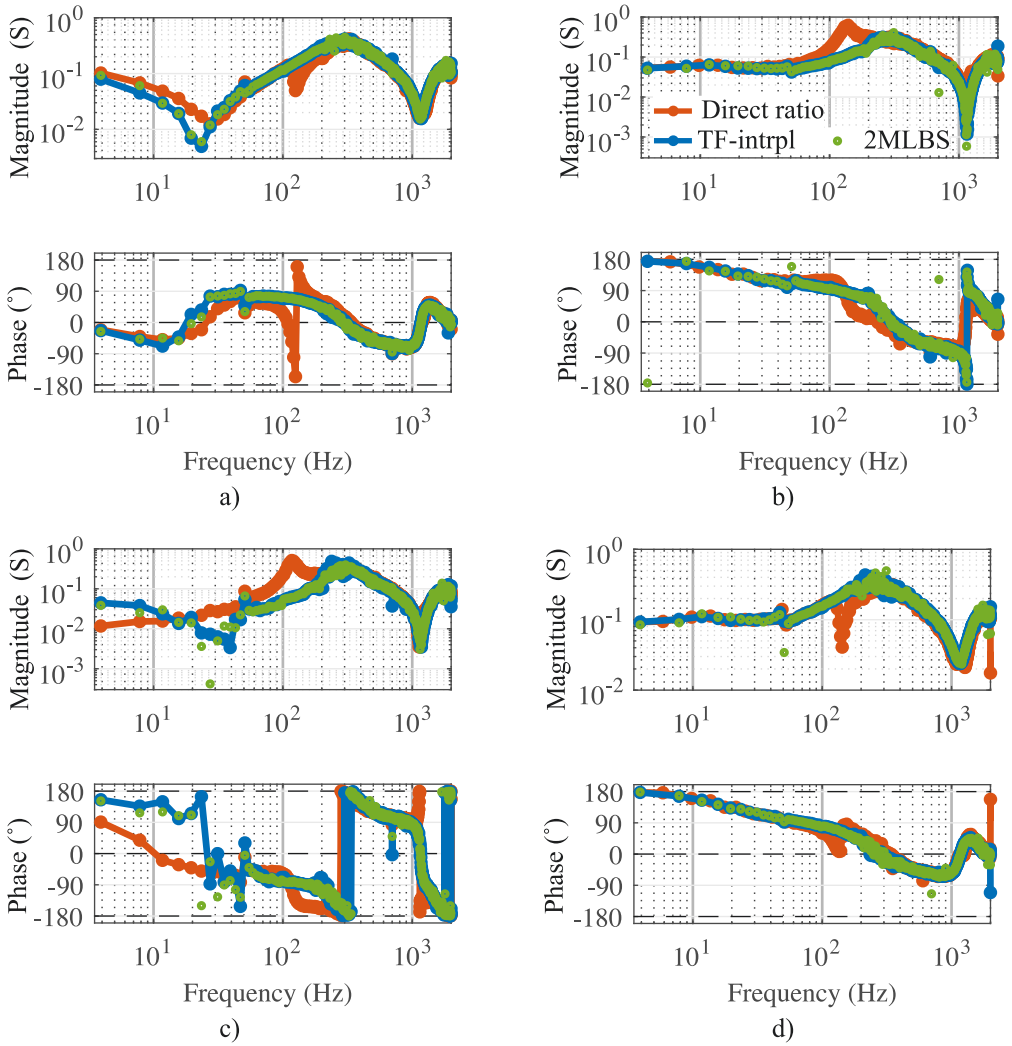


Figure 4.7: Experimental PV inverter output admittance (a) d component, (b) qd component, (c) dq component, and (d) q component with different measurement methods.

Fig. 4.7 shows the output admittance measured with the different methods. The proposed transfer-function interpolation method tackles the impedance coupling that is visible in the direct-ratio-method results [P1]. The low-frequency resonance, which is caused by the direct voltage controller, in $Y_{\text{o-d}}$ is caught by the proposed method as accurately as with the traditional sequential method (2MLBS). The negative incremental resistance region caused by the PLL is visible in $Y_{\text{o-q}}$. Between 200 Hz and 700 Hz, the measurements by all methods are slightly noisy. This is because the voltage is perturbed by the grid emulator, and the additional grid impedance and the output admittance of the inverter act as a voltage divider, which leads to a low voltage perturbation amplitude at the inverter output that is prone to noise [P1].

Chapter 5

# Conclusions

The next decade is likely to witness a considerable rise in the electrical energy generation from renewable sources, the exploitation of which is essential for slowing down climate change. Renewable power generators are commonly interfaced by power-electronic converters to the distribution grid. However, the grid-connected converters can interact detrimentally with each other and the grid, which can lead to harmonic resonances and compromise the stability of the electric power distribution system. Therefore, possible detrimental interactions should be considered in the design phase of the converters.

Improved controller design of grid-connected converters through the use of a measured grid impedance has received much attention recently. Real-time measurement methods that can be performed in a short time by injecting orthogonal sequences to different inputs of the multiple-input multiple-output three-phase system have been proposed. The methods based on orthogonal sequences enable simultaneous measurement of the synchronous-reference frame impedance elements. The shortcoming of this approach has been clearly recognized; the injected sequences can leak between the synchronous-reference-frame channels unintentionally due to an impedance coupling of the equivalent system impedances.

This thesis has proposed a novel impedance measurement procedure that tackles the coupling of the synchronous-reference-frame equivalent system impedances affecting the measurement. In the proposed method, two orthogonal sequences are used to simultaneously perturb the system. The deterministic nature of the used orthogonal sequences is taken advantage of, and an interpolation from the frequencies of the second orthogonal sequences to the first orthogonal sequence is done on measured and Fourier-transformed currents and voltages in order to obtain two independent sets of measurements at the same frequencies. As a result, the impedance elements can be solved from a group of equations without relying on sequentially performed measurements that have been required to tackle the impedance coupling in existing non-parametric methods.

Another issue affecting the dynamics of a grid-connected inverter is the voltage error caused by the deadtime effect. This thesis has shown that the deadtime effect can change

the inverter dynamics substantially under low-load conditions. Through analytical models and experiments, the thesis has shown that the inverter output impedance becomes significantly nonlinear under low-load conditions due to the deadtime effect, and a linearization is no longer correct modeling method. The proposed model for the nonlinear deadtime effect is based on the describing function method.

The analysis on the nonlinear deadtime effect and the developed synchronous-reference frame measurement method can be summarized as follows.

- The nonlinear deadtime effect is characterized in the frequency domain. Under low load conditions, the deadtime effect can be modeled with a describing function of a dead zone, a slope, and a saturation region. The inductor current amplitude limits for the dead zone and the saturation are developed based on the inductor current ripple, the direct voltage, the deadtime length, and the synchronous-frequency current amplitude. The developed describing-function-method model for the nonlinear deadtime effect makes it possible to solve the sinusoidal steady state of an inverter with a deadtime.

- The impedance coupling is characterized to occur with a feedback-controlled grid-connected converter-performed grid-impedance measurement. A measurement method that is based on perturbing the three-phase converter system with two orthogonal sequences is developed. Due to the simultaneous injection of the sequences, the novel method provides more efficient averaging capability compared to the traditional measurement technique, which is based on sequentially performed injections.

The proposed nonlinear deadtime effect model and synchronous-reference frame measurement technique were verified by experimental measurements. The results showed that the describing-function model catches the nonlinear current-amplitude-dependent damping. The synchronous-reference-frame measurement method was shown to yield equivalent results with an existing method, both in the measurement of the grid impedance and the PV inverter output admittance.

## Discussion and Criticism

The proposed model for the nonlinear deadtime effect is based on the describing function method, which is a powerful tool for the analysis of a system with a nonlinearity. However, there are several potential sources for error in the application of the describing function method for the deadtime effect.

The describing function is an approximate method, and it relies on the assumption that the system has low-pass characteristics so that only the fundamental-frequency component of the modeled waveform is significant. Inevitably, some inaccuracies occurred

in the application of the describing function method to the analyzed system containing an undamped resonance that amplified higher harmonics of the voltage error.

The peak-to-peak current ripple is an important parameter in modeling of the dead zone and the saturation of the amplitude dependent deadtime effect. However, the ripple was approximated by a rough estimate at the zero crossing of the synchronous-frequency inductor current with a unity power factor. Furthermore, the capacitor voltage ripple that affects the inductor current ripple was assumed to be zero. These approximations especially affect the transitions from the dead zone to the slope and from the slope to the saturation.

The deadtime effect was modeled to occur when the amplitude of the perturbation amplitude exceeds the derived limit for the dead zone and begins to saturate when the limit for the saturation is reached. However, the voltage error model is not dynamic and does not take into account the likelihood of such events occurring. It is plausible that, with a high perturbation frequency, the amplitude-dependent zero crossing is more likely to occur, and the appearance of the error is over-estimated at low perturbation frequencies. Furthermore, with a low perturbation frequency, close to the synchronous frequency, the phase difference between the synchronous-frequency component and the perturbation can have a significant effect on the error. The error was inspected only at perturbation frequencies that were at least one and a half times higher than the synchronous frequency. Despite the limitations of this method, the findings suggest that the proposed model is accurate enough to model the significant damping caused by the nonlinear effect.

Regarding the proposed synchronous-reference-frame measurement method that tackles the impedance coupling, there are some drawbacks. The proposed measurement method requires information about the spectrum of the second injected orthogonal sequence that is used to divide the Fourier-transformed measurements related to the injection. Processing the injected spectrum, and the interpolation required, are more computationally demanding than the existing sequential-injections method, which does not require the division followed by the interpolation of the method.

In the proposed measurement method, the orthogonal sequences were injected with the same amplitude as the amplitude of a single injection in the sequential method, and the length of a whole measurement cycle is the same with both methods. Therefore, the injected harmonic content is higher in the proposed method than in the sequential method because two sequences were injected simultaneously.

## Future Research Topics

This research has raised many questions in need of further investigation. The modeling of the nonlinear deadtime effect focused mainly on the output impedance of an open-loop single-phase inverter. Further studies are needed to estimate the nonlinear deadtime effect in the presence of a feedback controller where analysis from control-to-output dynamics

point of view is essential. Research is also needed to develop synchronous-reference frame models for the nonlinear deadtime effect on three-phase converters. The describing function based modeling used in this research can become inefficient in modeling of a three-phase converter due to the system complexity; therefore, other modeling approaches are recommended to be looked into.

The design and development of fast and reliable online impedance measurement methods for three-phase systems will still be a challenge in the future. The proposed impedance measurement based on simultaneously-injected orthogonal sequences and interpolation can serve as a base for future studies. Future work should concentrate on investigating the measurement under different types of disturbances in order to further evaluate the benefits of the proposed method in comparison to the conventional measurement method. An important issue is the selection of perturbation amplitude for simultaneously injected orthogonal sequences. Therefore, future studies are recommended in order to establish whether the averaging from the proposed methods yields results that are as accurate as the traditional method based on sequential injections if the harmonic content of both methods is adjusted to be the same.

# References


[1] M. Pacifici, P. Visconti, S. H. M. Butchart, J. E. M. Watson, F. M. Cassola, and C. Rondinini, "Species' traits influenced their response to recent climate change," *Nat. Clim. Chang.*, vol. 7, pp. 205–208, 2017.

[2] B. Bose, "Global Warming: Energy, Environmental Pollution, and the Impact of Power Electronics," *IEEE Ind. Electron. Mag.*, vol. 4, pp. 6–17, 2010.

[3] "Paris Agreement," United Nations, 2015.

[4] Q. C. Zhong, *Power Electronics-Enabled Autonomous Power Systems: Next Generation Smart Grids*. Wiley - IEEE, Wiley, 2020.

[5] "Communication from the Comission, The European Green Deal," European Commission, Cambridge, 2019.

[6] "Renewable Energy Statistics," Eurostat, 2020.

[7] E. Romero-cadaval, G. Spagnuolo, and L. G. Franquelo, "Grid-Connected Photovoltaic Generation Plants," *IEEE Ind. Electron. Mag.*, vol. 7, no. September, pp. 6–20, 2013.

[8] F. Iov, M. Ciobotaru, D. Sera, R. Teodorescu, and F. Blaabjerg, "Power Electronics and Control of Renewable Energy Systems," in Proc. *7th Int. Conf. Power Electron. Drive Syst.*, pp. 6–28, 2007.

[9] S. N. Vukosavic, *Grid-Side Converters Control and Design: Interfacing Between the AC Grid and Renewable Power Sources*. Power Electronics and Power Systems, Springer International Publishing, 2018.

[10] Y. Hase, *Handbook of Power Systems Engineering with Power Electronics Applications*. Wiley, 2012.

[11] M. Ahmad, *Operation and Control of Renewable Energy Systems*. Wiley, 2017.

[12] W. Xiao, *Photovoltaic Power System: Modeling, Design, and Control*. Wiley, 2017.

[13] B. Kroposki, B. Johnson, Y. Zhang, V. Gevorgian, P. Denholm, B.-M. Hodge, and B. Hannegan, "Achieving a 100% Renewable Grid: Operating Electric Power Systems with Extremely High Levels of Variable Renewable Energy," *IEEE Power Energy Mag.*, vol. 15, pp. 61–73, 2017.

[14] R. Abe, H. Taoka, and D. McQuilkin, "Digital Grid: Communicative Electrical Grids of the Future," *IEEE Trans. Smart Grid*, vol. 2, pp. 399–410, 2011.

[15] J. Rocabert, A. Luna, F. Blaabjerg, and P. Rodríguez, "Control of Power Converters in AC Microgrids," *IEEE Trans. Power Electron.*, vol. 27, pp. 4734–4749, 2012.

[16] J. A. Suul, S. D'Arco, P. Rodríguez, and M. Molinas, "Impedance-compensated grid synchronisation for extending the stability range of weak grids with voltage source converters," *IET Gener. Transm. Distrib.*, vol. 10, pp. 1315–1326, 2016.

[17] B. Wen, D. Boroyevich, R. Burgos, P. Mattavelli, and Z. Shen, "Inverse Nyquist Stability Criterion for Grid-Tied Inverters," *IEEE Trans. Power Electron.*, vol. 32, pp. 1548–1556, 2017.

[18] B. Wen, D. Boroyevich, P. Mattavelli, Z. Shen, and R. Burgos, "Experimental verification of the Generalized Nyquist stability criterion for balanced three-phase ac systems in the presence of constant power loads," in Proc. *IEEE Energy Convers. Congr. Expo.*, no. 1, pp. 3926–3933, 2012.

[19] D. Yang and X. Wang, "Unified Modular State-Space Modeling of Grid-Connected Voltage-Source Converters," *IEEE Trans. Power Electron.*, vol. 35, pp. 9700–9715, 2020.

[20] E. Ebrahimzadeh, F. Blaabjerg, X. Wang, and C. L. Bak, "Bus Participation Factor Analysis for Harmonic Instability in Power Electronics Based Power Systems," *IEEE Trans. Power Electron.*, vol. 33, pp. 10341–10351, 2018.

[21] J. Matevosyan, V. Vital, J. O'Sullivan, R. Quint, B. Badrzadeh, T. Prevost, E. Quitmann, D. Ramasubramanian, H. Urdal, S. Achilles, J. MacDowell, and S. H. Huang, "Grid-Forming Inverters: Are They the Key for High Renewable Penetration?," *IEEE Power Energy Mag.*, vol. 17, pp. 89–98, 2019.

[22] J. Sun, "Impedance-Based Stability Criterion for Grid-Connected Inverters," *IEEE Trans. Power Electron.*, vol. 26, no. 11, pp. 3075 – 3078, 2011.

[23] B. Wen, D. Dong, D. Boroyevich, R. Burgos, P. Mattavelli, and Z. Shen, "Impedance-Based Analysis of Grid-Synchronization Stability for Three-Phase Paralleled Converters," *IEEE Trans. Power Electron.*, vol. 31, pp. 26–38, 2016.

[24] H. Alenius and T. Roinila, "Impedance-Based Stability Analysis of Paralleled Grid-Connected Rectifiers: Experimental Case Study in a Data Center," *Energies*, vol. 13, p. 1-15, 2020.

[25] L. Jessen, S. Gunter, F. W. Fuchs, M. Gottschalk, and H.-J. Hinrichs, "Measurement results and performance analysis of the grid impedance in different low voltage grids for a wide frequency band to support grid integration of renewables," in Proc. *IEEE Energy Convers. Congr. Expo.*, pp. 1960–1967, 2015.

[26] T. Roinila, T. Messo, and A. Aapro, "Impedance measurement of three phase systems in DQ-domain: Applying MIMO-identification techniques," in Proc. *2016 IEEE*

*Energy Convers. Congr. Expo.*, pp. 1–6, 2016.

[27] T. Roinila, T. Messo, and E. Santi, "MIMO-Identification Techniques for Rapid Impedance-Based Stability Assessment of Three-Phase Systems in DQ Domain," *IEEE Trans. Power Electron.*, vol. 33, pp. 4015–4022, 2018.

[28] R. Luhtala, T. Roinila, and T. Messo, "Implementation of Real-Time Impedance-Based Stability Assessment of Grid-Connected Systems Using MIMO-Identification Techniques," *IEEE Trans. Ind. Appl.*, vol. 54, pp. 5054–5063, 2018.

[29] R. Luhtala, "Real-Time Identification and Adaptive Control of Grid-Connected Three-Phase Inverters," Doctoral Thesis, Tampere University, 2020.

[30] H. Gong, X. Wang, and D. Yang, "DQ-Frame Impedance Measurement of Three-Phase Converters Using Time-Domain MIMO Parametric Identification," *IEEE Trans. Power Electron.*, vol. 36, pp. 2131–2142, 2021.

[31] G. Francis, R. Burgos, D. Boroyevich, F. Wang, and K. Karimi, "An algorithm and implementation system for measuring impedance in the D-Q domain," in Proc. *IEEE Energy Convers. Congr. Expo.*, pp. 3221–3228, 2011.

[32] R. D. Middlebrook and S. Cuk, "A general unified approach to modelling switching-converter power stages," in Proc. *IEEE Power Electron. Spec. Conf.*, vol. 21, pp. 18–34, 1976.

[33] J. Sun and K. J. Karimi, "Small-Signal Input Impedance Modeling of Multipulse Rectifiers," in *SAE Tech. Pap.*, vol. 44, 2008.

[34] D. Dong, B. Wen, D. Boroyevich, P. Mattavelli, and Y. Xue, "Analysis of Phase-Locked Loop Low-Frequency Stability in Three-Phase Grid-Connected Power Converters Considering Impedance Interactions," *IEEE Trans. Ind. Electron.*, vol. 62, pp. 310–321, 2015.

[35] R. Mastromauro, M. Liserre, and A. Dell'Aquila, "Study of the Effects of Inductor Nonlinear Behavior on the Performance of Current Controllers for Single-Phase PV Grid Converters," *IEEE Trans. Ind. Electron.*, vol. 55, pp. 2043–2052, 2008.

[36] Y. Xia, M. Yu, X. Wang, and W. Wei, "Describing Function Method Based Power Oscillation Analysis of LCL -Filtered Single-Stage PV Generators Connected to Weak Grid," *IEEE Trans. Power Electron.*, vol. 34, pp. 8724–8738, 2019.

[37] W. Wei, Y. Xia, and F. Blaabjerg, "Nonlinear Stability Analysis for Three-Phase Grid-Connected PV Generators," *IEEE J. Emerg. Sel. Top. Power Electron.*, vol. 8, pp. 3487–3501, 2020.

[38] Seung-Gi Jeong and Min-Ho Park, "The analysis and compensation of dead-time effects in PWM inverters," *IEEE Trans. Ind. Electron.*, vol. 38, pp. 108–114, 1991.

[39] E. dos Santos and E. R. da Silva, *Advanced Power Electronics Converters: PWM Converters Processing AC Voltages*. IEEE Press Series on Power Engineering, Wiley, 2014.

[40] I. Batarseh and A. Harb, *Power Electronics: Circuit Analysis and Design.* Springer International Publishing, 2018.

[41] Y. Yang, K. Zhou, H. Wang, and F. Blaabjerg, "Analysis and Mitigation of Dead-Time Harmonics in the Single-Phase Full-Bridge PWM Converter With Repetitive Controllers," *IEEE Trans. Ind. Appl.*, vol. 54, pp. 5343–5354, 2018.

[42] C. D. Townsend, G. Mirzaeva, and G. C. Goodwin, "Deadtime Compensation for Model Predictive Control of Power Inverters," *IEEE Trans. Power Electron.*, vol. 32, pp. 7325–7337, 2017.

[43] Nambo Hur, Kwanghee Nam, and Sangchul Won, "A two-degrees-of-freedom current control scheme for deadtime compensation," *IEEE Trans. Ind. Electron.*, vol. 47, pp. 557–564, 2000.

[44] S. Ahmed, Z. Shen, P. Mattavelli, D. Boroyevich, and K. J. Karimi, "Small-Signal Model of Voltage Source Inverter (VSI) and Voltage Source Converter (VSC) Considering the DeadTime Effect and Space Vector Modulation Types," *IEEE Trans. Power Electron.*, vol. 32, pp. 4145–4156, 2017.

[45] M. Zhang, D. Yang, and X. Wang, "Accurate Open-Loop Impedance Model of Single-Phase Voltage Source Inverter (VSI) Considering the Dead-Time Effects," in Proc. *20th Work. Control Model. Power Electron.*, no. 2, pp. 1–5, 2019.

[46] Y. Familiant, K. Corzine, J. Huang, and M. Belkhayat, "AC Impedance Measurement Techniques," in Proc. *IEEE Int. Conf. Electr. Mach. Drives, 2005.*, pp. 1850–1857, 2005.

[47] J. Huang, K. A. Corzine, and M. Belkhayat, "Small-Signal Impedance Measurement of Power-Electronics-Based AC Power Systems Using Line-to-Line Current Injection," *IEEE Trans. Power Electron.*, vol. 24, pp. 445–455, 2009.

[48] Z. Shen, M. Jaksic, B. Zhou, P. Mattavelli, D. Boroyevich, J. Verhulst, and M. Belkhayat, "Analysis of Phase Locked Loop (PLL) influence on DQ impedance measurement in three-phase AC systems," in *2013 Twenty-Eighth Annu. IEEE Appl. Power Electron. Conf. Expo.*, pp. 939–945, IEEE, 2013.

[49] M. Jaksic, Z. Shen, I. Cvetkovic, D. Boroyevich, R. Burgos, C. DImarino, and F. Chen, "Medium-Voltage Impedance Measurement Unit for Assessing the System Stability of Electric Ships," *IEEE Trans. Energy Convers.*, vol. 32, no. 2, pp. 829–841, 2017.

[50] A. Rygg and M. Molinas, "Apparent Impedance Analysis: A Small-Signal Method for Stability Analysis of Power Electronic-Based Systems," *IEEE J. Emerg. Sel. Top. Power Electron.*, vol. 5, pp. 1474–1486, 2017.

[51] H. Gong, D. Yang, and X. Wang, "Impact Analysis and Mitigation of Synchronization Dynamics for DQ Impedance Measurement," *IEEE Trans. Power Electron.*, vol. 34, pp. 8797–8807, 2019.

[52] V. Pirsto, J. Kukkola, M. Hinkkanen, and L. Harnefors, "Inter-Sample Modeling of the Converter Output Admittance," *IEEE Trans. Ind. Electron.*, Early Access, 2020.

[53] K. Godfrey, *Perturbation Signals for System Identification.* Englewood Cliffs, NJ, USA: Prentice-Hall, 1993.

[54] A. Tan and K. Godfrey, *Industrial Process Indentification.* Cham, Switzerland: Spirnger, 2019.

[55] H. Gong, D. Yang, and X. Wang, "Identification of the DQ Impedance Model for Three-Phase Power Converter Considering the Coupling Effect of the Grid Impedance," in Proc. *2019 IEEE Appl. Power Electron. Conf. Expo.*, vol. 2019-March, pp. 120–126, 2019.

[56] S. Cobreces, F. Huerta, D. Pizarro, F. J. Rodrguez, and E. J. Bueno, "Three-phase power system parametric identification based on complex-space recursive least squares," in Proc. *2007 IEEE Int. Symp. Intell. Signal Process.*, pp. 1-6, 2007.

[57] J. Kukkola, M. Routimo, and M. Hinkkanen, "Real-Time Grid Impedance Estimation Using a Converter," in Proc. *2019 IEEE Energy Convers. Congr. Expo.*, pp. 6005–6012, 2019.

[58] A. Vidal, A. G. Yepes, F. D. Freijedo, O. Lopez, J. Malvar, F. Baneira, and J. Doval-Gandoy, "A Method for Identification of the Equivalent Inductance and Resistance in the Plant Model of Current-Controlled Grid-Tied Converters," *IEEE Trans. Power Electron.*, vol. 30, pp. 7245–7261, 2015.

[59] J. Xie, Y. X. Feng, and N. Krap, "Network Impedance Measurements for Three-phase High-voltage Power Systems," in Proc. *Asia-Pacific Power Energy Eng. Conf.*, no. 3, pp. 1–5, 2010.

[60] M. Ciobotaru, R. Teodorescu, P. Rodriguez, A. Timbus, and F. Blaabjerg, "Online grid impedance estimation for single-phase grid-connected systems using PQ variations," in Proc. *IEEE Power Electron. Spec. Conf.*, no. 1, pp. 2306–2312, 2007.

[61] L. Harnefors, M. Bongiorno, and S. Lundberg, "Input-Admittance Calculation and Shaping for Controlled Voltage-Source Converters," *IEEE Trans. Ind. Electron.*, vol. 54, pp. 3323–3334, 2007.

[62] T. Suntio, T. Messo, and J. Puukko, *Power Electronic Converters: Dynamics and Control in Conventional and Renewable Energy Applications.* Weinheim: Wiley-VCH, 2017.

[63] J. Liu, L. Zhou, and M. Molinas, "Damping region extension for digitally controlled LCL-type grid-connected inverter with capacitor-current feedback," *IET Power Electron.*, vol. 11, pp. 1974–1982, 2018.

[64] Z. Shen, M. Jaksic, S. Ahmed, P. Mattavelli, and D. Boroyevich, "Parametric study of dead time effect on three phase AC output impedance of Voltage Source Inverter (VSI)," *Proc. 2011 14th Eur. Conf. Power Electron. Appl. EPE 2011*, pp. 1-8, 2011.

[65] A. Rodriguez-Cabero, M. Prodanovic, and J. Roldan-Perez, "Analysis of Dynamic Properties of VSCs Connected to Weak Grids Including the Effects of Dead Time and Time Delays," *IEEE Trans. Sustain. Energy*, vol. 10, pp. 1066–1075, 2019.

[66] W. Qiu, S. Mercer, Z. Liang, and G. Miller, "Driver Deadtime Control and Its Impact on System Stability of Synchronous Buck Voltage Regulator," *IEEE Trans. Power Electron.*, vol. 23, pp. 163–171, 2008.

[67] Z. Zhang, S. Tian, and K. D. T. Ngo, "Small-Signal Equivalent Circuit Model of Quasi-Square-Wave Flyback Converter," *IEEE Trans. Power Electron.*, vol. 32, pp. 5885–5888, 2017.

[68] S. Ahmed, Z. Shen, P. Mattavelli, D. Boroyevich, M. Jaksic, K. Karimi, and J. Fu, "Small-signal model of a voltage source inverter (VSI) considering the dead-time effect and space vector modulation types," in Proc. *Twenty-Sixth Annu. IEEE Appl. Power Electron. Conf. Expo.*, vol. 32, pp. 685–690, 2011.

[69] A. Guha and G. Narayanan, "Small-Signal Stability Analysis of an Open-Loop Induction Motor Drive Including the Effect of Inverter Deadtime," *IEEE Trans. Ind. Appl.*, vol. 52, pp. 242–253, 2016.

[70] A. Guha and G. Narayanan, "Impact of Dead Time on Inverter Input Current, DC-Link Dynamics, and Light-Load Instability in Rectifier-Inverter-Fed Induction Motor Drives," *IEEE Trans. Ind. Appl.*, vol. 54, pp. 1414–1424, 2018.

[71] X. Mao, R. Ayyanar, and A. K. Jain, "Dead time effect in two-level space vector PWM voltage source inverters with large current ripple," in Proc. *Twenty-Sixth Annu. IEEE Appl. Power Electron. Conf. Expo.*, pp. 679–684, 2011.

[72] D. G. Holmes and T. A. Lipo, *Pulse Width Modulation for Power Converters: Principles and Practice*. IEEE Press Series on Power Engineering, Wiley, 2003.

[73] R. W. Erickson and D. Maksimović, *Fundamentals of Power Electronics, 2nd Edition*. Springer International Publishing, 2001.

[74] S. Jayalath and M. Hanif, "Generalized LCL-Filter Design Algorithm for Grid-Connected Voltage-Source Inverter," *IEEE Trans. Ind. Electron.*, vol. 64, pp. 1905–1915, 2017.

[75] G. Lo Calzo, A. Lidozzi, L. Solero, and F. Crescimbini, "LC filter design for on-grid and off-grid distributed generating units," *IEEE Trans. Ind. Appl.*, vol. 51, pp. 1639–1650, 2015.

[76] A. Kouchaki and M. Nymand, "Analytical Design of Passive LCL Filter for Three-Phase Two-Level Power Factor Correction Rectifiers," *IEEE Trans. Power Electron.*, vol. 33, pp. 3012–3022, 2018.

[77] X. Ruan, X. Wang, D. Pan, D. Yang, W. Li, and C. Bao, *Control Techniques for LCL-Type Grid-Connected Inverters*. CPSS Power Electronics Series, Springer Singapore, 2018.

[78] A. Rothstein and V. Staudt, "Detailed analysis of converter-output-voltage errors under light-load conditions," in Proc. *2017 Int. Conf. Optim. Electr. Electron. Equip. 2017 Intl Aegean Conf. Electr. Mach. Power Electron.*, pp. 336–341, 2017.

[79] O. Wing, *Classical Circuit Theory*. Springer US, 2008.

[80] T. M. Rowan and R. J. Kerkman, "A New Synchronous Current Regulator and an Analysis of Current-Regulated PWM Inverters," *IEEE Trans. Ind. Appl.*, vol. IA-22, pp. 678–690, 1986.

[81] H. Akagi, E. H. Watanabe, and M. Aredes, *Instantaneous Power Theory and Applications to Power Conditioning*. IEEE Press Series on Power Engineering, Wiley, 2017.

[82] L. Nousiainen, J. Puukko, A. Mäki, T. Messo, J. Huusari, J. Jokipii, J. Viinamäki, D. T. Lobera, S. Valkealahti, and T. Suntio, "Photovoltaic Generator as an Input Source for Power Electronic Converters," *IEEE Trans. Power Electron.*, vol. 28, pp. 3028–3038, 2013.

[83] T. Suntio, T. Messo, M. Berg, H. Alenius, T. Reinikka, R. Luhtala, and K. Zenger, "Impedance-Based Interactions in Grid-Tied Three-Phase Inverters in Renewable Energy Applications," *Energies*, vol. 12, pp. 1-31, 2019.

[84] J. Tenreiro-Machado, A. M. Lopes, A. M. Galhano, and D. Valério, *Solved Problems in Dynamical Systems and Control*. Control, Robotics and Sensors, Institution of Engineering and Technology, 2016.

[85] Jian Li and F. C. Lee, "New Modeling Approach and Equivalent Circuit Representation for Current-Mode Control," *IEEE Trans. Power Electron.*, vol. 25, pp. 1218–1230, 2010.

[86] A. K. Mandal, *Introduction to Control Engineering: Modeling, Analysis and Design*. New Age International (P) Limited, 2006.

[87] K. J. Åström and R. M. Murray, *Feedback Systems: An Introduction for Scientists and Engineers, Second Edition*. Princeton University Press, electronic ed., 2020.

[88] H. K. Khalil, *Nonlinear Systems*. Pearson Education, Prentice Hall, 2002.

[89] R.-M. Sallinen, A. Aapro, M. Berg, and T. Messo, "Complete Small-Signal Model of Three-Phase Photovoltaic Inverter Considering the Source and Load Effects," in Proc. *IECON - 44th Annu. Conf. IEEE Ind. Electron. Soc.*, vol. 1, pp. 2237–2244, 2018.

[90] M. Berg, A. Aapro, R. Luhtala, and T. Messo, "Small-Signal Analysis of Photovoltaic Inverter With Impedance-Compensated Phase-Locked Loop in Weak Grid," *IEEE Trans. Energy Convers.*, vol. 35, pp. 347–355, 2020.

[91] T. Suntio, *Dynamic Profile of Switched-Mode Converter: Modeling, Analysis and Control*. Weinheim: Wiley-VCH, 2009.

[92] T. Roinila, J. Huusari, and M. Vilkko, "On Frequency-Response Measurements of Power-Electronic Systems Applying MIMO Identification Techniques," *IEEE Trans. Ind. Electron.*, vol. 60, pp. 5270–5276, 2013.

[93] T. Roinila, T. Messo, R. Luhtala, R. Scharrenberg, E. C. W. de Jong, A. Fabian, and Y. Sun, "Hardware-in-the-Loop Methods for Real-Time Frequency-Response Measurements of on-Board Power Distribution Systems," *IEEE Trans. Ind. Electron.*, vol. 66, pp. 5769–5777, 2019.

[94] R. Luhtala, T. Messo, T. Roinila, H. Alenius, E. de Jong, A. Burstein, and A. Fabian, "Identification of Three-Phase Grid Impedance in the Presence of Parallel Converters," *Energies*, vol. 12, pp. 1-15, 2019.

[95] R. Luhtala, H. Alenius, T. Messo, and T. Roinila, "Online Frequency Response Measurements of Grid-Connected Systems in Presence of Grid Harmonics and Unbalance," *IEEE Trans. Power Electron.*, vol. 35, pp. 3343–3347, 2020.

# Publications

# Publication I

**Rapid Multivariable Identification of Grid Impedance in DQ Domain Considering Impedance Coupling**

M. Berg, H. Alenius, and T. Roinila

*IEEE Journal of Emerging and Selected Topics in Power Electronics, Early Access, 2020.*

# Rapid Multivariable Identification of Grid Impedance in DQ Domain Considering Impedance Coupling

Matias Berg, *Student Member, IEEE,* Henrik Alenius, *Student Member, IEEE,* and Tomi Roinila, *Member, IEEE*

***Abstract*—Identifying grid-impedance at the point of common coupling is essential for the adaptive control and the online stability analysis of grid-connected converters. A balanced three-phase system is commonly modeled by d and q components in the synchronous reference frame. In identification of the synchronous reference-frame impedance components, errors may occur due to the coupling of the system impedances; for example, a measurement injection that is intended to perturb only the d-channel current may also perturb the q-channel current thus distorting the impedance measurements. Traditionally sequentially performed measurements, where different injections are performed one after another at same frequencies, have been required to tackle the impedance coupling. However, the sequential measurements are prone to changes in the operating conditions between the measurements. The present paper proposes a method to simultaneously obtain all the grid-impedance components within a single measurement cycle with no coupling effect. In the method, two orthogonal binary injections are simultaneously injected into the d and q current references of the inverter controller. Then, a frequency-domain interpolation technique is applied to adjust the measured current and voltage responses. As a result, the impedance coupling is avoided in the measured grid impedance. The proposed technique is validated by experimental measurements.**

***Index Terms*—frequency response, identification, three-phase VSI, grid-impedance, MIMO**

## I. Introduction

Replacing conventional energy sources with renewable sources has been recognized as an important tool for retarding climate change [1]. The remarkable feature of renewable energy sources is that they commonly need to be connected through power-electronic interfaces to the grid. Therefore, grid-connected three-phase converters are increasingly becoming a vital factor in the operation of distribution grids. However, the grid-connected converters are prone to adverse impedance-based interactions between the grid impedance and other converters, which disturbs the power quality and may even introduce stability issues [2]–[6]. In order to prevent the adverse interactions, information on the grid impedance is often required for improved control design or adaptive control.

Accurate identification of the grid impedance or the converter impedance generally requires an external injection to the system. The injection can be made by a grid-connected converter [7]–[9] or by a separate measurement device [10], [11]. The grid-impedance identification may rely on the assumption of the grid-impedance shape. The grid-impedance is occasionally assumed to be a series resistor-inductor (RL) circuit [12], [13]. In [13], the identification method was based on a step response, and while in [12] the method was based on a current injection at a single frequency. However, the grid-impedance may vary significantly from a series RL circuit [14]–[16]. Therefore, identification at a wide frequency range may be more advantageous, and it is required for an accurate multi-variable stability analysis, such as with the generalized Nyquist criterion [11], [17].

Recent studies have presented a number of wideband techniques to measure the grid impedance [7]–[9], [18], [19]. In such techniques the impedance is measured by injecting a broadband perturbation such as a pseudo-random binary sequence (PRBS), for example, into the inverter controller reference. The resulting grid voltages and currents are measured, and Fourier methods are applied to obtain the grid impedance. The PRBS exhibits multiple favorable characteristics for use in online impedance identification, such as periodic and deterministic nature, and the lowest possible peak factor [20].

In the synchronous-reference frame, a three-phase converter system is a multiple-input-multiple-output system and consists of direct (d) and quadrature (q) channels [10], [11] that must be identified for a proper analysis. Both channels can be identified simultaneously in a brief time by using orthogonal binary injections [7]–[9]. In practice, however, the d and q channels are cross-coupled. Due to the cross-coupling and the interaction between the system impedances, an impedance coupling occurs. The impedance coupling may cause an intended d-channel current injection to appear also in the current q channel. Therefore, for example the response in the voltage d component would not only be caused by the intended d-channel current but also by q-channel current. A thorough analysis of the impedance coupling was performed in [21].

It was reported in [21] that the orthogonal injections applied into dq-domain systems in [7]–[9], [22] can give erroneous results if the impedance coupling effect is overlooked. However, the authors in [21] made a hasty generalization regarding the issue of the orthogonal injections because a DC-DC converter system that has not been reported to have d and q channels was analyzed in [22]. To avoid the impedance-coupling effect, a time-domain parametric identification method was proposed in [21] where uncorrelated binary sequences were used to perturb the system. However, the presented uncorrelated broadband injections, whose design algorithms were not given, differ

This work was supported in part by Business Finland Project SolarX.

M. Berg*, H. Alenius, and T. Roinila are with the Faculty of Information Technology and Communication Sciences, Tampere University, Finland, *e-mail: matias.berg@tuni.fi.

greatly from the analytically derived uncorrelated sequences that have been used in the field of process identification in [23], [24]. The orthogonal-sequence-generation methods from [23], [24] have been applied in identification of power electronic systems in [7]–[9], [22] and are used in the present paper.

In tackling the impedance-coupling effect without parametric model, sequential independent injections have been proven to be an adequate method for obtaining the accurate multivariable impedance [10], [11], [25], [26]. By applying this method, the impedance-coupling effect can be taken into account in the calculation of impedance components. However, applying multiple sequential measurements relies on the assumption that the impedance does not change between the injections [10].

The present paper proposes a novel measurement procedure that utilizes orthogonal binary broadband injections in the elimination of impedance interactions. An orthogonal sequence is injected to the current reference d component, and a second orthogonal sequence is injected to the current reference q component. The result of the q-channel measurement is interpolated to the frequencies of the d-channel measurement. The result is used as an independent measurement. However, obtaining an accurate interpolation result is not straightforward due to the random phase behavior of the binary sequences; the results must be divided by the spectrum of the injected sequence before the interpolation. The original orthogonal binary sequence and the interpolation result are independent of each other, and can be used to accurately identify the grid impedance. As a result, the accurate multivariable impedance can be identified non-parametrically with simultaneous broadband excitations.

The remainder of this paper is structured as follows. Section II presents the system and the broadband injections. Section III describes the impedance coupling in the measurement and revises an existing method to obtain accurate results in the presence of the impedance coupling. The novel identification procedure is derived and simulated in Section IV. Experimental verification of the proposed technique is presented in Section V. Conclusions are drawn in the final section.

## II. Converter system and identification sequences

This section begins by introducing the parameters and the controller structure of the grid-connected converter. Then, characteristics and the generation of orthogonal broadband binary injections are revised.

### A. Grid-connected inverter

A block diagram of the system under study is shown in Fig. 1. The traditional synchronous-reference-frame phase-locked loop (PLL) is used to synchronize the rotating synchronous reference frame to the grid voltages at the point of common coupling [27]. The converter-side inductor currents are controlled with PI controllers. The perturbation signal, which is required for the grid impedance identification, is injected to the inductor current reference. The system and control parameters are given in Table I.

The diagram in Fig. 1 shows that the grid-impedance is identified from the output voltage ($\mathbf{v}$) and the output current ($\mathbf{i}$) measurements. Therefore, the filter capacitor ($C_\mathrm{f}$) is not included in the impedance that is identified. A small error in the traditional measurement arises from the current angle shift at the filter capacitor.

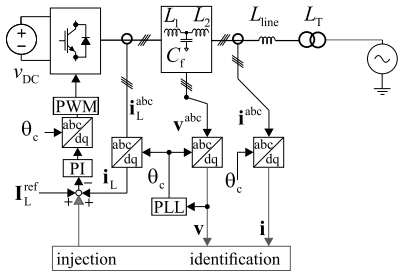


Figure 1: Block diagram of the grid-connected three-phase inverter and the control system.

### B. Orthogonal broadband binary injections

Pseudorandom binary sequences are broadband signals that can be used for fast frequency response measurements because multiple frequencies are injected simultaneously. One of the most common of such signals is the maximum-length binary sequence (MLBS), which has two levels and can be generated with low computational effort by using shift registers [23]. The sequence is periodic, with a length of $N = 2^n - 1$, where $n$ is the length of the shift register. [23]. The lowest frequency with energy is $f_\mathrm{gen}/N$, where $f_\mathrm{gen}$ is the generation frequency. When considering up to the $f_\mathrm{gen}$, the frequencies at which the MLBS has energy can be given as:

$$f_k^\mathrm{MLBS} = k\frac{f_\mathrm{gen}}{N}, k = 1, 2, 3...N \tag{1}$$

where $k$ denotes the sequence number of the spectral line.

An inverse repeat sequence (IRS) can be generated from the MLBS by applying the Hadamard modulation discussed in [23]. The IRS generated from a $N$-bit-long MLBS has a length of $2N$, and the IRS has energy at frequencies:

$$f_k^\mathrm{IRS} = (2k-1)\frac{f_\mathrm{gen}}{2N}, k = 1, 2, 3...N \tag{2}$$

The excited frequencies of the IRS fall exactly between the frequencies of the MLBS; therefore, the MLBS and the IRS are orthogonal. They can be used for simultaneous identification of multiple transfer functions from a multiple-input and multiple-output system [7], [28]. The advantage is that both measurements are done simultaneously under the same conditions [29].

Fig. 2a shows a sample to the MLBS and IRS time-domain waveforms and 2b shows the amplitude and the phase of the MLBS and IRS whose magnitude is scaled by 1.2 for illustrative purposes. The present paper uses $n = 9$ and, therefore, the lengths of the MLBS and the IRS are 511 bits and 1022 bits, respectively. The generation frequency $f_\mathrm{gen}$ is 4 kHz, and the amplitude of both sequences, $A_\mathrm{MLBS}$ and

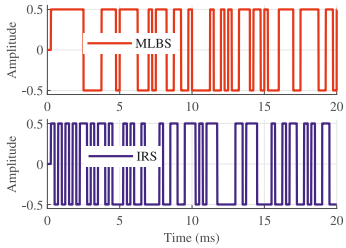


(a)

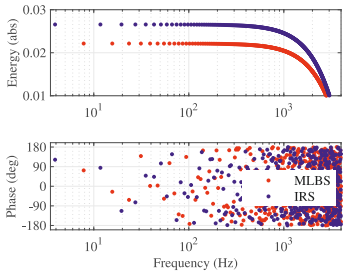


(b)

Figure 2: (a) Part of the MLBS and the IRS in time domain and (b) frequency-domain amplitude and phase of the used MLBS and IRS. The IRS is set to have larger amplitude for illustration.

$A_{\mathrm{IRS}}$, is 0.5. The energy of the MLBS drops to zero at $f_{\mathrm{gen}}$, and the practical measurement bandwidth is up to $0.45 f_{\mathrm{gen}}$ [9]. Fig. 3, where $\frac{1}{z}$ denotes the unit delay, shows how the sequences are generated with shift registers.

## III. Impedance Coupling in Measurements

This section begins by inspecting the equivalent small-signal model of the grid-connected converter to analyze the effect of the impedance coupling on the measurement injections. Then, an existing measurement procedure that is not affected by the impedance coupling is revised.

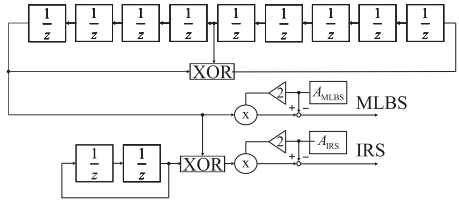


Figure 3: Block diagram of the MLBS and the IRS shift-register generation ($n$ = 9).

### A. Impedance-based interaction

Fig. 4 shows the equivalent small-signal circuit diagram of the grid-connected converter. The dynamic model of the converter has been derived in [30], but now the system is fed from a voltage source instead of photovoltaic panel. The inductor current reference, the output current, and the output voltage vectors are denoted by $\hat{\mathbf{i}}_{\mathrm{L}}^{\mathrm{ref}}$, $\hat{\mathbf{i}}$, and $\hat{\mathbf{v}}$, respectively. The perturbations in the grid-voltage $\hat{\mathbf{v}}_{\mathrm{g}}$ are assumed to be zero here because we are analyzing a perturbation caused by the inverter and identifying the grid-impedance. The transfer matrices $\mathbf{G}_{\mathrm{co}}$, $\mathbf{Y}$, and $\mathbf{Z}$ that denote the unterminated control-to-output dynamics, the inverter output admittance, and the grid impedance describe the relations between the variables:

$$\overbrace{\begin{bmatrix}\hat{i}_{\mathrm{d}}\\ \hat{i}_{\mathrm{q}}\end{bmatrix}}^{\hat{\mathbf{i}}} = \overbrace{\begin{bmatrix}G_{\mathrm{co-d}} & G_{\mathrm{co-qd}}\\ G_{\mathrm{co-dq}} & G_{\mathrm{co-q}}\end{bmatrix}}^{\mathbf{G}_{\mathrm{co}}} \overbrace{\begin{bmatrix}\hat{i}^{\mathrm{ref}}_{\mathrm{L-d}}\\ \hat{i}^{\mathrm{ref}}_{\mathrm{L-q}}\end{bmatrix}}^{\hat{\mathbf{i}}_{\mathrm{L}}^{\mathrm{ref}}} \tag{3}$$

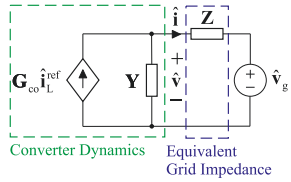


Figure 4: Equivalent small-signal circuit diagram of the grid-following converter control-to-output-dynamics-affected injection.

Table I: Grid-connected inverter parameters and operating point values.

| Parameter | Symbol | Value | Parameter | Symbol | Value |
|---|---|---|---|---|---|
| Input voltage | $V_{\mathrm{DC}}$ | 413 V | Grid voltage rms | $V_{\mathrm{g}}$ | 120 V |
| Output current d component | $I_{\mathrm{d}}$ | 10.6 A | Output current q component | $I_{\mathrm{q}}$ | 0.71 A |
| Synchronous frequency | $\omega_{\mathrm{s}}$ | $2\pi 50$ rad/s | Switching frequency | $f_{\mathrm{s}}$ | 8 kHz |
| Filter capacitor capacitance | $C_{\mathrm{f}}$ | 10 $\mu$F | Filter inductance | $L$ | 2.5 mH |
| $C_{\mathrm{f}}$ ESR and damping resistor | $r_{\mathrm{Cf}}$ | 1.81 $\Omega$ | $L$ ESR | $r_{\mathrm{L}}$ | 0.065 $\Omega$ |
| Filter inductance 2 | $L_2$ | 0.1 mH | $L_2$ ESR | $r_{\mathrm{L2}}$ | 0.022 $\Omega$ |
| Line inductance | $L_{\mathrm{line}}$ | 8.83 mH | Line inductance ESR | $r_{\mathrm{Lg}}$ | 0.262 $\Omega$ |
| Transformer inductance | $L_{\mathrm{T}}$ | 0.507 mH | Transformer inductance ESR | $r_{\mathrm{T}}$ | 0.417 $\Omega$ |
| Current controller P gain | $K_{\mathrm{p\text{-}c}}$ | 0.0149 | Current controller I gain | $K_{\mathrm{i\text{-}c}}$ | 23.4 |
| PLL P gain | $K_{\mathrm{p\text{-}pll}}$ | 0.0120 | PLL I gain | $K_{\mathrm{i\text{-}pll}}$ | 0.0144 |

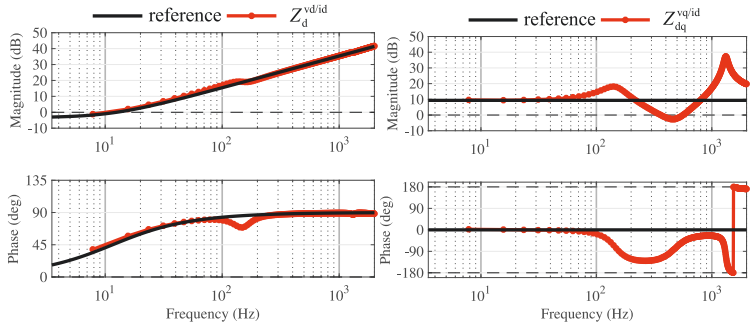


(a) (b)

Figure 5: Frequency response of the simulation identifications grid-impedance a) d component and b) qd component. $Z_{\mathrm{d}}^{\mathrm{vd/id}}$ and $Z_{\mathrm{dq}}^{\mathrm{vq/id}}$ are based on the assumption that only the intended channel is perturbed.

$$\overbrace{\begin{bmatrix}\hat{i}_{\mathrm{d}}\\ \hat{i}_{\mathrm{q}}\end{bmatrix}}^{\hat{\mathbf{i}}} = \overbrace{\begin{bmatrix}Y_{\mathrm{d}} & Y_{\mathrm{qd}}\\ Y_{\mathrm{dq}} & Y_{\mathrm{q}}\end{bmatrix}}^{\mathbf{Y}} \overbrace{\begin{bmatrix}\hat{v}_{\mathrm{d}}\\ \hat{v}_{\mathrm{q}}\end{bmatrix}}^{\hat{\mathbf{v}}} \tag{4}$$

$$\overbrace{\begin{bmatrix}\hat{v}_{\mathrm{d}}\\ \hat{v}_{\mathrm{q}}\end{bmatrix}}^{\hat{\mathbf{v}}} = \overbrace{\begin{bmatrix}Z_{\mathrm{d}} & Z_{\mathrm{qd}}\\ Z_{\mathrm{dq}} & Z_{\mathrm{q}}\end{bmatrix}}^{\mathbf{Z}} \overbrace{\begin{bmatrix}\hat{i}_{\mathrm{d}}\\ \hat{i}_{\mathrm{q}}\end{bmatrix}}^{\hat{\mathbf{i}}} \tag{5}$$

where subscripts d and q denote the direct and quadrature components, respectively. The transfer matrix from the current reference-to-output voltage is denoted as follows:

$$\overbrace{\begin{bmatrix}\hat{v}_{\mathrm{d}}\\ \hat{v}_{\mathrm{q}}\end{bmatrix}}^{\hat{\mathbf{v}}} = \overbrace{\begin{bmatrix}G_{\mathrm{cv-d}} & G_{\mathrm{cv-qd}}\\ G_{\mathrm{cv-dq}} & G_{\mathrm{cv-q}}\end{bmatrix}}^{\mathbf{G}_{\mathrm{cv}}} \overbrace{\begin{bmatrix}\hat{\mathrm{i}}_{\mathrm{L-d}}^{\mathrm{ref}}\\ \hat{\mathrm{i}}_{\mathrm{L-q}}^{\mathrm{ref}}\end{bmatrix}}^{\hat{\mathbf{i}}_{\mathrm{L}}^{\mathrm{ref}}} \tag{6}$$

The dq-frame impedance matrix of the identified impedance is given as follows

$$\mathbf{Z} = \begin{bmatrix} r_{\mathrm{eq}} + sL_{\mathrm{eq}} & -L_{\mathrm{eq}}\omega_{\mathrm{s}} \\ L_{\mathrm{eq}}\omega_{\mathrm{s}} & r_{\mathrm{eq}} + sL_{\mathrm{eq}} \end{bmatrix} \tag{7}$$

where $s$ is the Laplace variable, $L_{\mathrm{eq.}} = L_2 + L_{\mathrm{line}} + L_{\mathrm{T}}$, and $r_{\mathrm{eq.}} = r_2 + r_{\mathrm{line}} + r_{\mathrm{T}}$. The parameter descriptions and values are given in Table I. In order to demonstrate a strong impedance-based interaction, a relatively high line inductance (8.83 mH) is used.

The grid impedance elements $Z_{\mathrm{d}}$ and $Z_{\mathrm{dq}}$ are identified by injecting the MLBS on top of the d current reference. To avoid the effect of harmonic voltages, the number of averaged periods is chosen to be 80 throughout this paper so that an integer amount of fundamental cycles are included in the experimental measurement data [18]. Then, the responses in the voltages and currents are measured, and by computing the ratios of $\hat{v}_{\mathrm{d}}$ to $\hat{i}_{\mathrm{d}}$ and $\hat{v}_{\mathrm{q}}$ to $\hat{i}_{\mathrm{d}}$ the impedance elements are obtained. Fig. 5a shows the experimental measurement result of $Z_{\mathrm{d}}^{\mathrm{vd/id}}$. The result clearly has an error compared to

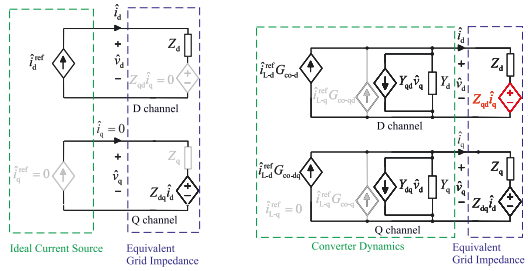


(a) (b)

Figure 6: Equivalent small signal circuit of (a) an ideal current injection to a dq-frame impedance and (b) a current injection with a converter to a dq-frame impedance.

the reference grid impedance below 150 Hz. Fig. 5b shows the identified $Z_{\mathrm{qd}}^{\mathrm{vd/iq}}$ that is erroneous in the whole frequency range from 150 Hz to 1250 Hz. The errors are caused by the impedance coupling.

In order to study the effect of the impedance coupling, an ideal current injection into an equivalent dq-frame impedance is first considered. The circuit diagram of such a system is shown in Fig. 6a. The elements that cross-couple the d and q channels of the equivalent grid impedance can be seen as current-dependent voltage sources. Both d and q channels are injected using ideal current sources. At the desired frequencies, $\hat{i}_{\mathrm{q}}$ can be kept zero while $\hat{i}_{\mathrm{d}}$ is be perturbed. To illustrate this, the circuit elements that are dependent on $\hat{i}_{\mathrm{q}}$ are grayed out. The ratio of $\hat{v}_{\mathrm{d}}$ to $\hat{i}_{\mathrm{d}}$ results in $Z_{\mathrm{d}}$:

$$\frac{\hat{v}_{\mathrm{d}}}{\hat{i}_{\mathrm{d}}} = Z_{\mathrm{d}} \tag{8}$$

In practical systems there are no ideal current sources. The perturbations are injected into the converter current references, and the responses in the currents and voltages are affected by the converter dynamics and the grid. Fig. 6b represents a

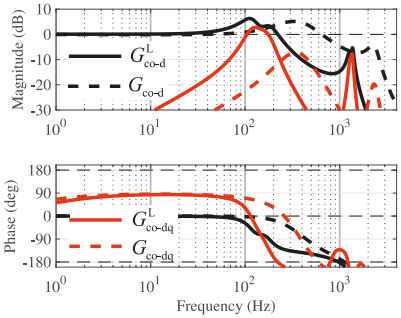


Figure 7: Modeled unterminated and load-affected 'L' control-to-output dynamics d and dq components.

case where a perturbation is added to $\hat{i}^{\mathrm{ref}}_{\mathrm{L-d}}$ and $\hat{i}^{\mathrm{ref}}_{\mathrm{L-q}}$ is not perturbed. The circuit elements that are affected only by $\hat{i}^{\mathrm{ref}}_{\mathrm{L-q}}$ are grayed out. The cross couplings in the converter output admittance are modeled by the voltage-dependent current sources. In contrast to the previous case, the response in $i_{\mathrm{q}}$ is not zero because the interaction among the circuit elements forms a path from $\hat{i}^{\mathrm{ref}}_{\mathrm{L-d}}$ to $\hat{i}_{\mathrm{q}}$. It is highlighted in red that $Z_{\mathrm{qd}}\hat{i}_{\mathrm{q}}$ may have a nonzero value unlike in the case of the ideal current injection. Therefore, the ratio of $\hat{v}_{\mathrm{d}}$ to $\hat{i}_{\mathrm{d}}$ may not result in $Z_{\mathrm{d}}$:

$$\frac{\hat{v}_{\mathrm{d}}}{\hat{i}_{\mathrm{d}}} = \frac{Z_{\mathrm{d}}\hat{i}_{\mathrm{d}} + Z_{\mathrm{qd}}\hat{i}_{\mathrm{q}}}{\hat{i}_{\mathrm{d}}} \neq Z_{\mathrm{d}} \tag{9}$$

Similarly, the other impedance elements $Z_{\mathrm{qd}}$, $Z_{\mathrm{dq}}$, and $Z_{\mathrm{q}}$ cannot be identified by computing the ratios of the corresponding frequency domain voltage and current.

The transfer function from the current references to the output currents can be modeled by grid-impedance-load-affected control-to-output dynamics as [31]:

$$\mathbf{G}^{\mathrm{L}}_{\mathrm{co}} = (\mathbf{I} + \mathbf{YZ})^{-1}\mathbf{G}_{\mathrm{co}} \tag{10}$$

where superscript "L" denotes that the transfer matrix is load-affected. The dynamics from $\hat{i}^{\mathrm{ref}}_{\mathrm{L-d}}$ to $\hat{i}_{\mathrm{q}}$ are modeled by transfer function $G^{\mathrm{L}}_{\mathrm{co-dq}}$ that is shown in more detail in Appendix A. The gain of the transfer function may be low depending on the parameters and the impedance coupling may have no significant effect. For example, if the grid impedance was only resistive

$$\mathbf{Z} = \begin{bmatrix} Z_{\mathrm{d}} & Z_{\mathrm{qd}} \\ Z_{\mathrm{dq}} & Z_{\mathrm{q}} \end{bmatrix} = \begin{bmatrix} r_{\mathrm{eq}} & 0 \\ 0 & r_{\mathrm{eq}} \end{bmatrix}, \tag{11}$$

the current-dependent voltage sources in Fig. 6b would disappear and no impedance coupling occurs. However, no such assumption can be made if an unknown system is identified.

Fig. 7 shows the Bode plots of the modeled unterminated and the load-affected control-to-output dynamics d component and dq component transfer functions. In the load-affected case, where the line inductance ($L_{\mathrm{g}}$) and the transformer inductance ($L_{\mathrm{T}}$) are connected in series with the grid-side filter inductor $L_2$, the responses from $\hat{i}^{\mathrm{ref}}_{\mathrm{Ld}}$ to $\hat{i}_{\mathrm{d}}$ and $\hat{i}_{\mathrm{q}}$ have a gain that is approximately the same magnitude. From 105 Hz to 200 Hz and 1250 Hz to 1410 Hz, the difference in gains of $G^{\mathrm{L}}_{\mathrm{co-dq}}$ and $G^{\mathrm{L}}_{\mathrm{co-d}}$ is small. Consequently, an injection to d-component reference at these frequencies results not only in a response in $\hat{i}_{\mathrm{d}}$, but also in $\hat{i}_{\mathrm{q}}$ that cannot be neglected. Therefore, the result from $\hat{v}_{\mathrm{d}}/\hat{i}_{\mathrm{d}}$ would not give $Z_{\mathrm{d}}$ because $\hat{v}_{\mathrm{d}}$ is also affected by $Z_{\mathrm{qd}}\hat{i}_{\mathrm{q}}$. These observations give background for the error in the measurement results in Fig. 5. In [21], the impedance coupling was illustrated by a block diagram and the exact erroneous measurement result was derived step-by-step. Similarly to the present paper, the system consisted of an inverter and a grid-impedance. However, an external device was used to inject the current perturbations.

### *B. Existing solution*

The impedance coupling can be avoided by using multiple independent injections in the measurement [10], [11], [17], [25], [26]. Here this is accomplished by first injecting the MLBS to $i^{\mathrm{ref}}_{\mathrm{L-d}}$, while the injection to $i^{\mathrm{ref}}_{\mathrm{L-q}}$ is zero. The second MLBS injection is made to $i^{\mathrm{ref}}_{\mathrm{L-q}}$, while the injection to $i^{\mathrm{ref}}_{\mathrm{L-d}}$ is zero. This method is denoted here by "2MLBS" because it is implemented by two sequential MLBSs. All currents and voltages are recorded from both injections. It has to be assumed that the grid-impedance does not change between the measurements and two sets of equations can be written [10]:

$$\begin{aligned} V_{\mathrm{d1}} &= Z_{\mathrm{d}}I_{\mathrm{d1}} + Z_{\mathrm{qd}}I_{\mathrm{q1}} \\ V_{\mathrm{q1}} &= Z_{\mathrm{q}}I_{\mathrm{q1}} + Z_{\mathrm{dq}}I_{\mathrm{d1}} \end{aligned} \tag{12}$$

$$\begin{aligned} V_{\mathrm{d2}} &= Z_{\mathrm{d}}I_{\mathrm{d2}} + Z_{\mathrm{qd}}I_{\mathrm{q2}} \\ V_{\mathrm{q2}} &= Z_{\mathrm{q}}I_{\mathrm{q2}} + Z_{\mathrm{dq}}I_{\mathrm{d2}} \end{aligned} \tag{13}$$

where subscript 1 and 2 denote the first and the second injection, respectively. The capital letters are used to denote the discrete Fourier transform (DFT) of the variables. The equations can be presented in matrix form [10]:

$$\begin{bmatrix} V_{\mathrm{d1}} & V_{\mathrm{d2}} \\ V_{\mathrm{q1}} & V_{\mathrm{q2}} \end{bmatrix} = \begin{bmatrix} Z_{\mathrm{d}} & Z_{\mathrm{qd}} \\ Z_{\mathrm{dq}} & Z_{\mathrm{q}} \end{bmatrix} \begin{bmatrix} I_{\mathrm{d1}} & I_{\mathrm{d2}} \\ I_{\mathrm{q1}} & I_{\mathrm{q2}} \end{bmatrix} \tag{14}$$

Eq. 14 can be easily solved for the impedance elements [10]:

$$\begin{bmatrix} Z_{\mathrm{d}} & Z_{\mathrm{qd}} \\ Z_{\mathrm{dq}} & Z_{\mathrm{q}} \end{bmatrix} = \begin{bmatrix} V_{\mathrm{d1}} & V_{\mathrm{d2}} \\ V_{\mathrm{q1}} & V_{\mathrm{q2}} \end{bmatrix} \begin{bmatrix} I_{\mathrm{d1}} & I_{\mathrm{d2}} \\ I_{\mathrm{q1}} & I_{\mathrm{q2}} \end{bmatrix}^{-1} \tag{15}$$

Figs. 8 shows the resulting impedance elements based on the two independent measurements ($Z^{\mathrm{2MLBS}}_{\mathrm{d}}$, $Z^{\mathrm{2MLBS}}_{\mathrm{qd}}$and $Z^{\mathrm{2MLBS}}_{\mathrm{dq}}$, and $Z^{\mathrm{2MLBS}}_{\mathrm{q}}$) and results obtained by the simple ratios of voltages to currents (the injection for measurement of $Z^{\mathrm{vd/iq}}_{\mathrm{qd}}$ and $Z^{\mathrm{vq/iq}}_{\mathrm{q}}$ was implemented by adding the IRS on top of the q current reference). The undesired impedance-based interaction is clearly no longer present in the measurement results. However, the main shortfall of the "2MLBS" method is the requirement of two sequential independent injections at the same frequencies. As a consequence, the measurement is more prone to changes in the operating point between the

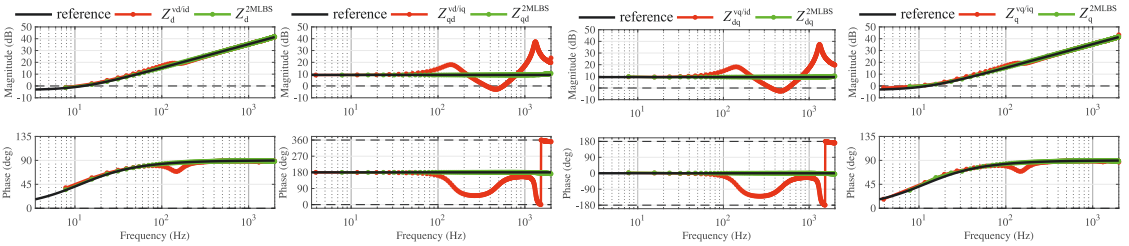


Figure 8: The simulation results with two independent injections are compared to the simple method. a) compares the $Z_{\mathrm{d}}^{\mathrm{vd/id}}$ to $Z_{\mathrm{qd}}^{\mathrm{2MLBS}}$ , b) compares $Z_{\mathrm{qd}}^{\mathrm{vd/iq}}$ to $Z_{\mathrm{qd}}^{\mathrm{2MLBS}}$, c) $Z_{\mathrm{dq}}^{\mathrm{vq/iq}}$ to $Z_{\mathrm{dq}}^{\mathrm{2MLBS}}$, and d) $Z_{\mathrm{q}}^{\mathrm{vq/iq}}$ to $Z_{\mathrm{q}}^{\mathrm{2MLBS}}$.

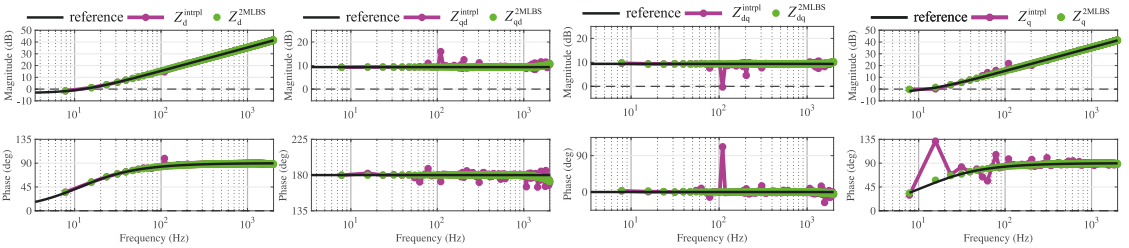


Figure 9: Comparison of (a) $Z_{\mathrm{d}}$, (b) $Z_{\mathrm{qd}}$, (z) $Z_{\mathrm{dq}}$, and (d) $Z_{\mathrm{q}}$ simulated identification results from the traditional two independent measurements and the simple interpolation method.

measurements. Below, an identification method is proposed that is based on two orthogonal injections, which allows the independent measurements to be performed simultaneously. As a result, similar results to the conventional method can be achieved without having to perform sequential injections.

## IV. Novel method

This section begins by inspecting a simple interpolation method to obtain an independent measurement at the MLBS frequencies from the IRS measurement. It is noted that the pseudorandom behavior in the IRS phase causes problems. To tackle this problem, a procedure where transfer functions from the injected sequence to the voltages and currents are used in the interpolation is proposed. The disturbance rejection capability of the proposed technique is demonstrated at the end of the section.

### A. Interpolation of IRS result in frequency domain

The objective is to obtain two sets of independent measurements at the same frequencies. However, the orthogonal injections, MLBS and IRS, have different frequency vectors, by definition. The solution is to interpolate the results from either of the simultaneously injected MLBS or IRS to the frequencies of another in the frequency domain. The interpolation from the IRS to the MLBS is chosen because the IRS has the lowest frequency. Because the excited frequencies of the MLBS are exactly in between the excited frequencies of the IRS according to (1) and (2), the interpolation becomes a straightforward arithmetic mean.

The frequency domain $I_{\mathrm{d2}}$, $V_{\mathrm{d2}}$, $I_{\mathrm{q2}}$, and $V_{\mathrm{q2}}$ are interpolated to the frequencies of the MLBS, $f_k^{\mathrm{MLBS}}$, from the frequencies of the IRS, $f_k^{\mathrm{IRS}}$. The interpolation of $V_{\mathrm{q2}}$ is given as an example:

$$V_{\mathrm{q2}}^{\mathrm{f-intrpl}-k} = \frac{V_{\mathrm{q2}}^{\mathrm{f-IRS}-k} + V_{\mathrm{q2}}^{\mathrm{f-IRS}-k+1}}{2} \tag{16}$$

which is the average of the complex-valued frequency bins, and superscript "intrpl" is used to denote that the variable is a result of the interpolation. The interpolated values are substituted into (15), and the impedance elements based on the interpolation ($Z_{\mathrm{d}}^{\mathrm{intrpl}}$, $Z_{\mathrm{qd}}^{\mathrm{intrpl}}$, $Z_{\mathrm{dq}}^{\mathrm{intrpl}}$, and $Z_{\mathrm{q}}^{\mathrm{intrpl}}$) are solved.

Fig. 9a compares the simulated identification results of the interpolation method ($Z_{\mathrm{d}}^{\mathrm{intrpl}}$) to the traditional measurement method ($Z_{\mathrm{d}}^{\mathrm{2MLBS}}$). In the case of the d component, the result is acceptable. $Z_{\mathrm{qd}}^{\mathrm{intrpl}}$, $Z_{\mathrm{dq}}^{\mathrm{intrpl}}$, and $Z_{\mathrm{q}}^{\mathrm{intrpl}}$ are shown in Figs. 9b, 9c, and 9d, respectively. While the impedance coupling is no longer present, it can be seen that the interpolated results clearly have deviations from the traditional method.

The response in $V_{\mathrm{q2}}$ originates from the injected IRS. As shown in Fig. 2b, the phase behavior of the IRS is pseudorandom. Fig. 10a shows a Bode plot of the $I_{\mathrm{Lq2}}^{\mathrm{ref-IRS}}$ and its interpolation ($I_{\mathrm{Lq2}}^{\mathrm{ref-intrpl}}$). The figure clearly shows that the interpolation result of the complex-valued bins gives mostly no reasonable result. This is due to the large changes in the

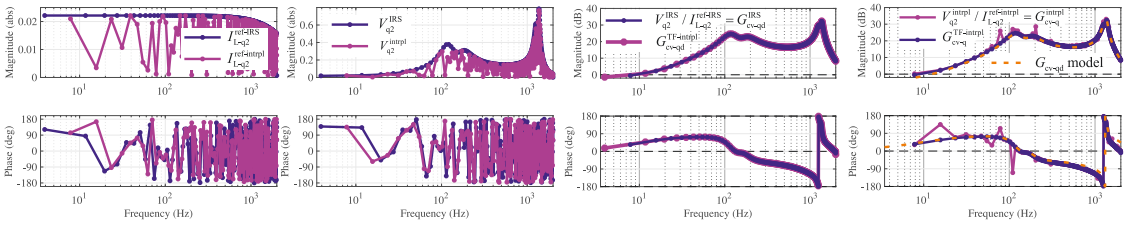


(a) (b) (c) (d)

Figure 10: (a) $I^{\mathrm{ref}}_{\mathrm{Lq2}}$ and its interpolation, (b) $V_{\mathrm{q2}}$ and its interpolation, (c) $V_{\mathrm{q2}}/I^{\mathrm{ref}}_{\mathrm{Lq2}}$ and its interpolation, and (d) comparison of $V^{\mathrm{intrpl}}_{\mathrm{q2}}/I^{\mathrm{ref-intrpl}}_{\mathrm{Lq2}}$ and $G^{\mathrm{TF-intrpl}}_{\mathrm{cv-q}}$. The results are from a Simulink simulation.

phase value between the frequencies that is a characteristic of the used pseudorandom sequence. A similar problem in the interpolation result of $V_2$ can be seen in Fig. 10b.

Fig. 10c illustrates the ratio of $V^{\mathrm{IRS}}_{\mathrm{q2}}$ to $I^{\mathrm{ref-IRS}}_{\mathrm{Lq2}}$ that is the transfer function $G^{\mathrm{IRS}}_{\mathrm{cv-q}}$. The preudorandom phase is no longer present in the data. The transfer function can be interpolated according to

$$G^{\mathrm{TF-intrpl}-k} = \frac{G^{\mathrm{f-IRS}-k} + G^{\mathrm{f-IRS}-k+1}}{2}\ , \tag{17}$$

where $G^{\mathrm{f-IRS}}$ is a general transfer function at the frequencies of the IRS. The procedure is named as a transfer function interpolation (TF-intprl). The result ($G^{\mathrm{TF-intrpl}}_{\mathrm{cv-q}}$) is smooth because the pseudorandom phase was not present in the interpolation. Fig. 10d compares $G^{\mathrm{TF-intrpl}}_{\mathrm{cv-q}}$ and $G^{\mathrm{intrpl}}_{\mathrm{cv-q}}$ . Clearly, the result where the ratio is calculated first and the resulting transfer function is interpolated gives more accurate result that follows the model.

### B. *Transfer-function interpolation*

Based on the previous analysis, the pseudorandom phase-behavior problem is solved by using transfer-function interpolation (here "TF-intrpl"). The technique is inspired by the practical one used in [11] where transfer functions from the injection reference to the currents and voltages were calculated as intermediate results. In [11], a single-phase perturbation was injected into a three-phase system.

Because the transfer functions are based on the system dynamics, it can be assumed that there are no abrupt changes within the resolution of the measurement. The grid-impedance d component ($Z_{\mathrm{d}}$) is used as an example. The solution to the grid impedance d component from (15) is calculated open:

$$Z_{\mathrm{d}} = \frac{V_{\mathrm{d1}} I_{\mathrm{q2}} - I_{\mathrm{q1}} V_{\mathrm{d2}}}{I_{\mathrm{d1}} I_{\mathrm{q2}} - I_{\mathrm{q1}} I_{\mathrm{d2}}} \tag{18}$$

The current and the voltages related to the second independent measurement can be replaced by the corresponding transfer functions from the q current reference ($I^{\mathrm{ref}}_{\mathrm{Lq2}}$) to the voltages (6) and the currents (3):

$$\begin{aligned} Z_{\mathrm{d}} &= \frac{V_{\mathrm{d1}} G_{\mathrm{co-q}} I^{\mathrm{ref}}_{\mathrm{Lq2}} - I_{\mathrm{q1}} G_{\mathrm{cv-qd}} I^{\mathrm{ref}}_{\mathrm{Lq2}}}{I_{\mathrm{d1}} G_{\mathrm{co-q}} I^{\mathrm{ref}}_{\mathrm{Lq2}} - I_{\mathrm{q1}} G_{\mathrm{co-qd}} I^{\mathrm{ref}}_{\mathrm{Lq2}}} \\ &= \frac{V_{\mathrm{d1}} G_{\mathrm{co-q}} - I_{\mathrm{q1}} G_{\mathrm{cv-qd}}}{I_{\mathrm{d1}} G_{\mathrm{co-q}} - I_{\mathrm{q1}} G_{\mathrm{co-qd}}} \end{aligned} \tag{19}$$

Because the injected IRS to $I^{\mathrm{ref}}_{\mathrm{Lq2}}$ and the responses at the IRS frequencies are known, the unknown transfer functions can be solved at the frequencies of the IRS as

$$\begin{bmatrix} G^{\mathrm{IRS}}_{\mathrm{co-qd}} \\ G^{\mathrm{IRS}}_{\mathrm{cv-qd}} \\ G^{\mathrm{IRS}}_{\mathrm{co-q}} \\ G^{\mathrm{IRS}}_{\mathrm{cv-q}} \end{bmatrix} = \begin{bmatrix} I^{\mathrm{IRS}}_{\mathrm{d2}} \\ V^{\mathrm{IRS}}_{\mathrm{d2}} \\ I^{\mathrm{IRS}}_{\mathrm{q2}} \\ V^{\mathrm{IRS}}_{\mathrm{q2}} \end{bmatrix} \frac{1}{I^{\mathrm{ref-IRS}}_{\mathrm{Lq2}}} \tag{20}$$

The equation also includes $G^{\mathrm{IRS}}_{\mathrm{cv-q}}$ because it is needed in order to identify $Z_{\mathrm{q}}$ and $Z_{\mathrm{dq}}$. Because the transfer functions are at the frequencies of the IRS, Eq. (19) cannot be directly applied. However, the solved transfer function can be interpolated to the frequencies of the MLBS by using (17). The interpolated transfer functions can be used to replace the second independent injection results in (15), which gives solutions to all impedance elements:

$$\begin{aligned} &\begin{bmatrix} Z^{\mathrm{TF-intrpl}}_{\mathrm{d}} & Z^{\mathrm{TF-intrpl}}_{\mathrm{qd}} \\ Z^{\mathrm{TF-intrpl}}_{\mathrm{dq}} & Z^{\mathrm{TF-intrpl}}_{\mathrm{q}} \end{bmatrix} \\ &= \begin{bmatrix} V_{\mathrm{d1}} & G^{\mathrm{TF-intrpl}}_{\mathrm{cv-qd}} \\ V_{\mathrm{q1}} & G^{\mathrm{TF-intrpl}}_{\mathrm{cv-q}} \end{bmatrix} \begin{bmatrix} I_{\mathrm{d1}} & G^{\mathrm{TF-intrpl}}_{\mathrm{co-qd}} \\ I_{\mathrm{q1}} & G^{\mathrm{TF-intrpl}}_{\mathrm{co-q}} \end{bmatrix}^{-1} \end{aligned} \tag{21}$$

The solution to $Z_{\mathrm{d}}$ is given as:

$$Z^{\mathrm{TF-intrpl}}_{\mathrm{d}} = \frac{V_{\mathrm{d1}} G^{\mathrm{TF-intrpl}}_{3} - I_{\mathrm{q1}} G^{\mathrm{TF-intrpl}}_{2}}{I_{\mathrm{d1}} G^{\mathrm{TF-intrpl}}_{3} - I_{\mathrm{q1}} G^{\mathrm{TF-intrpl}}_{1}} \tag{22}$$

Fig. 11 presents Simulink simulation results obtained by the proposed measurement procedure that is presented as a flow chart in Fig. 12. The identified $Z_{\mathrm{d}}$, $Z_{\mathrm{qd}}$, $Z_{\mathrm{dq}}$, and $Z_{\mathrm{q}}$ are shown in Figs. 11a, 11b, 11c, and 11d, respectively. The results obtained by the proposed method (TF-intrpl) are almost as accurate as those obtained by the traditional method (MLBS). The results obtained by the simple interpolation in Fig. 9 have

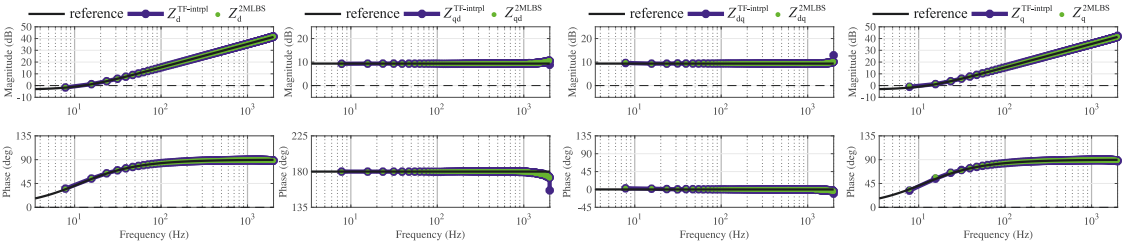


Figure 11: Comparison of the simulated identification results with the existing method and the proposed method.

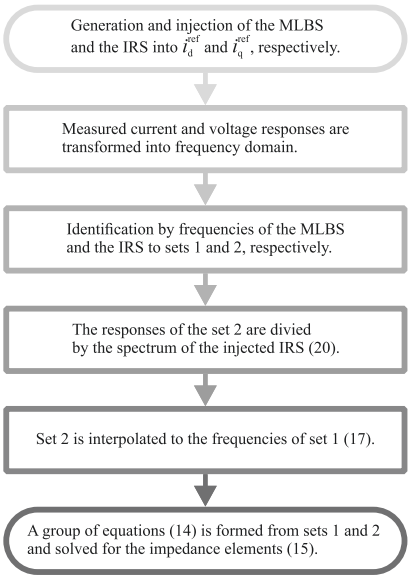


Figure 12: Flowchart of the proposed measurement procedure.

deviations caused the by the phase problem that is not present in the proposed transfer-function interpolation method.

In order to provide more validation of the result, a fit ratio is computed as follows:

$$\mathrm{FR} = \left(1 - \frac{\sum_{k=1}^{K} \left|\mathrm{Z}^{\mathrm{reference}}(k) - \mathrm{Z}^{\mathrm{identified}}(k)\right|^2}{\sum_{k=1}^{K} \left|\mathrm{Z}^{\mathrm{reference}}(k)\right|^2}\right) \times 100\% \quad (23)$$

where $Z^{\mathrm{reference}}$ is the reference to which the identification result ($\mathrm{Z}^{\mathrm{identified}}$) is compared, and K equals 256 when $n$ = 9 (because 256th element of the frequency vector is close to 2 kHz that is the reasonable measurement bandwidth). Here the fit ratio of the identification results obtained by the proposed technique to the reference model of the grid-impedance is computed. For $Z_{\mathrm{d}}^{\mathrm{TF-intrpl}}$, $Z_{\mathrm{qd}}^{\mathrm{TF-intrpl}}$, $Z_{\mathrm{dq}}^{\mathrm{TF-intrpl}}$, and $Z_{\mathrm{q}}^{\mathrm{TF-intrpl}}$, the fit ratios are 99.96 %, 99.47 %, 99.63 %, and 99.95 %, respectively. These numbers further validate the observations from the Bode plots in Fig. 11.

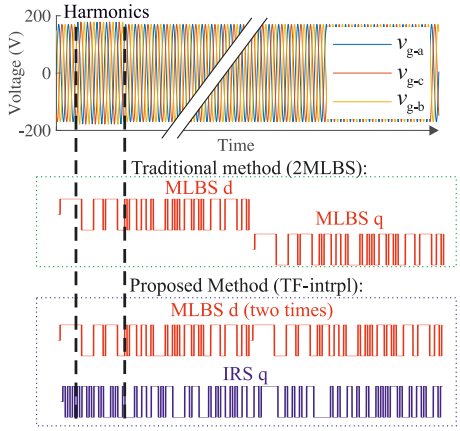


Figure 13: Illustration of the temporary harmonics in the grid voltages and how the harmonics relate to the injected sequences in the time domain.

### C. Disturbance rejection

The benefit of the proposed method is that both channels are injected and the impedance elements measured under the same operating conditions which provides rejection against effects of disturbances in the system during the measurement. In order to put the disturbance rejection to test, 5th, 7th, 11th, and 13th harmonics are added in the grid voltages during the measurement, and the identification results between the proposed method and the traditional method are compared.

Fig. 13 shows the grid-voltages and illustrates how the harmonics in the voltages affect the traditional and the proposed technique. The phase voltages are denoted by $v_{\mathrm{g-a}}$, $v_{\mathrm{g-b}}$ and $v_{\mathrm{g-c}}$, respectively. In the traditional method, the harmonics affect the measurement of the first MLBS when the d channel is injected. This implies that the DFT of the d channel will be distorted. The measurement of the q channel injection is not affected by the harmonics.

In the case of the proposed method in which the orthogonal sequences are applied, the effect of the harmonics in the grid voltages is different. The length of the IRS equals two times the length of the MLBS. Therefore, the proposed method and the traditional method have the same measurement time.

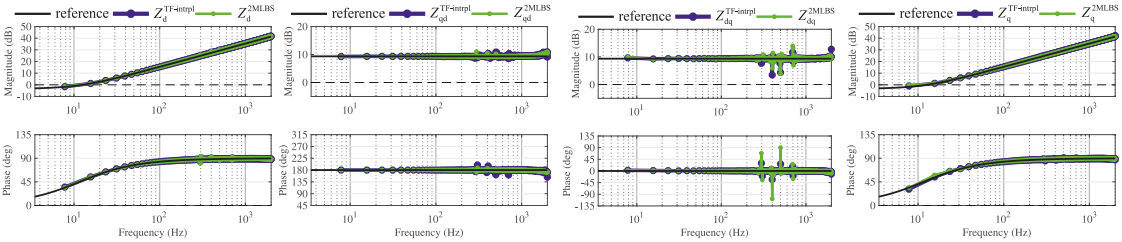


Figure 14: Comparison of the simulated identification results with the existing method and the proposed method under temporary harmonics in the grid voltages during the indentification.

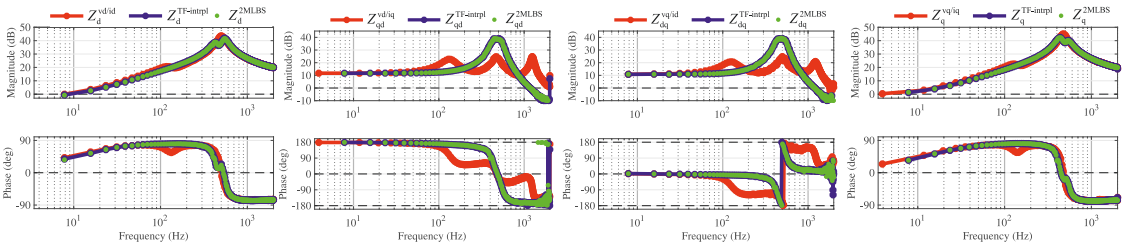


Figure 15: Experimentally identified grid impedance including the filter capacitor. (a) $Z_{\mathrm{d}}$, (b) $Z_{\mathrm{qd}}$, (c) $Z_{\mathrm{dq}}$, and (d) $Z_{\mathrm{q}}$.

Table II: Comparison of the fit ratio of the simulated results obtained by proposed method (TF-intrpl) and traditional (2MLBS) method to reference under grid voltage harmonics.

| **Impedance (Fig. 14)** | **Traditional method (2MLBS)** | **Proposed method (TF-intrpl)** |
|---|---|---|
| $Z_{\mathrm{d}}$ | 99.95 % | 99.96 % |
| $Z_{\mathrm{qd}}$ | 99.46 % | 99.05 % |
| $Z_{\mathrm{dq}}$ | 96.98 % | 98.96 % |
| $Z_{\mathrm{q}}$ | 99.98 % | 99.95 % |

However, in the proposed method, both channels are simultaneously injected and measured over the whole measurement time. Therefore, the harmonics affect the measurement of both channels but the time average is over a longer period of time in the case of the IRS. In the case of the MLBS, two sequences are averaged for every IRS period.

Fig. 14 shows simulated identification results in the case of the additional harmonics. In order to facilitate the comparison, fit ratios (23) are calculated for both methods (shown in Table II). The direct components ($Z_{\mathrm{d}}$ and $Z_{\mathrm{q}}$) are equal with both methods. In the case of $Z_{\mathrm{qd}}$, the traditional method is slightly better than the proposed method. In the case of $Z_{\mathrm{dq}}$, the results obtained by the traditional method have the largest deviations among all the results with both methods. In the proposed method, due to the good averaging capability, large deviations are more efficiently avoided than in the traditional method.

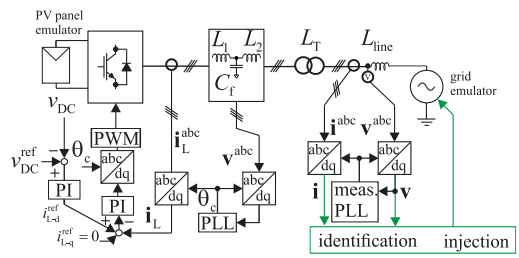


Figure 16: Block diagram of the grid-connected three-phase PV inverter and the control system.

## V. Verification of the Proposed Technique

This section provides experimental verification for the proposed technique. First, a grid impedance that has a resonance is identified by the grid-connected inverter. Then, the output admittance of a grid-connected PV inverter is identified.

### *A. Identification of Grid Impedance Including Filter Capacitor*

The used measurement setup is shown in Fig. 1. However, the identification procedure is changed so that the filter inductor current measurement is used for the identification. Therefore, the filter capacitor is included in the grid impedance, and the grid impedance becomes a parallel LC circuit with a resonance.

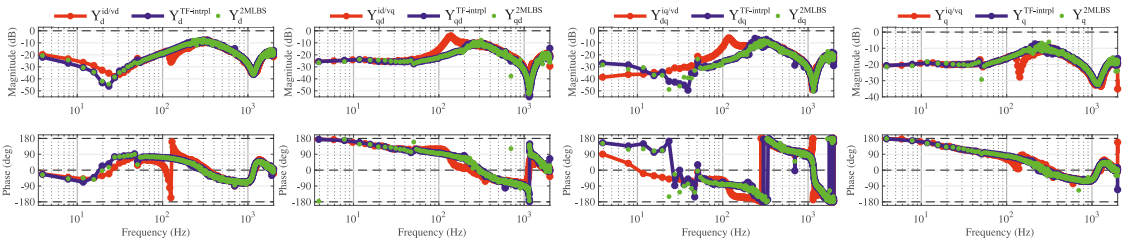


Figure 17: Experimentally identified output admittance of the grid-feeding PV inverter. (a) $Y_{\mathrm{d}}$, (b) $Y_{\mathrm{qd}}$, (c) $Y_{\mathrm{dq}}$, and (d) $Y_{\mathrm{q}}$.

Fig. 15 shows that the method that is based on ratios of the voltages to the currents clearly gives the results that are not the impedance elements of an LC circuit in the dq frame. In the dq frame, a parallel LC resonance has two peaks that are separated by two times the fundamental frequency. However, using the measurement method based on ratios of the voltages and currents, the resonance peaks appear combined in the measured impedance. Furthermore, in the direct components ($Z_{\mathrm{d}}$ and $Z_{\mathrm{q}}$) there are additional resonances at around 120 Hz. The existing method and the proposed method give practically identical results, and the interpolation does not cause problems.

The fit ratio is computed according to (23), and the results from the traditional method (2MLBS) are used as the reference to which the proposed method (TF-intrpl) in compared. Table III shows the fit ratios that clearly verify the applicability of the proposed method.

### *B. Identification of PV Inverter Output Admittance*

To further verify the proposed measurement procedure, the output admittance of a photovoltaic (PV) inverter is measured. Fig. 16 shows a block diagram of the system. The inverter is similar to the inverter in Fig. 1; however, the inverter is fed by a PV panel emulator instead of a DC voltage source. Therefore, a DC-voltage controller that produces the reference to the current d component is required. For the admittance identification, the currents and voltages are measured at the terminals of the isolation transformer; the transformer impedance is included to the converter output admittance that is identified. A measurement (meas.) PLL is used to synchronize the voltages at the transformer. The MLBS and IRS are added to the d and q voltage references of the grid emulator that is connected to the transformer over a line inductance. The interaction of the line impedance and converter impedance may cause an intended d-channel injection to appear in the q-channel and the impedance coupling occurs. The values of the passive components are given in Table I, and the controller parameters of the PV inverter and the measurement PLL that is used in the identification are given in Appendix B.

Table III: Fit ratio of the proposed method (TF-intrpl) to the (2MLBS) method in experiments.

| **Impedance (Fig. 15)** | **Fit ratio (FR)** | **Admittance (Fig. 17)** | **Fit ratio (FR)** |
|---|---|---|---|
| $Z_{\mathrm{d}}$ | 99.7 % | $Y_{\mathrm{d}}$ | 98.4 % |
| $Z_{\mathrm{qd}}$ | 99.2 % | $Y_{\mathrm{qd}}$ | 96.0 % |
| $Z_{\mathrm{dq}}$ | 99.3 % | $Y_{\mathrm{dq}}$ | 91.6 % |
| $Z_{\mathrm{q}}$ | 99.7 % | $Y_{\mathrm{q}}$ | 94.7 % |

The measurement procedure is slightly modified compared to the previously used procedure because now the inverter output admittance is identified. Eq. (21) becomes

$$\begin{bmatrix} Y_{\mathrm{d}} & Y_{\mathrm{qd}} \\ Y_{\mathrm{dq}} & Y_{\mathrm{q}} \end{bmatrix} = \begin{bmatrix} I_{\mathrm{d1}} & G_1 \\ I_{\mathrm{q1}} & G_3 \end{bmatrix} \begin{bmatrix} V_{\mathrm{d1}} & G_2 \\ V_{\mathrm{q1}} & G_4 \end{bmatrix}^{-1} \tag{24}$$

where $G_1$, $G_2$, $G_3$, and $G_4$ are TF-interpolated transfer functions from $V_{\mathrm{q2}}^{\mathrm{ref}}$ to $I_{\mathrm{d2}}$, $V_{\mathrm{d2}}$, $I_{\mathrm{q2}}$, and $V_{\mathrm{q2}}$, respectively. The transfer functions are calculated with respect to the reference q voltage ($V_{\mathrm{q2}}^{\mathrm{ref}}$) because the IRS is injected to the q-voltage reference of the grid-emulator. The amplitudes of the injected MLBS and IRS are 10 V, and the length of the shift register ($n$) is increased from the previously used 9 to 10 in order to improve the frequency resolution of the MLBS from 7.8 Hz to 3.9 Hz.

Fig. 17 shows the identified PV inverter output admittance obtained by different methods. Clearly, the method based on ratios of two variables deviates from the traditional method (2MLBS) and the proposed (TF-intrpl). As Fig. 17a. shows, the resolution of the proposed method is sufficient to reveal the resonance at 23 Hz caused by the DC-voltage control bandwidth. The negative incremental resistance region caused by the PLL whose bandwidth is 20 Hz is visible in $Y_{\mathrm{o-q}}$ in Fig. 17d.

Table III shows the fit ratio of the proposed methods to the traditional method. In (23), K equals 512 because $n$ = 10. In the case of PV inverter, there is more deviation in the fit ratio than in the case of the grid impedance. The reason for this deviation is that the relatively high line impedance damps the voltage perturbations that are implemented by the grid emulator. Furthermore, the converter admittance has a low magnitude resulting in a low current response that is prone to noise. Both 2MLBS and TF-intrpl methods suffer from the noise in the frequency range from 100 Hz to 1000 Hz. Nevertheless, the proposed method tackles the impedance coupling problem. The results could be enhanced by averaging

## APPENDIX A

$$G^{\mathrm{L}}_{\mathrm{co-dq}} = \frac{\mathrm{G_{co-dq}}(1+\mathrm{Y_d Z_d}+\mathrm{Y_{qd} Z_{dq}})-\mathrm{G_{co-d}}(\mathrm{Y_{dq} Z_d}+\mathrm{Y_q Z_{dq}})}{1+\mathrm{Y_d Z_d}+\mathrm{Y_{dq} Z_{qd}}+\mathrm{Y_{qd} Z_{dq}}+\mathrm{Y_q Z_q}+\mathrm{Y_d Y_q Z_d Z_q}-\mathrm{Y_d Y_q Z_{dq} Z_{qd}}-\mathrm{Y_{dq} Y_{qd} Z_d Z_q}+\mathrm{Y_{dq} Y_{qd} Z_{dq} Z_{qd}}} \tag{A1}$$

over a longer period of time or by increasing the injection amplitude.

The experiments verify the applicability of uncorrelated broadband injections in the presence of impedance coupling. The benefit of the proposed procedure lies in the short measurement time due to the use of the orthogonal binary perturbations. Furthermore, the method ensures that each channel is injected with the system in the same operating conditions, which may not be the case if sequential perturbations are applied. On the other hand, the method requires more signal processing than the existing method based on sequential injections. The reference signal must be recorded in the same reference frame as the voltages and currents which can set a limit for the PLL bandwidth. Another drawback of the interpolation is the introduction of small error. However, the interpolation error can be kept small by using an adequate frequency resolution.

## VI. CONCLUSIONS

The identification of the grid impedance at the point of common coupling of grid-connected converters is advantageous for the controller design and the adaptive control. An injection can be added to the converter current reference, and the identification can be made from the responses in the terminal currents and voltages. The interaction of the converter output impedance and the grid impedance causes an error in the impedance identification if an element of the multiple-input-multiple-output impedance is identified under an assumption that the injected perturbation affects only the intended channel.

In this work, orthogonal binary injections are used to obtain two independent sets of measurements from a grid-connected-converter system. Through the use of interpolation, one set of measurements can be moved to the frequencies of the other as an independent measurement. However, due to the pseudorandom phase behavior of the binary sequences, inferior results are obtained if the measured variables are interpolated directly in the frequency domain. In the proposed method, the variables are divided by the injected sequence and the obtained transfer functions are interpolated. The two acquired sets of measurements can be used to accurately identify the grid impedance by using existing methods. The presented method allows simultaneous measurement of the two independent measurement sets. The benefit lies in the fast measurement process and the mitigation of the possibility of excessive disturbances or changes in the grid impedance during the measurement.

## APPENDIX B

Table IV: Controller parameters of the experimental PV inverter.

| Parameter | Symbol | Value |
|---|---|---|
| Current controller P gain | $K_{\text{p-c}}$ | 0.0149 |
| Current controller I gain | $K_{\text{i-c}}$ | 23.4 |
| DC-voltage controller P gain | $K_{\text{p-v}}$ | -0.0962 |
| DC-voltage controller I gain | $K_{\text{i-v}}$ | -1.209 |
| PLL P gain | $K_{\text{p-pll}}$ | 0.7760 |
| PLL I gain | $K_{\text{i-pll}}$ | 39.52 |
| Measurement PLL P gain | $K_{\text{p-pll}}$ | 0.0120 |
| Measurement PLL I gain | $K_{\text{i-pll}}$ | 0.0144 |

## REFERENCES


[1] B. Bose, "Global warming: Energy, environmental pollution, and the impact of power electronics," *IEEE Ind. Electron. Mag.*, vol. 4, no. 1, pp. 6–17, mar 2010.

[2] C. Zhang, X. Cai, Z. Li, A. Rygg, and M. Molinas, "Properties and physical interpretation of the dynamic interactions between voltage source converters and grid: Electrical oscillation and its stability control," *IET Power Electron.*, vol. 10, no. 8, 2017.

[3] X. Wang, L. Harnefors, and F. Blaabjerg, "Unified impedance model of grid-connected voltage-source converters," *IEEE Trans. Power Electron.*, vol. 33, no. 2, pp. 1775–1787, feb 2018.

[4] Z.-X. Zou, G. Buticchi, and M. Liserre, "Grid identification and adaptive voltage control in a smart transformer-fed grid," *IEEE Trans. Power Electron.*, vol. 34, no. 3, pp. 2327–2338, mar 2019.

[5] S.-F. Chou, X. Wang, and F. Blaabjerg, "Two-port network modeling and stability analysis of grid-connected current-controlled vscs," *IEEE Trans. Power Electron.*, vol. 35, no. 4, pp. 3519–3529, apr 2020.

[6] D. Yang and X. Wang, "Unified modular state-space modeling of grid-connected voltage-source converters," *IEEE Trans. Power Electron.*, vol. 35, no. 9, pp. 9702–9717, sep 2020.

[7] T. Roinila, T. Messo, and E. Santi, "MIMO-identification techniques for rapid impedance-based stability assessment of three-phase systems in DQ domain," *IEEE Trans. Power Electron.*, vol. 33, no. 5, pp. 4015–4022, 2018.

[8] T. Roinila, T. Messo, and A. Aapro, "Impedance measurement of three phase systems in dq-domain: Applying mimo-identification techniques," *ECCE 2016 - IEEE Energy Convers. Congr. Expo. Proc.*, 2016.

[9] R. Luhtala, T. Roinila, and T. Messo, "Implementation of real-time impedance-based stability assessment of grid-connected systems using mimo-identification techniques," *IEEE Trans. Ind. Appl.*, vol. 54, no. 5, pp. 5054–5063, sep 2018.

[10] G. Francis, R. Burgos, D. Boroyevich, F. Wang, and K. Karimi, "An algorithm and implementation system for measuring impedance in the d-q domain," in *2011 IEEE Energy Convers. Congr. Expo.* IEEE, sep 2011, pp. 3221–3228.

[11] M. Jaksic, Z. Shen, I. Cvetkovic, D. Boroyevich, R. Burgos, C. DImarino, and F. Chen, "Medium-voltage impedance measurement unit for assessing the system stability of electric ships," *IEEE Trans. Energy Convers.*, vol. 32, no. 2, pp. 829–841, 2017.

[12] J. Kukkola, M. Routimo, and M. Hinkkanen, "Real-time grid impedance estimation using a converter," in *2019 IEEE Energy Convers. Congr. Expo.* IEEE, sep 2019, pp. 6005–6012.

[13] A. Vidal, A. G. Yepes, F. D. Freijedo, O. Lopez, J. Malvar, F. Baneira, and J. Doval-Gandoy, "A method for identification of the equivalent inductance and resistance in the plant model of current-controlled grid-tied converters," *IEEE Trans. Power Electron.*, vol. 30, no. 12, pp. 7245–7261, dec 2015.

[14] J. Xie, Y. X. Feng, and N. Krap, "Network impedance measurements for three-phase high-voltge power systems," *Asia-Pacific Power Energy Eng. Conf. APPEEC*, no. 3, pp. 1–5, 2010.

[15] L. Jessen, S. Gunter, F. W. Fuchs, M. Gottschalk, and H.-J. Hinrichs, "Measurement results and performance analysis of the grid impedance in different low voltage grids for a wide frequency band to support grid

integration of renewables," in *2015 IEEE Energy Convers. Congr. Expo.* IEEE, sep 2015, pp. 1960–1967.
[16] H. Alenius, T. Messo, T. Reinikka, and T. Roinila, "Aggregated modeling and power hardware-in-the-loop emulation of grid impedance," *2018 IEEE Energy Convers. Congr. Expo. ECCE 2018*, pp. 4179–4186, 2018.
[17] B. Wen, D. Boroyevich, R. Burgos, P. Mattavelli, and Z. Shen, "Small-signal stability analysis of three-phase ac systems in the presence of constant power loads based on measured d-q frame impedances," *IEEE Transactions on Power Electronics*, vol. 30, no. 10, pp. 5952–5963, 2015.
[18] R. Luhtala, H. Alenius, T. Messo, and T. Roinila, "Online frequency response measurements of grid-connected systems in presence of grid harmonics and unbalance," *IEEE Trans. Power Electron.*, vol. 35, no. 4, pp. 3343–3347, apr 2020.
[19] A. Riccobono, M. Mirz, and A. Monti, "Noninvasive online parametric identification of three-phase AC power impedances to assess the stability of grid-tied power electronic inverters in LV networks," *IEEE J. Emerg. Sel. Top. Power Electron.*, vol. 6, no. 2, pp. 629–647, jun 2018.
[20] T. Roinila, M. Vilkko, and J. Sun, "Broadband methods for online grid impedance measurement," in *2013 IEEE Energy Convers. Congr. Expo.* IEEE, sep 2013, pp. 3003–3010.
[21] H. Gong, X. Wang, and D. Yang, "DQ-frame impedance measurement of three-phase converters using time-domain MIMO parametric identification," *IEEE Trans. Power Electron.*, vol. 36, no. 2, pp. 2131–2142, feb 2021.
[22] T. Roinila, J. Huusari, and M. Vilkko, "On frequency-response measurements of power-electronic systems applying MIMO identification techniques," *IEEE Trans. Ind. Electron.*, vol. 60, no. 11, pp. 5270–5276, 2013.
[23] K. Godfrey, *Perturbation SignalsSyst. Identification*. Englewood Cliffs, NJ, USA: Prentice-Hall, 1993.
[24] A. Tan and K. Godfrey, *Industrial Process Identification*. Cham, Switzerland: Springer, 2019.
[25] Z. Shen, M. Jaksic, B. Zhou, P. Mattavelli, D. Boroyevich, J. Verhulst, and M. Belkhayat, "Analysis of phase locked loop (PLL) influence on DQ impedance measurement in three-phase AC systems," in *2013 Twenty-Eighth Annu. IEEE Appl. Power Electron. Conf. Expo.* IEEE, mar 2013, pp. 939–945.
[26] H. Gong, D. Yang, and X. Wang, "Impact analysis and mitigation of synchronization dynamics for DQ impedance measurement," *IEEE Trans. Power Electron.*, vol. 34, no. 9, pp. 8797–8807, sep 2019.
[27] T. Messo, J. Jokipii, A. Makinen, and T. Suntio, "Modeling the grid synchronization induced negative-resistor-like behavior in the output impedance of a three-phase photovoltaic inverter," in *2013 4th IEEE Int. Symp. Power Electron. Distrib. Gener. Syst.* IEEE, jul 2013, pp. 1–7.
[28] R. Luhtala, T. Roinila, and T. Messo, "Implementation of real-time impedance-based stability assessment of grid-connected systems using mimo-identification techniques," *IEEE Trans. Ind. Appl.*, vol. 54, no. 5, pp. 5054–5063, 2018.
[29] T. Roinila, T. Messo, R. Luhtala, R. Scharrenberg, E. C. De Jong, A. Fabian, and Y. Sun, "Hardware-in-the-loop methods for real-time frequency-response measurements of on-board power distribution systems," *IEEE Trans. Ind. Electron.*, vol. 66, no. 7, pp. 5769–5777, 2019.
[30] A. Aapro, T. Messo, T. Roinila, and T. Suntio, "Effect of active damping on output impedance of three-phase grid-connected converter," *IEEE Trans. Ind. Electron.*, vol. 64, no. 9, pp. 7532–7541, sep 2017.
[31] T. Suntio, T. Messo, M. Berg, H. Alenius, T. Reinikka, R. Luhtala, and K. Zenger, "Impedance-based interactions in grid-tied three-phase inverters in renewable energy applications," *Energies*, vol. 12, no. 3, p. 464, jan 2019.

**Matias Berg** (S'17) received the B.Sc. (Tech.) and M.Sc. (Tech.) degrees in Electrical Engineering from Tampere University of Technology in 2015 and 2017, respectively. He is currently a doctoral student at Tampere University, and his research interests include dynamic modeling of grid-following and grid-forming converters.

**Henrik Alenius** (S'18) received his M.Sc. degree in electrical engineering from Tampere University of Technology, Tampere, Finland, in 2018. Since then, he has worked as a doctoral student with the Faculty of Information Technology and Communication Sciences at Tampere University. His research interests include impedance-based interactions in grid-connected systems, broadband methods in impedance measurements, and stability analysis of multi-parallel inverters.

**Tomi Roinila** (M'10) received the M.Sc.(Tech.) and Dr.Tech. degrees in automation and control engineering from Tampere University of Technology, Tampere, Finland, in 2006 and 2010, respectively. He is currently an Assistant Professor in Tampere University, Finland.

His main research interests include modeling and control of grid-connected power-electronics systems, analysis of energy-storage systems, and modeling of multi-converter systems.

# Publication II

**Nonlinear Effect of Deadtime in Small-Signal Modeling of Power-Electronics System Under Low Load Conditions**

M. Berg and T. Roinila

*IEEE Journal of Emerging and Selected Topics in Power Electronics*,
*vol. 8, no. 4, pp. 3204—3213, 2020.*

# Nonlinear Effect of Dead Time in Small-Signal Modeling of Power-Electronic System Under Low-Load Conditions

Matias Berg, *Student Member, IEEE*, and Tomi Roinila, *Member, IEEE*

***Abstract*— Dead time is required to ensure that the switches of a synchronous switching inverter leg never conduct at the same time. During dead time, the current commutates to an antiparallel diode that can cause a voltage error depending on the instantaneous current direction. To measure a frequency response from a system, external injections are commonly required to perturb the system. The perturbation can change the current direction at the frequency of the injection, causing a voltage error at the injection frequency due to the dead time. The error depends on the perturbation amplitude, inductor current ripple, and fundamental current amplitude. This article proposes a describing-function method to model the dead-time effect under low-load conditions. It is shown that a nonlinear damping effect from the dead time can occur under low-load conditions and cannot be modeled with a resistor-like element. Real-time hardware-in-the-loop-simulation results are presented and used to demonstrate the effectiveness of the proposed method. Experimental measurements are used to verify the nonlinear dead-time effect.**

***Index Terms*— Dead time, describing function, frequency response, nonlinearity.**

## I. Introduction

FREQUENCY-RESPONSE analysis is among the most widely used techniques in dynamic analysis and controller tuning of the power electronic systems. The basis of deriving the dynamic models lies in the linearity of the inspected system or linearizing the system around an operation point that yields a linear frequency response. Impedance-based stability is an application that is based on the measured or modeled frequency responses and has received a great deal of attention in the last few years [1]–[3].

A possible source of nonlinearity is the dead time that is required to prevent the shoot-through faults in the synchronous switching power converters. Dead time causes a voltage error that is dependent on the inductor current sign [4]. The inductor current sign can change due to an external disturbance that can be caused, for example, by a frequency-response measurement.

A typical frequency-response-measurement method of a power-electronics system is based on an external voltage/current injection that is placed, for example, on the top of the nominal input voltage or current or control signal. Fourier methods are then applied to extract the spectral information between the desired input and the output variables [5]. In a power-electronics system with the dead time, a measurement injection can change the current sign at the injected frequency and cause a voltage error that acts as a damping.

The dead-time effect regarding the small-signal dynamics has gained some attention in the literature. Several studies have modeled the dead-time effect with a resistor-like element [6]–[10]. Three-phase converters were analyzed in [6] and [7], and single-phase converters in [8] and [9]. In [10], the dead-time effect on the dynamics of a synchronous switching buck converter was analyzed, focusing on the charging of the drain–source capacitance during the dead time. The dead-time effect on the dynamics of a quasi-square-wave flyback converter was analyzed in [11].

The importance of the ripple effect is shown in [8], and a describing-function-based method is used to solve a resistor-like element to model the dead-time effect. The model predicts damping to occur when the fundamental current amplitude is higher than half of the peak-to-peak current ripple. Furthermore, it is assumed that the inductor current amplitude is the same as the injection current. This assumption in [8] is well grounded, because the output filter of the analyzed full-bridge inverter consists of only an inductor. However, if there was a resonance that increases the inductor current with respect to injection, this assumption would not be valid.

This article studies the dead-time effect under a low-load condition, where the inductor current fundamental component amplitude is lower than half the peak-to-peak ripple. In [8], the opposite assumption and operating point were used. Furthermore, in this article, the response in the inductor current that causes the dead-time effect is not considered small. Instead, we propose a describing-function-based method that models the output impedance as a function of injection amplitude and frequency. We show that resonance in the system can increase the inductor current so that a voltage error occurs or even saturates. Therefore, a moderate injection amplitude does not guarantee a linear operating region.

The remainder of this article is structured as follows. Section II examines the dead-time effect and the amplitude dependence in the frequency-response measurements. Section III derives a describing-function model for the error. The proposed amplitude-dependent output impedance is

Manuscript received September 27, 2019; revised December 9, 2019; accepted January 5, 2020. Date of publication January 17, 2020; date of current version November 5, 2020. This work was supported in part by the Fortum Foundation under Grant 201800119. Recommended for publication by Associate Editor Santanu Kapat. *(Corresponding author: Matias Berg.)*

The authors are with the Faculty of Information Technology and Communication Sciences, Tampere University, 33100 Tampere, Finland (e-mail: matias.berg@tuni.fi).

Color versions of one or more of the figures in this article are available online at http://ieeexplore.ieee.org.

Digital Object Identifier 10.1109/JESTPE.2020.2967341

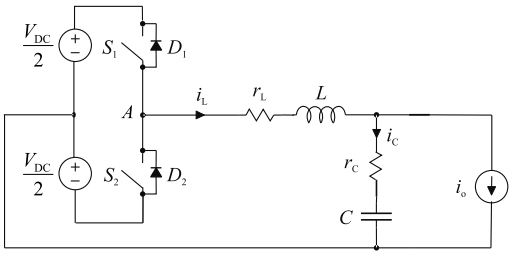


Fig. 1. Half-bridge inverter.

TABLE I
OPERATING POINT AND COMPONENT VALUES

| Parameter | Value | Parameter | Value |
|---|---|---|---|
| $V_{DC}$ | 700 V | $I_o$ | 0-1.8 A |
| $L$ | 4 mH | $r_L$ | 10 mΩ |
| $C$ | 10 $\mu$F | $r_C$ | 10 mΩ |
| $\omega_s$ | $2\pi$60 rad/s | $V_{o,rms}$ | 120 V |
| $f_s$ | 10 kHz | $T_{dead}$ | 4 $\mu$s |

introduced in Section IV. In Section V, hardware-in-the-loop (HIL) simulations and experimental measurements are used to verify the analyzed dead-time effect. Conclusions are drawn in Section VI.

## II. DEAD-TIME EFFECT

This section begins by inspecting the voltage error that is caused by the dead time. We then analyze and model how the dead-time effect is visible in the frequency-response measurements and how the operating point and system parameters affect the dead-time effect. Throughout this article, it is assumed that the frequency-response measurement is performed with a sinesweep, where one frequency at a time is injected and measured.

### A. Voltage Error Caused by Dead Time

Fig. 1 shows a half-bridge inverter that is used to analyze the dead-time effect. The switches and the diodes are analyzed with ideal components. However, in reality, the required dead time depends on the turn-off characteristics of the used semiconductor switches [12]. When the dead-time length is chosen, the changes in the switch characteristics with load current and temperature must be considered [13]. The dead time is not changed according to the operating conditions. In general, faster switching devices require shorter dead time than the lower switching devices. The operating point and the component values are given in Table I. A dead time value of 4 $\mu$s is applied in most parts of this article. This value (in a combination of the applied switching frequency of 10 kHz in the laboratory setup) was observed to demonstrate the nonlinear effect efficiently.

The dead time is used to delay the turn-on of switches $S_1$ and $S_2$, ensuring a period during which neither of the switches conducts. During dead time, the current commutates to either of diodes $D_1$ or $D_2$, depending on the instantaneous current sign [4]. Therefore, the dead time causes an instantaneous voltage error, $v_{err}$, in the inverter voltage during the dead time

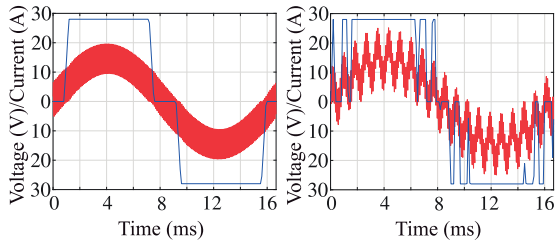


Fig. 2. Inductor current (red) and average voltage error (blue) waveforms when (a) fundamental current is higher than half the peak-to-peak current ripple and (b) with an added sinusoidal perturbation in the inductor current.

that can be given by

$$v_{err} = \text{sign}(i_L)V_{dc} \tag{1}$$

where $V_{dc}$ and $i_L$ are the dc voltage and the inductor current, respectively. In order to facilitate the analysis, the error is averaged over a switching cycle

$$v_{err}^{avg-Ts} = \frac{1}{T_s}\int_{\tau}^{\tau+T_s} v_{err}(t)dt \tag{2}$$

where $T_s$ and $T_{dead}$ are the switching cycle and the dead-time lengths, respectively. The resulting maximum average voltage error is

$$V_{err}^{max} = \left|v_{err}^{avg-Ts}\right| = \left|\text{sign}(i_L)\frac{T_{dead}}{T_s}V_{dc}\right| \tag{3}$$

which yields 28 V with the parameters of Table I. The fundamental component of a square wave with the amplitude of 28 V is $4/\pi$ 28 V = 35.56 V. The value of the average voltage error has been analyzed in the literature earlier [4], [12]

Fig. 2(a) shows the averaged voltage error over a 60-Hz fundamental cycle. The error has the same sign as the current. However, during the period of current zero crossings, the average voltage error is zero. In Fig. 2(b), a perturbation is added to the inductor current, and a voltage error appears at the perturbation frequency due to the changes in the current zero crossings. The zero-crossing period was modeled in [14], and a similar approach was used for modeling the dead-time effect in [9]. However, this article focuses on modeling the dead-time effect under a low-load condition, where the 60-Hz fundamental current component is lower than half the peak-to-peak inductor current ripple.

Fig. 3(a) and (b) shows the inductor current and the averaged voltage error under low-load conditions. In Fig. 3(a), there is no fundamental 60-Hz component in the inductor current, and in Fig. 3(b), the fundamental component is lower than half the peak-to-peak current ripple. The average voltage error during the whole fundamental cycle is zero, because the inductor current crosses zero during every switching cycle, and the instantaneous error has both signs during a switching cycle. Fig. 3(c) illustrates a case where a perturbation is added to the current fundamental component, and the sum has a higher amplitude than half the peak-to-peak current ripple. Therefore, a voltage error appears when there are no zero crossings within a switching cycle or a zero current clamping occurs.

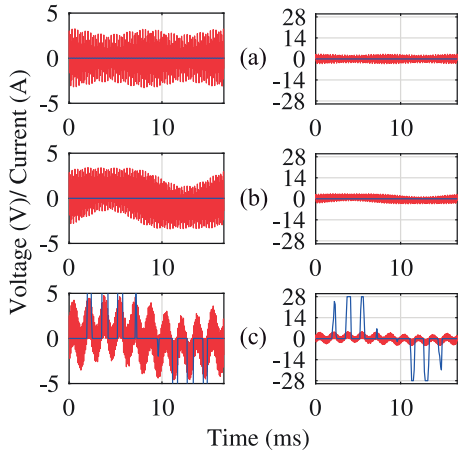


Fig. 3. Inductor current waveforms (red) and averaged voltage errors (blue) with different fundamental current amplitudes (a) 0, (b) 1, and (c) 1 A with a perturbation of 1.5 A at 600 Hz.

### *B. Perturbation Amplitude Dependence*

The half-bridge inverter in Fig. 1 is simulated with MATLAB/Simulink. A current injection is made with the output current, $i_o$, to measure the output impedance, $Z_o = \hat{v}_o/\hat{i}_o$. The fundamental load current, a 60-Hz component, $A_{\text{fund}}$, is provided by the current sink if required. In the following, the current sink draws no 60-Hz current component, and the current sink is used only for the injection. Fig. 4 shows the simulated measurement of the output impedance when no dead time is applied in the switching as the benchmark. The simulation is done two times with the injection amplitudes of 0.5 and 2 A.

A dynamic model of the system is created based on the parallel connection of the filter inductor impedance, $Z_L$, and filter capacitor impedance, $Z_C$

$$Z_C = r_C + \frac{1}{sC} \tag{4}$$

$$Z_L = r_L + sL \tag{5}$$

$$Z_o(s) = \frac{Z_C Z_L}{Z_C + Z_L} = \frac{r_C s^2 + \left(\frac{r_L r_C}{L} + \frac{1}{C}\right)s + \frac{r_L r_C}{CL}}{s^2 + \frac{r_L + r_C}{L}s + \frac{1}{CL}} \tag{6}$$

where $L$, $C$, $r_L$, and $r_C$ denote the inductance, capacitance, inductor resistance, and capacitor resistance, respectively. As shown in Fig. 4, the model corresponds to the simulations according to the linear circuit theory.

Next, the output impedance simulation is repeated when a dead time of 4 $\mu$s is applied in the switch control signals. Fig. 5 compares the results with the linear model, $Z_o(s)$. It is apparent from Fig. 5 that the dead time makes the system highly nonlinear, and the linear model cannot be used to model the system. With the injection amplitude of 0.5 and 1 A, the resonance is damped. On the other hand, with the injection amplitudes of 2 and 3 A, a damping appears at lower frequencies and the resonance is less damped.

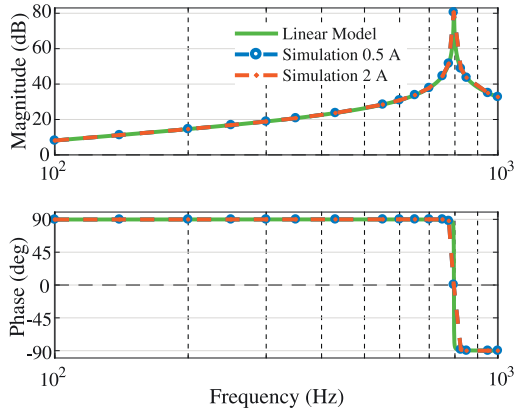


Fig. 4. Output impedance from a simulation without the dead time with different injection amplitudes.

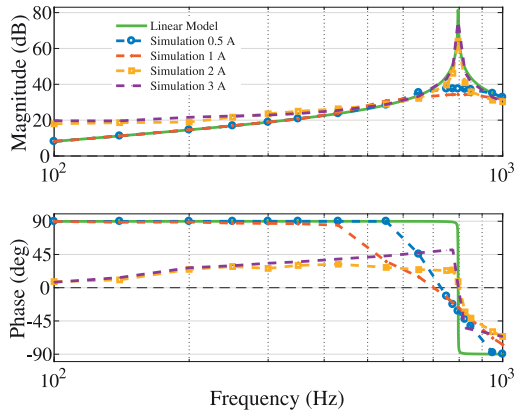


Fig. 5. Output impedance, $Z_o$, measured from a simulation with the dead time and different injection amplitudes.

Therefore, a resistor-like element that is constant at all frequencies cannot be used to model the dead-time effect.

It is known that the error caused by the dead time is dependent on the inductor current. Therefore, it is useful to look at the output current-to-inductor current dynamics. The transfer function can be given by

$$G_{oL}(s) = \frac{Z_C}{Z_C + Z_L} = \frac{\frac{r_C}{L}s + \frac{1}{CL}}{s^2 + \frac{r_L + r_C}{L}s + \frac{1}{CL}}. \tag{7}$$

Fig. 6 compares the modeled and simulated $G_{oL}(s)$. Similar to the case of the output impedance, the dead-time effect is visible and the linear model is not valid. Fig. 7 shows the absolute values of the inductor current and the voltage error with different injection amplitudes. It can be seen that the resonance amplifies the inductor current, which increases the voltage error. However, the voltage error has its maximum value $V_{\text{err}}^{\max}$ according to (3). When the error saturates to the maximum value, its effect on the frequency response begins

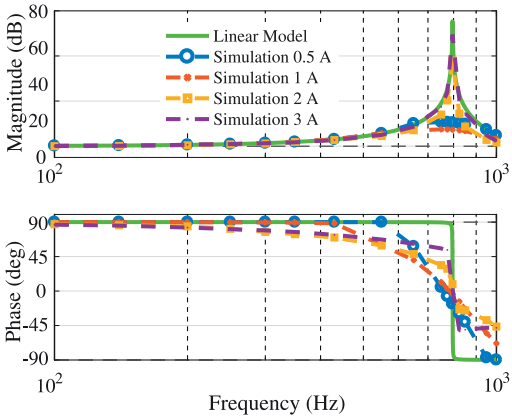


Fig. 6. Output current-to-inductor current transfer function, $G_{\mathrm{oL}}$, measured from a simulation with different injection amplitudes.

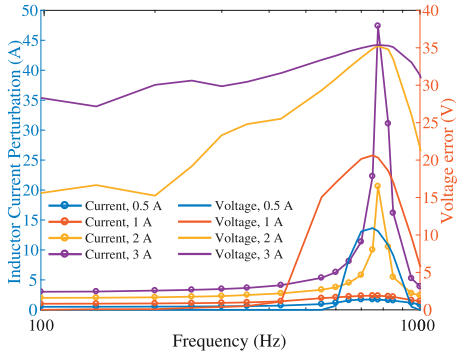


Fig. 7. Simulated absolute values of the inductor current and the voltage error with different injection amplitudes.

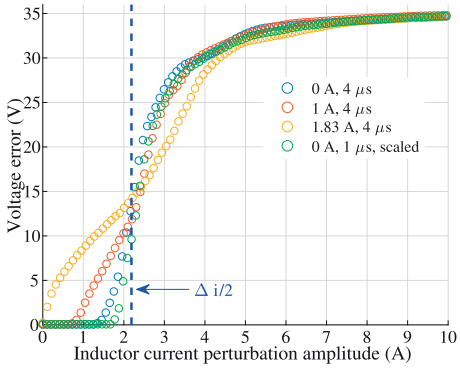


Fig. 8. Simulated voltage error as a function of the inductor current perturbation amplitude with different fundamental current amplitudes.

to diminish. It can be also noted that there is no voltage error at all if the inductor current amplitude is not high enough.

Fig. 8 illustrates how the error behaves as a function of the inductor current perturbation amplitude. For the simulations in Fig. 8, the filter capacitor was changed from 10 to 0.5 $\mu$F in order to reduce the reactive current fundamental component. All injections were made at 650 Hz. With zero fundamental current amplitude, there is a dead zone below which there is no voltage error. When the fundamental current amplitude is increased, the dead zone shortens until the fundamental amplitude is approximately half the peak-to-peak current ripple, $\Delta i/2$

$$\Delta i = \frac{V_{\mathrm{dc}} T_s}{4L}. \tag{8}$$

Half the peak-to-peak ripple, $\Delta i/2$, is 2.19 A with the parameters of Table I.

Because the gain of $G_{\mathrm{oL}}(s)$ is close to 0 dB at low frequencies, the injection amplitude must be higher than half the peak-to-peak ripple for the error to occur. This can be seen in Fig. 7. When the perturbation amplitude is high enough, the error saturates to the fundamental component of the square-wave voltage error. The saturation begins when the perturbation amplitude equals the sum of half the peak-to-peak current ripple and the fundamental current. After this point, the increase in the perturbation amplitude affects the whole fundamental cycle; this can be seen from Figs. 7 and 8. Between the dead zone and the saturation is a slope region that can be seen well from Fig. 8 in the case where the fundamental current amplitude is 1 A. This behavior of the voltage error under low-load conditions was illustrated in [9] but not analyzed.

Fig. 8 also shows the voltage error when the dead time is 1 $\mu$s. The error is scaled by multiplying it by 4 in order to have the maximum error, $V_{\mathrm{err}}^{\max}$, unchanged compared to the case with the dead time of 4 $\mu$s according to (3). By inspecting the error as a function of the current with $A_{\mathrm{fund}} = 0$, Fig. 8 shows that there is a voltage error on the lower inductor current perturbations than $\Delta i/2$. This is partly due to the approximation of $\Delta i/2$ in (8) that gives the ripple when the duty cycle is 0.5 (that is, around the fundamental component zero crossing).

Furthermore, Fig. 8 reveals that the dead-time length not only affects the maximum voltage error, $V_{\mathrm{err}}^{\max}$. With $T_{\mathrm{dead}} = 1$ $\mu$s, the error remains zero with higher inductor current-response amplitudes. This can be explained with a zero current clamping effect, which causes a voltage error. For a zero current clamping to occur, it is sufficient for the current to drop to zero during the dead time, and remain zero for the rest of the dead-time length. The maximum current change during the dead time is approximated by

$$i_{\mathrm{clamp}}^{\max} = \frac{V_{\mathrm{dc}} T_{\mathrm{dead}}}{2L}. \tag{9}$$

If the zero is crossed for $i_{\mathrm{clamp}}^{\max}$ or fewer Amperes before the current slope direction changes, a zero current clamping occurs. The zero current clamping effect is the first source of voltage error rather than the main dead-time effect. The zero current clamping effect and the voltage error have been analyzed in [15].

## III. Describing-Function Model

A describing-function model for the voltage error can be developed based on the observations from the voltage error

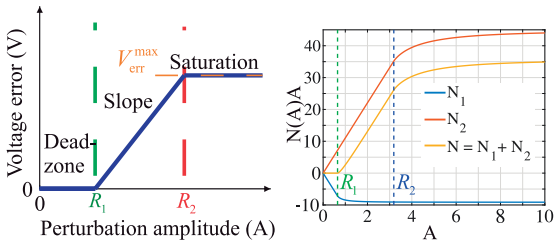


Fig. 9. (a) Dead zone, slope, and saturation that are modeled in frequency domain with (b) describing function.

as a function of the inductor current perturbation amplitude, current ripple, and current fundamental component in Fig. 8. Therefore, a describing-function model consisting of a dead zone, a slope, and a saturation illustrated in Fig. 9(a) must be created.

With lower current perturbation amplitudes, $A$, than $R_1$, there is no voltage error, and with higher than $R_2$, the error saturates. The zero current clamping effect reduces $R_1$ by $i_{\text{clamp}}^{\max}$ according to (9). $R_1$ and $R_2$ are defined by

$$R_1 = \frac{\Delta i}{2} - A_{\text{fund}} - i_{\text{clamp}}^{\max} \tag{10}$$

$$R_2 = \frac{\Delta i}{2} + A_{\text{fund}}\cos(\phi) \tag{11}$$

where $A_{\text{fund}}$ is the fundamental current amplitude. The reactive current produced by the capacitor with amplitude $A_{\text{react}}$ cannot be neglected, because it affects $R_2$ if the inductor current fundamental component is not in phase with the ripple. Therefore, the reactive current component has to be considered

$$A_{\text{react}} = V_o 2\pi 60C. \tag{12}$$

Therefore, the fundamental current amplitude is given by

$$A_{\text{fund}} = \sqrt{A_{\text{real}} + A_{\text{react}}}. \tag{13}$$

The angle $\phi$ in (11) is given by

$$\phi = \tan^{-1}\left(\frac{A_{\text{react}}}{A_{\text{real}}}\right) \tag{14}$$

where $A_{\text{real}}$ is the 60-Hz component current drawn by the current sink. Between $R_1$ and $R_2$, the error increases from zero to $V_{\text{err}}^{\max}$ by the slope $k$

$$k = \frac{V_{\text{err}}^{\max}}{R_2 - R_1}. \tag{15}$$

Therefore, the error model, $N(A)$, can be created by summing the two describing-function models, $N(A)_1$ and $N(A)_2$, both modeling slope and saturation [16]

$$N(A)_1 = \frac{-2k}{\pi}\left[\sin^{-1}\left(\frac{R_1}{A}\right) + \frac{R_1}{A}\sqrt{1-\left(\frac{R_1}{A}\right)^2}\right] \tag{16}$$

$$N(A)_2 = \frac{2k}{\pi}\left[\sin^{-1}\left(\frac{R_2}{A}\right) + \frac{R_2}{A}\sqrt{1-\left(\frac{R_2}{A}\right)^2}\right] \tag{17}$$

$$N(A) = \Re[N(A)_1 + N(A)_2]. \tag{18}$$

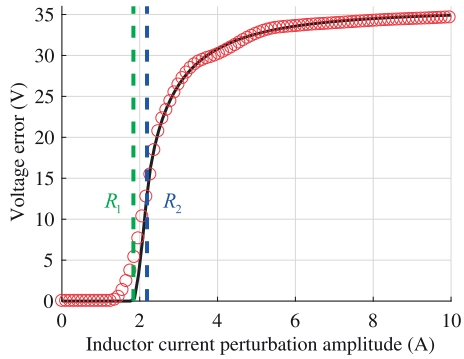


Fig. 10. Simulation (circles) and model (solid line) of the voltage error as a function of the inductor current perturbation amplitude with a fundamental current of 0 A.

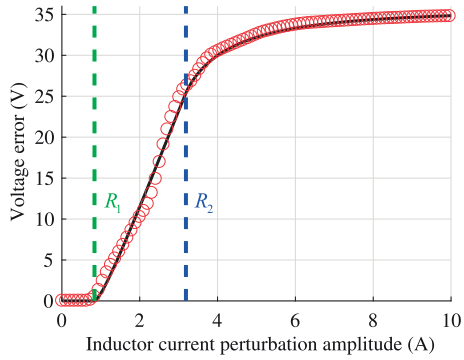


Fig. 11. Simulation (circles) and model (solid line) of the voltage error as a function of the inductor current perturbation amplitude with a fundamental current of 1 A.

Due to the dead zone, the sum of the slopes must be zero before $R_1$. Therefore, the slope of $N(A)_1$ is $-k$. Fig. 9(b) shows how $N(A)_1$ and $N(A)_2$ sum up to $N(A)$.

Figs. 10–12 compare the proposed model, $N(A)A$ as a function of $A$, with the simulated voltage error with the fundamental current amplitudes of 0, 1, and 1.83 A, respectively. The fundamental amplitude of 1.83 A was chosen in order to have $R_1$ in (10) zero. The proposed model estimates the nonlinear error sufficiently well. However, regardless of modeling, the zero current clamping effect the model for $R_1$ in Fig. 10 and the approximation with a single slope in Fig. 12 are not completely accurate.

## IV. Amplitude and Frequency Response

This section deals with the output impedance that is affected by the nonlinear dead-time effect. Based on the describing-function model $N(A)$, an output impedance model that depends on both the injection amplitude and injection frequency is derived.

Due to the nonlinear voltage error, a transfer function must be defined as a function of the amplitude $A$ and frequency $\omega$. Therefore, the notation of the inductor and capacitor

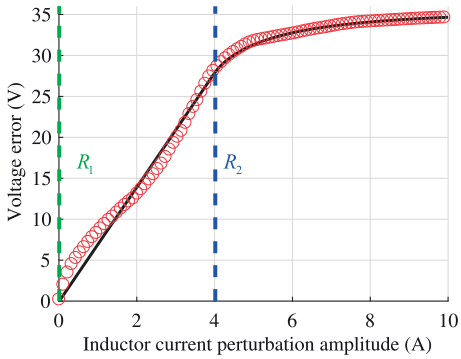


Fig. 12. Simulation (circles) and model (solid line) of the voltage error as a function of the inductor current perturbation amplitude with a fundamental current of 1.83 A.

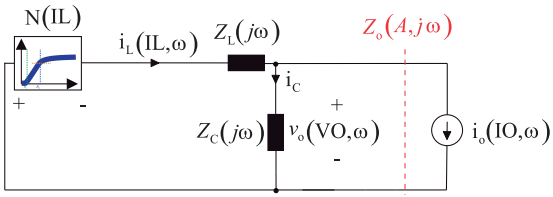


Fig. 13. Nonlinear frequency-domain circuit from where IL must be solved for every input combination of IO and $\omega$.

impedance subsystems is changed from $Z_L(s)$ and $Z_C(s)$ to $Z_L(j\omega)$ and $Z_C(j\omega)$, respectively. The effect of $N(A)$ is included in the output impedance and, therefore, becomes a function of the input amplitude in addition to the frequency Therefore, the output impedance is expressed as $Z_o(A, j\omega)$.

Fig. 13 shows a frequency-domain circuit presentation of the nonlinear system. The capacitor and inductor impedances are the traditional linear elements. However, the nonlinear voltage error is in series with the inductor impedance as a reverse-biased nonlinear current-dependent voltage source. The equation based on the circuit can be given by

$$|N(\mathrm{IL}) + Z_L(j\omega) + Z_C(j\omega)|i_L(\mathrm{IL},\omega) - |Z_C(j\omega)|i_o(\mathrm{IO},\omega) = 0. \quad (19)$$

IO, VO, and IL are the phasors of the output current, output voltage, and inductor current, respectively. IL must be solved for each input combination on IO and $\omega$. The phasors are analyzed separately at different frequencies, $\omega$. $N(\mathrm{IL})$ is the analytical expression from (18). The equation can be solved, for example, by using the MATLAB *fzero* function. The solved $i_L(\mathrm{IL},\omega)$ is in a zero phase shift, because the equation could be solved only for the absolute value. Thus, the output current $i_o$ must be resolved in order to find out the relational phase shift

$$i_o(\mathrm{IO},\omega) = \frac{[N(\mathrm{IL}) + Z_L(j\omega) + Z_C(j\omega)]i_L(\mathrm{IL},\omega)}{Z_C(j\omega)}. \quad (20)$$

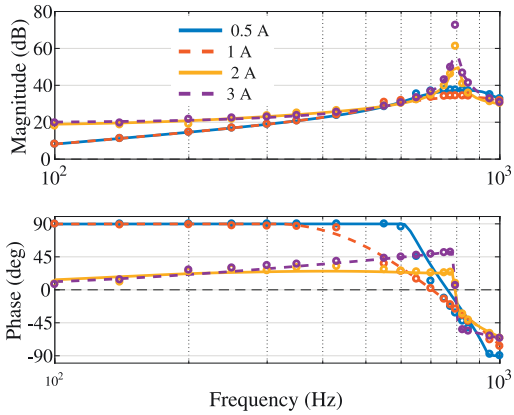


Fig. 14. Modeled (lines) and simulated (circles) output impedance with different perturbation amplitudes and a fundamental current of 0.64 A.

As the next step, the output impedance $Z_o(A, j\omega)$ can be solved

$$Z_o(A, j\omega) = -\frac{v_o(\mathrm{VO},\omega)}{i_o(\mathrm{IO},\omega)} = \frac{Z_C(j\omega)i_o(\mathrm{IO},\omega) - Z_C(j\omega)i_L(\mathrm{IL},\omega)}{i_o(\mathrm{IO},\omega)}. \quad (21)$$

Fig. 14 compares the modeled and the simulated output impedance, $Z_o(A, j\omega)$. The model predicts well that, with low injection current amplitudes when the inductor current perturbation amplitude is small enough, the resonance is damped. On the other hand, the error saturates around the resonance with higher injection amplitudes and the undamped resonance becomes visible again. Higher injection amplitudes than $R_1$ cause errors at lower frequencies, which can be seen as damping.

Fig. 15 shows the modeled amplitudes of the voltage error and inductor current corresponding to the case of Fig. 14. As it can be seen, the error saturates at the resonance in the case of injection amplitudes of 2 and 3 A. Due to this, the damping effect is diminished as it can be seen from Fig. 14. Figs. 16 and 17 compare the model with the simulation when the fundamental load current is 1 A and the inductor current is 1.19 A. However, the effect is modeled only at the fundamental frequency of the square-wave-like voltage error.

## V. HIL Simulation and Experimental Verification

This section deals with HIL simulations and experimental laboratory measurements. First, we take a look at the changes that are caused by dc capacitors of the used practical circuit. Second, a voltage injection is used to measure the output impedance in an HIL simulation. Third, a practical laboratory setup is used to verify the nonlinear dependence on the injection amplitude.

### A. Practical Circuit

Fig. 18 shows the circuit diagram of the experimental setup. In the practical half-bridge inverter, there are dc capacitors,

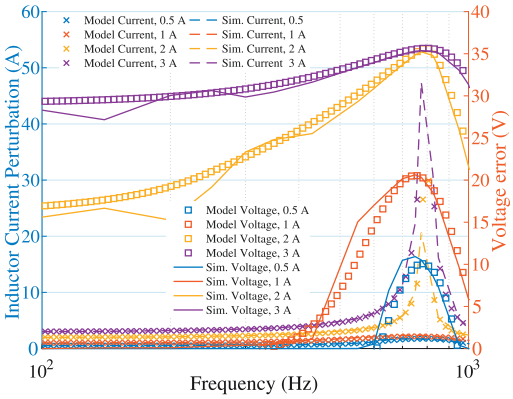


Fig. 15. Modeled and simulated inductor current amplitude and voltage error with different perturbation amplitudes and a fundamental current of 0.64 A.

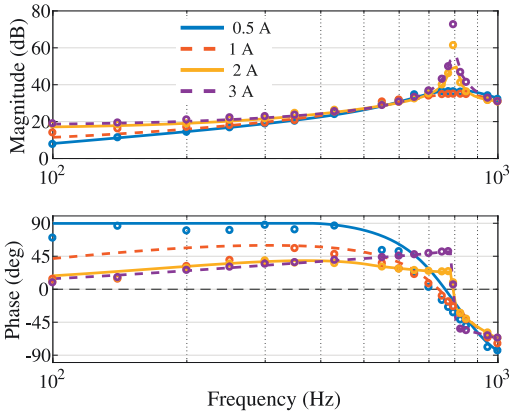


Fig. 16. Modeled (lines) and simulated (circles) output impedance with different perturbation amplitudes and a fundamental current of 1.19 A.

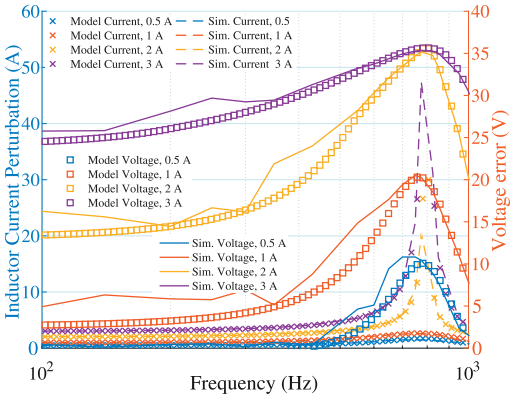


Fig. 17. Modeled and simulated inductor current amplitude and voltage error with different perturbation amplitudes and a fundamental current of 1.19 A.

$C_{dc}$, instead of the two ideal voltage sources that were used previously. Because the dc voltage source is a dynamic short circuit, a parallel connection of the dc capacitors, $Z^{par}_{dc-C}$,

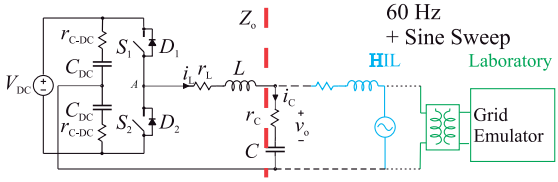


Fig. 18. Circuit diagram of the HIL simulations and laboratory experiment.

TABLE II
OPERATING POINT AND COMPONENT VALUES OF THE HIL SIMULATION

| Parameter | Value | Parameter | Value |
|---|---|---|---|
| $f_s$ | 20 kHz | $T_{dead}$ | 2 $\mu$s |
| $V_{DC}$ | 700 V | $V_{o,rms}$ | 120 V |
| $L$ | 1.2mH | $r_L$ | 0.16$\Omega$ |
| $C$ | 9.8 $\mu$F | $r_C$ | 0.11 $\Omega$ |
| $C_{DC}$ | 500 $\mu$F | $r_{C\text{-}DC}$ | 0.246 $\Omega$ |
| $\omega_s$ | $2\pi$60 rad/s | | |

is visible in series with the inductor and is, therefore, included in the inductor impedance

$$Z_{C-dc}(j\omega) = r_{C-dc} + \frac{1}{j\omega C_{dc}} \tag{22}$$

$$Z^{par}_{C-dc} = \frac{Z_{C-dc} Z_{C-dc}}{Z_{C-dc} + Z_{C-dc}} \tag{23}$$

$$Z_L(j\omega) = Z^{par}_{C-dc} + r_L + j\omega L \tag{24}$$

where $r_{C-dc}$ is the equivalent series resistance of the dc capacitor.

The analysis focuses on the antiresonance in (24), because with the used laboratory equipment, it was not possible to inject the voltages that cause high enough current at the *LC* parallel resonant frequency to demonstrate the saturation effect.

For the sake of simplicity, the filter capacitor is not included in the output impedance. Therefore, the nonlinear circuit equation that must be solved for IL reduces to

$$|N(IL) + Z_L(j\omega)|i_L(IL, \omega) + v_o(VO, \omega) = 0. \tag{25}$$

The output impedance can be solved from

$$Z_o(A, j\omega) = -\frac{v_o(VO, \omega)}{i_L(IL, \omega)}. \tag{26}$$

The parameters of the HIL simulation in this section are given in Table II.

### *B. HIL Simulations*

The circuit of Fig. 18 is simulated with Typhoon HIL model 402. The phase-locked loop (PLL) is omitted for simplicity. The inductor current amplitude, $I_L$, and the capacitor current amplitude, $I_C$, are 1.01 and 0.64 A, respectively. The 60-Hz fundamental voltage component is provided by the ideal voltage source that has a very small series-connected inductor and resistor to improve the simulation stability. The voltage source is also used to inject a sine sweep for the measurement. In order to demonstrate the nonlinear damping effect, high injection amplitudes are required.

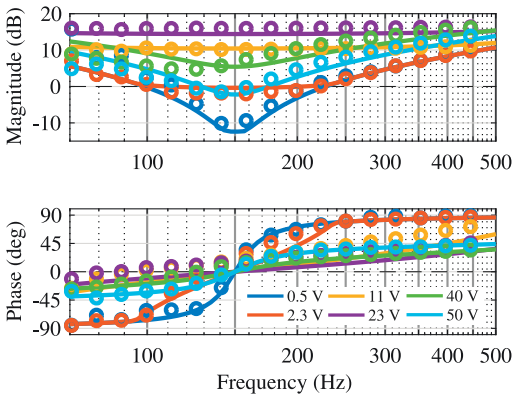


Fig. 19. HIL simulation (circles) and model (lines) of the open-loop output impedance of the grid-connected converter with different injection voltages.

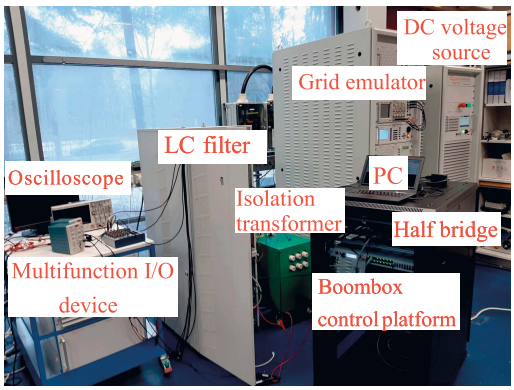


Fig. 20. Laboratory setup.

Fig. 19 shows the real-time HIL-simulated frequency response and the model around the antiresonance at 150 Hz. It can be seen that the model clearly predicts the damping as the function of the perturbation amplitude. The most striking result from Fig. 19 is that the damping increases when the injection amplitude is increased from 0.5 to 23 V. With injection amplitudes of 40 and 50 V, there is less damping, which is predicted correctly by the model. A notable change in the damping can be seen even with the injection amplitudes 0.5, 2.3, and 11 V, which are less than 10% of the fundamental 170-V component amplitude.

### *C. Laboratory Measurements and Comparison to Simulations*

The nonlinear damping by the dead time is verified by laboratory measurements. Fig. 20 shows the laboratory setup for the circuit in Fig. 18. A low-bandwidth PLL is used to synchronize the half-bridge converter to the 60-Hz voltage provided by the grid emulator. The frequency response of the output impedance is measured by injecting a sine sweep with

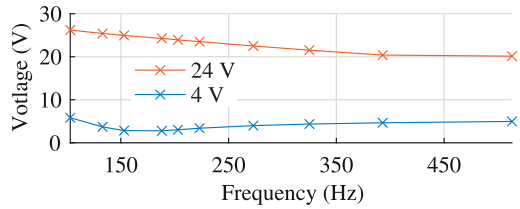


Fig. 21. Injected output voltage amplitude at different frequencies.

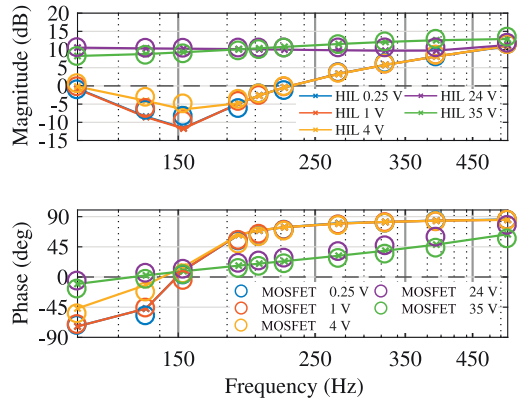


Fig. 22. Laboratory measurement of the open-loop output impedance of the grid-connected converter with MOSFETs with different injection voltages and HIL replication of the measurement.

a grid emulator. The measurements are performed separately with MOSFETs and insulated-gate bipolar transistors (IGBTs) in order to see the effect of nonideal switches. The used switch modules were the PEB Sic 8024 module and PEB 8032 module by Imperix.

Due to the used isolation transformer, there is a voltage drop in the value, which depends on the injected frequency, and the injected voltage over the capacitor is not the voltage over the grid emulator. Fig. 21 shows two injections as an example. The injected output voltage amplitude is not constant, and the injected voltage over the filter capacitor varies slightly between the IGBT and MOSFET measurements. The nominal values for the injections, 4 and 24 V, are chosen from the values at around 270 Hz. As it has been shown, the nonlinear dead-time effect is very amplitude-sensitive. Therefore, the practical measurement is replicated in an HIL simulation by injecting a voltage that in reality was over the filter capacitor.

Figs. 22 and 23 show the measured laboratory measurements with MOSFETs and IGBTs compared with the HIL simulations, respectively. The laboratory setup is shown in Fig. 20, and the passive component parameters of the setup are given in Table III. As stated earlier, ideal switches with ideal diodes were used in the HIL simulations.

The HIL simulation gives a result that corresponds to the laboratory measurements in the case of the MOSFETs, as shown in Fig. 22. Fig. 23 shows the converter output impedance with the IGBT. As shown in Fig. 23, there is a

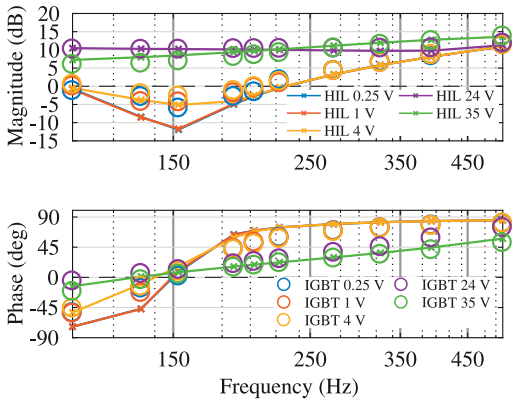


Fig. 23. Laboratory measurement of the open-loop output impedance of the grid-connected converter with IGBTs with different injection voltages and HIL replication of the measurement.

TABLE III
SYSTEM PARAMETER VALUES OF THE LABORATORY MEASUREMENTS

| Parameter | Value | Parameter | Value |
|---|---|---|---|
| $f_s$ | 10 kHz | $T_{dead}$ | 4 $\mu$s |
| $V_{DC}$ | 700 V | $V_{o,rms}$ | 120 V |
| $L$ | 1.2mH | $r_L$ | 0.13$\Omega$ |
| $C$ | 10 $\mu$F | $r_C$ | 0.1 $\Omega$ |
| $C_{DC}$ | 500 $\mu$F | $r_{C\text{-}DC}$ | 0.246 $\Omega$ |
| $\omega_s$ | $2\pi$60 rad/s | | |

more visible difference in damping between the simulation in laboratory measurement with low injection amplitudes compared with the case with the MOSFET. This implies that nonidealities with the IGBT cause more problems regarding the modeling of the dead-time effect. On the other hand, the used dead time of 4 $\mu$s is not relevant for the MOSFETs, because it is unnecessarily long. However, the purpose of this article is to study the damping that stems from the dead time. With the two highest injection amplitudes, the HIL simulation matches accurately to the laboratory measurements. Furthermore, with the highest injection amplitude, the damping decreases below the resonance frequency that is visible in both the laboratory measurements and the HIL simulation. The nonidealities with MOSFETs could become more visible with higher switching frequencies.

## VI. CONCLUSION

This article has investigated the nonlinear damping caused by the dead time effect under load conditions where the fundamental current component is less than half the peak-to-peak current ripple. The findings indicate that error caused by the dead time can be modeled with a dead zone, slope, and saturation as a function of the inductor current amplitude. Due to the dead zone, the effect cannot be modeled with a resistor-like element, as was used earlier in the literature with the dead time under different load conditions.

By using a describing function, we found a model for the error caused by the dead time under a low-load condition. The describing-function model in combination with linear circuit impedances was used to derive the output impedance of an inverter as a function of the injection amplitude. We observed that, even with a moderate measurement injection amplitude, a system resonance can increase the inductor current amplitude, making the nonlinearities become visible. This can occur especially in simulations, where ideal current source that can provide infinite voltage is used for the measurement injection. The proposed model works accurately with real-time HIL simulations that are becoming increasingly popular. Experimental measurements were provided for verifying the HIL simulations and the nonlinear dead-time effect.

This article represents the first occasion that the output impedance of a power electronic converter has been given as a function of the injection amplitude in addition to the injection frequency. Our article has some limitations regarding the nonidealities in practical semiconductor switches. In addition, low-order harmonics except the first one were assumed nonexistent. For example, considerable harmonics produced by a nonlinear load could change the effect. Nevertheless, we believe our article gives new theoretical background on the analysis of the nonlinear small-signal dead-time effect under low-load conditions. On a wider level, research is also needed to determine how the nonlinear dead-time effect and the measurement result behave under broadband injections that are becoming increasingly popular [5], [17].

## REFERENCES

[1] B. Wen, R. Burgos, D. Boroyevich, P. Mattavelli, and Z. Shen, "AC stability analysis and *dq* frame impedance specifications in power-electronics-based distributed power systems," *IEEE J. Emerg. Sel. Topics Power Electron.*, vol. 5, no. 4, pp. 1455–1465, Dec. 2017.

[2] A. Aapro, T. Messo, T. Roinila, and T. Suntio, "Effect of active damping on output impedance of three-phase grid-connected converter," *IEEE Trans. Ind. Electron.*, vol. 64, no. 9, pp. 7532–7541, Sep. 2017.

[3] T. Roinila, T. Messo, and E. Santi, "MIMO-identification techniques for rapid impedance-based stability assessment of three-phase systems in DQ domain," *IEEE Trans. Power Electron.*, vol. 33, no. 5, pp. 4015–4022, May 2018.

[4] S.-G. Jeong and M.-H. Park, "The analysis and compensation of dead-time effects in PWM inverters," *IEEE Trans. Ind. Electron.*, vol. 38, no. 2, pp. 108–114, Apr. 1991.

[5] R. Luhtala, H. Alenius, T. Messo, and T. Roinila, "Online frequency response measurements of grid-connected systems in presence of grid harmonics and unbalance," *IEEE Trans. Power Electron.*, vol. 35, no. 4, pp. 3343–3347, Apr. 2020.

[6] S. Ahmed, Z. Shen, P. Mattavelli, D. Boroyevich, and K. J. Karimi, "Small-signal model of voltage source inverter (VSI) and voltage source converter (VSC) considering the DeadTime effect and space vector modulation types," *IEEE Trans. Power Electron.*, vol. 32, no. 6, pp. 4145–4156, Jun. 2017.

[7] A. Rodriguez-Cabero, M. Prodanovic, and J. Roldan-Perez, "Analysis of dynamic properties of VSCs connected to weak grids including the effects of dead time and time delays," *IEEE Trans. Sustain. Energy*, vol. 10, no. 3, pp. 1066–1075, Jul. 2019.

[8] M. Zhang, D. Yang, and X. Wang, "Accurate open-loop impedance model of single-phase voltage source inverter (VSI) considering the dead-time effects," in *Proc. 20th Workshop Control Modeling Power Electron. (COMPEL)*, Jun. 2019, pp. 1–5.

[9] M. Berg, T. Messo, T. Roinila, and P. Mattavelli, "Deadtime impact on the small-signal output impedance of single-phase power electronic converters," in *Proc. 20th Workshop Control Modeling Power Electron. (COMPEL)*, Jun. 2019, pp. 1–8.

[10] W. Qiu, S. Mercer, Z. Liang, and G. Miller, "Driver deadtime control and its impact on system stability of synchronous buck voltage regulator," *IEEE Trans. Power Electron.*, vol. 23, no. 1, pp. 163–171, Jan. 2008.

[11] Z. Zhang, S. Tian, and K. D. T. Ngo, "Small-signal equivalent circuit model of quasi-square-wave flyback converter," *IEEE Trans. Power Electron.*, vol. 32, no. 8, pp. 5885–5888, Aug. 2017.
[12] A. Mora, J. Juliet, A. Santander, and P. Lezana, "Dead-time and semiconductor voltage drop compensation for cascaded H-bridge converters," *IEEE Trans. Ind. Electron.*, vol. 63, no. 12, pp. 7833–7842, Dec. 2016.
[13] R. L. Bonkowski, "A technique for increasing power transistor switching frequency," *IEEE Trans. Ind. Appl.*, vol. IA-22, no. 2, pp. 240–243, Mar. 1986.
[14] G. Grandi, J. Loncarski, and R. Seebacher, "Effects of current ripple on dead-time distortion in three-phase voltage source inverters," in *Proc. IEEE Int. Energy Conf. Exhibit. (ENERGYCON)*, Sep. 2012, pp. 207–212.
[15] A. Rothstein and V. Staudt, "Detailed analysis of converter-output-voltage errors under light-load conditions," in *Proc. Int. Conf. Optim. Electr. Electron. Equip. (OPTIM), Int. Aegean Conf. Electr. Mach. Power Electron. (ACEMP)*, May 2017, pp. 336–341.
[16] J. T. Machadoa, A. M. Lopesa, D. Valerio, and A. M. Galhano, *Solved Problems in Dynamical Systems and Control*. Edison, NJ, USA: IET, 2016.
[17] T. Roinila, M. Vilkko, and J. Sun, "Online grid impedance measurement using discrete-interval binary sequence injection," *IEEE J. Emerg. Sel. Topics Power Electron.*, vol. 2, no. 4, pp. 985–993, Dec. 2014.

**Matias Berg** (Student Member, IEEE) received the B.Sc. (Tech.) and M.Sc. (Tech.) degrees in electrical engineering from the Tampere University of Technology, Tampere, Finland, in 2015 and 2017, respectively. He is currently pursuing the doctoral degree with Tampere University, Tampere.

His research interest includes dynamic modeling of grid-following and grid-forming converters.

**Tomi Roinila** (Member, IEEE) received the M.Sc. (Tech.) and Dr.Tech. degrees in automation and control engineering from the Tampere University of Technology (TUT), Tampere, Finland, in 2006 and 2010, respectively.

He is currently an Academic Researcher with Tampere University. His main research interests include modeling and control of grid-connected power-electronics systems and modeling of multiconverter systems.

# Publication III

**Deadtime Impact on the small-signal output impedance of Single-Phase Power Electronic Converters**

M. Berg, T. Messo, T. Roinila, and P. Mattavelli

*IEEE 20th Workshop on Control and Modeling for Power Electronics*, *8 pages, 2019.*

# Deadtime Impact on the small-signal output impedance of Single-Phase Power Electronic Converters


1st Matias Berg
*Faculty of Information Technology and Communication Sciences*
*Tampere University*
Tampere, Finland
matias.berg@tuni.fi

2nd Tuomas Messo
*Faculty of Information Technology and Communication Sciences*
*Tampere University*
Tampere, Finland
tuomas.messo@tuni.fi

3rd Tomi Roinila
*Faculty of Engineering and Natural Sciences*
*Tampere University*
Tampere, Finland
tomi.roinila@tuni.fi

4th Paolo Mattavelli
*DTG*
*University of Padova*
Vicenza, Italy
paolo.mattavelli@unipd.it



***Abstract*—The deadtime is an important factor in design of power-electronics converters in order to prevent shoot-through faults. The deadtime may also cause a voltage error and undesired damping effect which, in turn, affect the converter stability. As most effects caused by the deadtime are highly nonlinear, conventional modeling techniques to analyze these effects cannot be straightforwardly applied. This paper proposes a novel frequency-domain approach to model the damping effect caused by the deadtime in single-phase half-bridge inverters. Hardware-in-the-loop (HIL) simulations and laboratory measurements are presented and used to demonstrate the effectiveness of the proposed method.**



***Index Terms*—frequency response, deadtime, damping**


## I. Introduction

One of the main goals in the design of synchronous switching power electronic converters is to prevent shoot-through faults. By delaying the turn-on of the switches by a period known as the *deadtime*, the shoot-through faults can be prevented [1], [2]. The deadtime length is the sum of the switch turn-off time and an additional safety margin. However, the deadtime causes a voltage error and undesired damping in the system, thus affecting the stability.

Fig. 1 presents the leg of a single-phase half-bridge inverter. During the deadtime, neither of the switches $S_1$ nor $S_2$ conducts, and the current commutates to an antiparallel diode, $D_1$ or $D_2$. The conducting diode is determined by the current direction; thus, the voltage applied over the leg during the deadtime depends on the current direction. The direction-dependency of the current causes a nonlinear voltage error [1].

A number of the previous research has focused on current and voltage distortions caused by the deadtime error [1], [3]–[5]. However, the deadtime effects in converter frequency-domain analysis have not been extensively considered in past studies. It is rarely specified, whether the effect of the deadtime is completely neglected or a compensation method is used. However, a few studies have addressed the issue of deadtime in a dynamic analysis of DC-DC converters [6] and three-phase inverters [7]–[10].

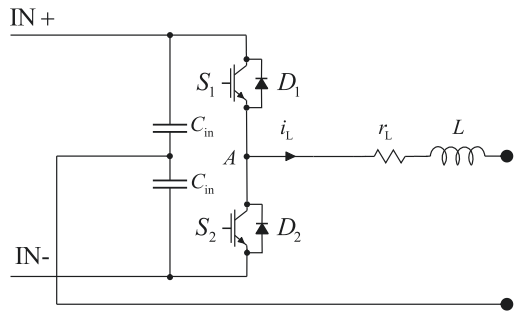


Figure 1: Leg from a half-bridge inverter.

In a dynamic power-converter analysis, the system is averaged over a switching cycle [11]. The fundamental problem in the analysis of deadtime effect is behind the fact that the effect is highly nonlinear. The effect is dependent on the current direction, and therefore, traditional averaging methods cannot be applied directly to solve the average effect of the deadtime. The deadtime is typically modeled as an equivalent series resistance in the small-signal modeling as in the case of the fundamental component in [2]. In [7], the fundamental components of the voltage errors were modeled in the phase domain and transformed to the synchronous reference frame. The results were time-invariant circuit elements that correspond to resistors among crosscoupling elements that appear in the synchronous reference frame. Furthermore, the small-signal effect has been shown to be a resistor also in [6]. The error caused by the deadtime effect in light load conditions was studied in detail in [12] and [13], but no frequency responses were shown. It has been shown that the resistor has its highest values under low load conditions [6]–[8]. Despite this interest, no one, to the best of our knowledge, has studied the deadtime effect on dynamics of single phase inverters. This paper examines how the deadtime affects the dynamics of a

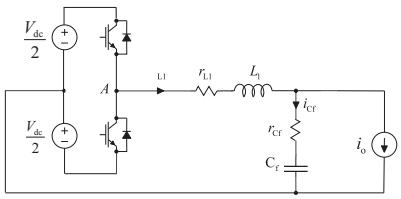


Figure 2: Half-bridge inverter.

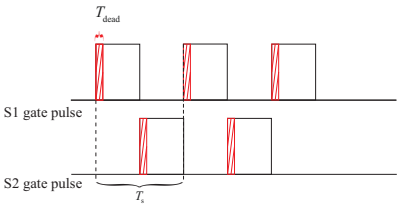


Figure 3: Gating pulses of a synchronous-switching half-bridge inverter.

Table I: Operating point and component values.

| Parameter | Value | Parameter | Value |
|---|---|---|---|
| $V_{dc}$ | 700 V | $C_{in}$ | 1.9 mF |
| $I_o$ | 15 A | $L_1$ | 2.5 mH |
| $V_{o,rms}$ | 120 V | $r_{L1}$ | 65 mΩ |
| $\omega_s$ | 2π60 rad/s | $C_f$ | 10 $\mu$F |
| $f_s$ | 10 kHz | $r_{Cf}$ | 0.3Ω |
| $T_s$ | 0.1 ms | $T_{dead}$ | 4 $\mu$s |

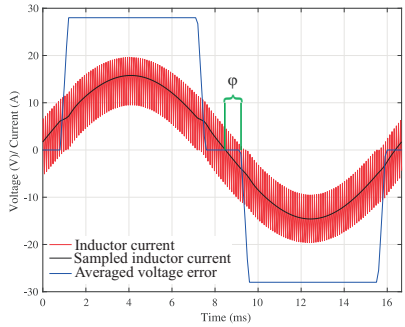


Figure 4: Current and average voltage error waveforms.

single phase AC system.

The remainder of the paper is organized as follows. Section II analyzes the voltage error caused by the deadtime as a function of the inductor current, the deadtime length, switching frequency, current perturbation amplitude and DC voltage. Section III presents the small-signal model of the inverter affected by deadtime, and verification by HIL simulations and laboratory measurements is presented. Finally, Section IV draws conclusions.

## II. Small-Signal Model

In this chapter, the deadtime effect on the dynamics of a half-bridge inverter is analyzed. First, a brief overview of an existing deadtime modeling method is given. Then, a Simulink model is used to show the effect of perturbations in the inductor current on the voltage error, and a model that is valid with reasonably high fundamental currents is derived based on analytical equations and the simulation results. Throughout the paper the voltage and current values refer to the amplitude of the AC waveform, unless otherwise stated.

### A. Background of the modeling principle

The half-bridge inverter under study is shown in Fig. 2 and the used parameters are shown in Table I. In order to analyze the unterminated dynamics of the converter, the load is modeled as an ideal current sink. In the case of a resistor as a load, the LC-resonance of the control-to-output transfer function would be highly damped.

The gating signals with the deadtime during the switching cycles, $T_s$ are shown in Fig. 3. The turn on of the both switches $S_1$ and $S_2$ is delayed by the deadtime, $T_{dead}$; thus, it is ensured that the switches are not on at the same time. The red area shows how the deadtime prevents a portion of the ideal gating pulse. If current $i_L$ is positive during the deadtime, it will commutate to the lower diode $D_2$. This will cause an error in the applied leg voltage if $S_1$ is conducting ideally. With negative $i_L$, the error in the voltage takes place when the turn on of $S_2$ is delayed, and the current flows through $D_1$. The losses of the switches and diodes are omitted because the focus is on the voltage error caused by the deadtime. Furthermore, a unity power factor operation is assumed.

The instantaneous voltage error, $v_{err}$, is given by

$$v_{err} = \text{sign}(i_L) V_{dc} \tag{1}$$

where $V_{dc}$ is the DC voltage. The error can be averaged over a switching cycle according to

$$v_{err}^{avg-Ts} = \frac{1}{T_s} \int_{\tau}^{\tau+T_s} v_{err}(t) dt. \tag{2}$$

Fig. 4 illustrates the waveforms of the voltage error that is averaged over a switching cycle, $v_{err}^{avg-Ts}$, and the inductor current $i_L$. In addition, the inductor current that is sampled at the switching frequency, $i_L^{Ts}$, is shown.

With the parameters of Table I, the amplitude of the average error is 28 V and the fundamental component of the error, $v_{err-f1}$, is given by

$$v_{err-f1} = \frac{4}{\pi} \frac{T_{dead}}{T_{sw}} V_{dc}. \tag{3}$$

It is apparent from Fig. 4 that the voltage error is not a square wave; the average of the voltage error is zero during the inductor current zero crossings because the sign of the instantaneous voltage error changes during a switching period. This zero crossing period was modeled with a modified sign

function in [5], and the resulting effect on the fundamental component is

$$v_{\mathrm{err-f1-mod}} = \frac{4}{\pi}\frac{T_{\mathrm{dead}}}{T_{\mathrm{sw}}}V_{\mathrm{dc}}\cos(\varphi) \tag{4}$$

where $\varphi$ is the angle corresponding to the zero crossings of the inductor current. The angle is dependent on [5] the inductor current fundamental component amplitude $A_{\mathrm{fund}}$ and the inductor current peak-to-peak ripple $\Delta I_{\mathrm{p-p}}$ according to

$$\varphi = \sin^{-1}\left(\frac{\frac{\Delta I_{\mathrm{p-p}}}{2}}{A_{\mathrm{fund}}}\right). \tag{5}$$

### *B. Novel small-signal modeling approach*

Regarding the modeling of the small-signal dynamics, a similar approach is used in this study as in the case of fundamental component in [5]. First, it is shown with simulations how a sinusoidal perturbation affects the voltage error waveform. Then, a model is developed based on the observations from the simulations.

The average voltage error waveform is studied under sinusoidal perturbations from the output current, $i_o$. In order to efficiently illustrate the deadtime effect, the perturbation amplitudes are increased to overly necessary values in the simulations. Figs. 5 and 6 show the simulation results under the same system operating conditions that were applied for obtaining the results in Fig. 4, but with the difference of added 2 A and 5 A sinusoidal injections at 1190 Hz in $i_{\mathrm{o}}$, respectively. Due to the perturbation, the voltage error has a visible component at the injection frequency. Since the voltage error is a function of the current, it could be modeled with a resistive element. However, the voltage error is dependent on the current perturbation amplitude and the fundamental inductor current amplitude. As shown in Figs. 5 and 6, with a lower perturbation amplitude, the error component at the perturbation frequency has a low amplitude, and it exists only around the original zero crossing of the unperturbed inductor current. As the amplitude of the perturbation is increased, the length of the fundamental cycle during which the average voltage error changes is longer. In addition, the amplitude of the error increases. It should be noted that some zero current clampings take place. They cause an instantaneous voltage error other than $\pm V_{\mathrm{dc}}$.

On combining the observations from the simulations, it can be deduced that the angle during which zero crossings take place is a key factor in modeling the deadtime effect. A model considering the zero crossings in the deadtime analysis was developed in [14], but a different model is proposed in this paper. Now there are two angles, $\varphi_1$ and $\varphi_2$, regarding the inductor current zero crossings. The angles are proportional to the perturbation amplitude, $A_{\mathrm{pert}}$, and inversely proportional to the fundamental amplitude ,$A_{\mathrm{fund}}$:

$$\varphi_1 = \sin^{-1}\left(\frac{\frac{\Delta I_{\mathrm{p-p}}}{2} - A_{\mathrm{pert}}}{A_{\mathrm{fund}}}\right) \tag{6}$$

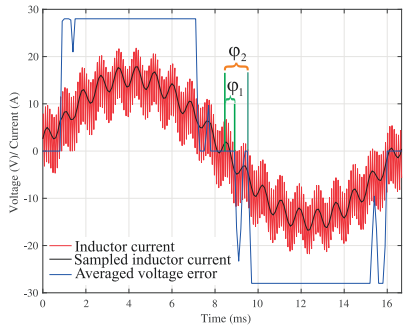


Figure 5: Current and average voltage error waveforms with a fundamental current amplitude of 15.2 A and perturbation amplitude of 2.2 A.

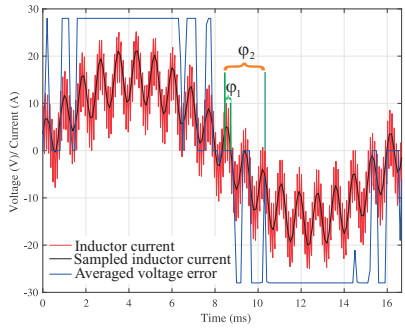


Figure 6: Current and average voltage error waveforms with a fundamental current amplitude of 15.2 A and perturbation amplitude of 5.4 A.

$$\varphi_2 = \sin^{-1}\left(\frac{\frac{\Delta I_{\mathrm{p-p}}}{2} + A_{\mathrm{pert}}}{A_{\mathrm{fund}}}\right) \tag{7}$$

where $\varphi_1$ is the angle during which the inductor current crosses zero every switching cycle, and $\varphi_2$ is the angle between the original fundamental zero crossing and the largest angle where a zero crossing takes place due to the perturbation. Applying (6) and (7), the proportion, $p$, of the switching cycle during which the current perturbation affects the voltage error can be expressed as shown in (8). Because the angles are between zero and $\pi$ radians and changed to a proportion between 0 and 1, a division by $\pi$ is required.

$$p = \frac{1}{\pi}\left(\varphi_2 - \varphi_1\right) \tag{8}$$

The average small-signal voltage error can be related to the proportion, $p$, and the amplitude of the square wave error:

$$\hat{v}_{\mathrm{err}}^{\mathrm{avg}}(A_{\mathrm{pert}}) = pK\frac{T_{\mathrm{dead}}}{T_{\mathrm{sw}}}V_{\mathrm{dc}} \tag{9}$$

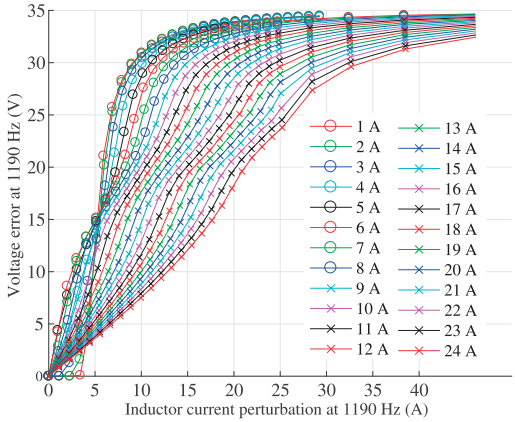


Figure 7: Current and voltage error at the injection frequency with different fundamental load current amplitudes.

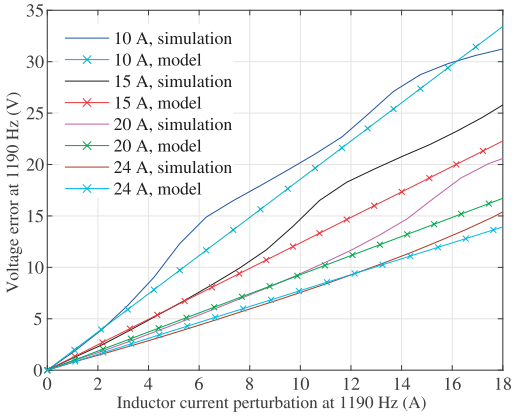


Figure 8: Simulated and modeled (using $r_{\mathrm{dead}}$) small-signal voltage error at the injection frequency with different fundamental load current amplitudes.

where $K$ is a gain other than $\frac{4}{\pi}$, because the error at the perturbation frequency is not a square wave.

In order to find the value for $K$, a heuristic approach is used. The error waveform at the perturbation frequency in Figs. 5 and 6 has properties of both a square wave and triangular wave; therefore, the average of the fundamental components of a square wave and triangle wave is given by

$$K = \frac{\frac{8}{\pi^2} + \frac{4}{\pi}}{2} = \frac{2\pi + 4}{\pi^2} \approx 1.04. \tag{10}$$

The final expression for the error is

$$\begin{aligned} \hat{v}_{\mathrm{err}}^{\mathrm{avg}}(A_{\mathrm{pert}}) = \\ \sin^{-1}\left(\frac{\frac{\Delta I_{\mathrm{p-p}}}{2} + A_{\mathrm{pert}}}{A_{\mathrm{fund}}}\right)\frac{K}{\pi}\frac{T_{\mathrm{dead}}}{T_{\mathrm{sw}}}V_{\mathrm{dc}} \\ -\sin^{-1}\left(\frac{\frac{\Delta I_{\mathrm{p-p}}}{2} - A_{\mathrm{pert}}}{A_{\mathrm{fund}}}\right)\frac{K}{\pi}\frac{T_{\mathrm{dead}}}{T_{\mathrm{sw}}}V_{\mathrm{dc}}. \end{aligned} \tag{11}$$

The effects of different combinations of the fundamental current amplitude and perturbation amplitude on the small-signal voltage error are shown in Fig. 7. The voltage error amplitude dependency on the perturbation amplitude is non-linear with fundamental currents lower than half the inductor current ripple, $\Delta I_{\mathrm{p-p}}$. However, the higher the fundamental current amplitude with reasonable perturbation amplitudes, the more linear is the dependency. Thus, the deadtime effect can be modeled with a constant resistor that is the derivative of $\hat{v}_{\mathrm{err}}^{\mathrm{avg}}(A_{\mathrm{pert}})$:

$$\begin{aligned} r_{\mathrm{DT}} =& \frac{d}{dA_{\mathrm{pert}}}\hat{v}_{\mathrm{err}}^{\mathrm{avg}}(A_{\mathrm{pert}}) \\ =& \frac{K\frac{T_{\mathrm{dead}}}{T_{\mathrm{sw}}}V_{\mathrm{dc}}/\pi}{A_{\mathrm{fund}}\sqrt{1-\left(\frac{\Delta I_{\mathrm{p-p}}/2+A_{\mathrm{pert}}}{A_{\mathrm{fund}}}\right)^2}} \\ &+ \frac{K\frac{T_{\mathrm{dead}}}{T_{\mathrm{sw}}}V_{\mathrm{dc}}/\pi}{A_{\mathrm{fund}}\sqrt{1-\left(\frac{\Delta I_{\mathrm{p-p}}/2-A_{\mathrm{pert}}}{A_{\mathrm{fund}}}\right)^2}}. \end{aligned} \tag{12}$$

As stated earlier, the fundamental current amplitude is assumed high. Furthermore, the perturbation amplitude is assumed small. With these assumptions, the equation for the average small-signal error reduces to (13).

$$r_{\mathrm{DT}} = \frac{2}{\pi A_{\mathrm{fund}}}K\frac{T_{\mathrm{dead}}}{T_{\mathrm{sw}}}V_{\mathrm{dc}} \tag{13}$$

Fig. 8 shows that the proposed model approximates the error well with high fundamental currents. It can be noted that the expression for $r_{\mathrm{DT}}$ bears a close resemblance to the existing model [7] with the term $\frac{T_{\mathrm{dead}}}{A_{\mathrm{fund}}T_{\mathrm{sw}}}V_{\mathrm{dc}}$. However, the proposed model is derived with a completely different approach for a different converter topology.

## III. Frequency Response Analysis

This section deals with the deadtime affected transfer functions. The transfer functions related to the control and output dynamics are derived, and the output impedances compared to the results obtained by the HIL simulations and the laboratory measurements.

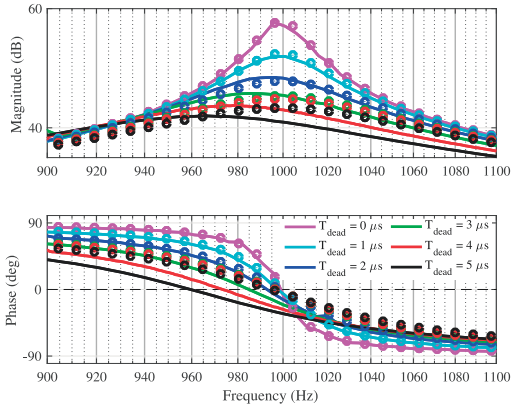


Figure 9: Open-loop output impedance $Z_{\mathrm{o-o}}$: HIL simulation (solid lines) and model (dots).

### A. HIL simulations

The transfer functions for the half-bridge inverter are defined by using the impedances of the filer inductor, $Z_{\mathrm{L}}$, and capacitor, $Z_{\mathrm{C}}$:

$$Z_{\mathrm{C}} = r_C + \frac{1}{sC_{\mathrm{f}}} \tag{14}$$

$$Z_{\mathrm{L}} = r_{\mathrm{DT}} + r_L + sL. \tag{15}$$

It is to be noted that $r_{\mathrm{DT}}$ in (13) is included in the filter inductor impedance in (15). If the DC capacitors are included in the model, they appear connected parallel (16) with the inductor.

$$Z_{\mathrm{DC-C}} = \frac{\left(r_{\mathrm{C-DC}} + \frac{1}{sC_{\mathrm{DC}}}\right)\left(r_{\mathrm{C-DC}} + \frac{1}{sC_{\mathrm{DC}}}\right)}{\left(r_{\mathrm{C-DC}} + \frac{1}{sC_{\mathrm{DC}}}\right) + \left(r_{\mathrm{C-DC}} + \frac{1}{sC_{\mathrm{DC}}}\right)} \tag{16}$$

The parallel connection of the filter inductor, $Z_{\mathrm{L}}$, and capacitor , $Z_{\mathrm{C}}$, impedances forms the open-loop output impedance, $Z_{\mathrm{o-o}}$, of the system:

$$Z_{\mathrm{o-o}} = \frac{Z_{\mathrm{C}}\left(Z_{\mathrm{L}} + Z_{\mathrm{DC-C}}\right)}{Z_{\mathrm{C}} + \left(Z_{\mathrm{L}} + Z_{\mathrm{DC-C}}\right)} \tag{17}$$

The open-loop control-to-output voltage transfer function, $G_{\mathrm{co-o}}$, is given by

$$G_{\mathrm{co-o}} = \frac{Z_{\mathrm{C}}}{Z_{\mathrm{C}} + Z_{\mathrm{L}}}. \tag{18}$$

A Typhoon HIL 402 simulator is used to verify the deadtime effect in frequency responses. The switches are modeled as ideal switches in the simulator, and the controller is implemented in the simulator so that a simulation can be run without the deadtime to exclude the deadtime effect for comparison. The output impedance, $Z_{\mathrm{o-o}}$, of the system is measured in an HIL simulation by making a parallel current injection to a resistive load. The deadtime damps the resonance in the output impedance, and Fig. 9shows that the proposed model is accurate with reasonable values of deadtime (1-2 $\mu$s).

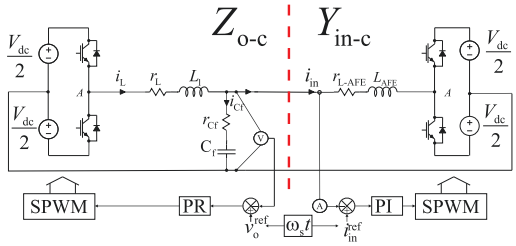


Figure 10: Interconnected AC half-bridge converters.

It is possible to state now that the deadtime effect can be clearly seen in the frequency responses. However, it is still unclear whether the damping is only a measurement effect or if it can affect the stability. The deadtime effect on the stability is studied with an interconnected system of an output voltage and input current controlled half-bridge AC converters. The circuit diagram is shown in Fig. 10. For the sake of simplicity, the phase-locked loop (PLL) and DC-voltage control of the active rectifier (AFE) are omitted. This simplification is justified because the LC resonance that is causing the instability is at higher frequencies than the bandwidths of the traditional PLL and DC voltage control.

The output voltage of the inverter and the input current of the AFE are controlled by a PR-controller and a PI-controller, respectively. The crossover frequency of the current loop gain is 942 Hz, the phase margin is 27° and the gain margin is 4.4 dB. The PR-controller can be given by

$$G_{\mathrm{vc}}(s) = K_{\mathrm{p-v}} + \frac{2K_{\mathrm{i-v}}\omega_{\mathrm{b}}s}{s^2 + 2\omega_{\mathrm{b}}s + \omega_{\mathrm{s}}^2}, \tag{19}$$

where $K_{\mathrm{p-v}}$, $K_{\mathrm{i-v}}$ and $\omega_{\mathrm{b}}$ are the proportional gain, integral gain and the bandwidth around the synchronous frequency, $\omega_{\mathrm{s}}$, respectively. Fig. 11 shows both the loop gains. The system parameters are shown in Table II.

The stability of the system is analyzed at the interface of $Y_{\mathrm{in-c}}$ and $Z_{\mathrm{o-c}}$. The closed-loop output impedance, $\mathrm{Z_{o-c}}$, is given by

$$\mathrm{Z_{o-c}} = \frac{\mathrm{Z_{o-o}}}{1 + G_{\mathrm{co-o}}G_{\mathrm{vc}}G_{\mathrm{del}}}, \tag{20}$$

where $G_{\mathrm{del}}$ is the Padé approximation for the delay that is 1.5 $T_{\mathrm{s}}$. Fig. 12 shows the modeled input and output impedances. The deadtime length has not as significant effect on the input impedance as it has on the output impedance; there is almost no difference in the input impedance with the deadtime lengths of 1 $\mu$ and 2 $\mu$. Due to the current controller of AFE, there is

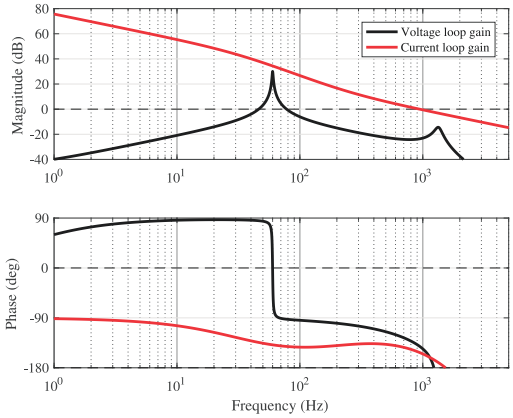


Figure 11: Control loops gains of half-bridge inverters: the PR-controller of voltage output inverter and the PI-controller of the AFE input current.

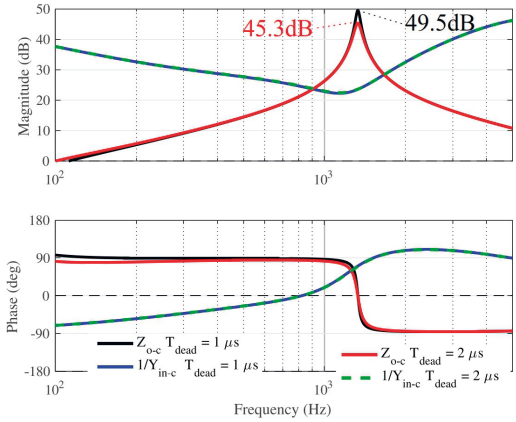


Figure 12: Output impedance of the output voltage controlled inverter and the input impedance of the input current controlled AFE with deadtime lengths of 1 $\mu$s and 2 $\mu$s .

already a high amount of damping and the relatively small $r_{\mathrm{DT}}$ has a non-visible effect. In the following, the same deadtime length is used for both the converters.

There is a potential for a harmonic instability at around 1.6 kHz because the gain curves overlap and the phase difference is more than 180° . When the deadtime length is increased from 1 $\mu$s to 2 $\mu$s, there is a decrease of 4.2 dB in the output impedance. An impedance based stability analysis is performed by using a Nyquist plot. Fig. 13 illustrates the Nyquist plot of the modeled impedance ratio $Z_{\mathrm{o-c}}Y_{\mathrm{in-c}}$ with the deadtime lengths of 1 $\mu$s and 2 $\mu$s . With a deadtime of 1 $\mu$s, the point (-1,0) is encircled; thus, the system is unstable in the operating point where the fundamental load current is 15 A.

Table II: Operating point and component values of interconnect converters.

| Parameter | Value | Parameter | Value |
|---|---|---|---|
| $V_{\mathrm{dc}}$ | 700 V | $C_{\mathrm{in}}$ | 1.9 mF |
| $I_{\mathrm{o}} = I_{\mathrm{in}}$ | 15 A | $L_1$ | 1.4mH |
| $V_{\mathrm{o,rms}}$ | 120 V | $r_{\mathrm{L1}}$ | 25 |
| $\omega_{\mathrm{s}}$ | 2$\pi$60 rad/s | $C_{\mathrm{f}}$ | 10 $\mu$F |
| $f_{\mathrm{s}}$ | 10 kHz | $r_{\mathrm{Cf}}$ | 10 m$\Omega$ |
| $T_{\mathrm{s}}$ | 0.1 ms | $T_{\mathrm{dead}}$ | 1-4 $\mu$s |
| $L_{\mathrm{AFE}}$ | 5.5mH | $r_{\mathrm{LAFE}}$ | 10 m$\Omega$ |
| $K_{\mathrm{P\text{-}AFE}}$ | 0.0452 | $K_{\mathrm{I\text{-}AFE}}$ | 65.28 |
| $K_{\mathrm{P\text{-}v}}$ | 0.0050 | $K_{\mathrm{I\text{-}v}}$ | 31.62 |
| $\omega_{\mathrm{b}}$ | $\pi$ rad/s | | |

The voltage and the input current reference waveforms are shown in Fig. 14 as the input current amplitude of the active rectifier is increased slowly to 15 A. With a deadtime of 1 $\mu$s, the system is harmonically unstable as it is predicted by the Nyquist diagram. The deadtime length of 2 $\mu$s stabilizes the system. Nevertheless, the LC resonance is not completely damped by $r_{\mathrm{dead}}$. It is emphasized that the only parameter that was changed between the two simulations was the deadtime

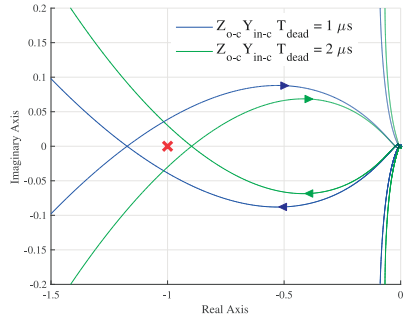


Figure 13: Nyquist diagram of the impedance ratio with the deadtime lengths of 1 $\mu$s and 2 $\mu$s.

length of both the half-bridges (from 1 $\mu$s to 2 $\mu$s). This confirms that the deadtime length can be a crucial factor affecting a power electronics system stability.

### *B. Laboratory measurements*

The applied experimental setup is shown in Fig. 15. The applied half bridge module and control platform are a PEB-8032 module and a Boombox control platform by Imperix, respectively. The LC-filtered half-bridge inverter is loaded by parallel connected resistors, and the operation point was defined by changing the number of parallel connected resistors. An amplifier with an injection transformer that is connected in series with one of the resistors was used to perturb the load current. The perturbation reference for the amplifier was created by a multipurpose I/O device by National instruments that was also used to record the waveforms. The same PR controller as in the simulation was used in the experimental measurements. The component parameters are given in Table III.

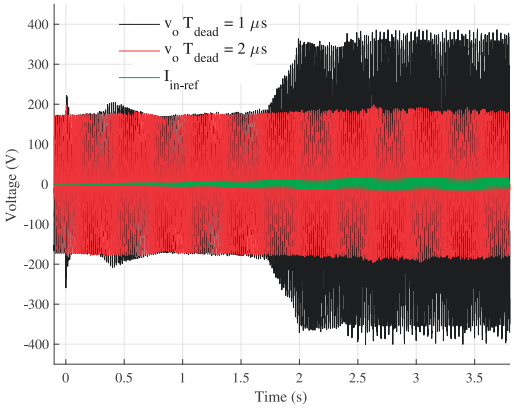


Figure 14: Voltage waveforms with the deadtime lengths of 1 $\mu$s and 2 $\mu$s.

Table III: Operating point and component values of experimental converter.

| Parameter | Value | Parameter | Value |
|---|---|---|---|
| $V_{dc}$ | 700 V | $C_{dc}$ | 500 $\mu$F |
| $I_o$ | 3—21 A | $L_1$ | 0.79mH |
| $V_{o,rms}$ | 120 V | $r_{L1}$ | 0.16—1.2Ω |
| $\omega_s$ | 2$\pi$60 rad/s | $C_f$ | 9.8 $\mu$F |
| $f_s$ | 20 kHz | $r_{Cf}$ | 0.11 Ω |

Fig. 16 shows the measured output impedance with the deadtime length of 1 $\mu$s and different values of the output current. The damping effect of the deadtime can clearly be seen in the frequency responses. Both the resonance from the parallel connected L and C at 1.8 kHz and the antiresonance from the DC capacitors and the inductor at 200 Hz are damped. It can be seen that with low fundamental current amplitudes (3 A and 4.5 A) there is some damping. This is in line with the observations from Fig. 7. Because the fundamental current is lower than half the inductor current ripple (here 8.7 A), the perturbations from the load current have little effect on zero crossings in the inductor current; thus, the deadtime effect is small. When the fundamental current amplitude is close to half the peak-to-peak current ripple, the damping is high and the damping decreases as the fundamental current amplitude is increased.

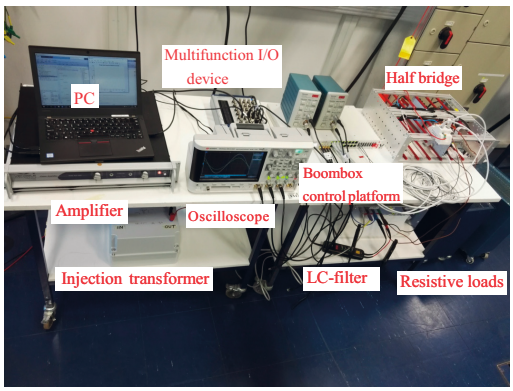


Figure 15: Laboratory setup.

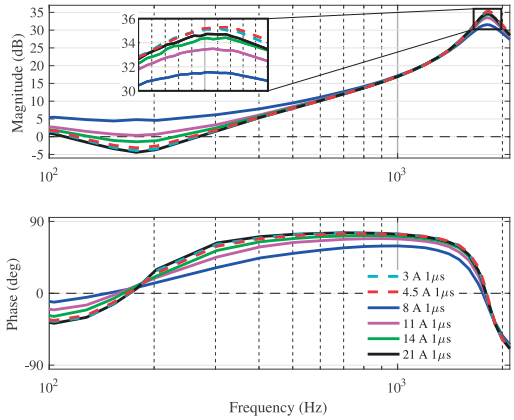


Figure 16: Experimental frequency response of the closed-loop output impedance.

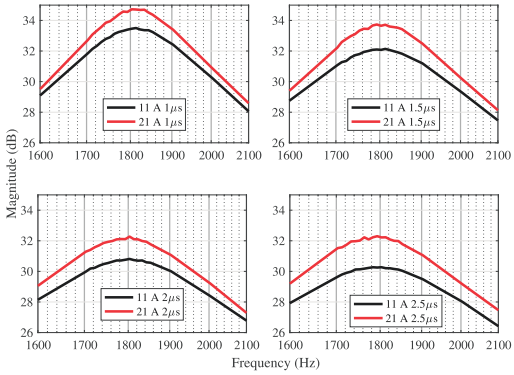


Figure 17: Measured fundamental current amplitude effect on the deadtime damping.

Fig. 17 compares the measured output impedance resonance peak magnitude with the deadtime lengths of 1, 1.5, 2 and 2.5 $\mu$s and the fundamental output current of 11 A and 21 A. The measurements verify that the higher the fundamental current, the lower the damping with a given deadtime length.

In Figs. 18 and 19, the measurements are compared with the proposed model. The experimental results clearly verify that increasing the deadtime length increases damping of the system. The comparison is done separately around both the antiresonance and the resonance frequency, because the ESR of the inductor changes due to the proximity and skin effects and no frequency dependent ESR model is used [15]. Fig.

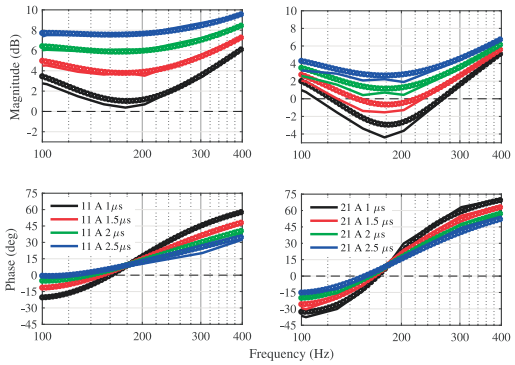


Figure 18: Measurements (solid line) and model (dots) of the antiresonance peak damped by the deadtime with fundamental currents of 11 A (left) and 21 A (right).

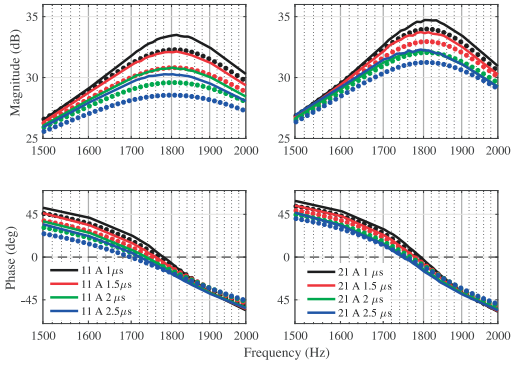


Figure 19: Measurements (solid line) and model (dots) of the resonance peak damped by the deadtime with fundamental currents of 11 A (left) and 21 A (right).

18 shows that the model correctly predicts the damping at low frequencies with the load currents of 11 A and 21 A. At higher frequencies, the model is not as accurate as it can be seen from Fig. 19. However, the model predicts the change in the damping relatively well.

## IV. Conclusions

This paper has provided a frequency-domain analysis of the deadtime effect, which gives a novel heuristic approach to approximate the deadtime effect in single-phase AC systems. The damping effect was verified by experimental measurements on the closed-loop output impedance of a voltage controlled half-bridge inverter.

HIL-simulations were used to show that by increasing the deadtime length, an unstable system can be stabilized. The importance of selecting correct deadtime length in simulation cannot be stressed too much. The selection of the correct deadtime length is very important.

Given the limited number of different load conditions applied caution must be exercised, because the proposed model clearly has some limitations. The most important limitation in the heuristic model lies in the assumption that the wave forms are clean sinusoidal and the power factor is one. In addition, ideal switches were used in the model derivation. Further experimental tests are needed to estimate the deadtime effect on practical systems stability. More research is needed to determine the contribution of the zero current clamping on the small-signal deadtime effect.

## References


[1] Seung-Gi Jeong and Min-Ho Park, "The analysis and compensation of dead-time effects in PWM inverters," *IEEE Trans. on Ind. Electron.*, vol. 38, no. 2, pp. 108–114, apr 1991.

[2] D. Holmes and T. Lipo, *Pulse Width Modulation for Power Converters: Principles and Practice*, ser. IEEE Press Series on Power Engineering. John Wiley & Sons, 2003.

[3] A. Mora, J. Juliet, A. Santander, and P. Lezana, "Dead-time and semiconductor voltage drop compensation for cascaded H-bridge converters," *IEEE Trans. Ind. Electron.*, vol. 63, no. 12, pp. 7833–7842, dec 2016.

[4] R. Shan, X. Xiao, Z. Yin, and Q. Liu, "Compensation strategy of switching dead-time effect based on frequency domain model," *2010 5th IEEE Conference on Industrial Electronics and Applications*, vol. 2, pp. 997–1001, 2010.

[5] G. Grandi, J. Loncarski, and R. Seebacher, "Effects of current ripple on dead-time distortion in three-phase voltage source inverters," *2012 IEEE International Energy Conference and Exhibition (ENERGYCON)*, pp. 207–212, 2012.

[6] W. Qiu, S. Mercer, Z. Liang, and G. Miller, "Driver deadtime control and its impact on system stability of synchronous buck voltage regulator," *IEEE Trans. Power Electron.*, vol. 23, no. 1, pp. 163–171, 2008.

[7] S. Ahmed, Z. Shen, P. Mattavelli, D. Boroyevich, and K. J. Karimi, "Small-signal model of voltage source inverter (VSI) and voltage source converter (VSC) considering the deadtime effect and space vector modulation types," *IEEE Trans. Power Electron.*, vol. 32, no. 6, pp. 4145–4156, jun 2017.

[8] A. Rodriguez-Cabero, M. Prodanovic, and J. Roldan-Perez, "Analysis of dynamic properties of VSCs connected to weak grids including the effects of dead-time and time delays," *IEEE Trans. Sustainable Enery*, Early Access.

[9] A. Guha and G. Narayanan, "Impact of undercompensation and overcompensation of dead-time effect on small-signal stability of induction motor drive," *IEEE Trans. Ind. Appl.*, vol. 54, no. 6, pp. 6027–6041, 2018.

[10] J. Svensson and M. Lindgren, "Influence of nonlinearities on the frequency response of a grid-connected vector-controlled VSC," *IEEE Trans. on Ind. Electron.*, vol. 46, no. 2, pp. 319–324, apr 1999.

[11] R. D. Middlebrook, "Small-signal modeling of pulse-width modulated switched-mode power converters," *Proceedings of IEEE*, vol. 76, no. 4, pp. 343–354, 1988.

[12] A. Rothstein and V. Staudt, "Detailed analysis of converter-output-voltage errors under light-load conditions," in *2017 International Conference on Optimization of Electrical and Electronic Equipment (OPTIM) & 2017 Intl Aegean Conference on Electrical Machines and Power Electronics (ACEMP)*. IEEE, may 2017, pp. 336–341.

[13] S. M. Seyyedzadeh and A. Shoulaie, "Accurate modeling of the nonlinear characteristic of voltage source inverter for better performance in near zero currents," *IEEE Trans. Ind. Electron.*, vol. 66, no. 1, pp. 71–78, 2018.

[14] S. Chen, Z. Chen, and W. Yu, "Multiple PR current regulator based dead-time effects compensation for grid-forming single-phase inverter," *2018 IEEE Energy Conversion Congress and Exposition, ECCE 2018*, pp. 3134–3141, 2018.

[15] H. Matsumori, T. Shimizu, F. Blaabjerg, X. Wang, and D. Yang, "Stability Influence of Filter Components Parasitic Resistance on LCL-Filtered Grid Converters," in *2018 International Power Electronics Conference (IPEC-Niigata 2018 -ECCE Asia)*. IEEE, may 2018, pp. 3357–3362.

# Publication IV

**Frequency Response Analysis of Load Effect on Dynamics of Grid-Forming Inverter**

M. Berg, T. Messo, and T. Suntio

*International Power Electronics Conference 2018 -ECCE Asia*,
*pp. 963—970, 2018.*

# Frequency Response Analysis of Load Effect on Dynamics of Grid-Forming Inverter

Matias Berg*, Tuomas Messo, Teuvo Suntio
Laboratory of Electrical Energy Engineering, Tampere University of Technology, Tampere, Finland
*E-mail: matias.berg@tut.fi

***Abstract*—The grid-forming mode of the voltage source inverters (VSI) is applied in uninterruptible power supplies and micro-grids to improve the reliability of electricity distribution. During the intentional islanding of an inverter-based micro-grid, the grid-forming inverters (GFI) are responsible for voltage control, similarly as in the case of uninterruptible power supplies (UPS). The unterminated model of GFI can be developed by considering the load as an ideal current sink. Thus, the load impedance always affects the dynamic behavior of the GFI. This paper proposes a method, to analyze how the dynamics of GFI and the controller design are affected by the load. Particularly, how the frequency response of the voltage loop gain changes according to the load and, how it can be used to the predict time-domain step response. The frequency responses that are measured from a hardware-in-the-loop simulator are used to verify and illustrate explicitly the load effect.**

***Keywords*—grid-forming inverter, dynamics, dq-domain, load effect**

## I. Introduction

The recent years have witnessed a huge growth in the number of installed distributed photovoltaic generation systems. Distributed generation with an energy storage system in a micro-grid enables the intentional islanding of the micro-grid during a failure in the utility network [1], [2]. If there are no rotating generators in the micro-grid, the inverters that normally operate in the grid-feeding mode, have to form the grid during the intentional islanding [3]. The dynamics of the grid-forming inverter (GFI) differ from the dynamics of the grid-feeding inverter. The grid-forming inverter is a voltage-output converter and the grid-feeding inverter is a current-output converter [4]. An ideal current sink as the load of GFI is the basis fo the dynamic analysis, but the load effect has to be taken into account.

The importance of modeling the output impedance of power-electronics-based systems has been widely addressed [5]–[7]. In order to derive the output impedance, the output current has to be considered an input variable. The output impedance has been derived this way in [5]. The output impedance modeled in [5] is verified by frequency response measurements, but the other transfer functions are not measured. Dynamics of an LC-filter has been included to the input admittance of an active rectifier for the purposes of impedance-based analysis in [8]. Passive loads have been modeled as a part of system consisting of grid-connected solar inverter and an active rectifier in [9]. However, the analysis is focused on the frequency responses of impedances and the effect of the filter on control-to-output transfer functions was not analyzed in [8], [9].

The control-related transfer functions change if the load is changed from a current sink to a passive or active load. The output impedance of the grid-forming inverter has been derived also in [10] and the output current is considered as an input variable. The unterminated dynamics are analyzed when the controllers are tuned. However, the simulation and practical tests are done with passive and non-linear loads without analyzing the load effect to the control loops. In [11] the output current of a single-phase system is considered as an input variable and the unterminated model is used to derive the transfer functions. The time-domain behavior is tested under a resistive load and a non-linear load. However, the load effect on the loop gains is not shown.

A load-affected transfer function is directly derived in phase domain in [1]. However, no frequency-response verification is presented. A dynamic model of a passive load is derived in [12], but it is not used for frequency response analysis of the system. In [2] the load is analyzed in the dq-domain and included in the system model, but frequency response analysis is missing. A passive load has been addressed also in [13] and [14], but no frequency responses are analyzed.

This paper proposes a method, that can be used to analyze the load effect on the unterminated dynamics of GFI in the frequency domain. The rest of the paper is organized as follows: Section II introduces the modeling of the unterminated dynamics of the three-phase grid-forming inverter in dq-domain. Section III examines the load effect on the dynamics of GFI. Frequency response analysis of the load effect is used to tune the controllers and to predict the time-domain response in Section IV. The conclusions are finally presented in Section V.

## II. Unterminated small-signal model

The used averaging and linearizing method originates from the work of Middlebrook [15]. Figure 1 shows the circuit diagram of a three-phase grid-forming inverter. The load is assumed to be an ideal three phase current sink in the dynamic analysis. Thus, the grid inductance or load side inductors of the LCL-filter cannot be included in the unterminated models due to violation of Kirchoff's law. Output impedance of the grid-forming inverter and the other input-to-output transfer function can be derived by analyzing the power stage in Fig. 1. The input variables are input voltage, duty-ratios and output currents. The

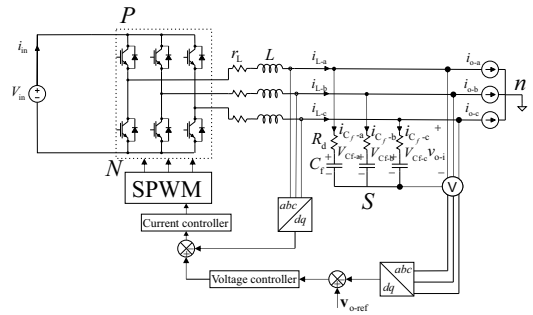


Figure 1. Circuit diagram of the grid-forming inverter including a simplified control system.

output variables are input current, inductor currents and output voltages. The inductor currents are chosen as output variables, because they are commonly needed in the cascaded control of the output voltage.

A state-space model of the grid-forming inverter is derived. The capacitor voltages and inductor currents are chosen as the state variables. Modeling in the synchronous reference frame is applied. For brevity, the equations are shown directly in the synchronous reference frame (DQ-frame). In the following equations, subscripts d and q denote whether the corresponding variable is either the direct or quadrature component. $i_{\mathrm{L}}$ is the inductor current, $i_{\mathrm{o}}$ the output current, $d$ the duty ratio, $v_{\mathrm{in}}$ the input voltage, $v_{\mathrm{Cf}}$ the filter capacitor voltage, $i_{in}$ the input current. Angle brackets around the variables in (1)–(7) denote that equations are averaged over one switching period. Thus, on and off-time equations are not shown separately.

$$\langle i_{in} \rangle = \frac{3}{2} \left( d_{\mathrm{d}} \langle i_{\mathrm{Ld}} \rangle + d_{\mathrm{q}} \langle i_{\mathrm{Lq}} \rangle \right) \tag{1}$$

$$\begin{aligned} \frac{\mathrm{d} \langle \mathrm{i_{Ld}} \rangle}{\mathrm{dt}} = \frac{1}{L} \big[ & d_{\mathrm{d}} \langle v_{\mathrm{in}} \rangle - (r_{\mathrm{L}} + r_{\mathrm{sw}} + R_{\mathrm{d}}) \langle i_{\mathrm{Ld}} \rangle \\ & + \omega_s i_{\mathrm{Lq}} + R_{\mathrm{d}} \langle i_{\mathrm{od}} \rangle - \langle v_{\mathrm{Cfd}} \rangle \big] \end{aligned} \tag{2}$$

$$\begin{aligned} \frac{\mathrm{d} \langle \mathrm{i_{Lq}} \rangle}{\mathrm{dt}} = \frac{1}{L} \big[ & d_{\mathrm{q}} \langle v_{\mathrm{in}} \rangle - (r_{\mathrm{L}} + r_{\mathrm{sw}} + R_{\mathrm{d}}) \langle i_{\mathrm{Lq}} \rangle \\ & - \omega_s i_{\mathrm{Ld}} + R_{\mathrm{d}} \langle i_{\mathrm{oq}} \rangle - \langle v_{\mathrm{Cfq}} \rangle \big] \end{aligned} \tag{3}$$

$$\frac{\mathrm{d} \langle \mathrm{v_{Cfd}} \rangle}{\mathrm{dt}} = \frac{1}{C_f} \left[ \langle i_{\mathrm{Ld}} \rangle + \omega_s v_{\mathrm{Cfq}} - \langle i_{\mathrm{od}} \rangle \right] \tag{4}$$

$$\frac{\mathrm{d} \langle \mathrm{v_{Cfq}} \rangle}{\mathrm{dt}} = \frac{1}{C_{\mathrm{f}}} \left[ \langle i_{\mathrm{Lq}} \rangle - \omega_s v_{\mathrm{Cfd}} - \langle i_{\mathrm{oq}} \rangle \right] \tag{5}$$

$$\langle v_{\mathrm{od}} \rangle = \langle v_{\mathrm{Cfd}} \rangle + R_{\mathrm{d}} \langle i_{\mathrm{Ld}} \rangle - R_{\mathrm{d}} \langle i_{\mathrm{od}} \rangle \tag{6}$$

$$\langle v_{\mathrm{oq}} \rangle = \langle v_{\mathrm{Cfq}} \rangle + R_{\mathrm{d}} \langle i_{\mathrm{Lq}} \rangle - R_{\mathrm{d}} \langle i_{\mathrm{oq}} \rangle , \tag{7}$$

where $C_f$, $L$, $d$, $r_{sw}$ and $\omega_{\mathrm{s}}$ denote filter capacitor, filter inductor, duty ratio, parasitic resistance of a switch, grid angular frequency, respectively. $r_L$ is the equivalent series resistance of the filter inductor. The damping resistance that includes the filter capacitor equivalent series resistance is denoted by $R_D$. Capital letters denote steady-state values at the operating point.

Equations (1)–(7) are linearized at the steady-state operation point and transformed into the frequency domain. The linearized equations are expressed by coefficient matrices $\mathbf{A}$, $\mathbf{B}$, $\mathbf{C}$ and $\mathbf{D}$ , input variable vector $\mathbf{U}$, output variable vector $\mathbf{Y}$ and state variable vector $\mathbf{X}$. Equation (8) shows the state space after transformation to frequency domain using the Laplace variable 's' and the output and input variable vectors are shown in (9) and (10), respectively.

$$\begin{aligned} s\mathbf{X}(s) &= \mathbf{A}\mathbf{X}(s) + \mathbf{B}\mathbf{U}(s) \\ \mathbf{Y}(s) &= \mathbf{C}\mathbf{X}(s) + \mathbf{D}\mathbf{U}(s) \end{aligned} \tag{8}$$

The coefficient matrices are shown in (11)–(14).

$$\mathbf{Y} = \begin{bmatrix} \hat{i}_{\mathrm{in}} & \hat{i}_{\mathrm{Ld}} & \hat{i}_{\mathrm{Lq}} & \hat{v}_{\mathrm{od}} & \hat{v}_{\mathrm{oq}} \end{bmatrix}^T \tag{9}$$

$$\mathbf{U} = \begin{bmatrix} \hat{v}_{\mathrm{in}} & \hat{i}_{\mathrm{od}} & \hat{i}_{\mathrm{oq}} & \hat{d}_{\mathrm{d}} & \hat{d}_{\mathrm{q}} \end{bmatrix}^T \tag{10}$$

$$\mathbf{A} = \begin{bmatrix} -\frac{r_{\mathrm{eq}}}{L} & \omega_{\mathrm{s}} & -\frac{1}{L} & 0 \\ -\omega_{\mathrm{s}} & -\frac{r_{\mathrm{eq}}}{L} & 0 & -\frac{1}{L} \\ \frac{1}{C_{\mathrm{f}}} & 0 & 0 & \omega_{\mathrm{s}} \\ 0 & \frac{1}{C_{\mathrm{f}}} & -\omega_{\mathrm{s}} & 0 \end{bmatrix} \tag{11}$$

$$\mathbf{B} = \begin{bmatrix} \frac{D_{\mathrm{d}}}{L} & \frac{R_{\mathrm{d}}}{L} & 0 & \frac{V_{\mathrm{in}}}{L} & 0 \\ \frac{D_{\mathrm{q}}}{L} & 0 & \frac{R_{\mathrm{d}}}{L} & 0 & \frac{V_{\mathrm{in}}}{L} \\ 0 & -\frac{1}{C_{\mathrm{f}}} & 0 & 0 & 0 \\ 0 & 0 & -\frac{1}{C_{\mathrm{f}}} & 0 & 0 \end{bmatrix} \tag{12}$$

$$\mathbf{C} = \begin{bmatrix} \frac{3D_{\mathrm{d}}}{2} & \frac{3D_{\mathrm{q}}}{2} & 0 & 0 \\ 1 & 0 & 0 & 0 \\ 0 & 1 & 0 & 0 \\ R_{\mathrm{d}} & 0 & 1 & 0 \\ 0 & R_{\mathrm{d}} & 0 & 1 \end{bmatrix} \tag{13}$$

$$\mathbf{D} = \begin{bmatrix} 0 & 0 & 0 & \frac{3I_{\mathrm{Ld}}}{2} & \frac{3I_{\mathrm{Lq}}}{2} \\ 0 & 0 & 0 & 0 & 0 \\ 0 & 0 & 0 & 0 & 0 \\ 0 & -R_{\mathrm{d}} & 0 & 0 & 0 \\ 0 & 0 & -R_{\mathrm{d}} & 0 & 0 \end{bmatrix}, \tag{14}$$

where $r_{\mathrm{eq}}$ denotes $r_{\mathrm{L}} + r_{\mathrm{sw}} + R_{\mathrm{d}}$. The transfer functions from the inputs to the outputs can be solved as shown in (15).

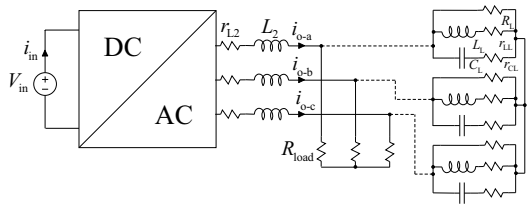


Figure 2. Circuit diagram of the grid-forming inverter including the load-side inductor and a resistive load or alternatively a RLC-load.

$$\mathbf{Y}(s) = \overbrace{\left(\mathbf{C}(s\mathbf{I}-\mathbf{A})^{-1}\mathbf{B}+\mathbf{D}\right)}^{\mathbf{G}}\mathbf{U}(s), \qquad (15)$$

where matrix $\mathbf{G}$ contains the transfer functions. Different transfer functions can be collected from the matrix as shown in (16).

$$\begin{bmatrix} Y_{\rm in} & T_{\rm oid} & T_{\rm oiq} & G_{\rm cid} & G_{\rm ciq} \\ G_{\rm ioLd} & G_{\rm oLd} & G_{\rm oLqd} & G_{\rm cLd} & G_{\rm cLqd} \\ G_{\rm ioLq} & G_{\rm oLdq} & G_{\rm oLq} & G_{\rm cLdq} & G_{\rm cLq} \\ G_{\rm iod} & -Z_{\rm od} & -Z_{\rm oqd} & G_{\rm cod} & G_{\rm coqd} \\ G_{\rm ioq} & -Z_{\rm odq} & -Z_{\rm oq} & G_{\rm codq} & G_{\rm coq} \end{bmatrix} \qquad (16)$$

In this paper the transfer functions are merged into transfer matrices [5], [16]. Equation (17) shows the transfer matrices that were solved in (15) and the corresponding input and output variables. Hats over the input and output variables denote small-signal variables. Input voltage and input current are scalar variables and their small signal dependency is denoted by $Y_{\rm in}$. The input and output variables that are collected into 2-by-1 vectors are shown in (18).

$$\begin{bmatrix} \hat{i}_{\rm in} \\ \hat{\mathbf{i}}_{\rm L} \\ \hat{\mathbf{v}}_{\rm o} \end{bmatrix} = \begin{bmatrix} Y_{\rm in} & \mathbf{T}_{\rm oi} & \mathbf{G}_{\rm ci} \\ \mathbf{G}_{\rm iL} & \mathbf{G}_{\rm oL} & \mathbf{G}_{\rm cL} \\ \mathbf{G}_{\rm io} & -\mathbf{Z}_{\rm o} & \mathbf{G}_{\rm co} \end{bmatrix} \begin{bmatrix} \hat{v}_{\rm in} \\ \hat{\mathbf{i}}_{\rm o} \\ \hat{\mathbf{d}} \end{bmatrix} \qquad (17)$$

$$\begin{aligned} \hat{\mathbf{i}}_{\rm L} &= \begin{bmatrix} \hat{i}_{\rm Ld} & \hat{i}_{\rm Lq} \end{bmatrix}^T \hat{\mathbf{v}}_{\rm o} = \begin{bmatrix} \hat{v}_{\rm od} & \hat{v}_{\rm oq} \end{bmatrix}^T \\ \hat{\mathbf{i}}_{\rm o} &= \begin{bmatrix} \hat{i}_{\rm od} & \hat{i}_{\rm oq} \end{bmatrix}^T \hat{\mathbf{d}} = \begin{bmatrix} \hat{d}_{\rm d} & \hat{d}_{\rm q}^T \end{bmatrix} \end{aligned} \qquad (18)$$

## III. Load effect

Grid-feeding inverters are commonly equipped with an LCL-filter. It is assumed that an inverter that is used in the grid-feeding mode will be used also in the grid-forming mode. In the case of grid-feeding inverters, load impedances have been included in the model in [17] and analytical equations for generalized source and load interactions are shown in [4]. The effect of load dynamics on the unterminated dynamics has been analyzed in the case of DC-DC converters in [18]. Fig. 2 shows a circuit diagram of the grid-forming inverter, where the load is a resistor or alternatively a parallel RLC-load (as depicted using dashed lines). The load-side inductor is taken into account in the model. In the unterminated model in Fig. 1 the load-side inductor is not included, because the series connection of an inductor and current sink is inconsistent according to circuit theory.

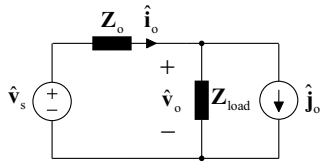


Figure 3. An equivalent small-signal circuit that has been widely used to analyze to impedance based stability.

Fig. 3 shows an equivalent small-signal circuit of two interconnected systems. Very similar circuits have been widely used in the literature for impedance-based stability analysis [7], [9], [19], [20]. Variables $\hat{\mathbf{v}}_{\rm s}$ and $\hat{\mathbf{j}}_{\rm o}$ denote small-signal source voltage and load current, respectively. However, they do not indicate, how the voltage and current are dependent on the inverter input parameters. In following, the general voltage source is replace by the control-to-output transfer function matrices so that the load-affected transfer functions can be solved.

The output dynamics of the grid-forming inverter are shown as an equivalent linear circuit in Fig. 4(a) which corresponds to the equation of $\hat{\mathbf{v}}_{\rm o}$ in (17) that is developed from the case the load is an ideal current sink in Fig. 1. However, the load effect of the load-side inductor, its ESR and the load resistor in Fig. 2 must be taken into account. Figure 4(b) shows the output dynamics model, where the load impedance $\mathbf{Z}_{\rm load}$ and the impedance of the load-side inductor $\mathbf{Z}_{\rm L2}$ are included. The transfer functions for the load and the inductor impedance are derived similarly as the unterminated model. Appendix A shows the state-space coefficient matrices that are used to solve as the admittance matrix of the grid-side inductor. The inverse of the admittance matrix is $\mathbf{Z}_{\rm L2}$. Appendix B shows the coefficient matrices for the RLC-load. Equations for the small-signal output voltage $\hat{\mathbf{v}}_{\rm o}$ are written for the both circuits in Figs. 4(a) and 4(b). The equations are shown in (19) and (20), respectively.

$$\hat{\mathbf{v}}_{\rm o} = \mathbf{G}_{\rm io}\hat{v}_{\rm in} - \mathbf{Z}_{\rm o}\hat{\mathbf{i}}_{\rm o} + \mathbf{G}_{\rm co}\hat{\mathbf{d}} \qquad (19)$$

$$\hat{\mathbf{v}}_{\rm o} = \mathbf{Z}_{\rm L2}\hat{\mathbf{i}}_{\rm o} + \mathbf{Z}_{\rm load}\hat{\mathbf{i}}_{\rm o} - \mathbf{Z}_{\rm load}\hat{\mathbf{j}}_{\rm o} \qquad (20)$$

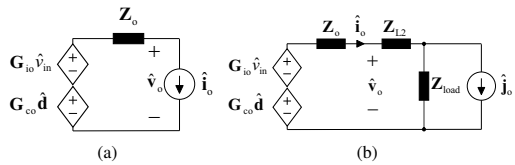


Figure 4. a) Output dynamics and b) load-affected output dynamics.

Small-signal output current vector $\hat{\mathbf{i}}_\mathrm{o}$ is solved from (20). The solution is shown in (21).

$$\begin{aligned}\hat{\mathbf{i}}_\mathrm{o} =&(\mathbf{Z}_{\mathrm{L}2}+\mathbf{Z}_\mathrm{load})^{-1}\hat{\mathbf{v}}_\mathrm{o}\\ &+(\mathbf{Z}_{\mathrm{L}2}+\mathbf{Z}_\mathrm{load})^{-1}\mathbf{Z}_\mathrm{load}\hat{\mathbf{j}}_\mathrm{o}\end{aligned} \tag{21}$$

Eq. (22) shows the result when $\hat{\mathbf{i}}_\mathrm{o}$ in (21) is substituted to (19). The $(\mathbf{I}+\mathbf{Z}_\mathrm{o}(\mathbf{Z}_{\mathrm{L}2}+\mathbf{Z}_\mathrm{load})^{-1})^{-1}$ is the common factor in all of the equations. The load-affected control-to-output transfer functions are collected from the bottom row of the matrix in (27). The transfer functions from $\hat{\mathbf{j}}_\mathrm{o}$ to $\hat{\mathbf{v}}_\mathrm{o}$ could be also manipulated to (23). This format shows that the small-signal current $\hat{\mathbf{i}}_\mathrm{o}$ is solved analogously to circuit theory by dividing $\hat{\mathbf{j}}_\mathrm{o}$ according to the impedances and the multiplying by $-\mathbf{Z}_\mathrm{o}$ to solve the output voltage $\hat{\mathbf{v}}_\mathrm{o}$.

$$\begin{aligned}\hat{\mathbf{v}}_\mathrm{o} =&(\mathbf{I}+\mathbf{Z}_\mathrm{o}(\mathbf{Z}_{\mathrm{L}2}+\mathbf{Z}_\mathrm{load})^{-1})^{-1}\\ &(\mathbf{G}_\mathrm{io}\hat{v}_\mathrm{in}-\mathbf{Z}_\mathrm{o}(\mathbf{Z}_{\mathrm{L}2}+\mathbf{Z}_\mathrm{load})^{-1}\mathbf{Z}_\mathrm{load}\hat{\mathbf{j}}_\mathrm{o}\\ &+\mathbf{G}_\mathrm{co}\hat{\mathbf{d}})\end{aligned} \tag{22}$$

$$\hat{\mathbf{v}}_\mathrm{o}=-(\mathbf{Z}_\mathrm{o}+\mathbf{Z}_{\mathrm{L}2}+\mathbf{Z}_\mathrm{load})^{-1}\mathbf{Z}_\mathrm{load}\mathbf{Z}_\mathrm{o}\hat{\mathbf{j}}_\mathrm{o} \tag{23}$$

The control-to-output voltage transfer function $\mathbf{G}_\mathrm{co}^\mathrm{L}$ can be solved also directly from the load affected output dynamics diagram in Fig. 4(b). The load affected circuit can be understood as a voltage divider, which divides the small-signal voltage caused by $\mathbf{G}_\mathrm{co}$ or $\mathbf{G}_\mathrm{io}$ over the impedances $\mathbf{Z}_\mathrm{o}$, $\mathbf{Z}_{\mathrm{L}2}$ and $\mathbf{Z}_\mathrm{load}$. A very similar equations has been analyzed in [19], [20]. However, in [19], [20] the equations are derived in the case of an arbitrary voltage source as in Fig. 3 – not in the case of input-output dynamics of the converter.

The remaining load-affected transfer functions in (27) are solved by substituting $\hat{\mathbf{i}}_\mathrm{o}$ in (17) by (21) as shown in (24) and then substituting $\hat{\mathbf{v}}_\mathrm{o}$ by (22). Solving for $\hat{i}_\mathrm{in}$ and $\hat{\mathbf{i}}_\mathrm{L}$ as a function of $\hat{v}_\mathrm{in}$, $\hat{\mathbf{j}}_\mathrm{o}$ and $\hat{\mathbf{d}}$ gives the load affected transfer functions. Equation (25) shows the result in the case of inductor current. Load-affected output transfer functions $\mathbf{G}_\mathrm{io}^\mathrm{L}$, $\mathbf{G}_\mathrm{o}^\mathrm{L}$ and $\mathbf{G}_\mathrm{co}^\mathrm{L}$ are used for brevity in (25) instead of using the expression in (22). The load affected input current dynamics (26) can be solved similarly as the load affected inductor current dynamics.

$$\begin{aligned}\hat{\mathbf{i}}_\mathrm{L} =&\mathbf{G}_\mathrm{iL}\hat{v}_\mathrm{in}+\mathbf{G}_\mathrm{oL}((\mathbf{Z}_{\mathrm{L}2}+\mathbf{Z}_\mathrm{load})^{-1}\hat{\mathbf{v}}_\mathrm{o}\\ &+(\mathbf{Z}_{\mathrm{L}2}+\mathbf{Z}_\mathrm{load})^{-1}\mathbf{Z}_\mathrm{load}\hat{\mathbf{j}}_\mathrm{o})+\mathbf{G}_\mathrm{cL}\hat{\mathbf{d}}\end{aligned} \tag{24}$$

$$\begin{aligned}\hat{\mathbf{i}}_\mathrm{L} =&(\mathbf{G}_\mathrm{iL}+\mathbf{G}_\mathrm{oL}(\mathbf{Z}_{\mathrm{L}2}+\mathbf{Z}_\mathrm{load})^{-1}\mathbf{G}_\mathrm{io}^\mathrm{L})\hat{v}_\mathrm{in}\\ &+(\mathbf{G}_\mathrm{cL}+\mathbf{G}_\mathrm{oL}(\mathbf{Z}_{\mathrm{L}2}+\mathbf{Z}_\mathrm{load})^{-1}\mathbf{G}_\mathrm{co}^\mathrm{L})\hat{\mathbf{d}}\\ &+\mathbf{G}_\mathrm{oL}((\mathbf{Z}_{\mathrm{L}2}+\mathbf{Z}_\mathrm{load})^{-1}\mathbf{Z}_\mathrm{load}\\ &-((\mathbf{Z}_{\mathrm{L}2}+\mathbf{Z}_\mathrm{load})^{-1}(-\mathbf{G}_\mathrm{o}^\mathrm{L})))\hat{\mathbf{j}}_\mathrm{o}\end{aligned} \tag{25}$$

$$\begin{aligned}\hat{i}_\mathrm{in} =&(Y_\mathrm{in}+\mathbf{T}_\mathrm{oi}(\mathbf{Z}_{\mathrm{L}2}+\mathbf{Z}_\mathrm{load})^{-1}\mathbf{G}_\mathrm{io}^\mathrm{L})\hat{v}_\mathrm{in}\\ &+(\mathbf{G}_\mathrm{ci}+\mathbf{T}_\mathrm{oi}(\mathbf{Z}_{\mathrm{L}2}+\mathbf{Z}_\mathrm{load})^{-1}\mathbf{G}_\mathrm{co}^\mathrm{L}))\hat{\mathbf{d}}\\ &+\mathbf{T}_\mathrm{oi}((\mathbf{Z}_{\mathrm{L}2}+\mathbf{Z}_\mathrm{load})^{-1}\mathbf{Z}_\mathrm{load})\\ &-((\mathbf{Z}_{\mathrm{L}2}+\mathbf{Z}_\mathrm{load})^{-1}(-\mathbf{G}_\mathrm{o}^\mathrm{L})))\hat{\mathbf{j}}_\mathrm{o}\end{aligned} \tag{26}$$

$$\begin{bmatrix}\hat{i}_\mathrm{in}\\ \hat{\mathbf{i}}_\mathrm{L}\\ \hat{\mathbf{v}}_\mathrm{o}\end{bmatrix}=\begin{bmatrix}Y_\mathrm{in}{}^\mathrm{L} & \mathbf{T}_\mathrm{oi}^\mathrm{L} & \mathbf{G}_\mathrm{ci}^\mathrm{L}\\ \mathbf{G}_\mathrm{iL}^\mathrm{L} & \mathbf{G}_\mathrm{oL}^\mathrm{L} & \mathbf{G}_\mathrm{cL}^\mathrm{L}\\ \mathbf{G}_\mathrm{io}^\mathrm{L} & -\mathbf{G}_\mathrm{o}^\mathrm{L} & \mathbf{G}_\mathrm{co}^\mathrm{L}\end{bmatrix}\begin{bmatrix}\hat{v}_\mathrm{in}\\ \hat{\mathbf{j}}_\mathrm{o}\\ \hat{\mathbf{d}}\end{bmatrix} \tag{27}$$

The resulting load-affected dynamics can be expressed as shown in (27), where superscript L denotes that the transfer functions are affected by the load impedance. It should be noted that $\hat{\mathbf{j}}_\mathrm{o}$ replaces $\hat{\mathbf{i}}_\mathrm{o}$ as an input variable as it can be seen from Fig. 4(b). Since $\hat{\mathbf{j}}_\mathrm{o}$ and $\hat{\mathbf{v}}_\mathrm{o}$ are not defined at an interface according to the definition of an impedance, a transfer function matrix $\mathbf{G}_\mathrm{o}^\mathrm{L}$ is used instead of an impedance matrix.

References [21] and [22] have pointed out that the impedances of interconnected three-phase systems should be shifted to a global reference frame to enable impedance-based stability analysis. However, the load impedance matrix of the pure resistive load and the RLC-load analyzed in this paper are symmetric, which means that no impedance shifting is required.

## IV. Frequency response analysis

The parameters and the operating point values of the grid-forming inverter are shown in Tables I and II. The resistive load in Fig. 2 is considered first. Fig. 6 shows both the frequency response given by analytical model $G_\mathrm{cod}^\mathrm{L}$ and the frequency response measured from a hardware-in-the-loop simulator. $G_\mathrm{cod}^\mathrm{L}$ is the transfer function from the duty ratio d-component to the output voltage d-component, which has major importance for control design. The resistive load $R_\mathrm{load}$ is chosen according to (28) so that nominal operation point is maintained. Eq. (29) shows, how the load impedance matrix is defined in the case of the resistive load.

$$R_\mathrm{load}=\frac{V_\mathrm{od}}{I_\mathrm{od}}-r_{L2} \tag{28}$$

$$\mathbf{Z}_\mathrm{load}=\begin{bmatrix}R_\mathrm{load} & 0\\ 0 & R_\mathrm{load}\end{bmatrix} \tag{29}$$

Table I. Inverter parameter values

| Parameter | Value | Parameter | Value |
|---|---|---|---|
| $L$ | 1.4 mH | $r_\mathrm{L}$ | 25 mΩ |
| $L_2$ | 0.47 mH | $r_{\mathrm{L}2}$ | 22 mΩ |
| $C_\mathrm{f}$ | 10 $\mu$F | $R_\mathrm{d}$ | 1.96 Ω |
| $f_\mathrm{s}$ | 10 kHz | $r_\mathrm{sw}$ | 10 mΩ |
| $\omega_\mathrm{s}$ | $2\pi$60 Hz | | |

Table II. OPERATING POINT VALUES

| Parameter | Value | Parameter | Value |
|---|---|---|---|
| $V_{\mathrm{od}}$ | 169.7 V | $V_{\mathrm{oq}}$ | 0.0000 V |
| $I_{\mathrm{od}}$ | 19.64 A | $I_{\mathrm{oq}}$ | 0.0000 A |
| $I_{\mathrm{Ld}}$ | 19.65 A | $I_{\mathrm{Lq}}$ | 0.6397 A |
| $V_{\mathrm{Cfd}}$ | 169.7 V | $V_{\mathrm{Cfq}}$ | -1.254 V |
| $V_{\mathrm{in}}$ | 416.0 V | $I_{\mathrm{in}}$ | 16.93 A |
| $D_{\mathrm{d}}$ | 0.4088 | $D_{\mathrm{q}}$ | 0.0250 |

The correlation between the measured and predicted based frequency responses in Fig. 6 confirms that the proposed model is correct. The mainly resistive load damps the resonance caused by the LC-filter. The instruments utilized in the measurements were Typhoon HIL -real time simulator, Boombox control platform from Imperix and Venable frequency response analyzer. A photograph of the HIL simulation setup is shown in Fig. 5. An oscilloscope was used additionally.

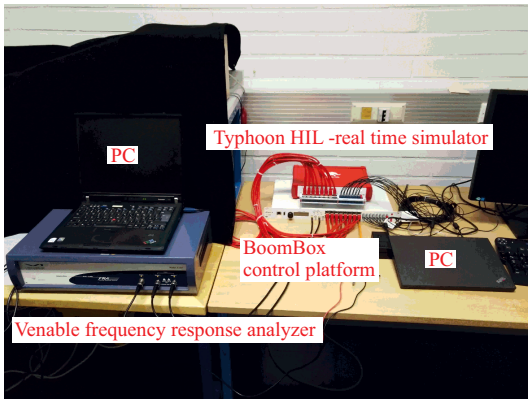


Figure 5. Real-time simulation setup: PC, Venable frequency response analyzer, Boombox control platform, and Typhoon HIL -real time simulator.

Taking advantage of the steps to derive the load-affected transfer function, the load effect can be also removed from the frequency response. Eq. (30) shows, how $\mathbf{G}_{\mathrm{co}}$ can be calculated if the load-affected transfer function matrix, $\mathbf{G}_{\mathrm{co}}^{\mathrm{L}}$ is known from measurements, i.e., the unterminated dynamic model can be solved even if the load is not an ideal current sink.

$$\mathbf{G}_{\mathrm{co}} = (\mathbf{I} + \mathbf{Z}_{\mathrm{o}}(\mathbf{Z}_{\mathrm{L2}} + \mathbf{Z}_{\mathrm{load}})^{-1})\mathbf{G}_{\mathrm{co}}^{\mathrm{L}} \tag{30}$$

Fig. 6 shows also a comparison between the derived $G_{\mathrm{cod}}$ in (17) and the transfer function calculated according to (30). $G_{\mathrm{cod}}$ corresponds to the situation of Fig. 1, where the load is an ideal current sink. Thus, the ideal transfer functions can be illustrated even though, the converter is affected by the load impedance. Assuming that the impedance matrices $\mathbf{Z}_{\mathrm{o}}$, $\mathbf{Z}_{\mathrm{L2}}$ and $\mathbf{Z}_{\mathrm{Load}}$ are known.

A cascaded controller is commonly used to control the output voltage of the grid-forming inverter [5], [23], [24]. The controller consists of the inner inductor current loop and outer output voltage loop. The controller is tuned according to the control-to-inductor-current and control-to-output voltage transfer functions affected by the R-load. Fig. 7 shows the measured and model-based frequency response of the $G_{\mathrm{cLd}}^{\mathrm{L}}$. The unterminated control-to-current d-component $G_{\mathrm{cLd}}$ is also shown in Fig. 7. The resistive load clearly damps the resonance and increases the low-frequency gain, which greatly simplifies the tuning of the current controller. The current controller $\mathrm{G_{cc}}$ is a PI-controller. Consisting of an integrator, a zero at 1 kHz and a gain of 36.8 dB.

Fig. 8 shows the frequency response of the full-order current loop gain $L_{\mathrm{outCd}}^{\mathrm{FO}}$. The phase margin is 65.4 °at 551 Hz. The gain margin is 8.51 dB. The full-order current loop gain includes the cross-coupling between d and q-components. The loop gain is given in (31) and it has been derived in [4]. The delay caused by sampling and PWM is 1.5 $1/f_{\mathrm{s}}$ and it is modeled by a third order Padé approximation [16]. The delay transfer function is omitted for brevity from (31), but it is shown in (32) and in completed block diagram of the system in Fig. 11.

$$L_{\mathrm{outCd}}^{\mathrm{FO}} = G_{\mathrm{cLd}}^{\mathrm{L}}\mathrm{G_{cc}} - \frac{G_{\mathrm{cLqd}}^{\mathrm{L}}G_{\mathrm{cLqd}}^{\mathrm{L}}}{1 + G_{\mathrm{cLq}}^{\mathrm{L}}G_{\mathrm{cc}}}\mathrm{G_{cc}G_{cc}} \tag{31}$$

The matrix current loop gain is shown in (32).

$$\mathbf{L}_{\mathrm{outC}} = \mathbf{G}_{\mathrm{cL}}\mathbf{G}_{\mathrm{del}}\mathbf{G}_{\mathrm{cc}}\mathbf{G}_{\mathrm{seC}} \tag{32}$$

The current loop is closed in (33) and (34) shows, how the inductor current reference-to-output voltage transfer function $\mathbf{G}_{\mathrm{co}}^{\mathrm{sec}}$ is calculated. Superscript 'sec' denotes secondary and means that the secondary control loop (i.e. current loop) is closed. $G_{\mathrm{cod}}^{\mathrm{sec}}$ is used to tune the voltage controller. Fig. 11 shows the control block diagram of the complete system. The block diagram can be used to calculate also other closed-loop transfer functions and loop gains.

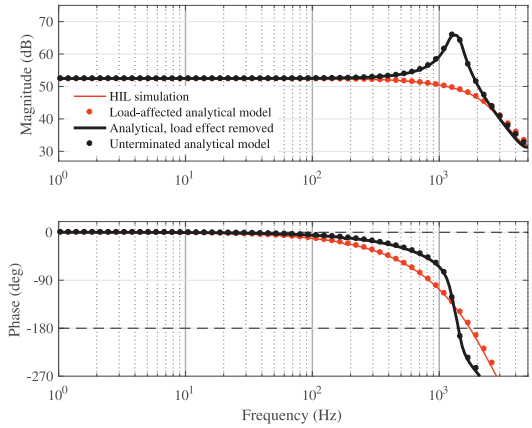


Figure 6. Measured and model-based frequency responses of $G_{\mathrm{cod}}^{\mathrm{L}}$ (resistive load).

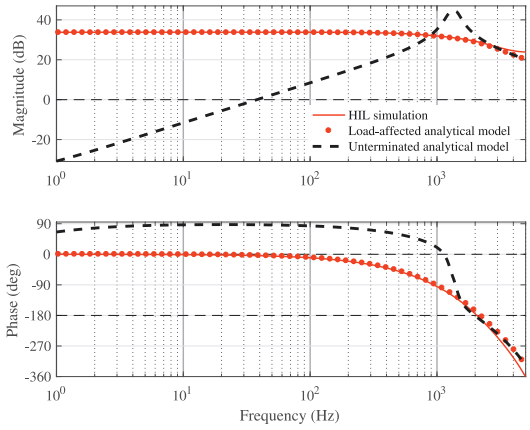


Figure 7. Bode plot of HIL-simulated and derived $G^{\mathrm{L}}_{\mathrm{cLd}}$ for the R-load and the unterminated $G_{\mathrm{cLd}}$.

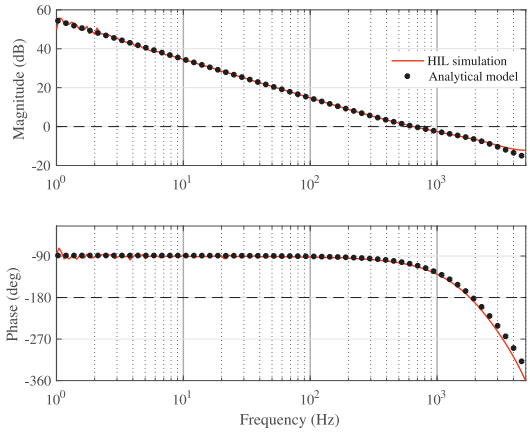


Figure 8. Bode plot of measured and derived current loop gain $L^{\mathrm{FO}}_{\mathrm{outCd}}$ for the R-load.

$$\mathbf{G}^{\mathrm{sec}}_{\mathrm{cL}} = (\mathbf{I} + \mathbf{L}_{\mathrm{outC}})^{-1}\mathbf{G}^{\mathrm{L}}_{\mathrm{cL}}\mathbf{G}_{\mathrm{del}}\mathbf{G}_{\mathrm{cc}} \tag{33}$$

$$\begin{aligned}\mathbf{G}^{\mathrm{sec}}_{\mathrm{co}} =& \mathbf{G}^{\mathrm{L}}_{\mathrm{co}}\mathbf{G}_{\mathrm{del}}\mathbf{G}_{\mathrm{cc}} \\ &- \mathbf{G}^{\mathrm{L}}_{\mathrm{co}}\mathbf{G}^{-1}_{\mathrm{cL}}\,\mathbf{L}_{\mathrm{outC}}\,\mathbf{G}^{\mathrm{sec}}_{\mathrm{cL}}\end{aligned} \tag{34}$$

$$L^{\mathrm{FO}}_{\mathrm{outV-d}} = G^{\mathrm{L}}_{\mathrm{cod}}\mathrm{G}_{\mathrm{vc}} - \frac{G^{\mathrm{L}}_{\mathrm{coqd}}G^{\mathrm{L}}_{\mathrm{coqd}}}{1 + G^{\mathrm{L}}_{\mathrm{coq}}G_{\mathrm{vc}}}\mathrm{G}_{\mathrm{vc}}\mathrm{G}_{\mathrm{vc}} \tag{35}$$

Fig. 9 shows the simulated and the frequency response of the analytic voltage loop gain $L^{\mathrm{FO}}_{\mathrm{outVd}}$ (35) and the model of $\mathbf{G}^{\mathrm{sec}}_{\mathrm{cod}}$. The crossover frequency the voltage loop is 53.9 Hz and the phase margin is 93.5 °when the load is pure resistance. The voltage controller $\mathrm{G}_{\mathrm{vc}}$ consists of an integrator, a zero at 200 Hz, a pole at 600 Hz and a gain of 31.6 dB.

The cascaded controller is kept unchanged, but the

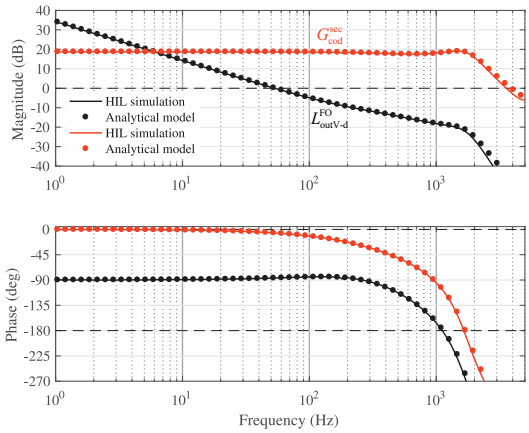


Figure 9. Bode plot of simulated and derived voltage controller loop gain $L^{\mathrm{FO}}_{\mathrm{outVd}}$ and the current loop affected control-to-output dynamics $G^{\mathrm{Lsec}}_{\mathrm{cod}}$.

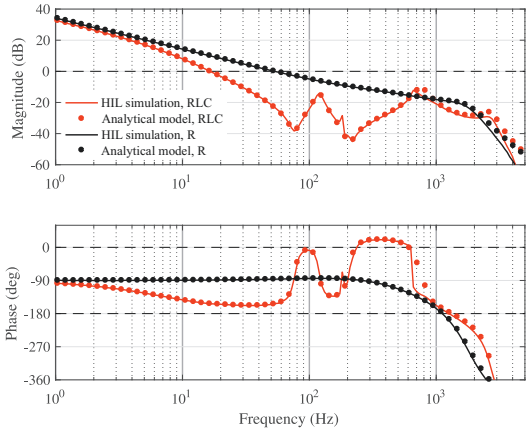


Figure 10. Bode plot of measured and derived voltage controller loop gain $L^{\mathrm{FO}}_{\mathrm{outVd}}$ for the R-load and for the RLC-load.

load is changed to the RLC-load that is similar to the RLC-load used in [13]. $L_{\mathrm{L}}$ and $C_{\mathrm{L}}$ are 4.584 mH and 1.535 mF, respectively. The resonance frequency is at around 60 Hz as in [13]. 30 mΩ resistances $r_{\mathrm{LL}}$ and $r_{\mathrm{CL}}$ are connected in series with the parallel capacitance and inductance, respectively. $R_{\mathrm{L}}$ of the parallel load equals $R_{\mathrm{load}}$, the load of the first case. Figure 10 shows also the frequency response of the voltage loop in this case. It can be seen that the crossover frequency is 16.5 Hz and the phase margin is reduced to 26.7 °. The low phase margin indicates that there will be oscillation in the step response of the system.

A step response comparison by using the R and RLC-loads is done. The system is simulated in Typhoon HIL as in the case of frequency-domain measurement. An oscilloscope is connected to the analog outputs of Imperix Boombox to analyze the response in detail in dq-domain. Fig. 12 shows the output voltage response to a step

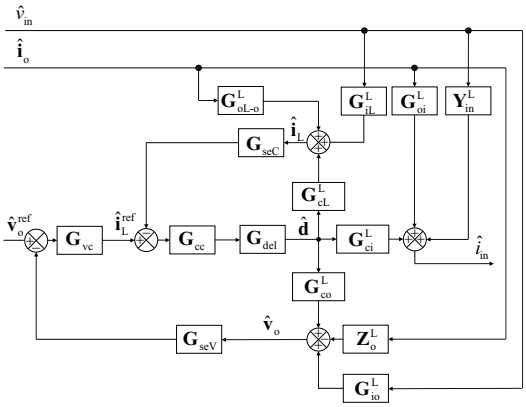


Figure 11. Control block diagram of the closed-loop system.

change in the voltage reference d-component as the R-load is used. The step is from 155 V to the nominal amplitude 169,7 V. There is no overshoot or oscillation in the response. The response with the RLC-load as the controller remains unchanged is also shown in Fig. 12. A significant overshoot and decaying oscillation is present in the response.

The model is used to retune the controllers so that a proper step-response is achieved with the RLC-load. The current controller pole location is changed to 100 Hz and the new gain is 24.8 dB. The voltage controller zero is moved to 5 Hz, two poles are located at 60 Hz and the new gain is 24.1 dB. Fig. 13 shows the predicted and HIL-simulated voltage loop gains. The phase margin is 58.2 ° at 20.6 Hz. The gain margin is 14 dB at 129 Hz. The step response in Fig. 14 is good, as the higher phase margin than with previous controller tuning implies.

The previous analysis shows that the proposed model can be used to analyze the effect of different loads on the control dynamics. Frequency responses of the load-affected transfer functions can be used to predict the time-domain behavior and to design the controllers according

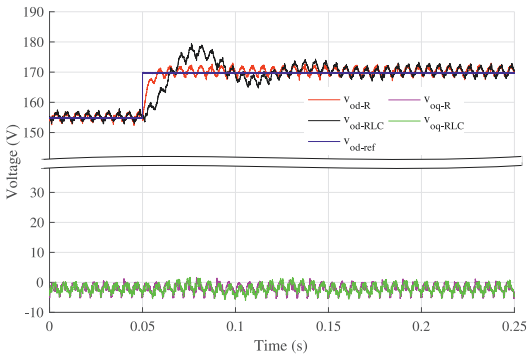


Figure 12. Typhoon HIL simulation of output voltage d and q-components step response to a reference step for the R-load and for the RLC-load.

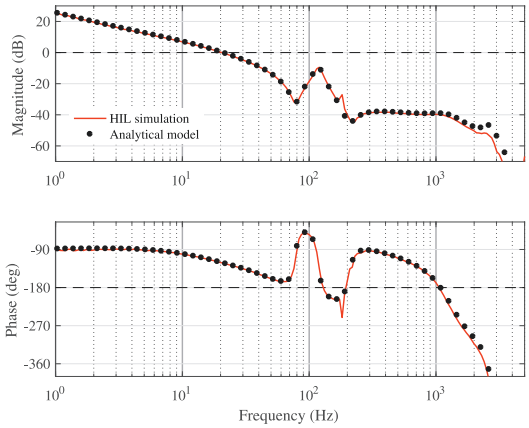


Figure 13. Bode plot of simulated and predicted voltage loop gain with the controller that is tuned for the RLC-load.

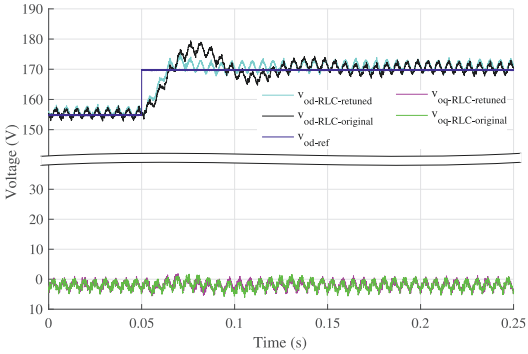


Figure 14. Typhoon HIL simulation of output voltage d and q-component step responses to a reference step with the RLC-load with the original controller and the controller retuned for RLC-load.

to a specific load or a worst-case scenario.

## V. Conclusion

This paper proposes a method to model unterminated dynamics of a grid-forming inverter. The effect of a non-ideal load is included in the model by calculating, how the load impedance affects the output dynamics. Furthermore, the unterminated model of the grid-forming inverter includes the output impedance that is required to calculate the load-affected model and an important tool in the stability analysis of interconnected systems.

The HIL measurements provided in this paper confirm that the frequency response analysis is a powerful tool for predicting the time-domain response of the grid-forming inverter under distinct loads. One possible application of the proposed modeling technique is to tune the controller according to a specific load so that a desired time-domain response is achieved. The model can be also used to examine worst-case load conditions. The load effect can be also removed from the measured load affected frequency response and the unterminated model can be

verified. Future work will concentrate on the on the load-affected dynamics in the case of an active load, such as an active rectifier.

## APPENDIX A

Eq. (36) shows the grid-side inductor admittance state-space coefficient matrices.

$$\mathbf{A}_{\mathrm{L2}} = \begin{bmatrix} \frac{-r_{\mathrm{L2}}}{L_2} & \omega_{\mathrm{s}} \\ -\omega_{\mathrm{s}} & \frac{-r_{\mathrm{L2}}}{L_2} \end{bmatrix} \quad \mathbf{B}_{\mathrm{L2}} = \begin{bmatrix} \frac{1}{L_2} & 0 \\ 0 & \frac{1}{L_2} \end{bmatrix}$$
$$\mathbf{C}_{\mathrm{L2}} = \begin{bmatrix} 1 & 0 \\ 0 & 1 \end{bmatrix} \qquad \mathbf{D}_{\mathrm{L2}} = \begin{bmatrix} 0 & 0 \\ 0 & 0 \end{bmatrix} \tag{36}$$

## APPENDIX B

Eq. (37) shows the RLC-load admittance state-space coefficient matrices.

$$\mathbf{A}_{\mathrm{RLC}} = \begin{bmatrix} \frac{-r_{\mathrm{LL}}}{L_{\mathrm{L}}} & \omega_{\mathrm{s}} & 0 & 0 \\ -\omega_{\mathrm{s}} & \frac{-r_{\mathrm{LL}}}{L_{\mathrm{L}}} & 0 & 0 \\ 0 & 0 & \frac{-1}{C_{\mathrm{L}} r_{\mathrm{CL}}} & \omega_{\mathrm{s}} \\ 0 & 0 & -\omega_{\mathrm{s}} & \frac{-1}{C_{\mathrm{L}} r_{\mathrm{CL}}} \end{bmatrix}$$
$$\mathbf{B}_{\mathrm{RLC}} = \begin{bmatrix} \frac{1}{L_{\mathrm{L}}} & 0 \\ 0 & \frac{1}{L_{\mathrm{L}}} \\ \frac{1}{C_{\mathrm{L}}} & 0 \\ 0 & \frac{1}{C_{\mathrm{L}}} \end{bmatrix} \quad \mathbf{C}_{\mathrm{RLC}} = \begin{bmatrix} 1 & 0 & \frac{-1}{r_{\mathrm{CL}}} & 0 \\ 0 & 1 & 0 & \frac{-1}{r_{\mathrm{CL}}} \end{bmatrix}$$
$$\mathbf{D}_{\mathrm{RLC}} = \begin{bmatrix} \frac{1}{R_{\mathrm{L}}} + \frac{1}{r_{\mathrm{CL}}} & 0 \\ 0 & \frac{1}{R_{\mathrm{L}}} + \frac{1}{r_{\mathrm{CL}}} \end{bmatrix} \tag{37}$$

## REFERENCES


[1] I. J. o. Balaguer, "Control for grid-connected and intentional islanding operations of distributed power generation," *IEEE Trans. Ind. Electron.*, vol. 58, no. 1, pp. 147–157, 2011.

[2] M. Rasheduzzaman, J. A. Mueller, and J. W. Kimball, "An accurate small-signal model of inverter- dominated islanded microgrids using dq reference frame," *IEEE Trans. Emerg. Sel. Topics Power Electron.*, vol. 2, no. 4, pp. 1070–1080, 2014.

[3] J. Rocabert *et al.*, "Control of power converters in AC microgrids," *IEEE Trans. Power Electron.*, vol. 27, no. 11, pp. 4734–4749, nov 2012.

[4] T. Suntio, T. Messo, and J. Puukko, *Power Electronic Converters: Dynamics and Control in Conventional and Renewable Energy Applications*. Wiley VCH, 2017.

[5] B. Wen *et al.*, "Modeling the output impedance of three-phase uninterruptible power supply in D-Q frame," in *2014 IEEE Energy Conversion Congress and Exposition (ECCE)*. IEEE, 2014, pp. 163–169.

[6] S. Lissandron *et al.*, "Experimental validation for impedance-based small-signal stability analysis of single-phase interconnected power systems with grid-feeding inverters," *IEEE Journal of Emerging and Selected Topics in Power Electronics*, vol. 4, no. 1, pp. 103–115, 2016.

[7] T. Roinila, T. Messo, and E. Santi, "Mimo-identification techniques for rapid impedance-based stability assessment of three phase systems in DQ domain," *IEEE Trans. Power Electron.*, vol. 33, no. 5, pp. 1–1, 2017.

[8] B. Wen *et al.*, "AC stability analysis and dq frame impedance specifications in power-electronics-based distributed power systems," *IEEE Trans. Emerg. Sel. Topics Power Electron.*, vol. 5, no. 4, pp. 1455–1465, dec 2017.

[9] B. Wen and othe, "Impedance-based analysis of grid-synchronization stability for three-phase paralleled converters," *IEEE Trans. Power Electron.*, vol. 31, no. 1, pp. 26–38, 2016.

[10] M. Ramezani, S. Li, and S. Golestan, "Analysis and controller design for stand-alone vsis in synchronous reference frame," *IET Power Electron.*, vol. 10, no. 9, pp. 1003–1012, 2017.

[11] J. M. Guerrero *et al.*, "Output impedance design of parallel-connected UPS inverters with wireless load-sharing control," *IEEE Trans. Ind. Electron.*, vol. 52, no. 4, pp. 1126–1135, 2005.

[12] A. Yazdani, "Control of an islanded distributed energy resource unit with load compensating feed-forward," in *2008 IEEE Power and Energy Society General Meeting - Conversion and Delivery of Electrical Energy in the 21st Century*. IEEE, 2008, pp. 1–7.

[13] R. J. Vijayan, S. Ch, and R. Roy, "Dynamic modeling of microgrid for grid connected and intentional islanding operation," in *2012 International Conference on Advances in Power Conversion and Energy Technologies (APCET)*. IEEE, aug 2012, pp. 1–6.

[14] T. Vandoorn *et al.*, "Theoretical analysis and experimental validation of single-phase direct versus cascade voltage control in islanded microgrids," *IEEE Trans. Ind. Electron.*, vol. 60, no. 2, pp. 789–798, 2013.

[15] R. D. Middlebrook, "Small-signal modeling of pulse-width modulated switched-mode power converters," *Proc. IEEE*, vol. 76, no. 4, pp. 343–354, 1988.

[16] A. Aapro *et al.*, "Effect of active damping on output impedance of three-phase grid-connected converter," *IEEE Trans. Ind. Electron.*, vol. PP, no. 99, pp. 1–1, 2017.

[17] J. Puukko and T. Suntio, "Modelling the effect of non-ideal load in three-phase converter dynamics," *Electronics Letters*, vol. 48, no. 7, p. 402, 2012.

[18] T. Suntio, *Dynamic Profile of Switched-Mode Converter: Modeling, Analysis and Control*. Weinheim, Germany: Wiley, 2009.

[19] B. Wen and other, "D-Q impedance specification for balanced three-phase AC distributed power system," in *2015 IEEE Applied Power Electronics Conference and Exposition (APEC)*. IEEE, 2015, pp. 2757–2771.

[20] R. Burgos *et al.*, "On the ac stability of high power factor three-phase rectifiers," in *2010 IEEE Energy Conversion Congress and Exposition*. IEEE, 2010, pp. 2047–2054.

[21] A. Rygg *et al.*, "On the equivalence and impact on stability of impedance modelling of power electronic converters in different domains," *IEEE Trans. Emerg. Sel. Topics Power Electron.*, no. 4, pp. 1–1, 2017.

[22] J. Chen and J. Chen, "Stability analysis and parameters optimization of islanded microgrid with both ideal and dynamic constant power loads," *IEEE Trans. Ind. Electron.*, vol. 65, no. 4, pp. 1–1, 2017.

[23] Poh Chiang Loh *et al.*, "A comparative analysis of multiloop voltage regulation strategies for single and three-phase UPS systems," *IEEE Trans. Power Electron.*, vol. 18, no. 5, pp. 1176–1185, 2003.

[24] P. Loh and D. Holmes, "Analysis of multiloop control strategies for LC/CL/LCL-filtered voltage-source and current-source inverters," *IEEE Trans. Ind. Appl.*, vol. 41, no. 2, pp. 644–654, 2005.

# Publication V

**Impedance Measurement of Megawatt-Level Renewable Energy Inverters using Grid-Forming and Grid-Parallel Converters**

M. Berg, T. Messo, H. Alenius, and T. Roinila

*International Power Electronics Conference 2018 -ECCE Asia*,
*pp. 4205—4212, 2018.*

# Impedance Measurement of Megawatt-Level Renewable Energy Inverters using Grid-Forming and Grid-Parallel Converters

Matias Berg[1*], Tuomas Messo[1], Tomi Roinila[2], Henrik Alenius[2]
1 Electrical Energy Engineering, Tampere University of Technology, Tampere, Finland
2 Hydraulics and Automation, Tampere University of Technology, Tampere, Finland
*E-mail: matias.berg@tut.fi

***Abstract*—Harmonic resonance and power quality problems have been reported in grid-connected photovoltaic and wind power systems. The AC-side impedance of three-phase converter is an important characteristic, which can be effectively used as a design parameter to avoid instability and excessive harmonics. A number of methods to measure the three-phase AC impedance have been reported. However, solutions for high power applications such as wind and photovoltaic converters with a power rating of several megawatts, have not been discussed. This paper introduces a new method to measure impedance from high power three-phase converter. The impedance is identified by perturbing the converter first by voltage-type injection utilizing high-power grid-forming inverter, and subsequently by current-type injection by utilizing low-power grid-parallel converter. The main benefit of the proposed setup is the possibility to measure the converter impedance online in its natural operating point both at high and low frequencies. The paper presents a proof-of-concept by validating the method using a switching model.**

***Keywords*—Impedance Measurement, Identification, Small-Signal Modeling, Three-Phase Power Conversion**

## I. Introduction

The share of renewable energy generation in power systems is experiencing a rapid growth. New energy sources are connected to the grid using power converters ranging from a few kilowatts up to megawatts. Power converters of several megawatts are nowadays a standard solution in offshore wind parks and large PV power plants.

The large share of renewable energy is expected to challenge the stability of large power systems in near future, especially due to smaller inertia [1]. Stability, power quality problems and unwanted disconnection of the converter from the power system have been reported recently [2], [3]. The prime source of such problems can be often found in the small-signal impedance characteristics of power converters [4], [5]. In fact, the power converter impedance should be shaped to have high magnitude or passive characteristics to avoid instability induced by the underdamped resonance between the converter and the grid impedance [6], [7], [8].

There is a growing interest in the industry and academia to obtain reliable analytical impedance models that would allow more accurate harmonic and stability analysis [9]. However, the derivation of impedance models may be difficult due to numerous unknown parameters, such as internal control parameters, which are most often well-protected secrets of converter manufacturer. The ability to measure the converter impedance accurately would allow generating impedance models by, e.g., different curve-fitting tools, which in principle would not jeopardize the intellectual property. Therefore, measurement method which can accurately capture the output impedance of a high-power three-phase converter, at its nominal operating point, is desperately needed.

Impedance measurement setup for power converter with power rating of few tens of kilowatts can be done accurately using standard laboratory equipment [10]. New methods need to be developed as the power level increases since standard laboratory power supplies are not able to sink the generated electrical power. An impedance measurement unit for shipboard MVDC systems presented in [11] was shown to capture the impedance up to 1 kHz. However, power converters usually employ an LCL-filter which may have very sharp resonance around few kilohertz. Therefore, the impedance measurement setup should have higher bandwidth than the LCL-filter resonance to fully characterize the impedance. The method presented in [12] relies on making a step change in the passive load of the power converter. However, the method is not applicable to grid-connected converters, since the load is the power system itself. A noninvasive method was introduced in [13], which is based on monitoring the grid waveforms. However, this method is not suitable for power converters with high output impedance, because measuring their impedance generally requires perturbation signal with sufficient amplitude.

This paper proposes a method to identify the inverter impedance using a combination of grid-forming and grid-parallel converters. A voltage-type injection is generated by using a high-power grid-forming inverter, which is capable for characterizing the low-frequency impedance of the power converter. Subsequently, a current-type injection is generated using a grid-parallel converter capable of measuring the high-frequency part of the impedance. Accuracy of the proposed method is compared to an ideal measurement setup using a switching model.

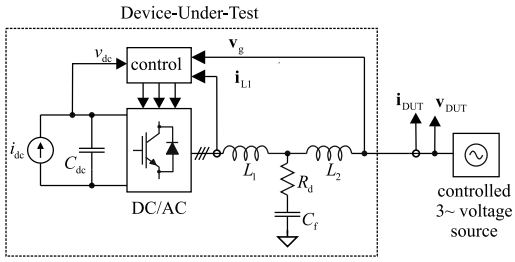


Fig. 1. Principle of measurement setup to identify inverter output impedance.

## II. Three-Phase Impedance in the DQ-Domain

Three-phase sinusoidal variables can be transformed into the dq-domain, where the fundamental component appears as a DC signal. The transformation is done using the Park's transformation according to (1).

$$\begin{bmatrix} x_\mathrm{d} \\ x_\mathrm{q} \\ x_0 \end{bmatrix} = \mathbf{T}^\mathrm{dq} \begin{bmatrix} x_\mathrm{a} \\ x_\mathrm{b} \\ x_\mathrm{c} \end{bmatrix} \tag{1}$$

where the transformation matrix is given by

$$\mathbf{T}^\mathrm{dq} = \frac{2}{3} \begin{bmatrix} \cos(\theta) & \cos\left(\theta - \frac{2\pi}{3}\right) & \cos\left(\theta - \frac{4\pi}{3}\right) \\ -\sin(\theta) & -\sin\left(\theta - \frac{2\pi}{3}\right) & -\sin\left(\theta - \frac{4\pi}{3}\right) \\ \frac{1}{2} & \frac{1}{2} & \frac{1}{2} \end{bmatrix}. \tag{2}$$

The angle $\theta$ should follow the real phase angle of a three-phase system, i.e., the phase angle changes with the fundamental grid frequency. The phase angle can be generated internally by the impedance measurement setup or it can be obtained using a low-bandwidth phase-locked-loop. It is customary to align the dq-reference frame so that the steady-state value of grid voltage q-component appears as zero.

Inverter impedance can be defined in the dq-domain by four independent impedance components as in Eq. (3). $Z_\mathrm{dd}$ is the impedance d-component, which is defined as the ratio of voltage and current d-components $(v_\mathrm{d}/i_\mathrm{d})$. $Z_\mathrm{qd}$ is the cross-coupling impedance from q to d-component $(v_\mathrm{d}/i_\mathrm{q})$ and $Z_\mathrm{dq}$ is the cross-coupling impedance from d to q-component $(v_\mathrm{q}/i_\mathrm{d})$. Finally, $Z_\mathrm{qq}$ is the impedance q-component, defined as the ratio of voltage and current q-components $(v_\mathrm{q}/i_\mathrm{q})$. Ideally, all the four impedance components should be measured to allow full characterization of the converter impedance [6].

$$\mathbf{Z}_\mathrm{inv} = \begin{bmatrix} Z_\mathrm{dd} & Z_\mathrm{qd} \\ Z_\mathrm{dq} & Z_\mathrm{qq} \end{bmatrix} \tag{3}$$

## III. Maximum-Lenght Binary Sequence (MLBS)

Pseudo-random binary sequence (PRBS) is a periodic broadband signal based on a sequence of length $N$. The most commonly used signals are based on maximum-length binary sequences (MLBS). Such sequences exist for $N = 2^n - 1$, where $n$ is an integer. They are popular because they can be generated using feedback shift-register circuits [14].

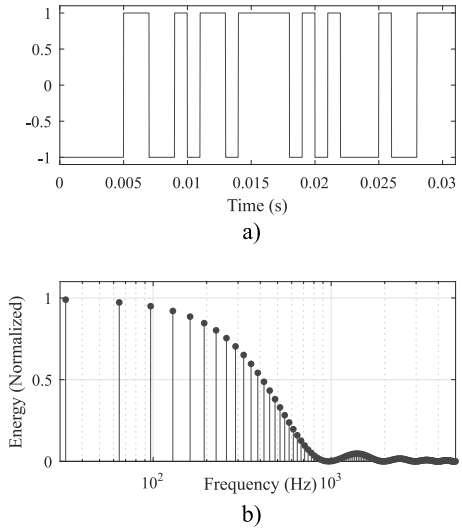


Fig. 2. a) MLBS signal in time-domain and b) its frequency-spectrum.

Fig. 2 shows the MLBS sequence, which is generated at 1 kHz using a $5^\mathrm{th}$-degree shift-register and has signal levels $\pm$1V. The figure also shows the energy spectrum, which contains almost constant energy up to one third of the generation frequency. The energy drops to zero at the generation frequency and its harmonics. An MLBS signal $x$ has the lowest possible peak factor regardless of its length $|x|_\mathrm{peak}/x_\mathrm{rms} = 1$, which means that the sequence is well suited for sensitive systems which require small-amplitude perturbation. Due to the deterministic nature of the sequence, the signal can be repeated and injected precisely and the signal-to-noise ratio (SNR) can be increased by synchronous averaging of the response periods. The MLBS signal is used in this paper to perturb the inverter output terminal waveforms to necessitate measuring the impedance components in (3).

## IV. Ideal Impedance Measurement Setup

Fig. 1 illustrates principle of the ideal three-phase impedance measurement setup. A three-phase grid-feeding inverter, such as a photovoltaic inverter, is connected to a balanced three-phase voltages source. The inverter includes all the necessary control functions, such as DC voltage control, AC current control and phase-locked-loop to synchronize its output currents with the grid voltages. Moreover, the inverter includes passive components, such as an LCL-filter, which are required to filter out ripple in DC and AC side waveforms. Table I summarizes the most important parameters of the three-phase inverter. Control delay is assumed to be 1.5 times the switching period and it was included as a transport delay within the current control of the inverter.

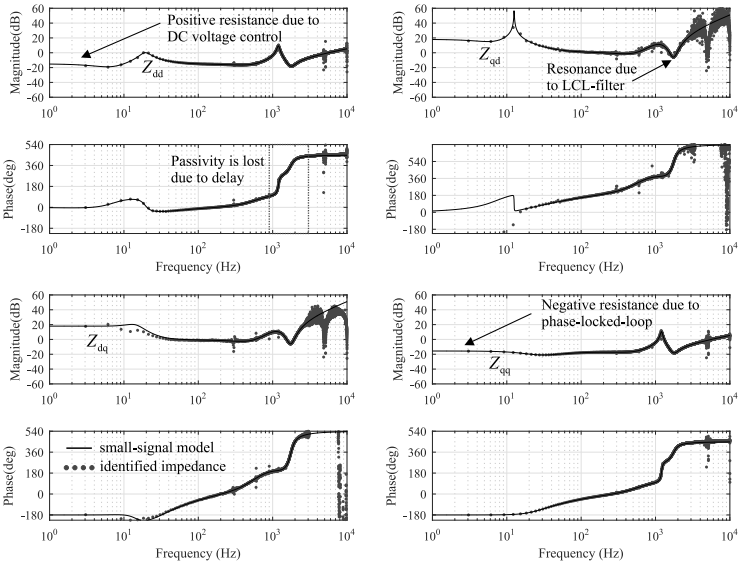


Fig. 3. Identified impedance from the simulator using ideal voltage-type injection.

TABLE I. INVERTER PARAMETERS.

| | | | |
|---|---|---|---|
| $P_{dc}$ | 1 MW | $L_1$ | 60 $\mu$H |
| $V_{ac}^{line\text{-}to\text{-}line}$ | 400 V | $L_2$ | 30 $\mu$H |
| $f_{ac}$ | 50 Hz | $C_{dc}$ | 20 mF |
| $V_{dc}$ | 1500 V | $C_f$ | 400 $\mu$F |
| $f_{sw}$ | 5 kHz | $R_d$ | 70m$\Omega$ |

The output impedance of the inverter is to be identified, which requires a wide-bandwidth perturbation to the voltages or currents on the AC side. In theory, the inverter could be connected to a high-power voltage amplifier, such as a linear amplifier, which can be used to inject the required perturbation. This is actually a practical way to measure the output impedance in the range of few tens of kilowatts [7]. However, in the case of megawatt-level converters using such arrangement is not practical, since the voltage amplifier has to sink all the produced power. The inverter impedance depends on the operating point and should be measured while the converter is online and operating at its nominal output power.

A wide-bandwidth perturbation is injected on top of the grid voltage waveforms $\mathbf{v}_{DUT}$ in the form of a Maximum-Length Binary-Sequence [15]. The MLBS signal is generated at 100 kHz with a peak-to-peak value of 50 V. The MLBS signal is added to d-component of the grid voltage reference value to measure impedance components $Z_{dd}$ and $Z_{qd}$ and to grid voltage q-component to measure $Z_{dq}$ and $Z_{qq}$. As an example, the frequency response of the impedance component $Z_{dd}$ can be computed from the ratio of Fourier-transformed voltage and current as in (4).

$$Z_{dd}(j\omega) = \frac{V_d(j\omega)}{I_d(j\omega)} \tag{4}$$

Fig. 6 shows the perturbed grid voltage and the corresponding output current of the inverter in the natural reference frame during the impedance measurement. The amplitude of grid voltage waveforms follows exactly the MLBS signal, as expected, since the controlled ideal voltage source does not attenuate the perturbation. The impedances obtained by using this arrangement are considered as the reference curves in the following chapters.

Fig. 3 shows the identified impedance components of the power converter which are obtained using the setup in Fig. 1. The switching model is implemented in MATLAB Simulink using the SimScape package. The identified impedance is compared against a small-signal impedance model of the inverter known to be accurate, which can be found in [16]. Fig. 3 shows all four components of the inverter impedance. The black curve is the analytical small-signal model and the blue dots represent the corresponding identified frequency response. The measurement is by theory accurate up to half of the generation frequency, i.e., up to 50 kHz. However, the swithcing ripple of the inverter distorts the measurement near 5 kHz. A few remarks can be done based on the impedance components:

*Effect of DC Voltage Control*

DC voltage control causes the impedance d-component $Z_{dd}$ to behave as a positive resistance within the bandwidth of DC voltage controller. The positive resistance behavior appears as a constant magnitude and phase close to zero degrees. The crossover frequency of DC voltage controller was set to 10 Hz with 47 degree phase margin.

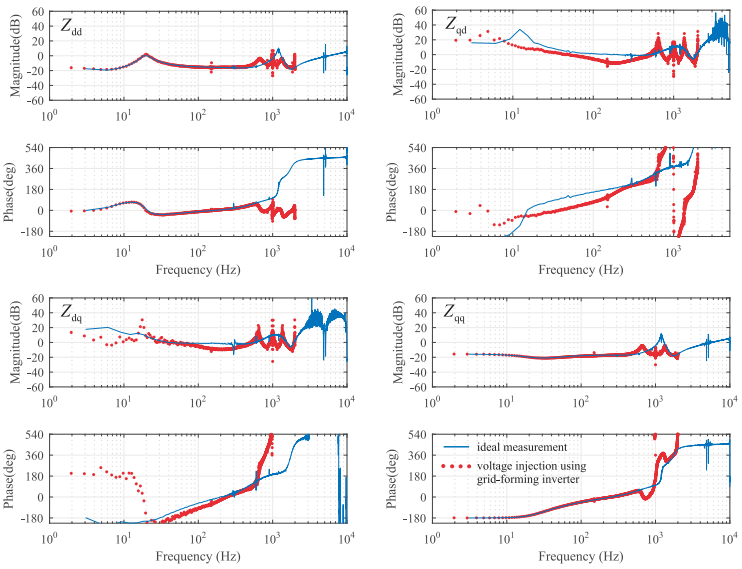


Fig. 4. Identified impedance from the simulator using grid-forming inverter to generate the voltage-type injection.

*Effect of Phase-Locked-Loop*

Phase-locked-loop makes the impedance q-component $Z_{\mathrm{qq}}$ to behave as a negative resistance within the bandwidth of the PLL. The PLL was tuned to have a crossover of 40 Hz with 65 degree phase margin. The negative resistance can be seen as a constant low-frequency magnitude and phase close to -180 degrees. The negative resistance is known to cause stability problems if PLL is tuned to have too fast dynamics [17].

*Effect of LCL-filter*

All impedance components experience a resonance near 1.7 kHz due to the use of LCL-filter. The series resonance is effectively damped by the passive damping resistor $R_{\mathrm{d}}$. Peaking at the resonant frequency can cause instability, especially if active damping is used [18].

*Effect of Control Delay*

Both impedance d and q-components $Z_{\mathrm{dd}}$ and $Z_{\mathrm{qq}}$ experience large positive peaking near the LCL-filter resonant frequency due to $1.5/f_{\mathrm{sw}}$ control delay. Moreover, the impedance does not behave as a passive circuit near the resonant frequency and may amplify harmonics and cause impedance-based instability. Passivity is lost when the phase curve does not stay between -90 and +90 degrees. A non-passive impedance is known to cause impedance-based interactions.

*Cross-Coupling Impedances*

It is often assumed that the cross-coupling impedance components are small and can be neglected, e.g., in impedance-based stability analysis. However, the magnitude of cross-coupling impedance components $Z_{\mathrm{dq}}$ and $Z_{\mathrm{qd}}$ differ from $Z_{\mathrm{dd}}$ and $Z_{\mathrm{qq}}$ only by roughly 12 dB near the resonant frequency. It is important to be able to measure the cross-coupling components to justify the validity assumptions in stability analysis, i.e., whether the cross-couplings can be neglected or not.

*Frequency Range of Interest*

The frequency range of interest can be defined based on the above observations. The measurement setup should be able to extract the impedance accurately from few hertz up to several kilohertz to capture the effects of slow control loops and the resonance of the LCL-filter. Moreover, the cross-coupling impedance components should be measured, since they may affect impedance-based stability [6].

## V. Impedance Measurement Using Grid-Forming Inverter

The inverter is connected to a grid-forming inverter according to Fig. 7. The grid-forming inverter is used to keep the inverter at its nominal operating point during the measurement and to sink the generated power. The DC side is modeled as an ideal voltage source, which would in reality be implemented by a grid-interfacing three-phase converter.

The grid-forming inverter controls its output voltages in the dq-domain using simple integral-type control. Integral-type control was found to be good compromise between stability and control bandwidth, since the grid-forming inverter control dynamics are inherently affected by the impedance of the grid-feeding inverter (impedance of the DUT). The detailed small-signal model and method to take the load-effect into account can be found in [19]. Fig. 8 shows the identified and modeled control loop gain of the grid-forming inverter of voltage d-component. The loop gain related to the q-component has effectively the same shape and is not shown here. The crossover

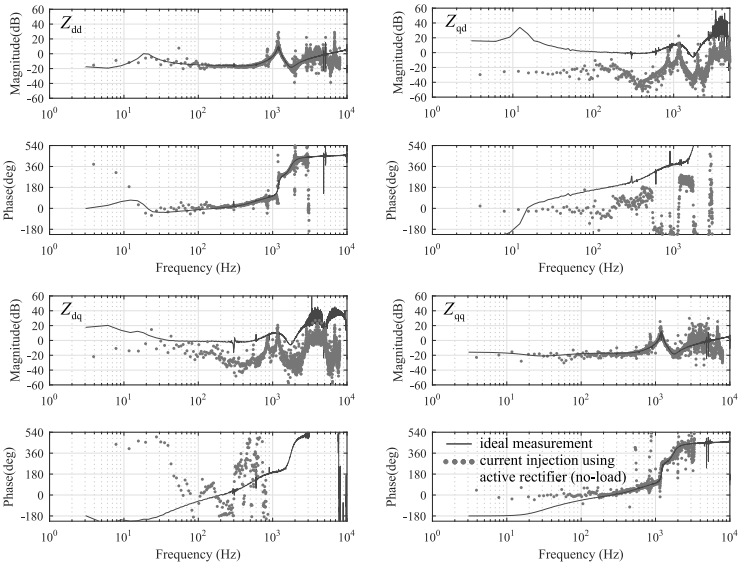


Fig. 5. Identified impedance from the simulator using grid-parallel converter to generate the current-type injection.

frequency of the control loop is approximately 140 Hz and the phase margin 75 degrees.

The purpose of the grid-forming inverter is to replicate the MLBS signal in its output voltages (d or q-component depending on what impedance component is to be identified). Therefore, the frequency response from reference value of the voltage d-component to the actual d-component, i.e., the closed-loop transfer function, should have as high bandwidth as possible to replicate all of the frequency components of the MLBS signal as accurately as possible. Fig. 9 shows the transfer function and the identified frequency response from the reference value of the voltage d-component to the actual voltage d-component. Bandwidth of the voltage control is 216 Hz (-3dB). This suggests that the spectral energy of the MLBS signal starts to attenuate at higher frequencies. Thus, the injection does not go through the control system at high frequencies. The transfer function related to the q-component shows almost identical behavior and is, therefore, not shown.

Fig. 10 shows the modeled transfer function from the reference value of the d-component to the actual q-component of the AC voltage. The identified frequency response deviates slightly from the modeled transfer function. The transfer function has very small magnitude at low frequencies which makes extracting it accurately challenging. Moreover, the gain was found out to be highly sensitive to small changes in the operating point. Thus, small inaccuracies in the simulation cause deviation between the modeled and identified frequency responses. However, the transfer function in Fig. 10 gives a decent idea at what frequencies the injection to d-component affects also the q-component. The transfer function should have as small magnitude as possible to prevent the injection from causing an unwanted perturbation to the q-component. E.g., measuring the $Z_{\mathrm{qq}}$ component in (3) requires that the system is perturbed only by q-component, while the d-component injection remains zero. However, the transfer function in Fig. 10 experiences slight increase in its magnitude near few hundred hertz, which affects the accuracy of the impedance measurement. The optimization of the grid-feeding inverter control system is considered as a future topic and is not discussed further in this paper.

The main parameters of the grid-feeding inverter are given in Table II. The generation frequency of the MLBS signal should be chosen well below the switching frequency of the inverter and over the bandwidth of the transfer function in Fig. 9. The MLBS signal has to be sampled at least two times higher frequency than the generation frequency. However, the sampling frequency should be lower than the switching frequency of the grid-feeding inverter to avoid aliasing-effects. As a compromise, the generation frequency is selected as 1 kHz. The perfect injection amplitude depends on the amount of external noise and the magnitude of the impedance. It was found out by simulations that 50 V peak-to-peak gives the best outcome in the example case. Fig. 11 shows the waveforms at the output terminals of the DUT when the MLBS is injected through the control system of the grid-feeding inverter. It is evident that the grid-forming inverter cannot replicate the MLBS signal accurately, which is expected due to low switching frequency. The voltage waveform is dominated by the 5 kHz switching frequency component. Moreover, the waveforms are affected by the sampling frequency of the grid-feeding inverter, since the control system was modeled in discrete-domain. The MLBS signal was generated by using $10^{\mathrm{th}}$-degree

TABLE II. GRID-FORMING INVERTER PARAMETERS.

| | | | |
|---|---|---|---|
| $V_{\mathrm{dc}}$ | 1500 V | $L^{\mathrm{GF}}$ | 60 $\mu$H |
| $R_{\mathrm{d}}^{\mathrm{GF}}$ | 200m$\Omega$ | $C_{\mathrm{f}}^{\mathrm{GF}}$ | 800 $\mu$F |
| $f_{\mathrm{sw}}$ | 5 kHz | $f_{\mathrm{MLBS}}$ | 1 kHz |
| $n$ | 10 | $V_{\mathrm{MLBS}}$ | 50 $V_{\mathrm{p\text{-}p}}$ |

shift-register, which results in frequency resolution of approximately one hertz. However, the waveforms include enough energy at low frequencies to allow identifying the low-frequency impedance.

Fig. 4 shows the impedance components, that were identified by using the grid-forming inverter as the source of injection. The impedance d and q-components $Z_{\mathrm{dd}}$ and $Z_{\mathrm{qq}}$ are accurately captured approximately up to 500 Hz. Thus, the effect of slow control loops such as DC voltage control and phase-locked-loop can be evaluated. However, the frequency range of the impedance measurement is limited by the low generation frequency of the MLBS signal (1 kHz). The cross-coupling impedances $Z_{\mathrm{qd}}$ and $Z_{\mathrm{dq}}$ contain slight error due to the fact that some of the injected perturbation leaks between d and q-components, as can be seen by analyzing Fig. 10. However, the accuracy could be increased by careful design of the grid-forming inverter control system. Some form of decoupling network should be designed to reduce the cross-coupling in the grid-forming inverter control dynamics, which is considered as a potential future topic.

## VI. IMPEDANCE MEASUREMENT USING GRID-PARALLEL CONVERTER

The bandwidth of the impedance measurement can be extended by using a parallel-connected three-phase converter accrording to Fig. 12. In principle the converter is an active rectifier. However, since the purpose of the converter is just to amplify the MLBS signal, it can be operated without a load on the DC side. The main parameters of the grid-parallel converter are given in Table III. The converter can have significantly lower power rating, because it is not required to sink any power.

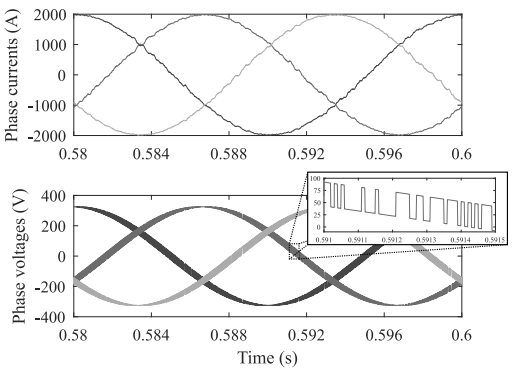


Fig. 6. Three-phase current and voltage waveforms in the ideal measurement setup.

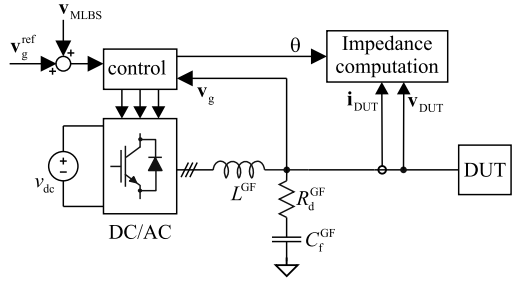


Fig. 7. Principle of measurement setup using grid-forming inverter.

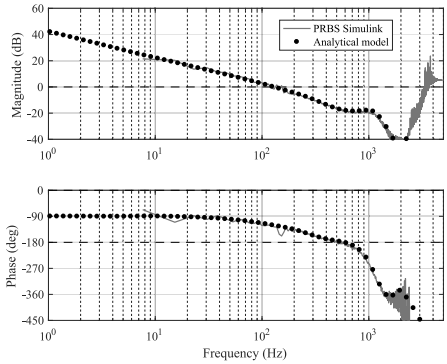


Fig. 8. Identified and modeled loop gain related to the control of voltage d-component.

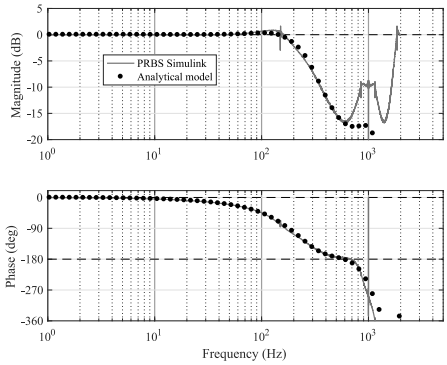


Fig. 9. Frequency response from the reference value of voltage d-component to voltage d-component.

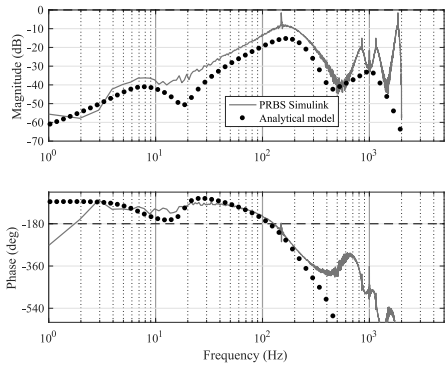


Fig. 10. Frequency response from the reference value of voltage d-component to voltage q-component.

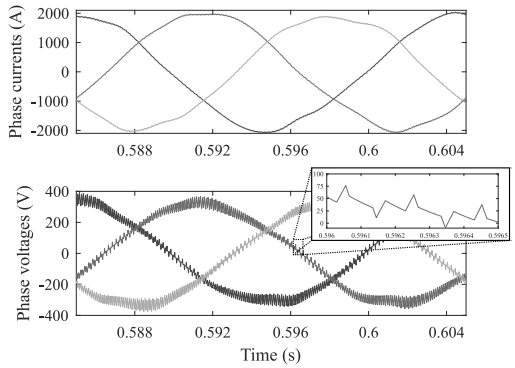


Fig. 11. Three-phase current and voltage waveforms with grid-forming inverter.

The converter was assumed to have maximum power rating of 10 kVA and, thus, its switching frequency can be much higher (20 kHz). The MLBS signal is added in the converter's control system to the reference values of of output currents.

The MLBS signal was generated at 4 kHz and sampled at two times higher frequency of 8 kHz. The amplitude was limited to 20 A peak-to-peak to avoid over-current stress of the switching components. A $10^{\text{th}}$-degree shift-register was used to generate the MLBS, which translates to a frequency resolution of roughly 4 Hz.

The average of the identified impedances in Fig. 5 follow the ideal measurement up to approximately 2 kHz

TABLE III. GRID-PARALLEL CONVERTER PARAMETERS.

| | | | |
|---|---|---|---|
| $V_{\text{dc}}$ | 1500 V | $L_{\text{f}}^{\text{GP}}$ | 1 mH |
| $R_{\text{d}}^{\text{GP}}$ | 1.36 Ω | $C_{\text{f}}^{\text{GP}}$ | 10 $\mu$F |
| $f_{\text{sw}}$ | 20 kHz | $f_{\text{MLBS}}$ | 4 kHz |
| $n$ | 10 | $V_{\text{MLBS}}$ | 20 $V_{\text{p-p}}$ |
| $L_2^{\text{GP}}$ | 200 $\mu$H | $C_{\text{dc}}$ | 2 mF |

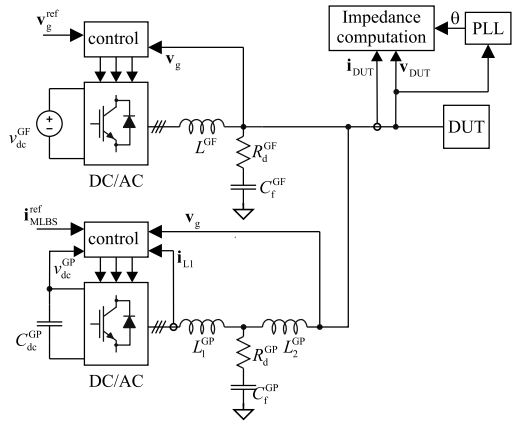


Fig. 12. Principle of measurement setup using the grid-parallel converter.

which is half of the generation frequency of the MLBS. The non-passive region around the resonant frequency of the LCL-filter can also be captured. The injection does not have enough energy to enable identification of cross-coupling impedance components. This is a matter that has been left as a future challenge. One option is to increase the power level of the grid-parallel inverter which, however, may reduce the switching frequency and thereby the maximum bandwidth of the measurement. Another option would be to use decoupling impedance placed before the grid-forming inverter to divert the high-frequency current toward the DUT. However, this may easily compromise the stability of the system and may require re-tuning of the grid-forming inverter control parameters.

Impedance measurement in the dq-domain requires that the grid angle is known. In the case of voltage-type injection the angle is known, since it is generated inside the control system of the back-to-back converter. However, in the case of the current-type injection this angle cannot be used directly, because the decoupling impedance causes a phase-shift. However, the angle can be estimated by using a slow phase-locked-loop as depicted in Fig. 12.

## VII. CONCLUSIONS

This paper shows the first attempt to identify the AC-side output impedance of a 1 MW grid-feeding inverter in its nominal operating point using a combination of grid-forming and grid-parallel converters. A grid-forming inverter is used to sink the power generated by the inverter and to add enough perturbation to inverter output voltages to measure impedance up to 500 Hz (in synchronous reference frame). An additional 10 kW grid-parallel inverter is used to generate perturbation to inverter output currents to measure impedance from 100 Hz up to 2 kHz. It is demonstrated that the combination of grid-forming and grid-parallel inverter can be effectively used in impedance measurement of multimegawatt inverters. This paper pro-

vides a proof-of-concept by providing preliminary simulation results based on a switching model, when the PRBS-method is used for impedance identification. Dynamic model of the grid-forming inverter is used to optimize the control loops for operation with the inverter-under-test.

## REFERENCES


[1] "Frequency Stability Evaluation Criteria for the Synchronous Zone of Continental Europe," RG-CE System Protection & Dynamics Sub Group, Entsoe, March 2016.

[2] C. Li, "Unstable Operation of Photovoltaic Inverter from Field Experiences," *IEEE Transactions on Power Delivery*, (early access), 2017, doi: 10.1109/TPWRD.2017.2656020.

[3] P. Belkin, "Event of 10/22/09", CREZ Technical Conference, Electrical Reliability Council of Texas, 2010.

[4] J. Sun, "Impedance-Based Stability Criterion for Grid-Connected Inverters," *IEEE Transactions on Power Electronics*, vol. 26, no. 11, pp. 3075-3078, Nov. 2011.

[5] X. Wang, F. Blaabjerg and W. Wu, "Modeling and Analysis of Harmonic Stability in an AC Power-Electronics-Based Power System," *IEEE Transactions on Power Electronics*, vol. 29, no. 12, pp. 6421-6432, Dec. 2014.

[6] T. Messo, A. Aapro and T. Suntio, "Generalized multivariable small-signal model of three-phase grid-connected inverter in DQ-domain," IEEE 16th Workshop on Control and Modeling for Power Electronics (COMPEL), pp. 1-8, 2015.

[7] T. Messo, A. Aapro, T. Suntio and T. Roinila, "Design of grid-voltage feedforward to increase impedance of grid-connected three-phase inverters with LCL-filter," IEEE 8th International Power Electronics and Motion Control Conference (IPEMC-ECCE Asia), pp. 2675-2682, 2016.

[8] B. Wen, D. Boroyevich, R. Burgos, P. Mattavelli and Z. Shen, "Small-Signal Stability Analysis of Three-Phase AC Systems in the Presence of Constant Power Loads Based on Measured d-q Frame Impedances," *IEEE Transactions on Power Electronics*, vol. 30, no. 10, pp. 5952-5963, Oct. 2015

[9] L. H. Kocewiak *et al.*, "Wind Turbine Harmonic Model and Its Applications," 14th International Workshop on Large-Scale Integration of Wind Power into Power System as well as on Transmission Networks for Offshore Wind Power Plants, pp. 1-6, 2015.

[10] J. Jokipii, T. Messo and T. Suntio, "Simple method for measuring output impedance of a three-phase inverter in dq-domain," 2014 International Power Electronics Conference (IPEC-Hiroshima 2014 - ECCE ASIA), pp. 1466-1470, 2014.

[11] M. Jakšić *et al.*, "Medium-Voltage Impedance Measurement Unit for Assessing the System Stability of Electric Ships," *IEEE Transactions on Energy Conversion*, vol. 32, no. 2, pp. 829-841, June 2017.

[12] V. Valdivia, A. Lázaro, A. Barrado, P. Zumel, C. Fernández and M. Sanz, "Impedance Identification Procedure of Three-Phase Balanced Voltage Source Inverters Based on Transient Response Measurements," *IEEE Transactions on Power Electronics*, vol. 26, no. 12, pp. 3810-3816, Dec. 2011.

[13] J. Hui, W. Freitas, J. C. M. Vieira, H. Yang and Y. Liu, "Utility Harmonic Impedance Measurement Based on Data Selection," *IEEE Transactions on Power Delivery*, vol. 27, no. 4, pp. 2193-2202, Oct. 2012.

[14] K. Godfrey, *"Perturbation Signals for System Identication"*. Prentice Hall, UK., 1993.

[15] T. Roinila, T. Messo and A. Aapro, "Impedance measurement of three phase systems in DQ-domain: Applying MIMO-identification techniques," IEEE Energy Conversion Congress and Exposition (ECCE), pp. 16 , 2016.

[16] T. Suntio, T. Messo and J. Puukko, *"Power Electronic Converters: Dynamics and Control in Conventional and Renewable Energy Applications"*, Wiley-VCH , pp. 633-661, 2017.

[17] T. Messo, J. Jokipii, A. Mäkinen and T. Suntio, "Modeling the grid synchronization induced negative-resistor-like behavior in the output impedance of a three-phase photovoltaic inverter", *4th IEEE International Symposium on Power Electronics for Distributed Generation Systems (PEDG)*, pp. 1-7, 2013.

[18] A. Aapro, T. Messo, Tomi Roinila and T. Suntio, "Effect of active damping on output impedance of three-phase grid-connected converter", *IEEE Transactions on Industrial Electronics*, vol 64, no 9, pp. 7532-7541, 2017.

[19] M. Berg, T. Messo and T. Suntio, "Frequency Response Analysis of Load Effect on Dynamics of Grid-Forming Inverter", International Power Electronics Conference, (IPEC-Niigata 2018 -ECCE Asia-), pp. 1-8, 2018.